COVENTRY UNIVERSITY

DOCTORAL THESIS

Universality and Dynamical Behaviour in Pure and Disordered Spin-1 Models

Author:
Alexandros VASILOPOULOS

Supervisors:
Dr. Nikolaos G. FYTAS
Prof. Dr. Martin WEIGEL
Examiners:
Prof. Nigel B. WILDING
Dr. Ran HOLTZMAN

Statistical Physics Group
Centre for Fluid and Complex Systems

Certificate of Ethical Approval

Applicant:	Alexandros Vasilopoulos
Project Title:	SPIN MODELS WITH RANDOM FIELDS

This is to certify that the above named applicant has completed the Coventry University Ethical Approval process and their project has been confirmed and approved as Low Risk

Date of approval:	06 Sep 2022
Project Reference Number:	P140774

Declaration of Authorship

I, Alexandros VASILOPOULOS, declare that this thesis titled "Universality and Dynamical Behaviour in Pure and Disordered Spin-1 Models" and the work presented therein are my own. I confirm that:

- This work was done wholly or mainly while in candidature for a research degree at this University.
- Where any part of this thesis has previously been submitted for a degree or any other qualification at this University or any other institution, this has been clearly stated.
- Where I have consulted the published work of others, this is always clearly attributed.
- Where I have quoted from the work of others, the source is always given. With the exception of such quotations, this thesis is entirely my own work.
- I have acknowledged all main sources of help.
- Where the thesis is based on work done by myself jointly with others, I have made clear exactly what was done by others and what I have contributed myself.

Signed: *Alexandros Vasilopoulos*

Date: *May 20, 2024*

"EN ΟΙΔΑ ΟΤΙ ΟΥΔΕΝ ΟΙΔΑ"

COVENTRY UNIVERSITY

Abstract

Universality and Dynamical Behaviour in Pure and Disordered Spin-1 Models

by Alexandros VASILOPOULOS

The present thesis deals with the Monte Carlo study of models under dilution due to a single-ion anisotropy, giving rise to a number of cross-over phenomena. The models considered are the Blume-Capel and spin-1 Baxter-Wu in a crystal field, both possessing a rich phase transition behaviour. Specifically, they tend to exhibit first-order-like traits, especially with the increase of the strength of the crystal field. Thus, as one approaches their multicritical point, the study becomes more complicated and elaborate, with finite-size effect appearing, especially for the Baxter-Wu case due to the triplet interactions leading to strong first-order-like characteristics.

This work focuses on a number of interconnected topics. For the spin-1 Baxter-Wu model under a crystal field, the aim is placed in elucidating the order of the transition and the universality class, a topic that is riddled by discrepancies in the literature. One would expect, from the renormalisation group theory and phenomenological arguments utilising the similar Blume-Capel model and dilute Potts models, that in the high-temperature regime the model undergoes a continuous transition that falls into the universality class of the spin-1/2 Baxter-Wu model. In fact, this is exactly the result recovered by the current work. Additionally, the development of a possibly improved method to further study the aforementioned system is attempted. Specifically, a hybrid algorithm is utilised and its dynamical scaling is thoroughly studied in the model's continuous-transitions regime. Such an approach could help in locating and studying its pentacritical point.

Since the two-dimensional Blume-Capel model has been thoroughly studied, especially in its pure form, in the current work it is considered under quenched disorder. Specifically, uncorrelated randomness is applied to the crystal-field strength, in the form of a bimodal distribution. In addition, an external oscillating magnetic field drives the model out of equilibrium. Studying this system in its multi-droplet regime, period averaged observables are calculated and their susceptibilities are shown to scale like their counterparts on the pure equilibrium model.

Summary of Work and Publications

The current manuscript is a narrative of the work embarked upon during my Ph.D. studies in *Coventry University*, at the *Centre for Fluid and Complex Systems* (FCS), between January 2020 and January 2024, and under the guidance and mentorship of my supervisors Dr. Nikolaos G. Fytas and Prof. Dr. Martin Weigel.

This work undertakes the study of models of statistical physics and critical phenomena via the use of Monte Carlo simulations. Barring some local runs on the personal laptop given to me by the university, the lion's share of computational time was done on the high performance computing (HPC) clusters *Zeus* and *EPYC*, provided by Coventry University.

The bulk of the simulations were written in the programming language *C++11* or higher, using the compiler GNU *g++7.1.0* to *g++10.2.0*, or *icc 2021.1.2 20201208*, depending on the purpose of the application and where it was run. For GPU coding, *cuda10.1.243* was used throughout. Some part of the data analysis was performed in *Python 3.9.7* or higher, and the fitting analysis and figure plotting were performed with *gnuplot 5.2.8* or higher.

The yield of these years was the following publications:

1. Alexandros Vasilopoulos, Zeynep Demir Vatansever, Erol Vatansever, and Nikolaos G. Fytas, "Monte Carlo study of the two-dimensional kinetic Blume-Capel model in a quenched random crystal field", Phys. Rev. E 104, 024108 (2021).

2. Nikolaos G Fytas, Alexandros Vasilopoulos, Erol Vatansever, Anastasios Malakis, and Martin Weigel, "Multicanonical simulations of the 2D spin-1 Baxter-Wu model in a crystal field", J. Phys.: Conf. Ser. 2207 012008 (2022).

3. Alexandros Vasilopoulos, Nikolaos G. Fytas, Erol Vatansever, Anastasios Malakis, and Martin Weigel, "Universality in the two-dimensional dilute Baxter-Wu model", Phys. Rev. E 105, 054143 – Published 25 May 2022.

4. A. R. S. Macêdo, A. Vasilopoulos, M. Akritidis, J. A. Plascak, N. G. Fytas, and M. Weigel, "Two-dimensional dilute Baxter-Wu model: Transition order and universality", Phys. Rev. E 108, 024140 (2023).

Additionally, the following works are currently being prepared and are expected to be ready in a relatively short time frame:

1. A. Vasilopoulos, M. Akritidis, N. G. Fytas, M. Weigel, "Dynamical scaling of the 2D pure and dilute Baxter-Wu model".

2. A. R. S. Macêdo, A. Vasilopoulos, M. Akritidis, J. A. Plascak, N. G. Fytas, and M. Weigel, "Universal distributions and universality in the spin-$S \geq 1/2$ Baxter-Wu model".

3. A. Vasilopoulos, N. G. Fytas, M. Weigel, “Cross-over effects in the ex-first-order regime of the two-dimensional Blume-Capel model”.

Lastly, the following works are expected to be finished in a longer time frame, since extra simulations are required:

1. A. Vasilopoulos, A. R. S. Macêdo, J. A. Plascak, N. G. Fytas, M. Weigel, “Mixed field distributions along the first- and second-order transition lines of the spin-1 Baxter-Wu model in a crystal field: Locating the pentacritical point”.

2. A. Vasilopoulos, M. Akritidis, N. G. Fytas, M. Weigel “Dynamical scaling of random Ising models in two dimensions”.

Acknowledgements

I would like to acknowledge the help and support of my project supervisors Dr. Nikolaos G. Fytas and Prof. Dr. Martin Weigel, whom I cannot possibly thank enough for their help. I will forever carry with me their way of thinking and remember their kindness and all the great times we had.

I am also indebted to Dr. Michail Akritidis for his help, the long discussions on physics, and his friendship. I am grateful I met my housemates Gene, Adrian, Zareth, and Anthony, who I already miss greatly. Also, I am thankful of my office comrades, who made working towards a Ph.D. a more bearable and fun experience.

I could not have undertaken this journey without my dear friend Eleftheria, and the friends I made along the way. Thank you for all the great times we had in these past years.

Lastly, this endeavour would not have been possible if it weren't for my mother and my brother.

Contents

Dedicated to the people that made me love physics. And to those that made me hate it. To repay these evils done to me, I refrain from mentioning all of you.

Introduction

Complex Systems

Complex systems have at least as many definitions as there are scientific disciplines, but in general they can be thought of as systems comprising of a very large number of individual agents which, through interactions, give rise to a whole. Some examples are: the human brain, the global economic market, societies, the global climate, transportations systems, cells, etc. Perhaps, the most important characteristic of these types of systems is that they can demonstrate collective behaviours. Usually, the individual units are content with acting only according to what their immediate surrounding dictate. Every so often though, if the conditions are just right, from these short range purviews can emerge long range collective phenomena. Consequently, it is not difficult to imagine that these events are placed at the heart of contemporary research in many fields, such as economics, biology, engineering, even philosophy, and of course, physics. Some instances of these type of emergent events can be found in: changes in crystal structures, ferromagnetism, critical opalescence at a gas-liquid transition, superconductivity and superfluidity, etc.

Many of the examples given above exhibit collective behaviour as a result of a change in one or more of the system's parameters. In turn, this causes a shift from an initially short-range-correlated state to a state with long-range correlations. Going in more depth with the examples, certain species of grasshoppers, under specific environmental conditions, can transform in just one generation from solitary entities to gregarious and nomadic beings [1, 2], even changing their external characteristics, producing such devastation in their path as to be mentioned in many ancient texts for the catastrophes they caused. Another similar example, stemming from the animal kingdom, is a flock of starlings producing magnificent shapes while in flight. Even though each bird can only perceive its immediate surrounding, the whole flock creates long range patterns, known as murmurations, sometimes even resembling discernable structures. Other paradigms include the human brain when experiencing a stroke [3], the global market undergoing a crash [4], human interactions and virus spread [5], voting systems [6, 7], and many more. All the above shifts can be classified as *phase transitions*.

Statistical Mechanics

The success of statistical physics is that it created a theoretical framework that allowed the examination of many-body systems. Starting from the need to study the physical world, one needs to consider that a small confine of space is expected to have a huge number of particles.[1] Solving for example the equations of motion in this case is not only impossible, but also intractable. Even supposing that the solution is known, it would be beyond the bounds of the human brain to understand it. It becomes then necessary to describe such systems thermodynamically, by their macroscopic properties.[2] Under the lens of statistical mechanics, these properties are defined by averages over microscopic states of the system.

Phase Transitions

This thesis deals with continuous and discontinuous phase transitions. In the latter, two (or more) different states coexist, as happens for example to water when it freezes. In this case, the states of matter involved coexist, until one is slowly reduced and the other prevails. These transitions have many applications, especially in engineering. An instance of that are "phase change materials" [9] that have the ability to absorb or release large amount of energy during transitions, making them useful when there is need to heat or cool substances. The other case of phase transitions to be discussed are continuous and are connected to the physics of critical points. These are more inline with the examples discussed above, where long-range correlations can derive from short-range interactions.

At the late 19^{th} century, it was noted that phase transitions undergone by seemingly entirely unalike systems present eerily identical characteristics. For example, physical quantities like the magnetic susceptibility and the specific heat, can display the same diverging behaviour across different systems [10–15], very close to the transition. Around the critical point, where the phase changes, observables follow scaling laws of the form $\sim t^x$. In this expression, $t = (T - T_c)/T_c$ is the *reduced temperature*, T_c is the temperature of the transition, and x is called a *critical exponent*.

These observations led to the establishment of the concept of *universality*, observed directly by the critical exponents and universal ratios that uniquely characterise these events. Models for whom these quantities coincide are said to fall in the same *universality class*. It is therefore commonplace, instead of studying the system of interest directly, to probe critical properties by investigating a simpler model of the same universality class.

Such considerations are regular, and perhaps easier realised, among many-body lattice systems with pairwise interactions. The most familiar and well researched example is the *Ising* model (colloquially called the fruit-fly model of statistical physics). Due to their conceptual

[1] In general, a small confine of space is expected to have an Avogadro's number of particles (approximately 10^{23}).
[2] For a brief study of thermodynamics see [8].

simplicity these magnetic models became the entry point to understanding phase transitions. Starting with Pierre Curie [16], the first concrete theory of magnetic transitions was developed to describe ferromagnetism. Later, around the 1920s, Wilhelm Lenz thought of a simple way of modelling interactions occurring in a magnet, with the aim of creating a toy model for phase transitions. He imagined a one-dimensional chain with equidistant molecules placed along its length, able to interact only with their closest neighbours. Formally, this model is described by the Hamiltonian

$$\mathcal{H} = -J \sum_{\langle ij \rangle} \sigma_i \sigma_j, \tag{1}$$

where the brackets $\langle \dots \rangle$ indicate that the sum is over all nearest neighbours, J is the strength of the exchange interactions, and the σ_i are binary variables able to take the values $\{-1, +1\}$. Colloquially, the σ_i are called spins.[3]

The idea behind this construction was that with a high temperature each spin would point randomly in any of the two directions, due to thermal fluctuations, thus creating a paramagnet. By decreasing the temperature, interactions between nearest neighbours that reduce the free energy could create long range order, possibly leading to the appearance of spontaneous magnetisation. This was the problem that Lenz gave to one of his students, Ernst Ising, from whom the name of the model is derived. Ising solved the model in one dimension and showed that there is no phase transition for non-zero temperatures [17, 18].

Almost a decade later, Rudolf Peierls made an argument for the existence of ferromagnetic order at finite temperatures for the two-dimensional Ising model [19, 20]. In 1944, Lars Onsager solved the two-dimensional Ising model analytically, showing that it actually exhibits a transition from a paramagnet to a ferromagnet [21]. This was a landmark event in the study of phase transitions, because the Ising model critical exponents calculated by Onsager did not agree with the ones predicted by theories trying to describe phase transitions [13]. It turns out that the aforementioned theories, such as mean field and the Landau–Ginzburg theory, did not capture fluctuations properly.

The most successful theory for describing phase transitions is that of *renormalisation group*, developed by Kenneth Geddes Wilson [22–24]. In this framework, as we shall see further in the thesis (Chapter 1), an understanding about how systems behave under different scales can be established, giving the ability for a unified understanding of transition phenomena.

Several methods that allow to study models of statistical physics, like the Ising model have been developed (see for example [25]). Unfortunately, even the simpler models do not yield to analytic solutions in the vast majority of cases, and thus approximate methods have been developed. In this work, the focus is placed on *Monte Carlo* methods to deal with the simulation

[3] Borrowing the nomenclature of quantum mechanics, these type of models are referred to as spin-1/2, due to fermions with spin-1/2 only being able to be observed at states were their spin is either in the $+1/2$ or in the $-1/2$ state.

of the magnetic system. The history of these methods dates back to the Los Alamos National Laboratory, with the development of the most famous Monte Carlo algorithm, the *Metropolis* algorithm [26, 27], commonly used in various forms in a large number of fields. The idea behind this process is to perform ensemble averages instead of following the kinematics of a system. These methods, along with the advancements in computer science and computer power, have paved the way for the development of further, more elaborate, and case specific approaches.

Scope of the Thesis

In the present work a number of interconnected two-dimensional problems will be tackled. The main commonalities revolve around finite-size and cross-over phenomena, especially in the case where a crystal-field anisotropy is introduced. This additional term in the Hamiltonian, acting to dilute the system (see Chapter 3) is known to make things behave in a more first-order-like manner, if one can say so, short of being rigorous. The main questions tackled are: the dynamics of the pure and dilute Baxter-Wu model, especially as one approaches the multicritical point of the latter, while incorporating a cluster update. Additionally, the questions of the order and universality of the phase transition of the aforementioned spin-1 Baxter-Wu model will be answered, and the foundations for the accurate location of its multicritical point will be laid. Lastly, the simpler but similar Blume-Capel model will be investigated under the inclusion of quenched disorder and an external, time varying, magnetic field, that drives the system out of equilibrium. This model undergoes a kinetic phase transition which, although characterised by similar observables, stands on less solid foundation in terms of theoretical understanding.

All the models mentioned above are conceptual derivatives of the Ising model, introduced in Eq. (1). In their spin-1 form, they include a term that is equivalent to the fugacity, in a grand canonical setting, making the number of spins a random variable around some mean, due to a chemical potential, Δ. This term can simply be expressed as

$$\Delta \sum_i \sigma_i^2. \tag{2}$$

For the Baxter-Wu model, the nearest-neighbour interactions are between three spins, making matters much more complicated, especially in the application of a cluster algorithm. The Blume-Capel model, being much more thoroughly studied in the literature, is a fertile ground to study the much richer and interesting case of quenched disorder. In a sense, due to its similarity to the spin-1 Baxter-Wu model, this can be seen as paving the way for similar studies in the latter, after resolving some essential questions for the Baxter-Wu first.

These subjects are intricately related, since all exhibit some form of cross-over effects. The Blume-Capel and spin-1 Baxter-Wu models' phase diagrams consist of both first- and second-order transition lines, connected by a multicritical point. Thus, by varying the system's fields, the behaviour changes from one regime to the other. For the Baxter-Wu model, as will be shown, the continuous transition has first-order characteristics, and the finite-size system behaviour exhibits a cross-over from an apparent discontinuous to a continuous transition. A naive interpretation of the behaviour of the smaller system sizes would thus lead to the incorrect characterisation of the transition. Including quenched disorder to models with such a phase diagram complicates things even further, since uncorrelated disorder is expected to soften the discontinuous transition to a continuous one [28], at least in two dimensions. This behaviour however is also riddled with finite-size effects [29].

Content Overview

After this short introduction, the rest of the text is structured as follows. Chapter 1 contains a statistical physics primer, describing phase transitions and the renormalisation group. There, the theory of transition phenomena will be discussed thoroughly, gathering the most important results that will be used in the following chapters. Additionally, the study of systems of finite sizes, in order to extrapolate results in the thermodynamic limit, is showcased. Also, the renormalisation group will help provide a framework, through which the behaviour of systems undergoing a phase transition can be inspected and understood. It will also provide a language, allowing to discuss more precisely the phenomena, questions, and results of the thesis.

In Chapter 2, the computational methods used by this work are described. These include single-spin-flip algorithms, such as the Metropolis and heat-bath techniques, as well as cluster algorithms, with the latter implemented in practice in hybrid applications later in the thesis. Furthermore, generalised ensemble methods will be utilised, such as the multicanonical and Wang-Landau approaches. All these algorithms were utilised, one way or the other, to produce and test the results present in the following chapters. Chapter 2 concludes with a short pass through additional methods, with which one can simulate similar models.

In Chapter 3, a study of the dynamical properties of the Baxter-Wu model is presented, with an emphasis on the implementation of clusters and whether they can be of use when studying the model towards the end of its second-order regime. The behaviour of the dynamical properties of clusters in spin-1 models, implemented via some hybrid scheme, poses an open questions in the literature. In fact, a cluster algorithm was never applied to the spin-1 Baxter-Wu model in any form before, and a cluster algorithm for the spin-1/2 case exists but has been severely underutilised. Such an algorithmic scheme might help to identify and study the multicritical point of the model.

In Chapter 4, the transition properties as well as the critical behaviour of the spin-1 Baxter-Wu model in a crystal field are considered. Past controversies with respect to the order of the transition and the universality class of the model are resolved. Finally, the universal distributions are shown, for a qualitative discussion of the finite-size effects that plague the model in the vicinity of the multicritical point. Specifically for the energy, these distributions will provide a simple paradigm for renormalisation-group concepts, highlighting the main ideas of universality.

Chapter 5 contains an investigation on the Blume-Capel model, under a quenched random crystal field. The application concerns uncorrelated disorder and will thus affect the behaviour of the ex-first-order regime of the model. An additional periodically oscillating magnetic field is included, and the model is studied in the multi-droplet regime, with many clusters forming and expanding at any given time. Considerations about the behaviour and scaling of period averaged observables showcase that the universality class of this kinetic model coincides with the equilibrium one.

To conclude, a final chapter offers a summary of all the thesis as a whole, and opens the discussion for future work. Lastly, the thesis has appendices, discussing subjects like data analysis (Appendix A) and summarising results from least-square fits (Appendix B) which would break the flow of the thesis were they placed in the main body of the text.

Chapter 1

Theoretical Preamble

It is possible to formulate phase transitions by mathematical means, through the framework of the renormalisation group. To discuss the complex phenomenon that is a phase transition, the language of statistical mechanics is required. Additionally, to expand upon it computationally, via Monte-Carlo methods, the concepts of phase spaces and statistical ensembles are necessary. To this end, the focus of this chapter is placed on introducing the bare minimum theoretical background necessary for the rest of the thesis. For thorough and detailed examinations of these subjects, the reader is referred to the following sources [10–15, 25, 30–38].

This chapter's structure is as follows: Section 1.1 includes an introduction to statistical physics. A general approach to phase transitions and critical phenomena can be found in Section 1.2. In Section 1.3, elements of the renormalisation group theory are given, while in Section 1.4 finite-size scaling is discussed. Additionally, in Section 1.5 a survey of discontinuous phase transitions can be found. Moreover, a discussion concerning disorder systems and the Harris criterion can be found in Section 1.6. Furthermore, an overview of cross-over phenomena that appear in computational studies of statistical physics systems is made in Section 1.7.

1.1 Statistical Physics Primer

1.1.1 Phase space

In a classical setting, to completely describe a system consisting of N particles, the knowledge of all positions and momenta is required, q_i and p_i respectively with $i = 1, 2, \dots 3N$ for a three-dimensional space.[1] This means that the system can be depicted by an abstract point, $\mathbf{\Gamma}(t) = (q_1(t), q_2(t), \dots, q_{3N}(t), p_1(t), p_2(t), \dots, p_{3N}(t))$, moving in a $6N$-dimensional space, called the *phase space*. The *microstate* of the system is defined by this point. In reality, only a certain number of macroscopic variables can be observed at one time and an enormous amount of microstates are in general compatible with this *macrostate*.

[1] In general N is a huge number, since in a small confine of space one can expect to find a number of particles of the order of 10^{23}.

Following the trajectory of point $\mathbf{\Gamma}$, a time average of any observable quantity $Q(\mathbf{\Gamma}, t)$ can be calculated by

$$\overline{Q} = \lim_{T\to\infty} \frac{1}{T} \int_0^T dt Q(\mathbf{\Gamma}(t), t). \tag{1.1}$$

Essentially, it would be impossible to accomplish the process implied by Eq. (1.1) for two reasons: Firstly, it is unfeasible to know the positions and momenta of a large number of particles, and secondly, it would be unworkable to follow their evolution through time. Thus, a more accessible method of studying average properties of the system is necessary, and a way of defining equilibrium and when it happens is also required. To surpass these difficulties, the concept of *statistical ensembles* is needed, which will transpose the conversation from the time evolution of one system to the distribution of microstates in phase space of an infinite amount of similar systems.

1.1.2 Statistical ensemble

A key idea is that, given enough time, through the movement of the single system in phase space, knowledge of the initial conditions would be totally lost, as a result of the complex interactions [13, 32, 39]. In that sense, one can imagine starting with an ensemble of an infinite number of systems, in different initial conditions, and following their time evolution, $\{\mathbf{\Gamma}_s(t)\}_{s=0}^{\infty}$. The result would be some density, $W(\mathbf{\Gamma}, t)$, in phase space. Barring cases where a system exhibits a very rugged energy landscape, which would force it to be stuck in some metastable area of phase space, then it should be safe to assume that after an infinite amount of time the ensemble would pass through every point of phase space. This is the crucial assumption of *ergodicity*, which allows to pass from time to ensemble averages.[2]

More specifically, the fraction of copies in any particular infinitesimal volume of phase space is $W(\mathbf{\Gamma}, t)d\Gamma$, where $d\Gamma = \mathcal{C} \prod_{i=1}^{3N} dq_i dp_i$, defining an ensemble average for any observable quantity $Q(\mathbf{\Gamma}, t)$ by

$$\langle Q(t) \rangle = \int W(\mathbf{\Gamma}, t) Q(\mathbf{\Gamma}, t) d\Gamma, \tag{1.2}$$

where the integral is taken over the whole phase space. The constant factor $\mathcal{C}$ in the metric needs to be included in the integration measure. Classically such a term cannot be justified, but the quantum mechanical limit necessitates its existence.[3] As will be discussed in the next section, in thermodynamic equilibrium the two averages of Eqs. (1.1) and (1.2) should give the same result. The next chapter will showcase why Monte Carlo methods can shine in this framework.

[2] This assumption does not hold for example for glassy systems where certain volumes of phase space are unavailable, depending on the initial conditions [40]. Nevertheless, these are not systems that will be considered in the current work.

[3] For further discussions on this matter see [13, 30, 32].

1.1.3 Liouville's theorem

Assuming that microstates cannot be created or destroyed, the flow of states through some volume $d\Gamma$ located around a point $\mathbf{\Gamma}$ can be calculated [32]

$$\frac{\partial W}{\partial t}(\mathbf{\Gamma}, t) = -W\nabla_{\mathbf{\Gamma}} \cdot \dot{\mathbf{\Gamma}} - \dot{\mathbf{\Gamma}} \cdot \nabla_{\mathbf{\Gamma}} W = -\nabla_{\mathbf{\Gamma}} \cdot \left[W\dot{\mathbf{\Gamma}}\right], \tag{1.3}$$

where $\nabla_{\mathbf{\Gamma}} = (\frac{\partial}{\partial q_1}, \ldots, \frac{\partial}{\partial q_{3N}}, \frac{\partial}{\partial p_1}, \ldots, \frac{\partial}{\partial p_{3N}})$, and the dot on $\dot{\mathbf{\Gamma}}$ symbolises the derivative with respect to time. Thus, a continuity equation can be defined

$$0 = \frac{\partial W}{\partial t} + \nabla_{\mathbf{\Gamma}} \cdot \left[W\dot{\mathbf{\Gamma}}\right] = \frac{\partial W}{\partial t} + \nabla_{\mathbf{\Gamma}} \cdot \mathbf{J}, \tag{1.4}$$

where $\mathbf{J} = W\dot{\mathbf{\Gamma}}$ is a current. This is *Liouville's theorem*. Integrating Eq. (1.4) in a volume of phase space, taking its limit to infinity, shows that W is conserved.

Since the total time derivative of $W(\mathbf{\Gamma}, t)$ is

$$\frac{dW}{dt} = \frac{\partial W}{\partial t} + \dot{\mathbf{\Gamma}} \cdot \nabla_{\mathbf{\Gamma}} W, \tag{1.5}$$

by combining Eqs. (1.3) and (1.5)

$$\frac{dW}{dt} = -W\nabla_{\mathbf{\Gamma}} \cdot \dot{\mathbf{\Gamma}}. \tag{1.6}$$

Interestingly, for Hamiltonian systems, where it holds that $\dot{q}_i = \partial\mathcal{H}/\partial p_i$ and $\dot{p}_i = -\partial\mathcal{H}/\partial q_i$, Eq. (1.6) is always equal to zero. In this case, the density $W(\mathbf{\Gamma}, t)$ can be thought of as an incompressible fluid in phase space, where the density in phase space is conserved along a trajectory, i.e.

$$\frac{dW}{dt} = 0. \tag{1.7}$$

From the above, an expression for the explicit time evolution of W is immediately available for Hamiltonian systems

$$\frac{\partial W}{\partial t} = -\dot{\mathbf{\Gamma}} \cdot \nabla_{\mathbf{\Gamma}} W. \tag{1.8}$$

For the distribution W to not explicitly change with time, implying thermodynamic equilibrium, it is necessary that $\partial W/\partial t = 0$. This then also implies that the flow of Eq. (1.4) is steady. Then, the ensemble average of Eq. (1.2) does not explicitly depend on time and is thus a stationary quantity. From the previous discussion it also follows that the density will not depend explicitly on the q_i and p_i. This can readily be seen from Eq. (1.5), since if $dW/dt = 0$ and $\partial W/\partial t = 0$, then also $\nabla_{\mathbf{\Gamma}} W$ is the zero vector.

Following the above discussion, there is a number of ways to define W, depending on the constraints imposed on the system. Starting from the entropy and attempting to maximise it

will give the appropriate distributions. More thorough discussion on the subject can be found in references [13, 30–32].

1.1.4 Entropy, partition function, and free energy

The *entropy* is colloquially described as a measure of the disorder of a system. In general, it is a quantity expressing how random a process is; the higher the entropy the less the knowledge about the system and vice versa. It can be defined for a system at equilibrium although, if a system out of equilibrium consists of a combination of subsystems, each very close to local equilibrium, entropy can still be defined (see for example [13, 32]). The key property of the entropy is that it cannot decrease in an isolated system. Given a probability distribution P, which defines the likelihood of appearance of each microstate $\mathbf{\Gamma}_i$, the entropy is defined as

$$S(P) = -\sum_{\mathbf{\Gamma}_i} P(\mathbf{\Gamma}_i) \log P(\mathbf{\Gamma}_i), \tag{1.9}$$

where $P(\mathbf{\Gamma}_i) \geq 0$ and $\sum_{\mathbf{\Gamma}_i} P(\mathbf{\Gamma}_i) = 1$.

In principle, the probabilities $P(\mathbf{\Gamma}_i)$ can be deduced by maximising the entropy. For example, assuming that the system is in some energy state in an interval $[E_0, E_0 + \Delta E]$, where ΔE is a small quantity, then its microstate could be any as long as it has energy $E \in [E_0, E_0 + \Delta E]$. Maximising the entropy, under the constraint that the sum of the probabilities of the accessible microstates is equal to one, returns the *microcanonical* distribution, were $P_i = 1/\Omega$. Ω is the number of accessible microstates. Note that the maximal entropy is then equal to

$$S(E) = \log \Omega(E). \tag{1.10}$$

Employing a different constraint, by assuming that the average energy of the system is equal to E, the maximum entropy is achieved when

$$P(\mathbf{\Gamma}) = \frac{1}{\mathcal{Z}} \exp\left\{-\beta \mathcal{H}\left(\mathbf{\Gamma}\right)\right\}, \tag{1.11}$$

where $\beta = 1/T$ is the inverse of the temperature,[4] and $\mathcal{H}(\mathbf{\Gamma})$ is the energy of configuration $\mathbf{\Gamma}$. Thus, the equilibrium system follows a Boltzmann distribution. This is the *canonical* ensemble. The normalisation constant $\mathcal{Z}$ is the partition function, defined for a discrete energy system as

$$\mathcal{Z} = \sum_{\mathbf{\Gamma}} \exp\left\{-\beta \mathcal{H}\left(\mathbf{\Gamma}\right)\right\} = \sum_{E} \Omega(E) \exp\left\{-\beta E\right\}. \tag{1.12}$$

In the final equality, the summation in all the microstates was replaced by a sum in all energy levels, with the addition of a density-of-states factor, $\Omega(E)$, which counts the degeneracy of

[4] The Boltzmann constant k_B is set to be equal to unity, also defining the units. For example, the temperature henceforth is measured in units of energy.

each energy level. This term cannot usually be calculated, in all but the simplest of systems. If it was known then, as will be shown in Section 1.1.5, any observable would be directly available through the partition function.

It is interesting to note that different densities could return the same constraints for the system, but not all would maximise the entropy. Meaning to say that the chosen distribution is not only consistent with the available knowledge of the system, but is also the one containing the least possible amount of information.

If on top of the energy of the system, the number of particles is allowed to vary around an average value N, then the *grand canonical* ensemble corresponds to a maximum entropy, with

$$P(\mathbf{\Gamma}) = \frac{1}{\mathcal{Z}} \exp\left\{-\beta\mathcal{H}\left(\mathbf{\Gamma}\right) - \mu N\right\}, \tag{1.13}$$

where μ is the *chemical potential*. This point of view will be useful when considering spin-1 systems in the next chapters. The term $\exp\left[-\mu N\right]$ of Eq. (1.13) defines the fugacity.

In general, for any number of constraints given from an observed macrostate, the entropy can be shown to be a concave function of the constraints [13]. For the canonical ensemble specifically, Eq. (1.11) maximises the entropy and substituting it to Eq. (1.9) results in $S = \ln\mathcal{Z} - \beta\partial\ln\mathcal{Z}/\partial\beta$, implying that the entropy is a Legendre transform of the logarithm of the partition function. Directly then from the definition of the partition function in Eq. (1.12), $S = \ln\mathcal{Z} + \beta E$. This last relation identifies the *free energy*, $\mathcal{F}$, as

$$-\beta\mathcal{F} = \ln\mathcal{Z}, \tag{1.14}$$

indicating that the logarithm of the partition function is a valid thermodynamic potential. In what follows, $\mathcal{Z}$ will be used extensively to derive observable quantities that will play a central role in the analysis of systems.

1.1.5 Observables

The models that this work focuses on are magnetic lattice models, where spins are placed on each site and communicate with their neighbours through multiplicative exchange interactions. These models are built with an ensemble description in mind. In general, for non-disordered systems, a blanket Hamiltonian can be written as

$$-\beta\mathcal{H} = \sum_{i=1}^{n} K_i S_i, \tag{1.15}$$

where the $\{S_i\}_{i=0}^{n}$ are combinations of possible spin interactions and the $\{K_i\}_{i=0}^{n}$ denote the strengths of these interactions. For example, for the Ising model, only one of the K is non-zero, and the accompanying S indicates a nearest-neighbour interaction, which can be written as

$S = \sum_{\langle ij \rangle} \sigma_i \sigma_j$, where σ_i can take the values ± 1 and it denotes the spin on the i^{th} lattice site, defining the Ising model as

$$-\beta \mathcal{H} = K \sum_{\langle ij \rangle} \sigma_i \sigma_j. \tag{1.16}$$

In a sense, the objects S of Eq. (1.15) can be though of as functions of the spins $\{\sigma_i\}$, or even as operators acting on the lattice and returning a number.

Moreover, note that Eq. (1.15) is able to indicate any possible interaction that exists between the spins; from nearest- and next-nearest-neighbour interactions, to triplets and plaquettes, or anisotropies and magnetic field terms. Writing the Hamiltonian as such, allows for a more general discussion for observable quantities. For example, a system with nearest-, next-nearest-, and square-plaquette-neighbour interactions, as well as a uniform magnetic field acting on each lattice site can be expressed in terms of Eq. (1.15) as

$$-\beta \mathcal{H} = K_1 \sum_{\langle ij \rangle} \sigma_i \sigma_j + K_2 \sum_{\langle\langle ij \rangle\rangle} \sigma_i \sigma_j + K_4 \sum_{[ijkl]} \sigma_i \sigma_j \sigma_k \sigma_l - h \sum_i \sigma_i, \tag{1.17}$$

where the first term of the right-hand side indicates a sum over nearest and the second over next-nearest neighbours. The third term is a four-spin nearest-neighbour plaquette interaction. The last term is a uniform magnetic field of magnitude $H = h/\beta$. Thus, the interaction strengths $\{K_i\}$ of Eq. (1.15) span the parameter space, where each point describes the Hamiltonian as well as the conditions under which the system operates.

Having written down the Hamiltonian, it is now straightforward to express observables of interest. Firstly, the average energy of the canonical ensemble can be written as a β derivative of the partition function. Specifically,

$$\langle E \rangle = \frac{\partial(\beta \mathcal{F})}{\partial \beta} = -\frac{\partial}{\partial \beta} \ln \mathcal{Z} = \frac{1}{\mathcal{Z}} \sum_{\Gamma} \mathcal{H}(\Gamma) \exp\{-\beta \mathcal{H}(\Gamma)\}, \tag{1.18}$$

which is evidently so, since the last expression is an average of the energy in the Boltzmann distribution. The specific heat, C, can be defined from the energy as

$$C = \frac{1}{V} \frac{\partial \langle E \rangle}{\partial T} = \frac{\beta^2}{V} \frac{\partial^2}{\partial \beta^2} \ln \mathcal{Z} = \frac{\beta^2}{V} \left(\langle E^2 \rangle - \langle E \rangle^2 \right) = \beta^2 V \left(\langle e^2 \rangle - \langle e \rangle^2 \right), \tag{1.19}$$

where V is the volume of the system, and e the energy per spin. In the same fashion, the magnetisation, M, and the magnetic susceptibility, χ, can be expressed with the help of magnetic-field derivatives. Respectively they are

$$\beta \langle M \rangle = \frac{\partial}{\partial H} \log \mathcal{Z}, \tag{1.20}$$

and

$$\chi = \frac{1}{V}\frac{\partial M}{\partial H} = \frac{\beta^{-1}}{V}\frac{\partial^2}{\partial H^2}\ln \mathcal{Z} = \frac{\beta}{V}\left(\langle M^2\rangle - \langle M\rangle^2\right) = \beta V\left(\langle m^2\rangle - \langle m\rangle^2\right), \tag{1.21}$$

where m is the magnetisation per spin. Even in the case were no such field exists, a fabricated field h can be used and in the end taken to the limit $h \to 0$.

Notice that both the specific heat [Eq. (1.19)] and the magnetic susceptibility [Eq. (1.21)] can be expressed as variances of the energy and the magnetisation, respectively. This is called the fluctuation-dissipation theorem, since it connects the responses to changes of outside fields, expressed by the derivatives, to the statistical variations around a mean of an observable quantity. This fact will be of great importance in the following chapters, where there will be need to measure these quantities by performing time-series analysis.

Another observable of great interest is the two-point correlation function, calculating the covariance of two spins separated by some distance vector $\mathbf{r}_i - \mathbf{r}_j$. To accomplish expressing this quantity in terms of the partition function, a term $\sum_i h_i\sigma_i$ can be arbitrarily added to it. Then, after all calculations are performed, this term can be turned off by taking the limit $h_i \to 0$, for all i. Thus

$$G_{\mathrm{c}}(\mathbf{r}_i - \mathbf{r}_j) = \beta^{-2}\left.\frac{\partial^2 \log \mathcal{Z}}{\partial h_i \partial h_j}\right|_{h_i,h_j=0} = \langle\sigma_i\sigma_j\rangle - \langle\sigma_i\rangle\langle\sigma_j\rangle. \tag{1.22}$$

This function is often dubbed the *connected correlation function*.[5] Away from a critical point and at large distances, the correlation function decays exponentially [14, 41]

$$G_{\mathrm{c}}(\mathbf{r}) \sim \exp\{-|\mathbf{r}|/\xi\}, \tag{1.23}$$

where ξ defines the correlation length, which is an indication of the spatial span of correlations in the system. It is also possible to define a characteristic correlation length for the system by taking into account the correlation function as weighted average of the square of the distances [14]

$$\xi^2 = \sum_{\mathbf{r}} |\mathbf{r}|^2 G_c(\mathbf{r}) \Big/ \sum_{\mathbf{r}} G_c(\mathbf{r}). \tag{1.24}$$

Similarly to Eq. (1.22), one defines the *disconnected correlation function* as

$$G_{\mathrm{d}}(\mathbf{r_i} - \mathbf{r_j}) = \langle\sigma_i\sigma_j\rangle. \tag{1.25}$$

Note that in the high temperature regime, where due to the fluctuations $\langle\sigma_i\rangle = 0$, the two correlation functions coincide.

[5] The logarithm of the partition function can be described as the generator of connected correlation functions.

A different but perhaps more workable definition of a characteristic length can be accomplished through the Fourier transform of the correlation function. For example, in a periodic lattice of linear size L, the correlation function can be Fourier transformed as

$$\hat{G}(\mathbf{k}) = \sum_{\mathbf{r}} G_{\mathrm{d}}(\mathbf{r}) \exp\left[-i\mathbf{k}\cdot\mathbf{r}\right] = \frac{1}{V}\langle|\hat{\sigma}(\mathbf{k})|^2\rangle, \tag{1.26}$$

where $\hat{\sigma}(\mathbf{k}) = \sum_{\mathbf{r}} \sigma(\mathbf{r}) \exp\left[-i\mathbf{k}\cdot\mathbf{r}\right]$ is the Fourier transform of the spins. The correlation length can be directly calculated from the first couple of moments [41], with

$$\xi = \frac{1}{2\sin\left(\pi/L\right)} \left(\frac{\hat{G}(\mathbf{0})}{\hat{G}(\mathbf{1})} - 1\right)^{1/2}. \tag{1.27}$$

The zero Fourier mode, $\hat{G}_{\mathbf{0}}$, is the squared magnetisation while the first mode, $\hat{G}_{\mathbf{1}}$, can be calculated by averaging over the first $\mathbf{k}$ vectors in the Brillouin zone. Thus, for example in a two-dimensional square lattice, the correlation length can be calculated directly from the magnetisation of the system and the average magnetisations of horizontal and perpendicular strips of the lattice.

1.2 Phase Transitions and Critical Phenomena

As mentioned in the introduction, the focus of this work is placed on models which undergo phase transitions, specifically of the continuous type. In these cases, the correlation length, ξ, diverges and fluctuations appear on all length scales [38]. In essence, the short range interactions, under the proper conditions, give rise to system-spanning correlations. Additionally, quantities like the specific heat and the magnetic susceptibility diverge as the temperature T approaches the critical temperature T_c. Also, the magnetisation scales with respect to T, when the magnetic field is set to zero. Specifically, defining $t = (T - T_c)/T_c$ as the reduced temperature, certain scaling laws are obeyed [12]:

$$\xi \sim |t|^{-\nu}, \tag{1.28a}$$
$$C \sim |t|^{-\alpha}, \tag{1.28b}$$
$$m \sim (-t)^{\beta}, \tag{1.28c}$$
$$\chi \sim |t|^{-\gamma}. \tag{1.28d}$$

When $t = 0$, the magnetisation scales with respect to the magnetic field h as

$$m \sim h^{1/\delta}. \tag{1.29}$$

The exponents $\nu, \alpha, \beta, \gamma, \delta$ are called *critical exponents* and describe the behaviour of observable variables of interest in the vicinity to the phase transition.[6]

Similarly, the correlation function of Eq. (1.22) also behaves according to different laws, depending on the proximity to a critical point. Away from criticality, $|t| \gg 0$, the correlation length will be finite and G_c will decay fast at large separations. Specifically, for $r = |\mathbf{r}| \gg \xi$ [10]

$$G_c(r) \sim \exp\{-r/\xi\}. \tag{1.30}$$

At the critical point the correlation length diverges, and the correlation function follows a power law behaviour

$$G_c(r) \sim 1/r^{d-2+\eta}, \tag{1.31}$$

where η is called the *anomalous* dimension [12]. To observe this behaviour though, the distance should be in the regime $r \gg a$, a being the lattice spacing.

As discussed with the general Hamiltonian of Eq. (1.15), the conditions under which the system is placed are described by parameters $\{K_i\}$, and a phase transition will take place in certain manifolds of parameter space. These manifolds split the parameter space, and the free energy of the system should exhibit singularities on them. From the form of the free energy [Eq. (1.14)], a divergence could only happen in the thermodynamic limit.[7] What happens there is that a symmetry of the Hamiltonian is no longer satisfied [25].

Arguably the simplest case to see this is that of the Ising model [see Eq. (1.16)], where there exists an up-down symmetry. Simplifying the discussion, for high temperatures the system is expected to be dominated by random excitations coming from the heat reservoir that is in contact with it. Thus, the spins should behave as uncorrelated random variables, randomly taking the value $+1$ or -1, resulting in a picture where the average magnetisation is zero. Indeed the system then possesses a space inversion symmetry, as expressed by the Hamiltonian. At low temperatures, at least in more than one dimension, ferromagnetic order emerges and the spins orient themselves pointing in one direction. The system, in the thermodynamic limit, cannot access its mirrored state, because it would require an infinite energy to flip all the spins. Thus, the symmetry is lost.

In reality the picture is more complicated with domain walls forming depending on the initial conditions. In the thermodynamic limit, the size of these non-parallel domains means that a huge (infinite) amount of energy is required to flip them, making it impossible for them to become parallel. The argument still remains though, since starting with a finite system, one can turn on a small magnetic field, forcing the spins to orient parallel to it. Then the thermodynamic

[6] Unfortunately, the letter β is commonly used for the magnetic exponent, for historical reasons. It will be distinguished from the symbol for the inverse temperature purely by the context.

[7] The thermodynamic limit is defined as the limit where the system size tends to infinity. At the same time however, the free energy per particle should remain finite [25].

limit can be taken, and only afterwards may the field be turned off. The end result would be a system with all the spins oriented in one direction and broken symmetry.[8]

Initially, experiments noted that seemingly very different systems can undergo continuous transitions while exhibiting the same critical behaviour, i.e. they possess the same critical exponents [Eq. (1.28)] and other renormalisation-group invariants, a concept termed as *universality*. Since different systems can behave in the same manner, it is understandable that physicists are interested in studying each universality class carefully.

On the other hand, discontinuous transitions are characterised by the coexistence of two or more phases. Here, discontinuities appear in first-order derivatives of the free energy, such as the energy and magnetisation. Thus, latent heat emerges as an energy barrier required to transform the system from one phase to the other. Due to the discontinuities, the critical exponents are readily available in the first order transitions (see Section 1.5).[9]

The contemporary point of view, under which to study and understand these phenomena is that of the renormalisation group. The ideas of the renormalisation group were developed by Kadanoff [43], as a way to pry into the properties of the Ising model near criticality, and were further advanced with the works of Wilson [22–24]. In very general terms, this theory offers a framework with which to view systems at different length scales. Taking advantage of the diverging correlation length and the fluctuations that appear in the critical region allows to extrapolate a number of general results.

1.3 Renormalisation Group

1.3.1 Introduction

When studying a system, it is important to not only accompany the discussion by internal parameters and external fields, but also the scale under which the study is being conducted. Changing the scale would not only change the units but also the effective theory that should be utilised.[10] To make the conversation more concrete, going back to Eq. (1.15), some system with local interactions in contact with a bath of inverse temperature β can be described by the parameters $\{K_i\}_{i=1}^{n}$. Under a change of length scale a new effective theory would arise, causing these parameters to be transformed. Thus, the initial Hamiltonian $\mathcal{H}$, which describes a system with local interactions, would transform in a coarser length scale as

$$-\beta\mathcal{H} = \sum_{i=1}^{n} K_i S_i \longmapsto \sum_{i=1}^{n'} K_i' S_i = -\beta'\mathcal{H}'. \tag{1.32}$$

[8] Reference [13] contains a very thorough conversation on the matter.

[9] For historical reasons, continuous and discontinuous transitions will sometimes be referred to as second- and first-order transitions, respectively, in the text [42].

[10] A more thorough and general conversation about this matter can be found in references [14, 44].

The new Hamiltonian that arises, $\mathcal{H}'$, describes a system in contact with a bath at inverse temperature β', with parameters $\{K_i'\}_{i=1}^{n'}$, in general different from the initial ones. When considering the new effective theory, it could be possible that additional terms should be considered for $\mathcal{H}'$, hence in general $n \neq n'$. It is also important to keep in mind that all distance units have changed post transformation. The symmetries of the system however should still be upheld by the new Hamiltonian. One general assumption is that since $\mathcal{H}$ was comprised of local interactions, $\mathcal{H}'$ should be local as well. Lastly, the transformation of the Hamiltonian defined by Eq. (1.32) is very general, and allows even for a constant term in $\mathcal{H}'$ appearing due to the integration over short wavelengths that comes with the coarse graining. In that sense, writing this constant as G, it can generally be said that

$$-\beta\mathcal{H} = -\beta'\mathcal{H}' + G. \tag{1.33}$$

Continuous transitions are particularly receptive to these considerations, due to the diverging correlation length. As alluded to in the previous section, critical systems possess scale invariance. In other words, if the initial system was critical, then the two pictures, before and after the transformation, would on average be the same. The only formal difference is in the different units used in the two pictures. Thus, in order to be able to compare the pictures, if one were to arbitrarily use the same units in the second system as in the first, the transformation would not change anything. In essence, this step changes the units, but not the any number accompanying them, "stretching" the picture in a sense, to make comparisons possible. For non-critical systems however, changing the scale of the study would inadvertently be accompanied by a change in the effective theory that should be used. Changing back the units of the transformed to those of the initial system would then reduce all distances. This process of changing length scales, transforming the effective theory, and then arbitrarily using the units of the initial system comprises a *Renormalisation Group Transformation* [12, 15].

Some quick initial observations can be made about this transformation, starting by assuming that the system is described by the parameters $\{K_i\}$, has a lattice spacing a, and is nowhere near a critical point. A change of scales that shrinks all distances by a factor of $b > 1$, would move $\{K_i\}$ to $\{K_i'\}$. Also, the initial spacing of 1 $[a]$ (one in units of a) would become 1 $[ba]$. Additionally, an initial correlation length ξ in units $[a]$ would become $\xi' = \xi/b$ in units $[ba]$. To complete the renormalisation-group transformation, the units in the new system should be made the same as the ones on the original. Thus the lattice spacing is the same as the initial one, but the correlation length is $\xi' = \xi/b < \xi$.[11] Since the transition happens when $\xi = \infty$, if $\xi \neq \infty$ the system is moved further away from criticality after the transformation. The only fixed point solutions of the transformation $\xi^* = \xi^*/b$ are $\xi^* = 0$ and ∞, with the former indicating an infinite temperature stable fixed point, and the later a critical point. Note that $\xi = \infty$ will necessarily be unstable.

[11] This comparison makes sense since the units of ξ and ξ' are now the same.

Starting from $\{K_i\}$ with $\xi = \infty$ would mean that the system is on a critical manifold of parameter space. After a renormalisation group transformation, the new point $\{K_i'\}$ would still have a diverging correlation length. After an infinite amount of transformations, all points in the manifold should flow towards the critical points of the transformation, defining basins of attraction [45]. It is what happens near a critical point that determines the critical behaviour of a system [14], meaning that very different systems can have the same critical properties. This readily explains the concept of universality.[12]

1.3.2 Properties

In general, performing two consecutive transformations of respective length scales b and b' would be equivalent to performing a single transformation bb'. Or, denoting these transformations by R_b and $R_{b'}$ respectively, then

$$R_{bb'} = R_b R_{b'} = R_{b'} R_b. \tag{1.34}$$

There is no unique way of defining R, and in fact many different coarse-graining approaches can be formulated.[13] In general, starting from a partition function of the form (1.12), a renormalisation-group transformation of length scale b would group spins together in blocks of size b^D, where D is the dimensionality of the system. The partition function of the renormalised system, following Eq. (1.32), becomes

$$\mathcal{Z}'(\{K'\}) = \sum_{\mathbf{\Gamma}'} \exp\left\{-\beta' \mathcal{H}'(\mathbf{\Gamma}', \{K'\})\right\} = \sum_{\mathbf{\Gamma}'} \sum_{\mathbf{\Gamma}} P(\mathbf{\Gamma}, \mathbf{\Gamma}') \exp\left\{-\beta \mathcal{H}(\mathbf{\Gamma}, \{K\})\right\}, \tag{1.35}$$

where the fact that the contraction of the initial system is used to obtain the renormalised one was taken into account. To that end, a summation over the initial degrees of freedom, $\mathbf{\Gamma}$, was added and consequently a projection operator P was needed to establish that the new degrees of freedom have their proper values. More generally, from Eq. (1.33) which includes the additional constant term of the transformation, Eq. (1.35) is generalised to

$$\mathcal{Z}'(\{K'\}) = \sum_{\mathbf{\Gamma}'} \exp\left\{-\beta' \mathcal{H}'(\mathbf{\Gamma}', \{K'\}) + G\right\} = \sum_{\mathbf{\Gamma}'} \sum_{\mathbf{\Gamma}} P(\mathbf{\Gamma}, \mathbf{\Gamma}') \exp\left\{-\beta \mathcal{H}(\mathbf{\Gamma}, \{K\})\right\}. \tag{1.36}$$

Specifically, $P(\mathbf{\Gamma}, \mathbf{\Gamma}')$ projects the microstate $\mathbf{\Gamma}$ of the original phase space, to the new phase space $\mathbf{\Gamma}'$, and thus depends on the coarse-grain approach chosen. To give an example, keeping things as simple as possible, in the one-dimensional spin-1/2 Ising model with N spins,

[12] Note that in this discussion there was no mention of possible limit cycles that might arise under the renormalisation transformations, and it was silently assumed that such cycles do not occur [12, 45].

[13] For a more precise approach see [12, 14, 15]. See also [22, 23, 43, 46, 47].

choosing a transformation that contract three spins together with a majority rule, the projection would look like

$$P(\mathbf{\Gamma}, \mathbf{\Gamma}') = \prod_{i=0}^{N/3-1} P_{\mathrm{b}} \left(\sigma_{3i+1}, \sigma_{3i+2}, \sigma_{3i+3}; \sigma_i'\right), \tag{1.37}$$

where P_{b} now depicts the projection in one of the blocks, instead of the whole chain, a simplification that can be made because blocks do not overlap. The σ variable concern the spins in the initial lattice and the σ' are their post-transformation equivalent. It was assumed that N is divisible by 3. The P_{b} projection behaves as follows:

$$P_{\mathrm{b}} \left(\sigma_{3i+1}, \sigma_{3i+2}, \sigma_{3i+3}; \sigma_i'\right) = \begin{cases} 1, \text{ if } \left(\sigma_{3i+1} + \sigma_{3i+2} + \sigma_{3i+3}\right) / \left|\left(\sigma_{3i+1} + \sigma_{3i+2} + \sigma_{3i+3}\right)\right| = \sigma_i' \\ 0, \text{ elsewhere,} \end{cases} \tag{1.38}$$

i.e. it is one if the majority of the spins in the i^{th} block point in the same direction as σ_i'. The important thing is that there is a unique σ_i' for any configuration of $\sigma_{3i+1}, \sigma_{3i+2}, \sigma_{3i+3}$. Thus $\sum_{\sigma_i'} P_{\mathrm{b}} \left(\sigma_{3i+1}, \sigma_{3i+2}, \sigma_{3i+3}; \sigma_i'\right) = 1$, for any configuration of the spins in the block i. This implies that $\sum_{\Gamma'} P(\Gamma, \Gamma') = 1$. This should be fact for any choice of projection. In general, if the blocking method $\sigma_b' = f(\{\sigma_i\}_{i \in b\text{block}})$, then the projection operator will look like

$$P(\mathbf{\Gamma}, \mathbf{\Gamma}') = \prod_b \delta \left(\sigma_b' - f(\{\sigma_i\}_{i \in b\text{block}})\right), \tag{1.39}$$

and the same discussion as the simpler example holds.

As mentioned, a number of rules can be used to form this projection operator; from a majority rule in a block of spins [48] (also given in the example), to more general transformations [49–51], and even rules more akin to machine learning [52, 53], depending on the application. Generally, the new variables must be able to acquire the same values as the initial ones. Since the exponentials that appear in Eq. (1.35) play the role of weight factors, they should be nonnegative, forcing $P(\mathbf{\Gamma}, \mathbf{\Gamma}')$ to be nonnegative as well. Additionally, the new system must have the same symmetries as the initial one, which have to be encoded in the projection operator. Lastly, an initial microstate $\mathbf{\Gamma}$ should have a unique projection to the $\mathbf{\Gamma}'$ phase space, and thus $\sum_{\Gamma'} P(\Gamma, \Gamma') = 1$. Then it directly follows from Eq. (1.35) that [38]

$$\mathcal{Z}' = \mathcal{Z}, \tag{1.40}$$

or from the more general Eq. (1.36):

$$\mathcal{Z}' \exp\left(G\right) = \mathcal{Z}. \tag{1.41}$$

The ground for calculating how the renormalisation group transforms the free energy is now set. Specifically, the transformed system will have $N' = N/b^D$ particles, where N is the number of particles of the initial system, an inverse temperature β' and a free energy $\mathcal{F}'$, hence, starting from equation Eq. (1.14) and taking into account the constant term of the Hamiltonian transformation, from Eq. (1.41) the free energy $\mathcal{F}$ transforms as

$$-\frac{\beta'\mathcal{F}'}{N'} - \frac{\beta' G'}{N'} = \frac{b^D}{N}\log\mathcal{Z}' - g = \frac{b^D}{N}\log\mathcal{Z} = -b^D\frac{\beta\mathcal{F}}{N}, \tag{1.42}$$

where, since G is a constant, the multiplicative factor of $-\beta'/N'$ was absorbed to define g.

Notice that only the singular part of the free energy scales, due to the constant terms that can appear in the transformation of the Hamiltonian, making its transformation inhomogeneous. Defining $f = \beta\mathcal{F}/N$, the transformation is $f = g + b^{-D}f'$, where g is an analytic function of the pre-transformation parameters [14]. To study the critical behaviour of a system, it is enough to consider the singular part of the free energy only. Defining the singular part as $\mathcal{F}_\mathrm{s}$, then

$$\frac{\beta'\mathcal{F}'_\mathrm{s}}{N'} = b^D\frac{\beta\mathcal{F}_\mathrm{s}}{N}, \tag{1.43}$$

or

$$f'_\mathrm{s} = b^D f_\mathrm{s}. \tag{1.44}$$

Going bask to the correlation function G_c and its definition, Eq. (1.22), it is also feasible to see how it changes under a transformation. The fact that the partition function does not change leads to

$$G'_\mathrm{c} = (\beta')^{-2}\frac{\partial^2\log\mathcal{Z}'}{\partial h'(\mathbf{r}_i)\partial h'(\mathbf{r}_j)} = b^{2(D-y_h)}G_\mathrm{c}. \tag{1.45}$$

1.3.3 The vicinity of the fixed point

It is interesting to see how a point $\{K_i\}$ of configuration space that is near a critical point $\{K_i^*\}$, transforms. Assuming $\delta K = K - K^*$ and $\delta K' = K' - K^*$, a renormalisation group transformation of scale b, denoted by R_b, would move the initial point to

$$K' = R_b K = K^* + R_b\delta K = K^* + \delta K'. \tag{1.46}$$

Assuming that the initial point was in very close proximity to the critical point, enough to allow for a Taylor expansion only up to linear terms, then

$$K'_i = K_i^* + \sum_j \left.\frac{\partial K'_i}{\partial K_j}\right|_{K_j=K_j^*}\delta K_j + o\left((\delta K)^2\right), \tag{1.47}$$

where in this regime one can define a linearised transformation as

$$\delta K_i' = \sum_j \frac{\partial K_i'}{\partial K_j}\bigg|_{K_j=K_j^*} \delta K_j = \sum_j M_{ij}^{(b)} \delta K_j. \tag{1.48}$$

In the above it was assumed that the new parameters K' are analytic functions of the old ones. It is enough then to study the matrix $M^{(b)}$ of the transformation. In general, $M^{(b)}$ needs not be symmetric and so a separation is necessary from left to right eigenvectors [12]. Writing the eigenvectors and eigenvalues as e_i and $\lambda_i^{(b)}$, respectively, then

$$M^{(b)} e_i = \lambda_i^{(b)} e_i. \tag{1.49}$$

By property of Eq. (1.34) ($R_b R_{b'} = R_{bb'}$), it follows that $M^{(b)} M^{(b')} = M^{(bb')}$. This implies that $\lambda^{(b)} \lambda^{(b')} = \lambda^{(bb')}$.[14] In turn, this means that $\lambda_i^{(b)} = b^{y_i}$, for some real y_i [12].

Expanding δK in terms of the transformation matrix eigenvectors, $\delta K_i = \sum_j a_{ij} e_j$, and using Eq. (1.48) implies that

$$\delta K_i' = M^{(b)} \sum_j a_{ij} e_j^{(b)} = \sum_j a_{ij} \lambda_j^{(b)} e_j^{(b)} = \sum_j a_{ij} b^{y_j} e_j^{(b)}, \tag{1.50}$$

indicating that under the transformation some components of δK grow, while others shrink, depending on its eigenvalues. Directions that shrink should be accompanied by a negative exponent y_i and are called irrelevant, since after infinite transformations they fade away. On the contrary, directions with positive exponents increase with consecutive applications of R_b and are called relevant. Lastly, when $y_i = 0$, the direction stays the same up to the linear approximation that was used and is called marginal.

This demarcation can help distinguish basins of attraction. If a point starts outside a critical manifold, then the relevant eigenvalues will keep increasing, driving it further and further away from criticality. On the contrary, if all relevant directions are set to zero then the system will, after infinite transformations, approach a point inside the basin.

1.3.4 Relevant directions

Assuming that the interactions of the system are such that the transformation matrix $M^{(b)}$ can be diagonalised, meaning that the directions of the $\{K_i\}$ do not mix when forming the eigenvectors, then it is easy to derive how the renormalisation-group transformation affects the system.[15] From Eq. (1.50), quantities would be transformed as

[14] Since it should not matter which scale transformation is performed first, that of b or b', the two matrices should commute.

[15] More generally, the $M^{(b)}$ will not be symmetric. Nevertheless, the left and right eigenvalues will be the same and if they are not degenerate, the left and right eigenvectors will be orthogonal.

$$K_i' - K_i^* = b^{y_i} \left(K_i - K_i^*\right). \tag{1.51}$$

These are quantities like the temperature, T or β, the external magnetic field, h, and others similar, as long as they are accompanied by their own unique direction, so that Eq. (1.48) can be written simply as Eq. (1.51).

By defining the reduced quantities

$$k_i = \frac{K_i - K_i^*}{K_i^*}, \tag{1.52}$$

Eq. (1.51) becomes

$$k_i' = b^{y_i} k_i, \tag{1.53}$$

where

$$y_i = \frac{1}{b} \log \left[\left. \frac{\partial K_i'}{\partial K_i} \right|_{K_i = K_i^*} \right]. \tag{1.54}$$

Consecutive transformations would change the k_i according to Eq. (1.53). After n transformations one can generally write

$$k_i^{(n)} = b^{n y_i} k_i. \tag{1.55}$$

On the same note, the correlation length would change by a factor of b^n, or $\xi^{(n)} = \xi / b^n$, allowing to write

$$\xi(\{k_i\}) = b^n \xi(\{b^{n y_i} k_i\}). \tag{1.56}$$

Setting all $k_i = 0$ except for the temperature would show how ξ transforms when only the T is a free parameter. Specifically, writing the reduced temperature as $t = (T - T^*)/T^*$, which implies $t^{(n)} = b^{n y_t} t$, gives

$$\xi(t) = b^n \xi(b^{n y_t} t). \tag{1.57}$$

The choice of b thus far in the discussion has been arbitrary. Setting $b = (c/|t|)^{1/y_t}$,[16] where c is a constant, gives the result [12]

$$\xi(t) = (|t|/c)^{-1/y_t} \xi(c). \tag{1.58}$$

[16] Equivalently, a more physical picture can be painted if this choice of b is thought of as repeating the renormalisation process enough times until $b^{n y_t} t \sim 1$ is reached [14].

Since $\xi(c)$ is a constant – it is the correlation length at some temperature –, it can be seen that ξ scales like

$$\xi \sim |t|^{-1/y_t}. \tag{1.59}$$

Comparing with the scaling relations from the start of the Chapter, Eq. (1.28a), then implies that

$$\nu = \frac{1}{y_t}. \tag{1.60}$$

It should be noted that these considerations apply close to the critical point, $t = 0$, but not on it. In that sense, the variable c is a large positive number. So, the constant $\xi(c)$ is the correlation length at some large temperature, and the scaling factor b can still arbitrarily be expressed by $(c/|t|)^{1/y_t}$.

On the same note, if the only k_i parameter not set equal to zero is the external field h, instead of the temperature, then a similar choice of b would show that

$$\xi(h) \sim |h|^{-1/y_h}, \tag{1.61}$$

diverging as $h \to 0$.

A similar discussion can be made for the free energy and Eq. (1.44). A scaling relation of the form

$$f(\{k_i\}) = b^{-nD} f(\{b^{ny_i} k_i\}), \tag{1.62}$$

will be obeyed. Replacing $b = (c/|t|)^{1/y_t}$ results in

$$f(t, h, \dots) = |t|^{D/y_t} c^{-D} f(c, h/|t|^{y_h/y_t}, \dots). \tag{1.63}$$

Thus, another success achieved by the renormalisation-group theory is that it reproduces the static scaling hypothesis [12, 31, 43]. By setting $\Delta = y_h/y_t$, Eq. (1.63) becomes

$$f(t, h) = t^{D/y_t} c^{-D} f(c, h/|t|^{\Delta}), \tag{1.64}$$

or

$$f(t, h) = t^{D/y_t} F(h/|t|^{\Delta}), \tag{1.65}$$

where F is the function defined by $F(x) = c^{-D} f(c, x)$.

1.3.5 Scaling laws

Making all k_i except for the temperature equal to zero, means that $f \sim t^{D/y_t}$. Since the second derivative of f with respect to T is the specific heat [see Eq. (1.19)], which scales like $C \sim t^{-\alpha}$ [see Eq. (1.28)], a scaling law follows immediately from Eqs. (1.60) and (1.63),

$$\nu D = 2 - \alpha, \tag{1.66}$$

known as Josephson's scaling law.

Similar considerations for the magnetisation, the magnetic susceptibility, and the response of the magnetisation to the external magnetic field at $t = 0$ give the following scaling laws [14]

$$\beta = (D - y_h)/y_t, \tag{1.67a}$$
$$\gamma = (2y_h - D)/y_t, \tag{1.67b}$$
$$\delta = y_h/(D - y_h). \tag{1.67c}$$

Note that all the critical exponents could be expressed in terms of the eigenvalue exponents y_t and y_h. So, by combining the above equations and Eq. (1.60), more scaling relations, similar to Joshephson's law, can be deduced. For example:

$$\alpha + 2\beta + \gamma = 2 \text{ (Rushbrooke scaling relation)}, \tag{1.68a}$$
$$\beta(\delta - 1) = \gamma. \tag{1.68b}$$

Another scaling law can be obtained from the transformation of the correlation function of Eq. (1.45), by iterating the transformation until $r/b^n = r_0$, where r_0 is some distance much larger than the interaction range. Using Eq. (1.31), the following relation can be proved [14]

$$\eta = D + 2 - 2y_h. \tag{1.69}$$

1.3.6 Irrelevant directions and corrections to scaling

Following Eqs. (1.62) and (1.63), for the general scaling of the singular part of the free energy, the terms that were omitted are essentially of the form $k_i t^{-|y_i|/y_t}$. To ease the notation, all variables are set to zero with the exception of only the temperature and one irrelevant variable k. Assuming that a Taylor expansion around $t = 0$ is possible,[17] then

$$f(t,k) = |t|^{D/y_t}\left(c_1 + c_2 k|t|^{-|y_k|/y_t} + \dots\right), \tag{1.70}$$

[17] See [12, 14] for discussions on when this is not the case.

where c_1, c_2 are constants from the expansion. Thus, the irrelevant variable gives rise to corrections-to-scaling of the free energy. Specifically, there is an exponent $\omega_k = |y_k|/y_t$ which gives rise to the behaviour

$$f(t) \sim t^{D/y_t} \left(1 + ct^{-\omega_k}\right), \tag{1.71}$$

up to first order, with c being some arbitrary constant.

1.4 Finite-Size Scaling

The application of the renormalisation-group theory for an infinite system in order to study a phase transition is not usually a feasible task. Specifically for Monte Carlo simulations, but also for many numerical methods, only the study of finite systems if feasible. In the end, the infinite-limit behaviour of a system can be extrapolated from finite sizes, by performing the process of *finite-size scaling*.

By construction, the transformations performed in the above section are all local, and thus they could have been applied to a finite system of linear size L, instead of an infinite system. To this end, all quantities considered will in general also be functions of L. Thus, Eq. (1.62) can be rewritten for a finite system as

$$f(\{k_i\}, L^{-1}) = b^{-nD} f(\{b^{ny_i} k_i\}, b^{ny_L} L^{-1}). \tag{1.72}$$

The reason for writing the above equation as a function of L^{-1} and not of L is the expectation that the phase transition will occur only when $L \to \infty$, or $L^{-1} = 0$, similarly to the other reduced relevant directions.

In general, like all other quantities, L^{-1} should transform like $\left(L^{-1}\right)' = b^{y_L} L^{-1}$, but by construction the renormalisation group scales all lengths by b^{-1}, and so $y_L = 1$. In that sense, L^{-1} is a relevant direction in parameter space and a phase transition can only occur when $L^{-1} = 0$, as expected, making the argument for Eq. (1.72) consistent. When $L^{-1} > 0$, replacing $b = (c/|t|)^{1/y_t}$ to Eq. (1.72) gives

$$f(t, L^{-1}) \sim |t|^{D/y_t} f\left(L^{-1}|t|^{-1/y_t}, \dots\right). \tag{1.73}$$

Directly then from Eq. (1.59), concerning the scaling of the correlation length,

$$f(t, L^{-1}) \sim |t|^{D/y_t} f\left(L^{-1}\xi(t, L = \infty) \ \dots\right), \tag{1.74}$$

where $\xi(t, L = \infty)$ is the correlation length of the infinite system at the same temperature. As discussed, the infinite-system critical behaviour is seen only when $L^{-1} = 0$. In that sense, the thermodynamic properties of the infinite system are returned when $L \gg \xi(t, L = \infty)$, i.e. when

the correlation length is not affected by the boundaries of the system. On the contrary, when $L \ll \xi(t, L = \infty)$, the correlation of the finite system cannot actually surpass L as $t \to 0$, and the critical behaviour cannot be observed [12, 14]. For this reason, as shall be seen in the results of the last chapters of the thesis, the peaks of observables are rounded and shifted.

Near a critical point, $\xi \sim L$, and thus the shift will be governed by

$$t_L \sim L^{-1/\nu}, \tag{1.75}$$

where t_L is the location of the peak of the finite system. Particularly, quantities of interest like the specific heat and the magnetic susceptibility will exhibit a scaling behaviour of the form [12]

$$C \sim L^{-\alpha/\nu}, \tag{1.76}$$

$$\chi \sim L^{-\gamma/\nu}, \tag{1.77}$$

and other observables will follow suit.[18]

The correlation length is the quantity that is most directly affected by the finite size of the system. Including the system size in Eq. (1.56), then

$$\xi(t, L^{-1}) = b\xi\left(b^{y_t}t, bL^{-1}\right) = (c/|t|)^{1/y_t}\xi\left(c, |t|^{-1/y_t}L^{-1}\right), \tag{1.78}$$

again with the transformation $b = (c/|t|)^{1/y_t}$. For an infinite L and $t \to 0$ (i.e. $|t|^{-1/y_t}L^{-1} \to 0$), the expected critical behaviour is recovered ($\xi \sim |t|^{-\nu}$). For finite L and $t \sim 0$, the correlation length of the finite system cannot expand beyond L, and so the right hand side of Eq. (1.78) tends to a constant. Thus, $\xi\left(c, |t|^{-1/y_t}L^{-1}\right)$ goes to zero as $|t|^{1/y_t}$. Expanding around $t = 0$ gives a first term that is a constant and a second term that is proportional to L^{-1} [12]

$$\frac{\xi(t, L^{-1})}{L} = c_1 + c_2 t L^{-y_t} + o(t^2), \tag{1.79}$$

So, up to first order, the curves $\xi(t, L^{-1})/L$ for different L overlap at $t = 0$, giving an estimate for the location of the critical point. This quantity defines a universal ratio, indicative of a universality class, but also dependent on the lattice type and boundary conditions.

1.5 Discontinuous Transitions

First order transitions are characterised by the coexistence of phases and they exhibit latent heat. In essence, the system requires energy, or has to dispose of it, in order to change its

[18] To extrapolate the effective critical exponents standard least-square fits were performed, using the gnuplot plotting program, which implements the Levenberg-Marquardt algorithm [54–57].

structure. For this reason, quantities like the energy and the magnetisation, that display discontinuities, become rounded in finite systems. The coexistence of two phases necessitates the appearance of double peaks in the distributions of the aforementioned observables, indicating a barrier connected to the surface tension between states.

The two peaks will be located in the energies e_{o} and e_{d} of the energy per particle in the ordered and the disordered phase, respectively. The distance of the two peaks indicates the latent heat of the system, $\Delta e = e_{\mathrm{d}} - e_{\mathrm{o}}$. On the other hand, the height of the peaks relative to that of the suppressed states between them is an indication of the free-energy barrier between the states.

Following [58–60], the free energy of a D-dimensional finite system, $\mathcal{F}_L$, can be thought of as comprising of two terms: one accounting for the bulk and the other for the surface. For an energy per particle e, one can then write

$$\mathcal{F}_L(e) = L^D \phi(e) + L^{D-1} \phi_\sigma(e), \tag{1.80}$$

where $\phi(e)$ is the bulk free energy per particle and ϕ_σ is the corresponding surface one. Also for finite systems, a new pseudo-critical temperature can be defined, where the heights of the two peaks are equal, $\mathcal{F}_L(e_{\mathrm{o}}) = \mathcal{F}_L(e_{\mathrm{d}})$. In this set-up, the states in the valley, $e_{\min}$, between the equal-height peaks are suppressed due to the surface term as

$$\Delta\mathcal{F}_L = \mathcal{F}_L(e_{\mathrm{d}}) - \mathcal{F}_L(e_{\min}) \sim L^{D-1}. \tag{1.81}$$

An interface tension can be defined by dividing the barrier with the surface, as $\Sigma(L) = \Delta F_L / L^{D-1}$, which has a non-zero value at $L \to \infty$. This barrier is readily available from a simulation which accumulates the distribution of e. Specifically, the surface part of the weight of a state can be accounted for by a term of the form $P_\sigma(e) \sim \exp[-\beta L^{D-1} \phi_\sigma(e)]$ [59, 61]. So, at the temperature where the distribution exhibits equal-height peaks, a comparison between the states at the peaks $e = e_{\mathrm{o}} = e_{\mathrm{d}}$ and the minimum $e = e_{\min}$, with probability densities $P_{\max}$ and $P_{\min}$ respectively, yields

$$\Sigma(L) = \frac{1}{\beta L^{D-1}} \log\left[\frac{P_{\max}}{P_{\min}}\right]. \tag{1.82}$$

Following the same arguments, there should also be a difference in the order parameters of the two phases. To keep the discussion simple, assume that the order parameter is the magnetisation [Eq. (1.20)]. The magnetisation per particle is defined by $m = \frac{\partial f}{\partial h}$. Under a renormalisation-group transformation, assuming that after the rescaling by a factor of b the free energy becomes f' and using Eq. (1.62), the magnetisation will transform as [12]

$$m = \frac{\partial f}{\partial h} = b^{-D} \frac{\partial f'}{\partial h} = b^{-D} \frac{\partial f'}{\partial h'} \frac{\partial h'}{\partial h} = b^{-D} \frac{\partial h'}{\partial h} m'. \tag{1.83}$$

At one phase the magnetisation will be equal to m_{o}, and at the other m_{d}. The difference between the two magnetisations, due to the discontinuity, is defined as $\Delta m = m_{\mathrm{o}} - m_{\mathrm{d}} \neq 0$, and so at least one of the magnetisations has to be different than zero, say m_{o}. In that sense, after n transformations, $m_{\mathrm{o}} = m^{(n)} \prod_{i=1}^{n} b^{-D} \frac{\partial h^{(i)}}{\partial h^{(i-1)}}$. So, each of the partial derivatives has to be non-zero. Taking the limit of $n \to \infty$, indicates that $\lim_{n\to\infty} b^{-D} \partial h^{(n+1)} / \partial h^{(n)} \sim 1$, or that for the fixed point of the transformation $y_h = D$.

Analogously, for the energy defined in Eq. (1.18), the energy per particle is equal to $e = \frac{\partial f}{\partial \beta}$, transforming in a similar fashion to Eq. (1.83). Using the same arguments, it is deduced that $y_t = D$. From y_t and y_h, using the scaling relations Eqs. (1.66) and (1.67), all the critical exponents are available.

First-order transitions are in a sense more straightforward, due to their lack of versatility. Specifically, the critical exponent y_t is always equal to the dimensionality of the system, D, unlike continuous transitions, where it can take any value less that D.

1.6 Disorder

Since real systems are always impure, disorder is of central importance to contemporary research, both from a theoretical point of view, due to their ability to test and expand the theory of critical phenomena [14, 62, 63], but also due to experimental and engineering applications. To try and keep the conversation somewhat broad, a general Hamiltonian is introduced in the form

$$\mathcal{H} = \sum_{\langle ij \rangle} J_{ij} \theta_i \sigma_i \theta_j \sigma_j + \sum_i h_i \theta_i \sigma_i + \ldots, \tag{1.84}$$

where the $\{J_{ij}\}$ and $\{h_i\}$ are random variables that can follow any specified distribution, and the $\{\theta_i\}$ can take the values $\{0, 1\}$ to indicate the absence or the presence of a spin in the lattice, respectively. The dots are there to show that more random interactions could be considered.

There are many possible ways to include disorder to a system, with some examples being: (i) Site dilution, where $J_{ij} = J$ for all neighbouring i, j and the $\{\theta_i\}$ dictate whether a site will be populated or not. (ii) Bond dilution, where $\theta_i = 1$ for all i and the $\{J_{ij}\}$ are either equal to some constant J or are set to zero, effectively severing some bonds. (iii) Bond disorder, where the $\{J_{ij}\}$ are drawn from a random distribution and all $\{\theta_i\}$ are unity. (iv) Random fields, where the $\{h_i\}$ are random variables. (v) Any combination of the above or any other way of adding disorder to the system.

Arguably, the most famous type of disorder system is that of spin glasses, where the $\{J_{ij}\}$ are able to take positive and negative values. That way, depending also on the geometry of the lattice, some bonds will not be able to be satisfied, giving rise to the phenomenon of frustration.

These problems are notoriously hard,[19] and are riddled with free energy barriers and local minima [40, 64].

Still, randomness gives rise to very interesting phenomena, even for disorder that disallows frustration. These problems are ridden with a rugged free-energy landscape and obscure finite-size effects, which makes their simulation a laborious endeavour and their analysis a non-trivial task.

1.6.1 The Harris criterion

Since quenched disorder is so important, the central question of how it affects critical behaviour needs to be elaborated. In the language of renormalisation group, it has to be identified whether a specific quenched disorder is a relevant or an irrelevant variable. The argument followed in this Section was first introduced by Harris [28]. Assuming that a quenched disorder is described by some variable p, indicating its strength, the disordered system will undergo a transition at a new temperature, $T_c(p)$, that depends on p. In general, $T_c(p)$ will be different from the original transition temperature, T_c. One can imagine a huge system split into different subsystems, still large enough to make surface interactions between subsystems small compared to the energy of the bulk [65]. Locally then, in these subsystems, the realisation of disorder would imply that the transition temperature would vary spatially, defining local variations from the transition temperature of the whole system, $\delta T_c(\mathbf{r})$, given by

$$\delta T_c(\mathbf{r}) = T_c(\mathbf{r}) - T_c(p). \tag{1.85}$$

The mean of $\delta T_c(\mathbf{r})$ should be zero, in order for the critical temperature to be $T_c(p)$. The two-point connected correlation [Eq. (1.22)] of the local variations over some region with volume V is equal to

$$\langle \delta T_c(\mathbf{r}) \delta T_c(\mathbf{r}') \rangle_V = \int_V \frac{d\mathbf{r}}{V} \int_V \frac{d\mathbf{r}'}{V} \delta T_c(\mathbf{r}) \delta T_c(\mathbf{r}'). \tag{1.86}$$

If the fluctuations decay fast with the distance, or the initial distribution from where the disorder was drawn does not allow for spatial correlations between random variables, then $\langle \delta T_c(\mathbf{r}) \delta T_c(\mathbf{r}') \rangle_V \sim V^{-1}$. So, on a volume confined by a correlation length $\langle \delta T_c(\mathbf{r}) \delta T_c(\mathbf{r}') \rangle_{\xi^D} \sim \xi^{-D}$, where D is the dimensionality of the system. According to Eqs. (1.28) and (1.59) the correlation length will scale like $\xi \sim |T - T_c(p)|^{-\nu(p)}$, where the critical exponent ν is expressed in terms of the disorder strength p. Substituting the scaling relation back to the fluctuations leads to $\langle \delta T_c(\mathbf{r}) \delta T_c(\mathbf{r}') \rangle_\xi \sim |T - T_c(p)|^{D\nu(p)}$.

From a physical perspective, the Harris criterion states that if close to $T_c(p)$ the correlation is small in comparison to $|T - T_c(p)|$, then the disorder will not affect the stability of the critical

[19] NP-hard to be exact.

point [28]. That happens when $\sqrt{\langle \delta T_c(\mathbf{r}) \delta T_c(\mathbf{r}') \rangle} < |T - T_c(p)|$. From the above discussion, over a volume confined by a correlation length, this implies that

$$|T - T_c(p)|^{D\nu(p)/2} < |T - T_c(p)|. \tag{1.87}$$

In the limit where the disorder vanishes, then the above relation implies that $D\nu/2 > 1$ or more clearly $\nu > 2/D$. Equivalently, using the Josephson scaling relation of Eq. (1.66), then $\alpha < 0$. So, when $\alpha < 0$ the disorder is irrelevant and the fixed point will be stable. On the other hand, $\alpha > 0$ implies that the disorder is relevant, and the system is led to a new set of critical exponents. The case were $\alpha = 0$ is a marginal one, with a characteristic example being the two-dimensional Ising ferromagnet, where logarithmic corrections are known to be present in the scaling forms [66].

This argument is not necessarily robust, and has been known to break. For example, even though this argument has been shown to be precise in two dimensions even for an infinitesimal disorder strength [67–69], in more than two dimensions quenched disorder is expected to be relevant only beyond a threshold strength [68–71]. An interesting example was found by Nvsen Ma et al., where relatively strong quenched disorder was applied in a two-dimensional quantum spin Heisenberg model, and the Harris criterion was found to be violated [72].

1.6.2 Finite-size scaling and disorder

Following the discussion of Section 1.4, the question of how to reconcile finite-size scaling with quenched disorder systems arises. Assume that an observable quantity Q_i has been sampled from n random systems, each one being a different realisation of some quenched disorder. This quantity can be something like the susceptibility, the specific heat, etc. The disorder average of Q will be equal to

$$[Q(T)] = \lim_{n\to\infty} \frac{1}{n} \sum_{i=1}^{n} \langle Q_i(T) \rangle. \tag{1.88}$$

Here, the square brackets, $[\dots]$, indicate an average over the disorder realisations, while the angular brackets, $\langle \dots \rangle$, indicate the usual thermal average of a specific realisation.

There are two conceivable ways of averaging for the maximum of the observable Q. One is by finding the maximum of $[Q(T)]$, defined as $[Q]^\star$, i.e.

$$[Q]^\star = \max\{[Q(T)]\}. \tag{1.89}$$

The other is by first finding the maxima in the individual realisations, $\langle Q_i \rangle^\star = \max\{Q_i(T)\}$, and then taking the disorder average, i.e.

$$[Q^\star] = \frac{1}{n} \sum \langle Q_i \rangle^\star. \tag{1.90}$$

To distinguish which of the two should be used, the concept of self averaging is needed. In a nutshell, averaging over the realisations and then finding the peak is a process that can be, at least in principle, improved by increasing the number of samples. In essence, the more disorder realisations used, the less the variance of the location and value of the peak $[Q]^*$ will be. On the other hand, first locating the peaks of each individual realisation and then averaging, is a process that does not necessarily improve by adding more realisations, due to the large variations from realisation to realisation.

Nevertheless, from each of the two processes a pseudo-critical temperature can be defined. First averaging over the realisations and then locating the peak results in a value $T_{[Q]^*}$. By locating the peaks in each realisation first and then averaging over the realisation gives an estimate $[T^*]$. It is expected that these temperatures should scale, in their simplest form, according to Eq. (1.75) with an exponent ν and a critical temperature T_c.

1.6.3 Self averaging

In essence, a singular observable Q will have different values under different realisations of the disorder. Thus it can be considered as a random variable, which in principle can be described by a distribution $P(Q;L)$, L indicating the size of the finite system. The distribution will have an average, $[Q]$, defined by averaging over the disorder realisations, and a variance $[Q^2]-[Q^2]=(\Delta Q)^2$. Then, self-averaging is exhibited in the thermodynamic limit if $(\Delta Q)^2/[Q]^2 \to 0$. In that sense, if a quantity is self-averaging, then the more samples that are added in the average, the smaller the relative fluctuations will be. The following definition will be useful for a system of linear size L:

$$R_Q(L) = (\Delta Q)^2/[Q]^2. \tag{1.91}$$

An argument made by Brout [65] was to separate a system far from criticality into n subsystems, much larger than the average correlation length, ξ. Assuming that surface effects are insignificant compared to the bulk, then the couplings of the neighbouring subsystems are negligible and the subsystems can be regarded as independent. It is then expected that for an extensive quantity, averaging over the whole system will coincide with the average over the different subsystems. The latter, according to the central limit theorem should follow a Gaussian distribution [73]. Hence, the variance is expected to decrease like $(\Delta Q)^2 \sim n^{-1} \sim L^{-D}$, where D is the dimensionality of the system. Meaning that $R_Q(L\to\infty)\to 0$ [74]. Thus, for the case of $\xi \ll L$, self-averaging is to be expected.

On the other hand, near a critical point, the case becomes more complicated. Two cases can be distinguished, following the Harris criterion [28]. First, when the disorder is irrelevant ($\nu > 2/D$ or $\alpha < 0$), it is expected that $R_Q(L) \sim L^{\alpha/\nu}$ [74, 75]. Thus, since $\alpha/\nu < 0$, in this case the property of self-averaging still exists, only with $R_Q(L)$ decreasing with a slower rate. Second, when disorder is relevant ($\nu < 2/D$ or $\alpha > 0$), there is no self-averaging [75]. This

result was also confirmed computationally, via simulations of the site-dilute Ising model in three dimensions [76].

1.7 Cross-over Phenomena

In many studies, especially when dealing with data obtained from Monte-Carlo simulation on finite-size systems, it is often the case that a system does not fall in its expected scaling regime. This can happen due to many reasons. It is possible, for example, that small system sizes in conjunction with strong corrections to scaling can result in a perceived different asymptotic scaling behaviour than the actual one. As the system size increases however, a cross-over in the behaviour appears, resulting in the expected scaling. Such an example will be seen in Chapter 4 where, by including small system sizes in the analysis, leads to the belief that the system under study exhibits a first-order transition, while in reality it undergoes a continuous transition.

Another example of a cross-over behaviour can be found in the Blume-Capel and Baxter-Wu models that will be studied in Chapters 3 – 5. Specifically, their phase diagrams consist of a line of continuous and a line of discontinuous transitions. The two regimes meet at a multicritical point. These systems exhibit a change in scaling from one set of exponents to another, upon crossing the multicritical point.

Another way for cross overs to appear is that of disorder, already discussed in (Section 1.6). Here the transition might or might not be affected by the disorder. This case can be ridden with finite-size effects as well. As per the Harris criterion, whether or not the critical behaviour changes under the application of uncorrelated disorder has to do with the value of the ν exponent, and if it is larger than $2/D$.

For first-order transitions, where $\nu = 1/y_t = 1/D$, the Harris criterion suggests that disorder is always relevant. Thus, uncorrelated disorder should soften the discontinuous transition to a continuous one [77]. This has been established in two-dimensional systems even for the case of infinitesimal disorder [67]. As shall be seen in Chapter 5 however, due to finite-size effects, one would need to show special care when handling systems of smaller sizes. The same arguments do not necessarily apply in three-dimensional cases, where there might be a finite disorder strength required to soften the transition. In that case, it is even more arduous to establish the thermodynamic behaviour of the system.

Chapter 2

Simulation Methods

In general, the choice of a Monte Carlo algorithm to simulate a statistical physics system is application based, and knowledge of the post-processing of data is necessary to design an experiment. The essential theory required for the data analysis of Monte Carlo experiments can be found in Appendix A. Many pedagogical and thorough texts have been written on the subject of Monte Carlo simulations, see for example [41, 78, 79], and so, in the rest of this chapter, the focus is solely placed on the methods that were applied in this thesis.

Monte Carlo simulations sample microstates in accordance to some probability distribution. The analysis of the data stringently depends on the Monte Carlo method chosen. The sampling distribution could in theory be flat, choosing microstates at random with a constant probability, but in general it is better to use a Boltzmann probability distribution in the sampling process, which can be achieved via importance sampling. Other more general distributions could be used as well.

Some of the most straightforward Monte Carlo algorithms, and all methods used in the current thesis, fall under the Markov-chain family [39]; meaning that the simulation procedure will lack memory of past events. Thus, when modifying a microstate, only the current state of the system will be taken into account. This, of course, is not the only method to accomplish the simulation of a system. For example there are cases where it might be necessary to use non-Markovian methods [80].

The rest of the chapter is structured as follows: Firstly, a general discussion of Monte Carlo experiments and the reason as to why a variety of methods exist is given in Section 2.1 and 2.2, respectively. Then, in Section 2.3 single-spin-flip algorithms are presented, like the Metropolis and heat-bath methods. In Section 2.4, multi-spin-flip cluster updates are presented. The Wang-Landau and multicanonical algorithms are described in Section 2.5, alongside the reweighting process necessary for the analysis of their data. A discussion about the dynamical scaling of the autocorrelation times with the system size is given in Section 2.6. Lastly, Section 2.7 gives an overview of different computational methods used extensively in the literature for probing similar systems to the ones under study in this work.

2.1 Markov-Chain Monte Carlo

Conceptually, to sample the phase space of a model, one can start from an initial configuration and in each step pick, at random, a new candidate state. The acceptance of the choice is carried out via some probability that depends only on the current and candidate configurations. This is the essence of a Markovian process. Since this work mostly deals with spin systems in equilibrium and in contact with a bath of temperature T, it is natural to describe them by a canonical Boltzmann probability distribution [Eq. (1.11)]. Using the spin configuration to represent the phase point of the system, this distribution can be written as

$$P(\{\sigma_i\}_{i=1}^N) = \frac{1}{\mathcal{Z}} \exp\left[-\beta \mathcal{H}\left(\{\sigma_i\}_{i=1}^N\right)\right]. \tag{2.1}$$

In the above expression, $P(\{\sigma_i\}_{i=1}^N)$ is the probability of finding the system in the microstate $\{\sigma_i\}_{i=1}^N$. This state has energy $E = \mathcal{H}(\{\sigma_i\}_{i=1}^N)$, where $\mathcal{H}$ is the Hamiltonian that describes the system and $\beta = 1/T$ is the inverse temperature of the bath.

Considering two possible states of the system, μ and ν, the flow towards state μ should be equal to the flow outwards, as was discussed in Section 1.1. If $p(\mu \to \nu)$ is the probability for the system to transition from state μ to ν and $P(\mu)$ the probability for the system to be at state μ, then

$$\sum_\nu P(\mu) p(\mu \to \nu) = \sum_\nu P(\nu) p(\nu \to \mu), \tag{2.2}$$

where the left hand side expresses the flow out of state μ and into any other state, while the right hand side expresses the flow to μ from any other state. Since the system has to end up in a state, $\sum_\nu p(\mu \to \nu) = 1$, and so

$$P(\mu) = \sum_\nu P(\nu) p(\nu \to \mu). \tag{2.3}$$

One simple way of achieving the requirement of Eq. (2.2) is through the condition of detailed balance [79], which states that the flow from μ to ν is the same as the flow in the opposite direction. Thus,

$$P(\mu) p(\mu \to \nu) = P(\nu) p(\nu \to \mu). \tag{2.4}$$

Using Eq. (2.4) and the fact that the system should follow the Boltzmann distribution, the condition for the transition probability is given by

$$\frac{p(\mu \to \nu)}{p(\nu \to \mu)} = \frac{P(\nu)}{P(\mu)} = \exp\left\{-\beta\left[E(\nu) - E(\mu)\right]\right\}. \tag{2.5}$$

An issue that needs to be addressed when choosing the transition probabilities is fulfilling the condition of ergodicity. In general, it is conducive to most applications that the simulation should be able to reach any point in the phase space of the system in a finite number of steps.

2.2 The Need for Different Simulation Methods

There are many heuristic algorithms that can be constructed from the above discussion [78, 79]: Single-spin-flip algorithms, where one spin is flipped at each iteration, cluster algorithms, where whole groups of spins are flipped at one time, entropic sampling algorithms, where the entropy of the system is sampled at an infinite temperature [81], and a plethora of other methods. Unfortunately, there is no panacea when it comes to simulating with Monte Carlo algorithms, and there is a number of elements that need to be taken into account before deciding which algorithm to implement.

One important consideration should always be the autocorrelation time of the resulting data set (see Section 2.6 and Appendix A). In a nutshell, when a sample consists of highly correlated data, then the statistics is reduced. There is then a need to know how many independent measurements will be produced from the simulation. Different algorithms have different autocorrelation times, rendering their statistics better or worse. This has to be taken into account alongside with how difficult an algorithm is to implement or how slow it is to run. For example, cluster algorithms have much smaller autocorrelation times around the critical region, compared to single-spin-flip algorithms, but they are also more difficult to implement and generally more demanding computationally. The increased computational demands however can be compensated by the need for smaller data samples. Considerations about the efficiency of some of the methods utilised in the current work are made in Chapter 3.

In some models, high energy barriers might prevent the proper sampling of configuration space. For example, if two very likely areas of energy space are separated by a very improbable region, then the system will have a hard time tunnelling between the two regions. This could have adverse effects in the sampling process. Generalised-ensemble methods can fix this problem by incorporating different sampling distributions, thus increasing the tunnelling rate between such regions. However, this necessarily means that the data analysis will not be straightforward, and that the sampling process is more intensive and delicate compared to simpler methods. On the other hand, one simulation is enough to extrapolate results in a large range of field values, at least in theory.

2.3 Single-Spin-Flip Algorithms

2.3.1 The Metropolis algorithm

The first conceptual leap that lead to the general application of Monte Carlo methods came with the invention of the Metropolis algorithm [26]. The novelty of this process was that instead of trying to evolve a many-body system according to its dynamics, sampling was performed directly from its phase space.

At each iteration of the algorithm, a candidate state is proposed and accepted or rejected based on a transition probability. It makes sense then to expand the probabilities that appear on the left hand side of Eq. (2.5) into the probabilities of two separate events: the choice of a new state and the acceptance of that proposal. Writing $C(\mu \to \nu)$ and $A(\mu \to \nu)$ respectively for these two probabilities, then Eq. (2.5) becomes

$$\frac{C(\mu \to \nu)A(\mu \to \nu)}{C(\nu \to \mu)A(\nu \to \mu)} = \exp\{-\beta\,[E(\nu) - E(\mu)]\}. \tag{2.6}$$

This gives a lot of freedom in the choice probabilities $C(\mu \to \nu)$, the simplest one being going from the starting state μ to the new one ν via a single-spin flip. For a system with N spins, picking one spin to flip to a new state would have a probability equal to $1/N$. Then the number of possible states a spin can take needs to be considered. Usually, the current state of the spin is excluded from the choice pool, in order to sample the phase space of the model faster, avoiding being stuck in a state for too long. For a spin-$\frac{1}{2}$ model, where the choice of a new spin state is unique, $C(\mu \to \nu) = 1/N$. In models where more that two states are allowed, such as the spin-1 models that will be studied in later chapters, then a site and a new state for the spin need to be picked. In these cases, if N_s is the number of possible spin states, $C(\mu \to \nu) \sim 1/(N(N_\mathrm{s} - 1))$. Due to the old state, μ, and the new one, ν, only differing by a single spin value, the probabilities $C(\mu \to \nu)$ and $C(\nu \to \mu)$ are equal. Hence, the acceptance probability of the newly proposed state should follow the rule

$$\frac{A(\mu \to \nu)}{A(\nu \to \mu)} = \exp\{-\beta\,[E(\nu) - E(\mu)]\} = \exp\{-\beta\Delta E\}, \tag{2.7}$$

where ΔE is the energy differences of the two states.

A way to pick the acceptance probabilities would be to choose $A(\mu \to \nu) \propto \exp\{-\beta E(\nu)\}$ and $A(\nu \to \mu) \propto \exp\{-\beta E(\mu)\}$. Since the two probabilities have the same normalization constant, there is no need to consider it. In order to facilitate a larger acceptance of new states, the Metropolis algorithm suggests a different approach, namely to make the transition probability equal to 1 if $\Delta E \leq 0$. Then, using Eq. (2.7) the acceptance probability becomes

$$A(\mu \to \nu) = \begin{cases} 1, \text{ if } \Delta E \leq 0, \\ \exp\{-\beta\Delta E\}, \text{ elsewhere.} \end{cases} \tag{2.8}$$

For conciseness, an iteration of the algorithm can be summarised as follows:

1. Pick a random spin, σ_i.
2. Pick a new candidate state for the spin, σ_i'.
3. Calculate the energy difference of the candidate state from the current state, $\Delta E = E(\sigma_i') - E(\sigma_i)$.
4. If $\Delta E \leq 0$, accept the proposed state.
5. Else, pick a random number $r \in [0, 1)$, and if $r < \exp[-\beta \Delta E]$, accept the proposed state.
6. Go back to step 1.

For a two-level system, the second step can be skipped, since the choice of a new candidate state is unique.

2.3.2 The Heat-Bath algorithm

The heat-bath (HB) algorithm [82] differs from the Metropolis in how the choice and acceptance probabilities of Eq. (2.6) are picked. When proposing a new candidate state for the system, this algorithm suggests picking a spin at random and choosing a candidate state not by equally distributed probabilities, but according to the likelihood of occurrence. Conceptually, the calculation of these probabilities is carried out by treating the rest of the lattice, around the picked spin, as a constant bath. This defines a local partition function, by taking into account only the possible states of the selected spin. If, for example, the spin i is chosen, the whole system's energy will be a function $E(\sigma_i)$. This notation was used to reiterate that the only possible change in the energy can be made through the chosen spin, σ_i. A local partition function for this spin is

$$\mathcal{Z}_{HB}^{(i)} = \sum_{\sigma_i} \exp\{-\beta E(\sigma_i)\}. \tag{2.9}$$

Starting from an initial state $\sigma_i = \sigma$, picking a new state $\sigma_i = \sigma'$ for the i-th spin can be carried out with the weight

$$C(\sigma_i = \sigma \to \sigma_i = \sigma') = \frac{1}{N} \frac{\exp\{-\beta E(\sigma')\}}{\mathcal{Z}_{HB}^{(i)}}, \tag{2.10}$$

where the factor $1/N$ comes from the equal-probability choice of one of the N spins. This choice for the probabilities of picking a new state automatically satisfies the condition of detailed balance of Eq. (2.6), and thus a trivial acceptance probability can be picked for the proposed move. $A(\mu \to \nu) = 1$ would then be the best choice for moving to new states faster.

However, it is useful to define a proposal scheme that excludes the current spin value. This defines the restricted heat-bath (RHB) algorithm [82]. Specifically, for the initial value of σ for the σ_i spin, the restricted local partition function is defined as

$$\mathcal{Z}^{(i)}_{RHB}(s) = \sum_{\sigma_i \neq \sigma} \exp\{-\beta E(\sigma_i)\}. \tag{2.11}$$

Then, the probability of choosing a spin value $\sigma_i = \sigma' \neq \sigma$ is

$$C(\sigma_i = \sigma \to \sigma_i = \sigma') = \frac{1}{N} \frac{\exp\{-\beta E(\sigma')\}}{\mathcal{Z}^{(i)}_{RHB}(\sigma)}. \tag{2.12}$$

Accounting for detailed balance using Eq. (2.6), the choice $C(\mu \to \nu)$ of going from the old state to the new becomes

$$C(\mu \to \nu) = C(\sigma_i = \sigma \to \sigma_i = \sigma') = \frac{1}{N} \frac{\exp\{-\beta E(\sigma')\}}{\mathcal{Z}^{(i)}_{RHB}(\sigma)}, \tag{2.13}$$

while the opposite choice, of proposing the backwards move, becomes

$$C(\nu \to \mu) = C(\sigma_i = \sigma' \to \sigma_i = \sigma) = \frac{1}{N} \frac{\exp\{-\beta E(\sigma)\}}{\mathcal{Z}^{(i)}_{RHB}(\sigma')}. \tag{2.14}$$

Putting together Eqs. (2.6), (2.13), and (2.14), the detailed balance condition for the acceptance probabilities reads

$$\frac{A(\sigma_i = \sigma \to \sigma_i = \sigma')}{A(\sigma_i = \sigma' \to \sigma_i = \sigma)} = \frac{\exp\{-\beta E(\sigma)\}}{\exp\{-\beta E(\sigma')\}} \frac{\mathcal{Z}^{(i)}_{RHB}(\sigma)}{\mathcal{Z}^{(i)}_{RHB}(\sigma')} \exp\{-\beta\left(E(\sigma') - E(\sigma)\right)\}, \tag{2.15}$$

where there is an obvious simplification that can be made on the right hand side; the first fraction and the rightmost exponential cancel each other out. Then, there is a simple choice of acceptance probabilities, since the remaining fraction on the right-hand side is either greater or not greater than unity,

$$A(\sigma_i = \sigma \to \sigma_i = \sigma') = \min\left\{1, \frac{\sum_{\sigma_i \neq \sigma} \exp\{-\beta E(\sigma_i)\}}{\sum_{\sigma_i \neq \sigma'} \exp\{-\beta E(\sigma_i)\}}\right\}. \tag{2.16}$$

A further simplification is straightforward, considering that most of the terms that appear in the energies of the two exponentials are the same.

An iteration of the restrictive heat-bath algorithm would then look like the following:

1. Pick a random spin, σ_i.

2. From the choice probabilities of Eq. (2.12) pick a candidate state for the spin, σ_i'.

3. From the acceptance probabilities of Eq. (2.16) accept or reject the proposed move.

4. Go back to step 1.

2.4 Cluster Algorithms

Although single-spin-flip algorithms are very straightforward to implement and versatile to apply, they fall short in terms of the critical slowing down that appears near critical points [79]. The application of methods with faster dynamics is in many cases necessary, and cluster algorithms offer exactly this benefit.

Rather than updating a single component of the system at each iteration, one can update a whole cluster of connected spins [78, 79]. To achieve this, bonds between spins are categorised into active and inactive, through a random process. Connected active bonds form a cluster, whose spins will be flipped simultaneously according to a single acceptance probability. Effectively, this procedure takes advantage of the correlations between neighbouring spins.

In essence, starting from an initial randomly picked seed spin, a random cluster is grown around it. For ferromagnetic systems, the cluster is confined to only include spins of the same orientation. If the probability to add a neighbouring spin to is equal to P_{add}, one would go from neighbour-to-neighbour checking if a spin will be added. After adding spins to the cluster, the new members' neighbours are checked. This process would eventually end when either all spins are added to the cluster or there are no new spins whose neighbours to test.

In general, this cluster forming procedure will take the initial state of the system, μ, to a new one, ν, after the cluster is flipped. The opposite process of going from ν to μ can be performed in a number of different ways; in general by starting from a different seed and growing the same cluster in a different series of moves. However, the probability of adding a spin to the cluster would be the same in the two processes. The only difference would be in the number of bonds that will be broken at the edges of the cluster. Assume that in the forward process, $\mu \to \nu$, m bonds at the edges of the cluster are broken with probability $(1 - P_{\text{add}})^m$, since the probability to not add a spin is $(1 - P_{\text{add}})$. In the opposite process, $\nu \to \mu$, n bonds are broken, with a probability of $(1 - P_{\text{add}})^n$. All other moves made to form the two cluster are essentially, probabilistically the same and thus cancel each other out, when considering detailed balance [Eq. (2.6)]. The probability of adding a spin to the cluster can then be inferred, since

$$(1 - P_{\text{add}})^{m-n} \frac{A(\mu \to \nu)}{A(\nu \to \mu)} = \exp\{-\beta [E(\nu) - E(\mu)]\}. \tag{2.17}$$

For pure ferromagnetic spin-1/2 systems, each broken bond will result in a $+2J$ energy increase. So $E(\nu) - E(\mu) = 2J(m - n)$. Substituting this to Eq. (2.17) results in

$$\frac{A(\mu \to \nu)}{A(\nu \to \mu)} = \left(\exp\{2\beta J\}(1 - P_{\text{add}})\right)^{m-n}. \tag{2.18}$$

Choosing $P_{\text{add}} = 1 - \exp\{-2\beta J\}$ is a very convenient choice, since it makes the right-hand side equal to 1, forcing the acceptances for both the forward and backward movements to be equal to 1, for a maximal acceptance of the proposed move. Note that for very high temperatures, $\beta \to 0$, the probability to add a spin becomes zero, implying that the correlations between the spins are non-existent for an infinite temperature, and very short range for high temperatures. On the other hand, for very low temperatures, $\beta \to \infty$, $P_{\text{add}} = 1$, implying that the cluster become geometric and not stochastic, i.e. spins are added with certainty in the cluster as long as a path of spins of the same orientation can be formed between them.

The above discussion explains the formulation of the Wolff cluster algorithm [83]. Due to the random selection of the seed spin, the cluster grown will be a subset of the largest geometric cluster more often than any other geometric cluster. This makes the algorithm very effective at studying the system in its critical region. Another way to implement the above cluster growing process is through the Swendsen-Wang cluster algorithm [84]. In this process, the whole system is populated by clusters formed with the above procedure. In the end, each of the clusters is flipped with a $1/2$ probability. This process still upholds the condition of detailed balance. Specifically, if c clusters are formed in the system, then the acceptance probabilities would be $(1/2)^c$ for both the forward, $\mu \to \nu$, and the backward, $\nu \to \mu$, moves. Additionally, due to the choice of $P_{\text{add}} = 1 - \exp\{-2\beta J\}$ detailed balance is directly satisfied.

A benefit of the Swendsen-Wang approach compared to the Wolff cluster algorithm, is that an iteration of the the first performs a whole sweep of the lattice, thus making its artificial time step directly comparable with a sweeps of a single-spin-flip algorithm. As a drawback though, the benefit of picking on average one of the larger cluster is lost. This generally slows down the dynamics of the algorithm. More on this will be discussed in Section 2.6.

Algorithmically, a Wolff cluster can be developed as follows:

1. Pick a seed spin and add it to an empty array which holds the spins in the current cluster.
2. Move one memory position forward in the current cluster array, thus choosing a current spin.
3. If there is no spins left, flip the spins in the cluster and exit.
4. Check the neighbours of the current spin and, if they are not already in the cluster array and are also parallel to the current spin, add them to the array with probability P_{add}.
5. Go to step 2.

In this process it is also useful to keep track of which spins already belong in a cluster, in order to avoid considering testing them more than once. A generalisation for the Swendsen-Wang cluster is readily available with minor modifications.

It is worthy to point out that cluster algorithms are predicated on the Hamiltonian symmetry of spin models, and in general are expected to work well for Potts models [85], because of their $O(n)$ symmetry. Potts models are defined by the Hamiltonian

$$H_{\text{Potts}} = -J \sum_{\langle ij \rangle} \delta_{\sigma_i, \sigma_j}, \tag{2.19}$$

where spins are allowed to take the values $1, 2, \ldots, q$. To give the simplest example, following the Fortuin-Kasteleyn representation [86–88], the partition function of the two-state Potts model at an inverse temperature β can be written as [41]

$$Z = \sum_{\{\sigma\}} \exp \left\{ \beta J \sum_{\langle ij \rangle} \delta_{\sigma_i, \sigma_j} \right\} = \sum_{\{\sigma\}} \sum_{\{n_{ij}\}} \prod_{\langle ij \rangle} \exp \{\beta J\} \left[(1-p)\delta_{n_{ij},0} + p\delta_{n_{ij},1} \right]. \tag{2.20}$$

In the above equation, n_{ij} indicates whether a bond is active or inactive (unity or zero respectively), and $p = 1 - exp\{-2\beta J\}$ is the probability to activate a bond. Equation (2.20) readily gives the same algorithm as the one discussed above, making clearer the role of symmetry as well. In the following Chapter, the efficacy of a cluster algorithm for a model in the 4-state Potts universality class that possesses three-spin interactions will be put into question. As will be seen, upon approaching a multicritical point, the efficacy of the algorithm also decreases.

2.4.1 Hybrid algorithms

There are many models were a cluster algorithm would simply be inadequate. An example of this are spin-1 models, whose spins can take the value zero. Such systems can be thought of as trying to mimic vacancies that can move around in a material, following the grand canonical ensemble [Eq. (1.13)]. If one of the spins that enter into an exchange interaction is zero, then the energy would not change regardless of the values of the rest of the spins in the exchange. For that reason, cluster algorithms can be chosen to either ignore the existence of zero spins, treating them as vacancies, or always expand on them, but never be able to flip them. Since however these zeros can also appear and disappear, a cluster algorithm cannot work to simulate such models. For this reason, in many studies [89–91], a cluster is often paired with a single-spin-flip algorithm. That way the efficiency of the multi-spin-flips of the cluster is still taken advantage of. At the same time, the single-spin flips guarantee that ergodicity is upheld and the state of the zero spins can still be modified.

2.5 Generalized Ensemble Sampling

Both single-spin-flip and cluster algorithms have the drawback of only allowing to extract results for a system in specific values of the field variables, i.e. temperature, external magnetic

field, etc. Then, in order to study a system whose behaviour is unknown, a large number of simulations is necessary. There is a group of algorithms though that offer the versatility of being able to give results for any value of the field variables, at least in principle. These are generalised ensemble methods. Here, focus is placed only on the Wang-Landau [92, 93] and multicanonical [94] algorithms.

2.5.1 Wang-Landau algorithm

As mentioned in Section 1.1.4, the main issue with analytically solving statistical physics systems is the inability to calculate the density of states, $\Omega(E)$ (see Eq. (1.12)). If the degeneracy $\Omega(E)$ was known then the partition function would directly allow to solve the system analytically. The Wang-Landau process [92, 93] is an iterative recipe for calculating the density. After $\Omega(E)$ is known, results can be extracted for any value of the external fields. The description of this scheme will be given for a single parameter system, with the generalisation to more parameters being easy to extrapolate.

To iteratively estimate the density of states, the Wang-Landau method accepts new candidate states with a probability proportional to the reciprocal of $\Omega(E)$. The process which suggests a new candidate state is not important for this discussion, but in most applications new states are produced by considering single-spin flips. That way, beginning with an initial state with energy E, a new state with energy E' would be accepted with probability $\Omega(E)/\Omega(E')$. For that reason, if the exact energy density was used, in the end a flat histogram in energy space would be sampled. However, since $\Omega(E)$ is unknown, an initial guess is needed. The usual choice is $\Omega(E) = 1$ for all energy levels.

After every proposed spin flip, $\Omega(E)$ is updated for the current energy of the system, using a modification factor f. Specifically, in the i^{th} iteration, $\Omega(E)$ becomes $f_i \times \Omega(E)$ for the current energy. Additionally, an energy histogram is stored. When it is flat enough, using some criterion to test the flatness, the modification factor is changed by the rule $f_{i+1} = \sqrt{f_i}$, where i indicates the number of times f has been modified. The initial value of f can be arbitrary, but usually is chosen to be $f_0 = e$. After each modification of f the energy histogram is reset.

It should be noted that due to the acceptance rate, the density of states is actually defined up to a multiplicative constant. Additionally, by construction and unlike the previous algorithms, nowhere in this discussion did the temperature appear. The Wang-Landau algorithm essentially tries to emulate a random walk in energy space and measure the geometric factor of how many microstates can produce a specific energy state.

Note that the factor f approaches unity very fast, with each modification. Thus, the longer the simulation runs for, the smaller the modifications to the density of states will be. In the end $\Omega(E)$ saturates and cannot actually reach the desired density of states. Lastly, since the weights are modified in every step, no detailed balance can be achieved [95]. Nevertheless, a number

of important soft-matter and biophysics applications have used this method successfully [96–102].

To avoid the aforementioned issues, the final density measured can be used in a production run at the end of the simulation. The time series produced thusly, together with the weights proportional to $1/\Omega(E)$, can be used to extract results for any value of the temperature. Since in this latest run the weights are unchanged, the issue of their constant modification is circumvented. Additionally, the reweighting process will make sure that each measurement is taken into account using a proper weight factor.

For two- or higher-parametric models, with more than one field, the energy of the system will be equal to $E = E_1 + E_2 + \ldots$, where for example E_1 might come from nearest- and E_2 from next-nearest-neighbour interactions. The Wang-Landau algorithm can be applied to calculate the multi-parametric density of states. Due to the increased size of the energy space, this will only allow the simulation of relatively small system sizes, which are not necessarily useful due to finite-size effects. For that reason, the random walk process can be applied only in one of the energies. The general method remains the same, and only the acceptance probabilities change. In a two dimensional energy space for example, starting from a point (E_1, E_2), a move (E_1', E_2') is accepted with probability $P(E_1, E_2 \to E_1', E_2')$ equal to

$$P(E_1, E_2 \to E_1', E_2') = \frac{\exp\left(-\beta E_1'\right)}{\exp\left(-\beta E_1\right)} \frac{\Omega(E_2)}{\Omega(E_2')}, \tag{2.21}$$

where Boltzmann weights were used for the E_1 parameter and the Wang-Landau process was used for the E_2.

Modifications and improvements on the Wang-Landau algorithm

One useful modification is to separate the energy-space into subranges and use different simulations to sample each of them [92, 93, 103]. Then, a concatenation process can be applied using the overlap in the ends of the ranges.

Another modification is to place a restriction on the energy-space, a practice that has been successful in studying pure [104, 105] and disordered [106–108] spin systems. In this approach, entries in the beginning and the end of the energy histogram are disallowed, as they are expected to play a small role in the averaging process. Specifically, to study the peak of an observable like the specific heat, only a relatively small range of energies is required. This *critical minimum energy subspace* can be defined [104, 105], depending on the necessary accuracy of the application.

Start by assuming that in a particular system at a temperature T, $\tilde{E}$ is the energy that produces the maximal term of the partition function of Eq. (1.12). For a finite system of linear size L, the interest lies in locating the maxima of thermodynamic observables and their location, or pseudocritical temperature T_L^*. Starting from $\tilde{E} = \tilde{E}(T_L^*)$, an energy subspace $\left(\tilde{E}_-, \tilde{E}_+\right)$ is

defined, with $\tilde{E}_{\pm} = \tilde{E} \pm \Delta\tilde{E}$. The practicality of this method is based on the expectation that $\Delta\tilde{E} \ll (E_{\max} - E_{\min})$, where $E_{\max}$ and $E_{\min}$ are the maximum and minimum values the energy can take, respectively.

From the definition of the free energy in Eq. (1.14), in the microcanonical ensemble one can define the distribution $f(E; T_L^*) \sim \exp\{S(E) - \beta E\}$. Then, a simple way of defining the sought after energy subspace would be to try and reduce the quantity

$$f(E; T_L^*)/f(\tilde{E}; T_L^*) = \exp\left\{(S(E) - \beta E) - \left(S(\tilde{E}) - \beta\tilde{E}\right)\right\} < r, \tag{2.22}$$

where r is some predefined parameter, setting the precision. However, the precision requested of the critical minimum energy subspace method should be better than the errors arising from the Monte Carlo simulation.

It is expected that $\Delta\tilde{E}$ will be of the order of the standard deviation of the energy [104, 105]. Using the definition of the specific heat in Eq. (1.19), then

$$\Delta\tilde{E} \sim \tilde{E}_+ - \tilde{E}_- \sim \sigma_E \sim \sqrt{NT^2C}. \tag{2.23}$$

A scaling law can be deduced for the range $\Delta\tilde{E}$, from the scaling law for the specific heat [Eq. (1.76)],

$$\left(\Delta\tilde{E}\right)^2 / L^D \sim L^{\alpha/\nu}. \tag{2.24}$$

It should be noted that the above assumptions are based on the fact that the mean of thermodynamic observables is expected to follow a Gaussian distribution, as per the central limit theorem (see Appendix A). The energy subspace then will have, from Eq. (2.23), a size of the order of $\sqrt{N}$. However, at the critical point, where the correlation length diverges, the distribution will not be Gaussian (see Section 1.6.3). It is expected though that the difference will not disallow the application of the method. In fact, the method has been applied with success in the past, measuring the critical exponent ration α/ν with adequate precision [104, 105].

2.5.2 Multicanonical algorithm

The multicanonical process [94] is similar in spirit and application to the Wang-Landau method. It also consists of using modified weights to simulate the system in order to produce flat histograms in energy space.[1] For a general discussion, the case of a multi-parametric energy space will be considered, and the multicanonical algorithm will be applied only to part of the energy space.

Let a system be described by an $\mathcal{N}$ dimensional energy space $\{E_i\}_{i=1}^{\mathcal{N}}$. A generalised partition function for this system can be written, where the Boltzmann weights of $\mathcal{M}$ of the energies

[1] In general, it is not necessary to use the energy histogram, and the method could be implemented centred around other parameters, like the magnetisation.

have been generalised to $W(\{E_i\}_{i=\mathcal{N}-\mathcal{M}+1}^{\mathcal{N}})$. For the rest of the energies nothing changes, so the multicanonical partition function is defined as

$$\mathcal{Z}_{\mathrm{MUCA}} = \sum_{\{E\}} \Omega(\{E\}) \exp\left(-\beta \sum_{i=1}^{\mathcal{N}-\mathcal{M}} E_i\right) W\left(\{E_j\}_{j=\mathcal{N}-\mathcal{M}+1}^{\mathcal{N}}\right), \tag{2.25}$$

where $\{E\}$ was used for brevity to represent all the energies, $\{E_i\}_{i=1}^{\mathcal{N}}$. The probability for a system to be in a specific energy $\{E\}$ is

$$P_{\mathrm{MUCA}} = \frac{\Omega(\{E\}) \exp\left(-\beta \sum_{i=1}^{\mathcal{N}-\mathcal{M}} E_i\right) W\left(\{E_j\}_{j=\mathcal{N}-\mathcal{M}+1}^{\mathcal{N}}\right)}{\mathcal{Z}_{\mathrm{MUCA}}}. \tag{2.26}$$

In order to produce a flat histogram in the manifold $\{E_i\}_{i=\mathcal{N}-\mathcal{M}+1}^{\mathcal{N}}$ of the energy space the marginal probability, obtained after summing out all other energies, should be constant. Solving for the modified weights then implies that

$$W\left(\{E_j\}_{j=\mathcal{N}-\mathcal{M}+1}^{\mathcal{N}}\right) \propto \mathcal{Z}_{\mathrm{MUCA}} \left[\sum_{\{E\}_{i=1}^{\mathcal{N}-\mathcal{M}}} \Omega(\{E\}) \exp\left(-\beta \sum_{i=1}^{\mathcal{N}-\mathcal{M}} E_i\right)\right]^{-1}. \tag{2.27}$$

These weights can be calculated in an iterative fashion, starting from an initial guess, which is usually unity for all possible combinations. At the n^{th} iteration, spins are flipped from state $\{E_j\}_{j=1}^{\mathcal{N}}$ to state $\{E'_j\}_{j=1}^{\mathcal{N}}$ using the weights

$$g^{(n)}\left(\{E'_j\}_{j=1}^{\mathcal{N}}\right) / g^{(n)}\left(\{E_j\}_{j=1}^{\mathcal{N}}\right), \tag{2.28}$$

where

$$g^{(n)}\left(\{E_j\}_{j=1}^{\mathcal{N}}\right) = \exp\left(-\beta \sum_{i=1}^{\mathcal{N}-\mathcal{M}} E_i\right) W^{(n)}\left(\{E_j\}_{j=\mathcal{N}-\mathcal{M}+1}^{\mathcal{N}}\right), \tag{2.29}$$

with the superscript (n) indicate the number of iterations. At each step, a histogram is accumulated, $H^{(n)}(\{E_j\}_{j=\mathcal{N}-\mathcal{M}+1}^{\mathcal{N}})$, of the energies for which the algorithm is used. This histogram will have the property

$$\begin{aligned} H^{(n)}\left(\{E_j\}_{j=\mathcal{N}-\mathcal{M}+1}^{\mathcal{N}}\right) &\propto P^{(n)}\left(\{E_j\}_{j=\mathcal{N}-\mathcal{M}+1}^{\mathcal{N}}\right) \\ &= \frac{1}{\mathcal{Z}_{\mathrm{MUCA}}} \sum_{\{E\}_{i=1}^{\mathcal{N}-\mathcal{M}}} \Omega(\{E\}) \exp\left(-\beta \sum_{i=1}^{\mathcal{N}-\mathcal{M}} E_i\right) W^{(n)}\left(\{E_j\}_{j=\mathcal{N}-\mathcal{M}+1}^{\mathcal{N}}\right) \\ &\propto \frac{W^{(n)}\left(\{E_j\}_{j=\mathcal{N}-\mathcal{M}+1}^{\mathcal{N}}\right)}{W\left(\{E_j\}_{j=\mathcal{N}-\mathcal{M}+1}^{\mathcal{N}}\right)}. \end{aligned} \tag{2.30}$$

The last proportionality indicates how to iteratively approach a flat histogram in the subspace $\{E_i\}_{i=\mathcal{N}-\mathcal{M}+1}^{\mathcal{N}}$ of the energy space by updating the weights using the scheme

$$W^{(n+1)} = \frac{W^{(n)}}{\mathcal{H}^{(n)}}, \tag{2.31}$$

where writing the argument $\{E_j\}_{j=\mathcal{N}-\mathcal{M}+1}^{\mathcal{N}}$ for each function was skipped. After the weights are updated, the histogram is emptied and resampled.

In the beginning of the simulation, the sampled histograms are not flat at all. After many iterations though, a flat histogram would be approached. When the desired flatness is reached, a final production run can be performed using the latest weights. The time series, together with the weights that produced it, can be used to extract results for any value of the fields that are coupled with the conjugate variables $\{E_j\}_{j=\mathcal{N}-\mathcal{M}+1}^{\mathcal{N}}$, where the multicanonical process was applied. More on the reweighting method required to do so can be found in the following Section and in Appendix A.

For the simplest case, where the energy space is one-dimensional, then simply replace in the above discussion $\mathcal{N} = \mathcal{M} = 1$. For the case of a two-parametric model, like the Blume-Capel and Baxter-Wu models, where the multicanonical method is going to be applied in the following chapters, $\mathcal{N} = 2$ and $\mathcal{M} = 1$.

Modifications and improvements on the multicanonical algorithm

The most commonplace modification made to the multicanonical algorithm, probably used in every implementation, is to save the logarithms of the weights $W^{(n)}$ instead of their actual value, since the latter always appear in ratios when it comes to the acceptance probability (see Eq. (2.28)). Sometimes this is necessary to be able to represent large weights at all in machine precision. One can also separate the order parameter range of interest into overlapping windows and work in a parallel fashion for these, stitching the results together self consistently using histogram reweighting. Nevertheless, this technique was not applied in the current work

A large benefit of the multicanonical algorithm is that it is highly parallelisable, specifically during the histogram sampling process. A relatively simple modification is to use many parallel systems with the same multicanonical weights, each sampling its own energy histogram, and each having a different random number generator.[2] The individual histograms may then be accumulated into a global histogram which could be used to modify the weights. This process keeps communication between the parallel workers minimum, something highly sought after in parallel applications [111].

This parallelisation can be performed on Graphical Processing Units (GPUs), taking advantage of their architecture. This however complicates the application of the algorithm, mostly

[2]The one chosen for the particular applications in this thesis was the Philox generator [109], which has been tested for parallel applications on GPUs in the past [110].

in the realm of memory access. First of all, GPUs usually possess much less memory, VRAM, compared to that available to a CPU, through RAM. So, memory intensive application might need to be modified to be performed on a GPU. Additionally, the way memory is accessed by a GPU works much differently than on RAM. For that reason, it is faster for an application to try to access adjacent memory locations as much as possible, in contrast with the random access memory of a CPU. A straightforward way to accomplish that is to place the lattice sites of the different systems running in parallel next to their counterparts. It is preferable for all lattices to be saved in an array where the first entry is the first spin of the first system, the second entry is the first spin from the second system, the third entry is the first spin of the third system and so on. Also, the same random number for choosing a spin would be used for all parallel systems. That way, only adjacent memory locations would need to be accessed during one implementation of the algorithm, and delays due to fetching random spin positions from memory for all lattices can be avoided. However, the random number for the choice and acceptance probabilities should still differ from system to system. Moreover, different types of memory available to the GPU could be utilised for different tasks. For example, texture memory could be used for arrays that are by construction accessed randomly, such as the weight $W^{(n)}$. For a thorough conversation on the subject, as well as discussions on performance and benchmarking see reference [111].

2.5.3 Reweighting process

In both Wang-Landau and multicanonical simulations, at least concerning the current thesis applications, a final production run is performed using modified weights. These weights can then be used to reweight the results in order to extract estimations of physical quantities for any value of the fields, at least theoretically. Specifically, for a particular observable quantity $\mathcal{O} = \mathcal{O}(\{\sigma\})$, where $\{\sigma\}$ indicates the configuration of the system, an average for any value of a desired field can be extrapolated from the results of one simulation. Using the terminology from the previous multicanonical section, and defining a set $\{f_i\}_{i=\mathcal{N}-\mathcal{M}+1}^{\mathcal{N}}$ as the desired values of the fields conjugate to the energies $\{E_j\}_{j=\mathcal{N}-\mathcal{M}+1}^{\mathcal{N}}$, the the mean is given by (see Appendix A)

$$\langle O \rangle_{\{f_i\}_{i=\mathcal{N}-\mathcal{M}+1}^{\mathcal{N}}} = \frac{\left\langle O(\{\sigma\}) W^{-1}\left(\{E_j\}_{j=\mathcal{N}-\mathcal{M}+1}^{\mathcal{N}}\right) \prod_{i=\mathcal{N}-\mathcal{M}+1}^{\mathcal{N}} \exp\left\{-\beta f_i E_i(\{\sigma\})\right\} \right\rangle_{\text{MUCA}}}{\left\langle W^{-1}\left(\{E_j\}_{j=\mathcal{N}-\mathcal{M}+1}^{\mathcal{N}}\right) \prod_{i=\mathcal{N}-\mathcal{M}+1}^{\mathcal{N}} \exp\left\{-\beta f_i E_i(\{\sigma\})\right\} \right\rangle_{\text{MUCA}}}. \tag{2.32}$$

The subscript "MUCA" is there to indicate that the averaging happens over the data sampled from the multicanonical simulation. Essentially this process counterbalances the weights W that produced the time series and averages with the proper equilibrium Boltzmann weights. At the same time it changes the normalisation, as seen by the denominator. This process then gives the ability to decide on the values of the fields post simulation.

Equation (2.32) is not useful only for the generalised ensemble methods. Arguably, it is used more often in conjunction with on of the algorithms discussed in the beginning of this Chapter. By performing a simulation at a constant value of the temperature T_0 for example, one can extrapolate results for additional values of T, close to T_0, by using the same time series and applying Eq. (2.32). Specifically, using the same concept of weighted averaging, the mean of an observable like the energy or the magnetisation at T will be given by

$$\langle O \rangle_\beta = \frac{\sum_i O_i \exp\{(\beta_0 - \beta)E_i\}}{\sum_i \exp\{(\beta_0 - \beta)E_i\}} \tag{2.33}$$

where $\beta_0 = 1/T_0$ and $\beta = 1/T$, and the sums run over the whole time series. A thorough discussion concerning the reweighting range $|T - T_0|$ that can still produce accurate results, or how this process can utilise the data of simulations at many different temperatures, can be found in reference [41].

2.5.4 Testing for flatness

An important test to perform in these generalised ensemble methods is to test the flatness of the histogram. In the Wang-Landau method this is clearly so, since when the histogram becomes flat, the modification factor is decreased. It is less evident however why testing for flatness can be useful in the case of the multicanonical algorithm. Since the simulations performed are in equilibrium, any weights utilised would give a correct answer. However, demanding that the weights be flat both in the iteration and the production processes can be a good extra test to see if indeed the system was in equilibrium during the iteration step of the algorithm. If this fails, it could indicate that different equilibration and sampling times should be used.

The most straightforward way to test for the flatness of the aforementioned histograms is to measure the relative deviation of the sample from a flat histogram. This method was applied for the Wang-Landau simulations of Chapter 4.

A more elaborate way that shows how distant two distributions are is the Kullback–Leibler divergence [112]. Given two distributions, P and Q, this metric is defined by the expectation value of difference of the logarithms of the distributions

$$D_{\mathrm{KL}}(P||Q) = -\sum_x P(x) \log \frac{Q(x)}{P(x)}, \tag{2.34}$$

which can also be seen as the relative entropy. Q is the test distribution, i.e. the flat one, while P is the sampled. That way, if for some x, $P(x) \to 0$, then $P(x) \log P(x) \to 0$ as well. This test can be very sensitive to very small values of Q, which seldom appear at the tails of distributions. Since however Eq. (2.34) is meant to be applied to test against a flat distribution, this problem does not arise here. The Kullback–Leibler divergence has already been applied in multicanonical simulations with success [111].

2.6 Dynamical Behaviour of Algorithms

The quintessential step after most Monte Carlo simulations concerning phase transitions of statistical physics models is to perform a finite-size scaling analysis, as discussed in Chapter 1. To accomplish this, the study of the behaviour of a system around a transition point for many different sizes is needed. It is then integral to have an estimate of how the resources needed by each algorithm increase with the system size, in order to know if the study undertaken is even feasible.

To answer the above question, the behaviour of the correlations within a time series can be calculated. If these correlations are large, then the simulation would need to run for longer in order to produce enough uncorrelated measurements. On the other hand, if the system decorrelates quickly, then even small runs could be adequate. The integrated autocorrelation time τ_{int} is a measure of how correlated a data set is. Specifically, for a time series $\{x_i\}_{i=1}^{N}$, as discussed in Appendix A, the variance of the average is given by

$$\sigma^2(\overline{x}) = \frac{\sigma^2(x_i)}{N} 2 \left[\frac{1}{2} + \sum_{k=1}^{N} \frac{A(k)}{A(0)} \left(1 - \frac{k}{N} \right) \right], \tag{2.35}$$

where $A(k)$ is the autocorrelation function, $A(k) = \langle x_1 x_{1+k} \rangle - \langle x_1 \rangle^2$, k being the lag between two measurements. The quantity in the brackets defines the integrated autocorrelation time

$$\tau_{\text{int}} = \frac{1}{2} + \sum_{k=1}^{N} \frac{A(k)}{A(0)} \left(1 - \frac{k}{N} \right). \tag{2.36}$$

For large N and after some value of k, the fraction $A(k)/A(0)$ would become very small. Usually, after an initial decay, this fraction will decay exponentially [79]. Additionally, for smaller values of k, the term in the parenthesis, which counts the frequency of appearance of each of the correlations, would be approximately equal to unity. These arguments justify the approximation of τ_{int} [41], by

$$\tau_{\text{int}} \approx \frac{1}{2} + \sum_{k=1}^{N} \frac{A(k)}{A(0)}. \tag{2.37}$$

Characteristic curves of the autocorrelation function $A(t)/A(0)$ and of the function

$$I(t) = \frac{1}{2} + \sum_{k=1}^{t} \frac{A(k)}{A(0)} \tag{2.38}$$

can be seen in Fig. 2.1. Note that after the plateau is reached, a systematic cut-off can be incorporated to extrapolate the value of τ_{int}. This figure is extracted from the results of the next chapter.

The integrated autocorrelation time will increase with the linear system size L, scaling like

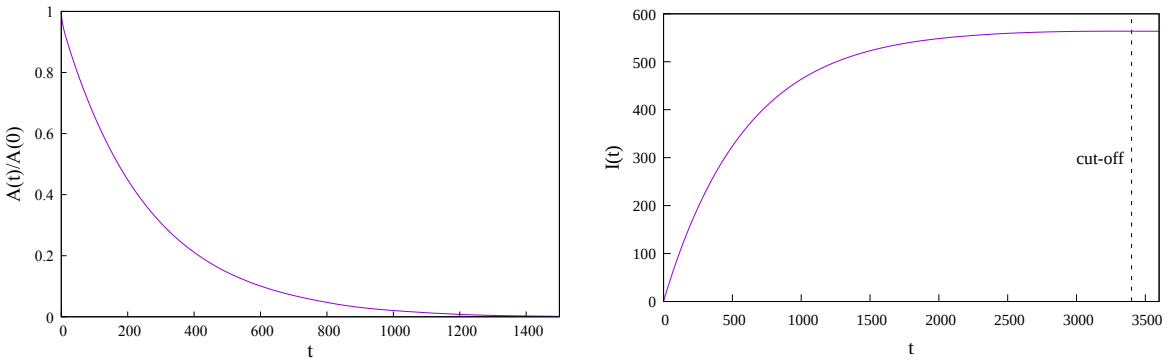

FIGURE 2.1: Characteristic curve of the autocorrelation function (see Eq. (2.35)) and of Eq. (2.38), showcasing how the integrated autocorrelation time can be defined using a cut-off.

$$\tau_{\text{int}} \sim L^z, \tag{2.39}$$

where z is called the dynamical critical exponent [78]. Similar to other critical exponents it is expected to be universal when it comes to the model studied, i.e. one expects that to depend on the spatial dimensionality of the system, the symmetries of the model, and the range of interactions. It should not be a surprise however that is also depends on the choice of the algorithm. See for example Section 2.3 and Section 2.4 where the differences and benefits of a cluster algorithm in comparison to a single-spin-flip method were discussed.

There are a number of works that have measured the z exponent in different cases. Generally, cluster algorithms have a much smaller z exponents compared to single-spin-flip algorithms. For example, in the two-dimensional Ising model, the dynamical critical exponents z of the Wolff cluster algorithm, calculated from the integrated autocorrelation time is $0.26(2)$ for the energy (E) and $0.13(2)$ for the magnetic susceptibility (χ) [83]. The same quantity for the Swendsen-Wang algorithm has the respective values $0.27(2)$ and $0.20(2)$ [83]. In three dimensions, the Wolff cluster yields $z = 0.28(2)$ for E and $0.14(2)$ for χ, while for the Swendsen-Wang $z = 0.50(3)$ for both E and χ [41]. The smaller exponent z for the Wolff algorithm can be attributed to the fact that the seed spin chosen in the first step of the development of a cluster is more likely to be a member of the largest geometric cluster of the system than any other smaller cluster. So, on average, it is expected that a certain amount of Wolff cluster proposed flips will decorrelate the system more than an equivalent amount of flips proposed by the Swendsen-Wang algorithm.

Single-spin-flip algorithms however tend to have a value of z a bit above 2, meaning that they scale a bit worse than a random walk. Specifically, using the Metropolis algorithm, for the pure Ising model $z = 2.1667(5)$ (two-dimensions) [113] and $z = 2.055(10)$ (three-dimensions) [114]. The above stated results are not necessarily consistent and directly comparable with each other, since some were from equilibrium and some from non-equilibrium studies. However, it is

evident that the dynamical scaling of the clusters is an order of magnitude better than what single-spin-flip algorithms can achieve.

2.7 Related Methodology

As far as the current discussion of statistical physics is concerned, Monte Carlo simulations go hand-in-hand with the concepts of renormalisation group. Many works in the past have focused on performing the renormalisation-group transformation with the aid of Monte Carlo simulations. This process began with the ideas of Shang-keng Ma [115], and was further developed in the following years [48, 50, 116–121]. In more resent times, with machine learning being at the forefront of contemporary research, there have been successful applications combining it with renormalisation-group ideas [122]. Additionally, Monte Carlo renormalisation group has been combined with neural networks [53], leaving it up to the neural network to decide on the blocking method. Since many ideas are common in both fields, there is room for development of both disciplines in a combined approach.

Another method, useful in the study of complex systems possessing rough free energy landscapes, is that of simulated tempering [123]. In this approach, an initial array of temperatures is set, and the system randomly changes its temperature during the simulation. Taking advantage of the fluctuations at large temperatures, this allows the system to move out of local minima. In this approach, parallelising the computer code is a major asset [124]. Studies of this form need to take into account the distribution of temperatures chosen and the number of Monte Carlo steps before each temperature change.

Population annealing [125–127] is another simulation scheme used in similar studies. There, an ensemble of system replicas is set at some initial temperature. From this set of copies, the ensemble is resampled, using Boltzmann weights, and each copy is evolved using a Monte Carlo algorithm. The temperature is then reduced, until the target has been reached. At each step, observables can be estimated directly from the ensemble. This method is suitable for parallelisation and there are a number of parameters that can be optimised, such as the number of replicas, temperature step, and number of Monte Carlo sweeps before each ensemble resampling.

On a different note, the development of quantum mechanics methods, such as the the density matrix renormalisation group [128–130], have led to further progress in classical applications as well, specifically, the concept of tensor-network renormalisation group [131–133] and corner transfer matrix renormalisation group [134, 135]. Since calculations with tensors have become much easier to perform due to software related to machine learning, it is expected that this area of research has still more room for further development.

Chapter 3

Dynamical Scaling in the Dilute Baxter-Wu Model

The dynamical critical scaling behaviour of the spin-1/2 and spin-1 Baxter-Wu models in a crystal-field Δ is investigated, employing a set of methods: a cluster and a single-spin-flip for the spin-1/2 case and a single-spin-flip and a hybrid algorithm for the spin-1 case. The latter method combines a cluster and a single-spin-flip update. Specifically, the equilibrium properties of the models are examined, with the aim being to implement and study the scaling of the cluster algorithm proposed by Novotny and Evertz [136]. Given the underutilisation of this cluster method in the past, its application holds promise for exploring the vicinity of the multicritical point of the spin-1 model. A finite-size scaling analysis provides the dynamical critical exponent z. For the spin-1 model, as Δ crosses to positive values it renders the hybrid update almost as inefficient as the single-spin-flip approach.

The rest of the Chapter is structured as follows: Section 3.3 provides a discussion on how to define an autocorrelation time, how to measure it, and how to extract the dynamical critical exponent z from a finite-size-scaling analysis. The pure and dilute Baxter-Wu models are introduced in Section 3.1, while the cluster algorithm is described and its correctness is tested against other simulation methods in Section 3.2. Results are shown in Section 3.4. Specifically, estimations of z for the cluster and Metropolis algorithms in the spin-1/2 model are performed in Section 3.4.1. In Section 3.4.2, the dynamical critical exponent z of the hybrid and heat-bath algorithms is calculated for the spin-1 Baxter-Wu model in the presence of a crystal field Δ, for various values of Δ along the critical transition line.

3.1 The Baxter-Wu Model

The Baxter-Wu model was first introduced by Wood and Griffiths [137] as a system which does not exhibit invariance under a global inversion of all spins. It is defined on a triangular lattice (see Fig. 3.1) by the Hamiltonian

$$\mathcal{H} = -J \sum_{\langle xyz \rangle} \sigma_x \sigma_y \sigma_z, \tag{3.1}$$

where the exchange interaction J is positive, the sum extends over all elementary triangles of a lattice with $N = L \times L$ sites, and $\sigma_x = \pm 1$ are Ising-like spin-1/2 variables. The triangular lattice can be divided into three sublattices, A, B, and C, as shown in Fig. 3.1, so that any triangular face contains one site of each sublattice. The ground state of the model is four-fold degenerate: there is one ferromagnetic state, with all spins up, and three ferrimagnetic states, with down spins in two sublattices and up spins in the third sublattice. Also, the model is self-dual [137, 138], having the same critical temperature as the spin-1/2 Ising model on the square lattice, i.e. $T_c/J = 2/\ln(\sqrt{2}+1) = 2.269185\ldots$.

To distinguish the paramagnetic from the ferromagnetic state, an order parameter can be defined. This cannot be the magnetisation, due to the ground state degeneracy. If the magnetisation per spin of each sublattice is defined as m_A, m_B, and m_C, an order parameter can be

$$m_{op} = \sqrt{\left(m_A^2 + m_B^2 + m_C^2\right)/3}. \tag{3.2}$$

Since in all ground states, $m_A^2 = m_B^2 = m_C^2 = 1$, then $m_{op} > 0$ in the ordered phase. On the contrary, in the disorder phase, the average magnetisation of each sublattice is equal to zero, resulting in $m_{op} = 0$, making m_{op} an adequate order parameter.

The exact solution of Baxter and Wu dates back to 1973 and provided the critical exponents $\alpha = 2/3$, $\nu = 2/3$, and $\gamma = 7/6$ [34, 139]. Later, it was shown that the critical behaviour of the model corresponds to a conformal field theory with central charge $c = 1$ [140, 141]. As was first pointed out by Domany and Riedel, the $q = 4$ Potts model should belong to the same universality class as the Baxter-Wu model, as both have the same symmetry and degree of degeneracy in the ground state [142, 143]. However, although the leading critical exponents are the same, one should note that these two models have different corrections to scaling: while the 4-state Potts model presents logarithmic corrections with the system size, as expected for the marginal case before the transition becomes first-order for $q > 4$ [143], the Baxter-Wu model has power-law corrections with a correction-to-scaling exponent $\omega = 2$ [140, 141]. This rather large value of ω allows for a safe determination of the asymptotic scaling behaviour even when dealing with systems of moderate size, see for instance reference [144]. As will be seen in the later sections, the accuracy of the results does not allow for the calculation of omega, and thus the value calculated by Alcaraz et al. was utilised.

An interesting extension of the Baxter-Wu model arises when one considers spin values $\sigma_x = \{-1, 0, 1\}$ and includes an extra crystal field (or single-ion anisotropy) Δ, so that the resulting Hamiltonian reads

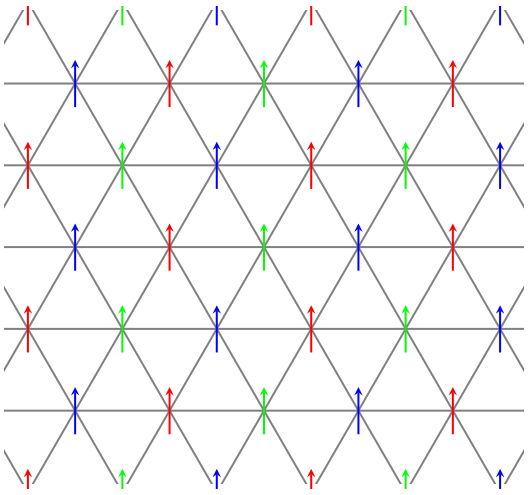

FIGURE 3.1: Representation of the Baxter-Wu triangular lattice as a superposition of the three sublattices A, B, and C. Each sublattice corresponds to spins of different color. The spins are shown in the ferromagnetic ground state.

$$\mathcal{H} = -J \sum_{\langle xyz \rangle} \sigma_x \sigma_y \sigma_z + \Delta \sum_x \sigma_x^2 = E_J + \Delta E_\Delta. \tag{3.3}$$

Unfortunately, there exists no exact solution for this model, and therefore approximation methods need to be employed. Note, however, that when $\Delta \to -\infty$, only configurations with $\sigma_x = \pm 1$ are allowed and the pure Baxter-Wu model is recovered.

The model of Eq. (3.3) resembles the well-known Blume-Capel model [145–148], which exhibits a phase diagram with ordered ferromagnetic and disordered paramagnetic phases separated by a transition line with first- and second-order segments (the latter in the Ising universality class) connected by a tricritical point. More details about the phase diagram and universality aspects of the general Blume-Capel model can be found in references [149–156]. In analogy to these findings, one might expect for the model defined in Eq. (3.3) a similar phase diagram but a different universality class. Nienhuis et al. [157] first discussed the analogy between the Baxter-Wu and diluted Potts models and pointed out that the general phase diagram will exhibit a line of continuous transitions that connects to a regime of first-order transitions through a multicritical point. Kinzel et al. [158] instead, using a finite-size scaling method, conjectured that a continuous transition only occurs for $\Delta \to -\infty$ (the pure Baxter-Wu model). More recent works has favoured the existence of a multicritical point at finite values of Δ [159]. In reference [160] the location of the pentacritical point was estimated as $(\Delta_{\rm pp}, T_{\rm pp}) \approx (0.8902, 1.4)$. This point refers to the coexistence of three ferrimagnetic and a ferromagnetic configuration, along with that of zero spins. The results of reference [160] for the critical exponents $\nu \approx 0.63$ and $\eta \approx 0.23$ point to the universality class of the pure spin-1/2 Baxter-Wu model where $\nu = 2/3$ and $\eta = 1/4$. Additional results exist [161–163] and allow for a very good picture of

the phase diagram (see Fig. 3.2).

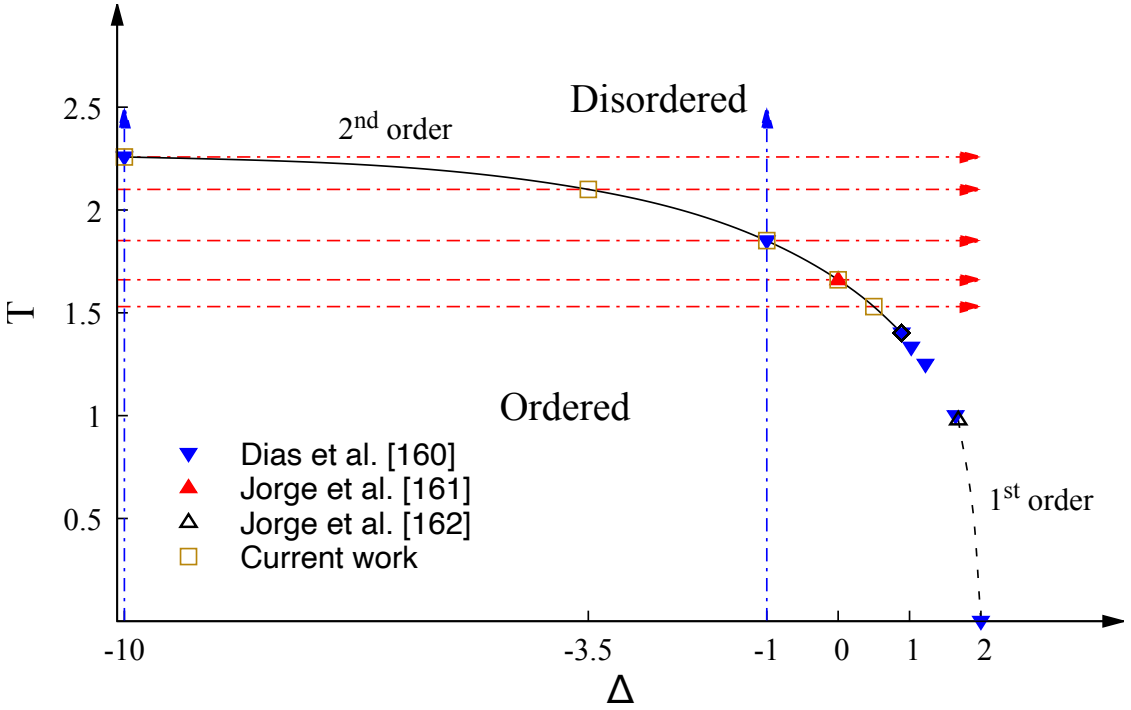

FIGURE 3.2: Phase diagram of the two-dimensional spin-1 Baxter-Wu model. The black dashed and continuous lines correspond to first- and second-order transitions. The black rhombus marks an estimation of the pentacritical point $(\Delta_{pp}, T_{pp}) \approx (0.8902, 1.4)$ [160]. The black triangle marks another estimation at $(1.68288, 0.98030)$ [162]. Several transition points are given including those obtained in the current work [163–165].

The next Chapter will focus on the continuous phase-transition properties of the spin-1 Baxter-Wu model in a crystal field. There, it will become apparent that the phase diagram looks indeed like the one depicted in Fig. 3.2. In the present section, a hybrid update will be implemented for the first time in the spin-1 model. Section 3.2 introduces said algorithm for the spin-1/2 model, following the work of Novotny and Evertz [136].

3.2 The Baxter-Wu Cluster Algorithm

3.2.1 The spin-1/2 case

A cluster algorithm for the spin-1/2 Baxter-Wu model was first proposed in 1993, see reference [136]. Because this algorithm has been underutilised, an overview of the cluster construction process is given in this Section. Its basis rests on the fact that the triangular lattice consists of three sublattices and that the triplets that appear in the Hamiltonian of Eq. (3.1) contain one spin from each sublattice, as shown in Fig. 3.1. The main idea is to freeze one sublattice at each

iteration of the algorithm and then grow the cluster in the other two sublattices. A picture of this mapping at a local scale can be seen in Fig. 3.3. There, a pair of spins and the two elementary triangles that they both belong to are shown. By freezing one of the sublattices, these spins now interact pairwise, but their exchange-interaction strength is affected by the constant-sublattice spins. It is then straightforward to apply one of the cluster algorithms discussed in Section 2.4.

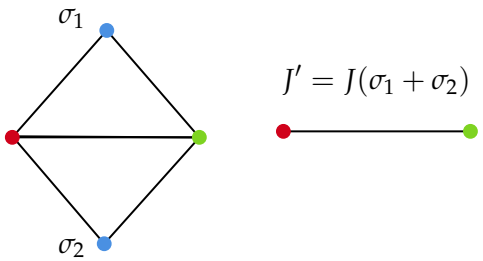

FIGURE 3.3: Mapping of the three-spin into two-spin interactions. In this specific picture the "blue" sublattice is frozen and its spins are absorbed in the effective spin-spin exchange-interaction strength.

The steps of the algorithm are as follows:

1. Pick at random one of the three sublattices, which is to remain constant during the iteration.

2. Grow a cluster on the other two sublattices, absorbing the spins of the constant sublattice in the interaction strength coefficients (see Fig. 3.3).

3. Go back to step 1 and repeat.

Essentially, what this algorithm does is to transform the triangular lattice into an hexagonal one. At the same time, the constant strength J of the three-spin interactions of the Hamiltonian [Eq. (3.1)] transforms into effective strengths for two-spin interactions. Any two spins of the initial lattice participate in two common elementary triangles (see Fig. 3.3). Locally, the energy due to these two triangles is $-J\sigma_1\sigma\sigma' - J\sigma_2\sigma\sigma'$, where the spins σ_1, σ_2 belong in the sublattice that will be frozen, while the spins σ, σ' each belongs in one of the two other sublattices. Factoring the local energy, $J'\sigma\sigma' = J(\sigma_1 + \sigma_2)\sigma\sigma'$, defines an effective interaction of two spins with strength $J' = J(\sigma_1 + \sigma_2)$. Since the spins can take the values ± 1, these new interactions can have strengths $J' \in \{-2, 0, +2\}$.

There are two interesting properties of this proposed update: firstly, there is no frustration due to the geometry of the hexagonal lattice. Secondly, the developed clusters are either solely ferromagnetic or antiferromagnetic, and cannot be of mixed interactions. This is because of the values that J can take and the positions of the spins of the frozen sublattice. Figure 3.4 shows comparative results for the specific heat (main panel) and the magnetic susceptibility (inset),

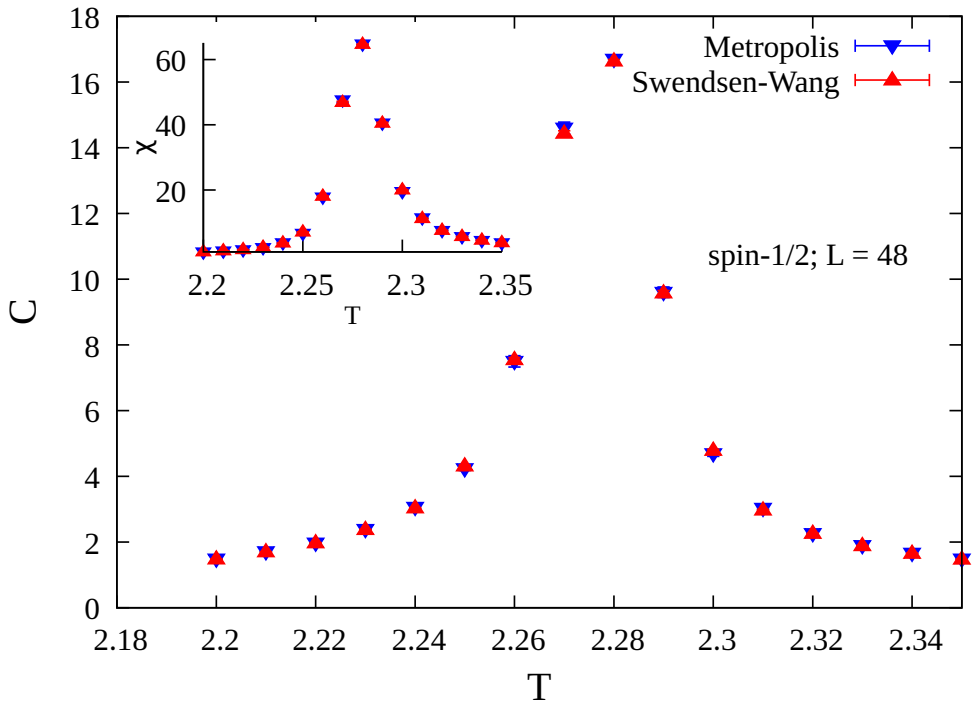

FIGURE 3.4: Comparison of the specific heat (main panel) and magnetic susceptibility (inset) for the spin-1/2 Baxter-Wu model for various values of the temperature, for a system size of $L = 48$, using the Metropolis and Swendsen-Wang cluster algorithms. The results agree nicely, within error bars.

between this scheme, using the Swendsen-Wang algorithm [84], and a simple Metropolis update, for a system of linear size $L = 48$, at various temperatures around the critical point. The agreement between the results is evident, proving the validity of the algorithm.

3.2.2 The spin-1 case

A hybrid algorithm was implemented to study the spin-1 Baxter-Wu model, comprised of two parts: one cluster and one single-spin update. For the former, a Swendsen-Wang cluster algorithm was utilised. The single-spin-flip algorithm was chosen to be a restricted heat-bath (HB) protocol (see references [82, 166] and Chapter 2), which is known to work better for spin-1 models compared to the Metropolis update [82].[1] Thus, every Monte Carlo step consists of one lattice sweep applying the Swendsen-Wang algorithm to all the non-zero spins, and another sweep using the heat-bath method. The success of hybrid schemes in similar models, such as the Blume-Capel model, has already been established [89, 91, 156]. The reason behind preferring the Swendsen-Wang over the Wolff algorithm is that the first makes it straightforward to

[1]Specifically, even though the two algorithms scale with the same dynamical exponent z, the autocorrelation time itself is generally smaller for the heat-bath algorithm, at least for models that have more than two possible states.

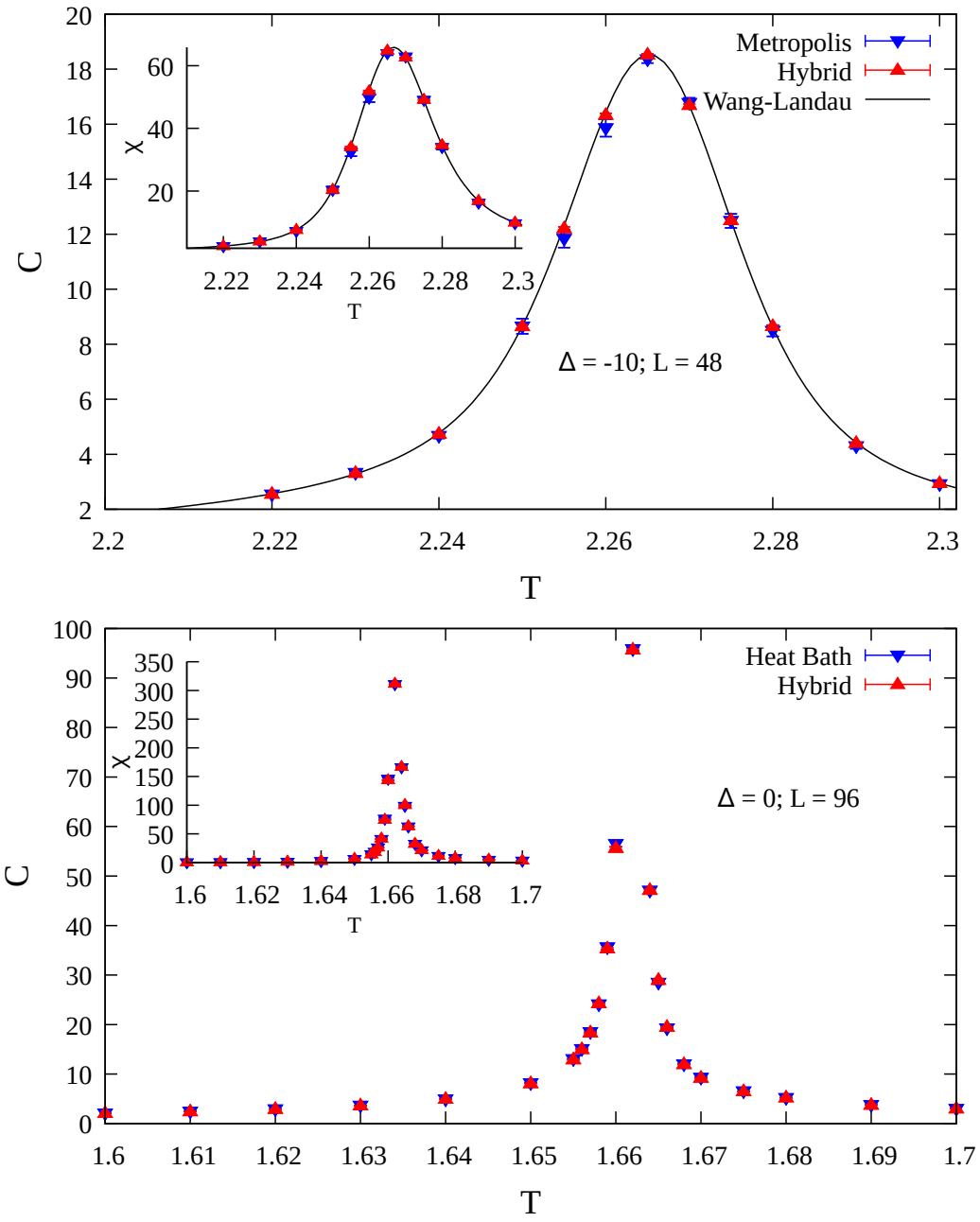

FIGURE 3.5: **Upper panel**: Comparisons of the specific heat (main panel) and the susceptibility (inset) of results for the spin-1 Baxter-Wu model at $\Delta = -10$ for various values of the temperature and a system size of $L = 48$, using the Metropolis, hybrid (Swendsen-Wang and heat bath), and Wang-Landau [164] algorithms. **Lower panel**: Similar to the upper panel, but for $\Delta = 0$ and $L = 96$. Notice the agreement within errors

define time units, which can be useful in an application where the interest lies in measuring autocorrelation times.

In the spin-1 model, when a sublattice is chosen to be frozen, the effective interactions arising can take the values $\{-2, -1, 0, +1, +2\}$. Due to the existence of zero spins, the clusters can now be ferromagnetic, antiferromagnetic, but also of mixed interactions, unlike the spin-1/2 case. Nevertheless, there is still no frustration due to the geometry. In the following, reduced units will be used, where $J = 1$.[2]

Comparisons utilising different simulation methods can be seen in Fig. 3.5, where the specific heat and the magnetic susceptibility for a system of $L = 48$ at $\Delta = -10$ are compared using a Metropolis update, the hybrid algorithm, and results from Wang-Landau simulations taken from reference [164]. All results are in agreement with each other. Furthermore, since for strongly negative Δ the system is very close to its spin-1/2 counterpart, results much closer to the multicritical point are presented in in the bottom panel of the same figure. There, results around the pseudocritical point of a system $L = 96$ at $\Delta = 0$ are presented, using the heat-bath and the hybrid update. Again, the results are in agreement within errors. Additionally, following the same arguments from Section 2.4, with the additional move of choosing one sublattice, it is straightforward to see that detailed balance is adhered to. Lastly, the algorithm allows in principle the system reach any possible microstate, making it ergodic. All these indicate that the hybrid algorithm can actually be used to simulate the spin-1 Baxter-Wu model in the presence of a crystal field.

It is important to note that as Δ increases, so does the density of the zero spins, possibly rendering the cluster algorithm less-and-less useful. Additionally, the lack of zero spins in the small values of Δ causes the clusters formed to be mostly ferromagnetic or antiferromagnetic, but not of mixed type, possibly stunning the growth of clusters. These will be studied in the following sections. Finally, the reason for the various comparisons, using different algorithms, is to establish that all the implemented methods agree with each other, in order to make more concrete the correctness of the cluster update and of the hybrid scheme overall.

3.3 Scaling of Autocorrelation Times

As mentioned in Chapter 2, Section 2.6, the integrated autocorrelation time, τ_{int}, and especially its finite-size scaling, play an important role in characterising the efficacy of a Monte Carlo algorithm. From Eq. (2.37), τ_{int} is defined as

$$\tau_{\text{int}} = \frac{1}{2} + \sum_{k=1}^{n} \frac{A(k)}{A(0)}, \tag{3.4}$$

with n being the sample size and $A(k) = \langle x_1 x_{1+k} \rangle - \langle x_1 \rangle^2$ is the reduced autocorrelation function. In this context, the parameter k is often referred to as lag. In general, the quantity $A(k)/A(0)$ starts from unity and decays. Due to the finiteness of the sampled time series,

[2] As a reminder, the Boltzmann constant k_B has been set to unity throughout the thesis, and temperature will be measured in units of energy given by $[J]$.

given enough time, $A(k)/A(0)$ eventually fluctuates around zero. For this reason, when performing the summation in Eq. (3.4), the estimation of τ_{int} increases until it reaches a plateau, around which it fluctuates.

A self consistent method for the calculation of the integrated autocorrelation time is usually defined by implementing a large enough integration cut-off [167]. In the past, a lot of success has been garnered when the numerical integration was stopped using the condition $k_{\text{max}} \geq a\tau_{\text{int}}$, where $3 \leq a \leq 10$ [168]. The integrated autocorrelation time relation would then become

$$\tau_{\text{int}} \approx \frac{1}{2} + \sum_{k=1}^{k_{\text{max}}} \frac{A(k)}{A(0)}. \tag{3.5}$$

This method guarantees that τ_{int} will have saturated but also that autocorrelations separated by very large time steps, for which the finite time series does not have enough information, will not be taken into account. Hence, for large enough samples, the fluctuations of $A(k)/A(0)$ that appear after some value of k are not being taken into account.

As mentioned in Section 2.6, the time τ_{int} will scale like

$$\tau_{\text{int}} \sim L^z, \tag{3.6}$$

or including corrections-to-scaling [168]

$$\tau_{\text{int}} = cL^z(1 + c'L^{-\omega}). \tag{3.7}$$

Here, c and c' are non-universal constants, to be determined from a fitting process, and ω is a universal corrections-to-scaling exponent.

On the other hand, in models were τ_{int}, and by extension k_{max}, become very large, there might be a need to sample a huge time series, in order to make sure that the precise calculation of τ_{int} is possible. This can lead to arduous simulations and unwieldy time series, due to the complexity that enters in the calculation of $A(k)$. To avoid summing up to a large k_{max}, Hasenbusch et al. [169] suggested a somewhat different-in-spirit approach for calculating z, and successfully applied it for the three-dimensional Ising model with dilution. This method does not deal with τ_{int} directly, but instead calculates times τ_x that scale with the same law, i.e. $\tau_x \sim L^z$. The advantage of this approach is that calculation for smaller lags are required in order to estimate τ_x, compared to τ_{int}, leading to faster as well as more precise estimations.

To define this time τ_x in the current case, the function $I(t)$ is necessary, with

$$I(t) = \frac{1}{2} + \sum_{k=1}^{t} \frac{A(k)}{A(0)}. \tag{3.8}$$

Reference [169] proved quite generally that the solution of the equation

$$\tau_x = I(x\tau_x) \tag{3.9}$$

scales like L^z, where x is a real positive number. It can be shown that τ_x exists and that it scales like τ_{int}.

Firstly, to see that a solution τ_x exists it is enough to define the function $h_x(t) = t - I(xt)$. Since $I(t)$ is defined only for integer values of t, an interpolation to all positive values of t is required. In what follows, a linear interpolation was chosen. It holds that $h_x(0) = -1/2$ and also that $h_x(t \to \infty) \to \infty$. Since $h_x(t)$ is continuous and differentiable, there exist at least one root $\tau_x > 0$ such that Eq. (3.9) is fulfilled.

Secondly, it can be proven that this solution scales like the integrated autocorrelation time τ_{int}. Starting from the inequality $0 < k < k_{\max}$, for some very large value $k_{\max}$, it follows that $1/2 < I(k) < I(k_{\max})$, since $I(t)$ is a continuous, positive, and increasing function. Without loss of generality, writing $k = x\tau_x$ implies that $1/2 < I(x\tau_x) < I(k_{\max})$. Then, from Eq. (3.9), $1/2 < \tau_x < I(k_{\max})$. Dividing with τ_{int}, which for finite systems is also finite, results in $1/(2\tau_{\text{int}}) < \tau_x/\tau_{\text{int}} < I(k_{\max})/\tau_{\text{int}}$. Since for finite systems $1/(2\tau_{\text{int}}) > 0$, then $0 < \tau_x/\tau_{\text{int}} < I(k_{\max})/\tau_{\text{int}}$. Lastly, taking the limit $k_{\max} \to \infty$ implies that $0 < \tau_x/\tau_{\text{int}} < 1$. The last set of inequalities suggests that τ_x is positive, smaller and also proportional to τ_{int}. Thus, τ_{int} and τ_x obey the same scaling law. So, for finite systems, the scaling relation $\tau_x \sim L^z$ holds.

Note that if x is chosen to be very large, then this method coincides in spirit with the cut-off discussed in the beginning of this section. This is due to the saturation of $I(t)$, for large arguments. However, the power of this approach can be seen when the choice of x is relatively small. Then, there is no need to calculate the autocorrelation function $A(k)/A(0)$ for large values of k.

3.4 Results

3.4.1 The spin-1/2 Baxter-Wu model: a dynamical scaling study for a cluster update

To calculate the dynamical exponent z of the cluster algorithm for the spin-1/2 Baxter-Wu model, simulations at the critical point $T_c = 2.269185314\ldots$ [34, 139] were performed. Specifically, a Swendsen-Wang cluster algorithm was implemented, whereas the original study of Novotny and Evertz [136], as well as a study by Velonakis and Martinos [170] used Wolff clusters. The value of z was measured using the methods discussed in Section 3.3, specifically for the order parameter of the model [Eq. (3.2)]. For the numerical summation of the autocorrelation functions, Eq. (3.5), a cut-off of $k_{\max} = 6\tau_{\text{int}}$ was used throughout this Chapter. The linear system sizes studied were $L = \{12, 15, 18, 24, 30, 36, 48, 60, 72, 96, 120, 144\}$. As can be seen, the system size is always a multiple of three, to make sure that all the ground states of the infinite system have the same energy in the finite systems. The simulation length was 10^6 Monte-Carlo

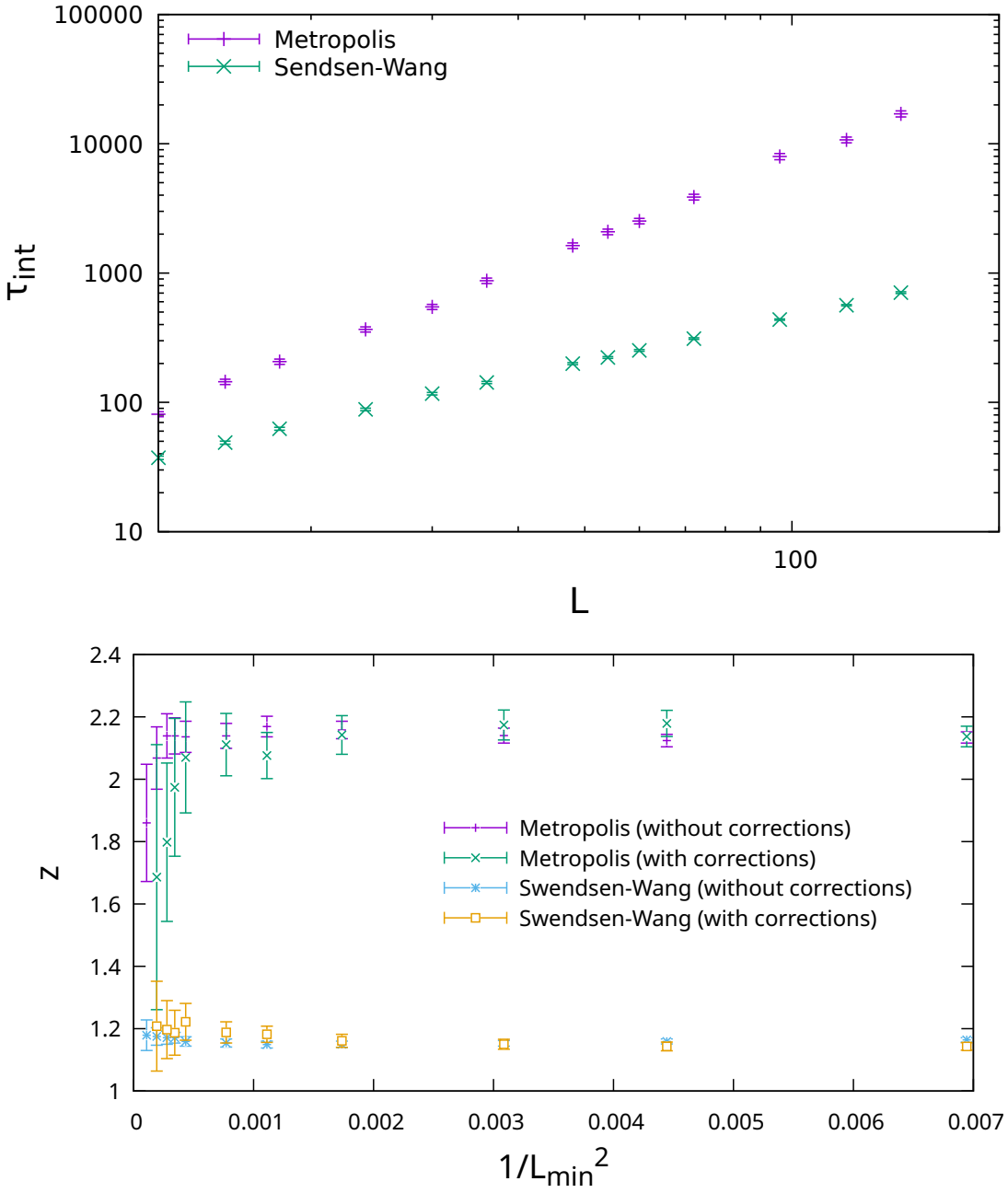

FIGURE 3.6: **Upper panel**: Integrated autocorrelation time from numerical summation of the form of Eq. (3.5), with a cut-off at $k_{\max} = 6\tau_{\text{int}}$, for the spin-1/2 Baxter-Wu model at the critical point, using the Metropolis and Swendsen-Wang algorithms. **Lower panel**: The dynamical critical exponent z following fits of the forms (3.6) and (3.7), i.e. with and without corrections, on the data of the upper panel. For each fit a different minimum system size, $L_{\min}$, was used.

sweeps for the smallest system of $L = 12$, with an additional one-tenth of those sweeps used for equilibration. For the rest of the systems, these numbers were increased by a factor $L^2/12^2$. From the autocorrelation times calculated, it is safe to assume that the system had reached equilibrium. Periodic boundary conditions were used and the corrections to scaling exponent is taken to be equal to $\omega = 2$ [140, 141]. Lastly, concerning the fitting procedure, similarly to all the previous chapters, the standard χ^2 goodness of fit test was employed [171]. The probability Q of finding a larger value for χ^2, compared to the one calculated from the process, was considered to be fair if $10\% \leq Q \leq 90\%$. This is the standard practice followed also in the remainder of the thesis.

The upper panel of Fig. 3.6 shows τ_{int} versus L, for the Swendsen-Wang and Metropolis algorithms. The errors were calculated using the jackknife method (see Appendix A). Specifically, the time series was separated into 50 bins, each bin being much larger than the autocorrelation time. That way, 50 virtually uncorrelated estimates of τ_{int} were calculated. From there it is straightforward to apply the jackknife method and estimate the mean τ_{int} and its error. Some tests, performed mostly for the smaller system sizes considered, indicated that varying the number of bins up to 100 did not really change the estimations of the means or the errors.

The lower panel of Fig. 3.6 shows results from fits performed on the τ_{int} estimations, each time using a different system size, L_{min}, as the smallest size of the fitting process. Both fits with and without corrections were considered. The results without corrections [Eq. (3.6)] suggest that $z = 1.164(7)$, with $Q = 0.60$ and $\chi^2/dof = 0.84$, with $L_{\text{min}} = 12$, for the Swendsen-Wang cluster, and $z = 2.158(28)$ with $Q = 0.37$, $\chi^2/dof = 1.08$, and $L\text{min} = 24$ for the Metropolis. Although these values depend on the L_{min} chosen, varying it does not change the results, at least for the cases where the quality of the fitting process is acceptable. Including corrections, the best estimate indicates $z = 1.143(14)$ for the Swendsen-Wang algorithm, with a fair quality of fit $Q = 0.86$ and $\chi^2/dof = 0.52$, with $L_{\text{min}} = 24$. For the Metropolis scheme, $z = 2.179(42)$, with $Q = 0.43$ and $\chi^2/dof = 1.01$, with $L_{\text{min}} = 15$. Again, variations of L_{min} do not change the result significantly, at least for the cases were Q and χ^2/dof are acceptable. The similarity of the results and the large error bars in the correction terms for the cluster, as well as the relatively worse quality of fit, indicate that corrections do not play a large role in the spin-1/2 cluster case, at least for the precision of the current simulations. Appendix B.1.1 has a detailed breakdown of all the fits performed.

On a similar note, the more recent method of reference [169] gave estimates on the time τ_x, for various values of x, for the Swendsen-Wang algorithm, as shown in the upper panel of Fig. 3.7. Both panels are plotted in full analogy to Fig. 3.6. Notice how smaller τ_x is compared to τ_{int} (of Fig. 3.6) for the cases of x considered. Results for z versus L_{min} are shown in the lower panel of Fig. 3.7. Another change that comes with x is the accuracy of the estimation. This is due to the need to calculate $A(k)/A(0)$ for larger values of k, when x is increased. The values of z for the cluster method for different x, using the best fit in each case, are:

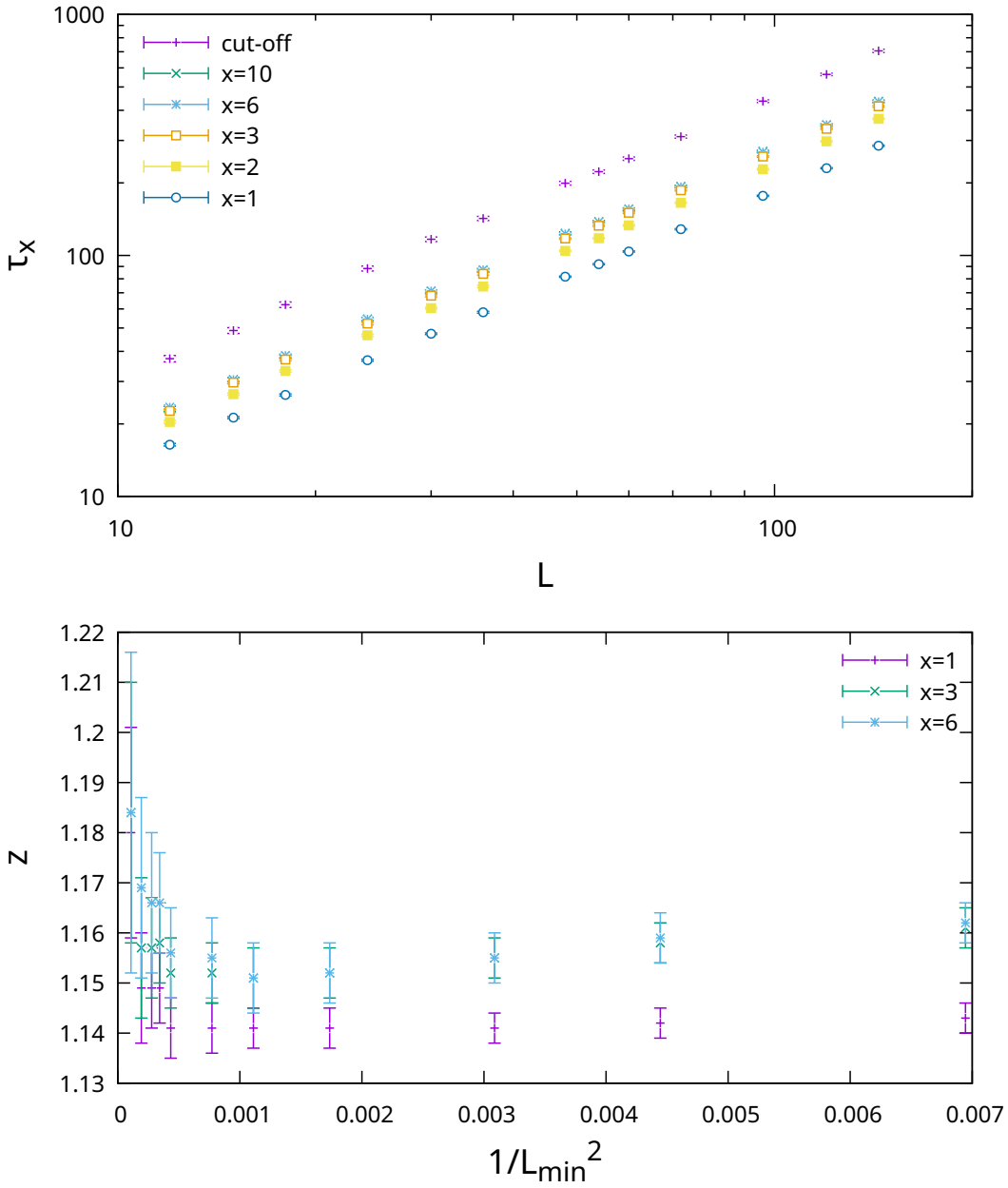

FIGURE 3.7: **Upper panel**: Autocorrelation time τ_x from solving Eq. (3.9), for the spin-1/2 Baxter-Wu, using various values of x. Note how smaller τ_x is compared to τ_{int} from Fig. 3.6. **Lower panel**: The dynamical critical exponent z, following fits of the form Eq. (3.6) vs the minimum length of the fit. Only some x values are shown, to make to plot more legible.

(i) $x = 1$, $z = 1.149(8)$, with $Q = 0.39$, $\chi^2/dof = 1.00$, and $L_{\text{min}} = 60$.
(ii) $x = 2$, $z = 1.155(3)$, with $Q = 0.47$, $\chi^2/dof = 0.97$, and $L_{\text{min}} = 15$.
(iii) $x = 3$, $z = 1.161(4)$, with $Q = 0.39$, $\chi^2/dof = 1.06$, and $L_{\text{min}} = 12$.

(iv) $x = 6, z = 1.159(5)$, with $Q = 0.48$, $\chi^2/dof = 0.95$, and $L_{\min} = 15$.
(v) $x = 10, z = 1.167(6)$, with $Q = 0.50$, $\chi^2/dof = 0.93$, and $L_{\min} = 12$.

These values are compatible with the result for the z estimations from τ_{int}, without errors and with each other. Since corrections seem to not play a large part in the cluster case for the spin-1/2 model, as a quoted end result the value $z = 1.164(7)$ is offered, which arose from the better-established in the literature τ_{int} fits. For the single-spin-flip algorithm, corrections seem to improve the results, although marginally. Additionally, the fits including and not-including corrections are very similar. In the end, the value $z = 2.18(4)$ is given for the Metropolis.

The above values are a bit smaller that the result given by Novotny and Evertz [136], where $z = 1.37(10)$, and Velonakis and Martinos [170], with $z = 1.272(3)$, both using the Wolff cluster. This discrepancy can possibly be attributed to the use of larger system sizes by the current study, reaching 144×144, compared to 96×96 in reference [136], and 102×105 in [170]. Nevertheless, it is evident that the cluster works better than a single-spin-flip algorithm. Specifically, previous studies have put the value of z for the latter algorithms in the range from $2.10(10)$ [136] to $2.30(11)$ [170], compatible with the value found in the current work , which is around the equivalent estimation for the Metropolis on the Ising model, $z = 2.1667(5)$ [113]. However, the gain is not as large as one might anticipate from a cluster algorithm.

3.4.2 The spin-1 Baxter-Wu model: a dynamical scaling study for a hybrid update

In full analogy to the previous section, the same study is carried out for the spin-1 Baxter-Wu model in a crystal field of strength Δ (see Eq. (3.3)), for various points along the second-order phase transition line. Specifically, the critical points considered were $(\Delta = -10, T = 2.2578)$, $(\Delta = -1, T = 1.8503)$, $(\Delta = 0, T = 1.6606)$, $(\Delta = 0.5, T = 1.5301)$ (see Fig. 3.2 and references [164, 165]). Additionally, the multicritical point estimate with the smallest value of Δ in the literature was also considered, with $(\Delta = 0.8902, T = 1.4)$ [160]. For $\Delta = -10$ and -1, due to the large separation from the multicritical point, linear system sizes $L = \{12, 15, 18, 24, 30, 36, 48, 60, 72, 96, 120, 144\}$ were used. Near the multicritical point, larger system sizes were also simulated, with the addition of $L = 192$ and 240, in order to reduce finite-size effects. The algorithm followed is the same as the one described Section 3.2.2. Each iteration consists of one heat-bath sweep and one Swendsen-Wang iteration. Some tests were also performed implementing the heat-bath algorithm, for $\Delta = -1$ and L up to 120, just to have a sense of comparison with the hybrid algorithm and the Metropolis algorithm in the spin-1/2 case. The length of each simulation follows the same scheme as in the spin-1/2 case and again periodic boundary conditions were used. Least square fits were considered fair when $0.10 \leq Q \leq 0.90$ and χ^2/dof should be near the value of 1.

Figure 3.8 shows estimates of the integrated autocorrelation time (upper panel) and for the dynamical critical exponents (lower panel) for various values of the crystal-field strength Δ.

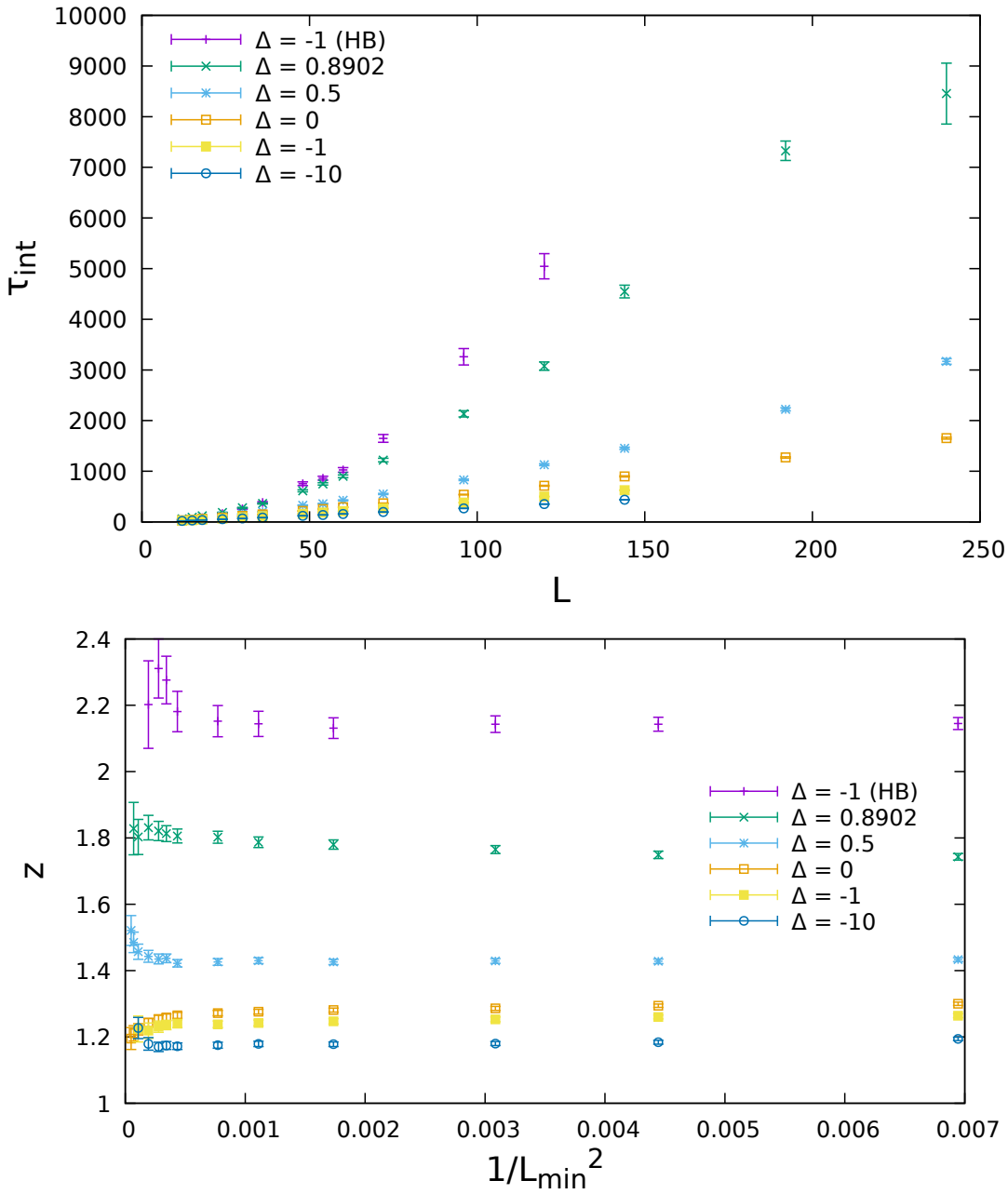

FIGURE 3.8: **Upper Panel**: Integrated autocorrelation time for various values of Δ, along the critical transition line of the spin-1 Baxter-Wu model, using the hybrid algorithm. One set of results concerns simulations at the critical point $\Delta = -1$, using the heat-bath algorithm, indicated by "(HB)" in the legend. As the multicritical point is approached, the integrated autocorrelation time increases for the hybrid algorithm. Additionally, the largest times belong to the heat-bath method. **Lower Panel**: Dynamical critical exponent z for the spin-1 Baxter-Wu model, following linear fits of the form of Eq. (3.6) for the integrated autocorrelation time τ_{int}, and a cut-off of $k_{\text{max}} > 6\tau_{\text{int}}$. Different values of L_{min} are considered in the fits. This figure is the equivalent of the lower panel of Fig. 3.6 for the spin-1/2 case. For the hybrid algorithm different regimes appear as Δ changes sign.

These estimates were calculated by fits according to Eq. (3.6) of the results for the integrated autocorrelation time, τ_{int}, as a function of the linear system size, L. Thus, corrections were not included in the figure. In the upper panel, two heat-bath iterations were taken as a time step, to make time comparisons with the integrated autocorrelation times from the hybrid simulations fairer. More on that subject will be discussed in the following subsection. The heat-bath simulation at $\Delta = -1$ is indicated by "(HB)" in the legend of the figures. Since all other simulation were of the hybrid update, they do not require special indication.

In the lower panel, each point was produced by modifying the L_{min} from where the fit starts, in essence removing each time the smaller system sizes, which makes it possible to see if finite-size effects were strong. The results indicate a value around $z \approx 1.2$ for $\Delta \leq 0$, while for values $\Delta > 0$, z appears to increase. Specifically, the best linear fits (without corrections) indicate the following:
(i) At $\Delta = -10$, $z = 1.172(10)$, with $Q = 0.47$ for $\chi^2/dof = 0.91$, and $L_{\text{min}} = 48$.
(ii) At $\Delta = -1$, $z = 1.260(6)$, with $Q = 0.33$ and $\chi^2/dof = 1.14$, for $L_{\text{min}} = 15$.
(iii) At $\Delta = 0$, $z = 1.276(7)$, with $Q = 0.33$ and $\chi^2/dof = 1.14$, for $L_{\text{min}} = 30$.
(iv) At $\Delta = 0.5$, $z = 1.435(15)$, with $Q = 0.41$ and $\chi^2/dof = 1.01$, for $L_{\text{min}} = 60$.
(v) At $\Delta = 0.8902$, $z = 1.786(35)$, with $Q = 0.38$ and $\chi^2/dof = 1.05$, for $L_{\text{min}} = 72$.
(vi) The value of $z = 2.31(9)$, with $Q = 0.37$ and $\chi^2/dof = 0.99$, for $L_{\text{min}} = 60$ is recovered for the single-spin-flip heat-bath algorithm at $\Delta = -1$. However, for $L_{\text{min}} = 12$, then $z = 2.145(18)$ with $Q = 0.42$ and $\chi^2/dof = 1.03$.
It should be noted that varying L_{min}, at least for the hybrid case, does not change the results. All these fits are presented exhaustively in Appendix B. Additionally, when including corrections, the following results are found (also see Appendix B for a more thorough breakdown):
(i) At $\Delta = -10$, $z = 1.202(40)$, with $Q = 0.40$ and $\chi^2/dof = 1.00$, for $L_{\text{min}} = 48$.
(ii) At $\Delta = -1$, $z = 1.234(27)$, with $Q = 0.45$ and $\chi^2/dof = 0.95$, for $L_{\text{min}} = 36$.
(iii) At $\Delta = 0$, $z = 1.262(9)$, with $Q = 0.42$ and $\chi^2/dof = 1.02$, for $L_{\text{min}} = 18$.
(iv) At $\Delta = 0.5$, $z = 1.494(33)$, with $Q = 0.37$ and $\chi^2/dof = 1.09$, for $L_{\text{min}} = 48$.
(v) At $\Delta = 0.8902$, $z = 1.837(79)$, with $Q = 0.46$ and $\chi^2/dof = 0.90$, for $L_{\text{min}} = 54$, although here the results for $L = 240$ were not included.
(vi) For the heat-bath at $\Delta = -1$, $z = 2.140(38)$, with $Q = 0.31$ and $\chi^2/dof = 1.17$, for $L_{\text{min}} = 12$. These fits, for the single-flip case, do not show the large discrepancy as L_{min} changes, which was seen in the case where no corrections were used.

Notice that all results, including or excluding corrections, are in agreement with each other, almost always within error bars. This is arguably due to the small corrections-to-scaling exponent $\omega = 2$. This is also the reason why the lower panel of Fig. 3.8 is plotted against L_{min}^{-2}, showcasing that no corrections can be seen, except for the results at $\Delta = 0.5$ and the heat-bath case. In the former, it seems that the dynamical critical exponent might continue to increase and larger L are needed to give a good estimate. Also, the large error bars of the correction

coefficients might indicate that corrections are not necessary, at least for the current results' accuracy. For a detailed reporting see Appendix B.1.2.

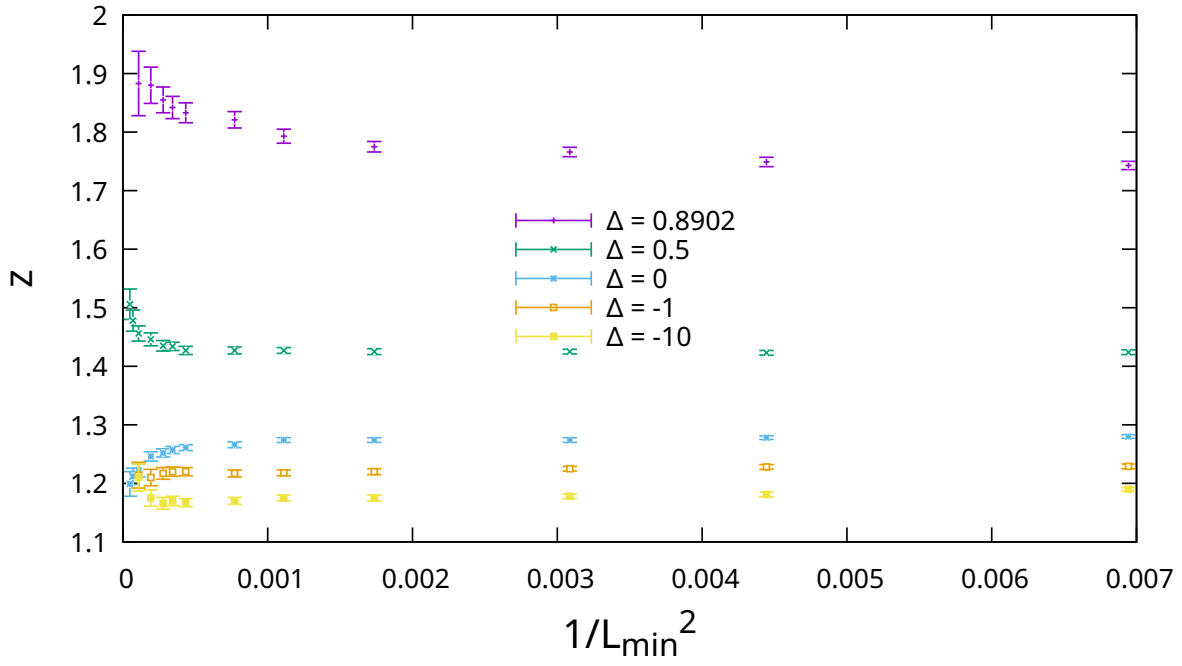

FIGURE 3.9: The dynamical critical exponent z for the spin-1 Baxter-Wu model, following the fits of the form Eq. (3.7) for the autocorrelation time τ_x. This figure is the equivalent of Fig. 3.7 of the spin-1/2 case. The results presented are for $x = 2$. Notice the similarity to Fig. 3.8, as well as the different regimes for positive and negative Δ. Other values of x tested showed similar results.

The method of solving Eq. (3.9) was also implemented. Specifically, after τ_x was calculated as described in Section 3.3, fits were performed using different smallest system sizes. See Fig. 3.9 for the case of $x = 2$. The results there agree with those of Fig. 3.8. Different values of x were also in agreement and so, to avoid unnecessary clutter in the figures, it was chosen not to show all of them. However, a breakdown of the results can be found in Appendix B.1.3.[3] After fits, not including corrections, the results for z were found to be the following:
(i) At $\Delta = -10$, $z = 1.155(3)$, with $Q = 0.24$ and $\chi^2/dof = 1.29$, for $L_{\min} = 24$.
(ii) At $\Delta = -1$, $z = 1.195(3)$, with $Q = 0.57$ and $\chi^2/dof = 0.84$, for $L_{\min} = 24$.
(iii) At $\Delta = 0$, $z = 1.229(8)$, with $Q = 0.36$ and $\chi^2/dof = 1.08$, for $L_{\min} = 96$.
(iv) At $\Delta = 0.5$, $z = 1.442(9)$, with $Q = 0.36$ and $\chi^2/dof = 1.06$, for $L_{\min} = 96$.
(v) At $\Delta = 0.8902$, $z = 1.826(11)$, with $Q = 0.40$ and $\chi^2/dof = 1.03$, for $L_{\min} = 48$.

Note the similarity with the results quoted above, but at the same time how consistently smaller the errors are. For all the above results $x = 1.5$ was used except for $\Delta = 0.8902$, where

[3]Note that the plot includes results only for the hybrid algorithm, which is the case of interest, and the more elaborate analysis of solving for Eq. (3.9) was not applied for the heat-bath data.

$x = 3$, which produced better fit qualities than smaller values of x tested. Moving on to the results from fits that include correction-to-scaling:
(i) At $\Delta = -10$, $z = 1.149(4)$, with $Q = 0.34$ and $\chi^2/dof = 1.12$, for $L_{\min} = 12$.
(ii) At $\Delta = -1$, $z = 1.187(5)$, with $Q = 0.47$ and $\chi^2/dof = 0.95$, for $L_{\min} = 18$.
(iii) At $\Delta = 0$, $z = 1.231(7)$, with $Q = 0.38$ and $\chi^2/dof = 1.06$, for $L_{\min} = 36$.
(iv) At $\Delta = 0.5$, $z = 1.460(15)$, with $Q = 0.41$ and $\chi^2/dof = 0.99$, for $L_{\min} = 60$.
(v) At $\Delta = 0.8902$, $z = 1.856(13)$, with $Q = 0.15$ and $\chi^2/dof = 1.51$, for $L_{\min} = 24$.

For the case of τ_x it seems that including corrections might be more important. Nevertheless, results are in good agreement with each other and show that there is an increase of z with Δ, which renders the algorithm less useful in the vicinity of the multicritical point.

As a last comment for all the above different fits, there is a case to be made that, for $\Delta \leq 0$, the dynamical exponents are very close to each other, and perhaps a joint fit could reveal that for small Δ only one regime for z exists. However, after performing the relevant tests, it was revealed that such a fit is not possible, with or without corrections. Thus, the current results are sensitive enough to spot the dependence of z on Δ.

Equivalent times

The previous section highlighted results for the dynamical scaling of a hybrid algorithm applied in the spin-1 Baxter-Wu model. Since in any actual application measurements are taken every few iterations, and since an iteration of the hybrid algorithm consists of one heat-bath sweep and a Swendsen-Wang cluster, it made sense to not take into account the fact that due to finite-size effects, the Swendsen-Wang cluster does not consistently perform the same number of steps on average for each system size.

Since the number of zero spins increases with Δ, the above analysis does not really use the same time units, and due to finite-size effects, even for the same Δ the time step was not consistent for different L. For the Swendsen-Wang algorithm, for different Δ and L, a different percentage of the total spins is flipped every time, due to the cluster disregarding the zeros. This means that one iteration of the hybrid algorithm is not equal to two lattice sweeps, as one might naively expect. Specifically, the heat-bath iteration performs one whole lattice sweep, updating $N = L \times L$ spins, while the cluster only updates E_Δ spins. Thus, a time step consists of $N + E_\Delta$, and not $2N$, spin updates. For that reason, even though the comparisons made in the previous section make sense from a programmer's point of view, physically they are not fair, since there is no consistency in the time units.

The upper panel of Fig. 3.10 shows how the density of the $\sigma = 0$ spins is affected with Δ; As expected, the number of zeros increases with increasing Δ. Additionally, the lower panel shows the average cluster size over the system size versus L for the values of Δ considered. There are two forces in play when growing a cluster in the spin-1 model: the increased number of zeros, begotten from large Δ-values, causes a cluster to have less room for growth. At the same time

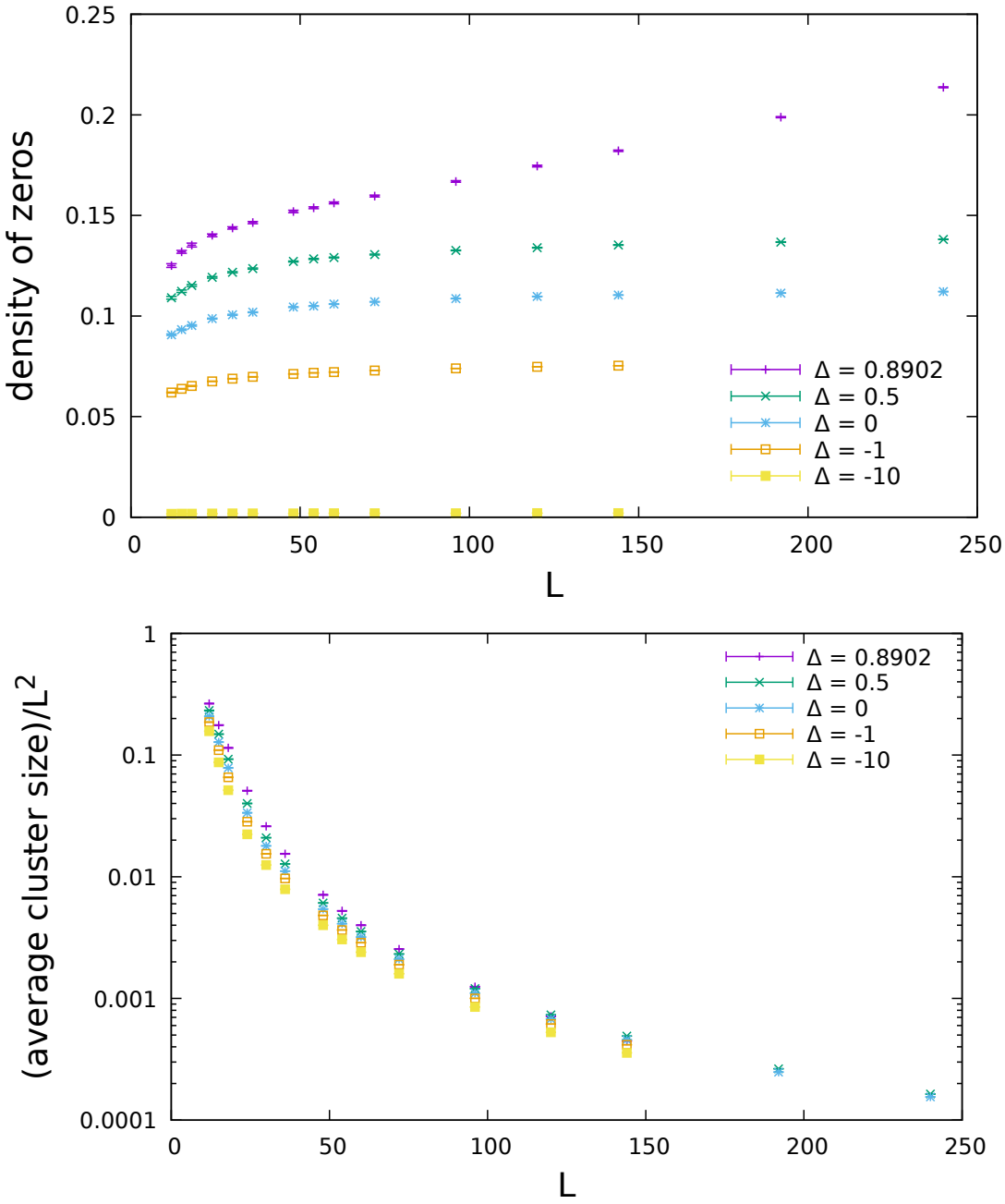

FIGURE 3.10: **Upper Panel**: Fraction of zero spins versus the linear system size for various values of the crystal-field strength Δ for the spin-1 Baxter-Wu model. **Lower Panel**: Similar as the upper panel, but now depicting the average cluster size over the system size, L^2.

however, lower values of Δ basically suppress the zero spins. This is strikingly evident from the results for $\Delta = -10$, shown in Fig. 3.10 (upper panel), where basically zero spins are non-existent. In this regime the model mimics its spin-1/2 counterpart. Then, due to the lack of zeros, a cluster is restricted to only include ferro- or antiferro-magnetic interactions and cannot be of mixed type. This also posses a restriction to the growth of a cluster, that might not be evident from a first read of the problem. The lower panel of Fig. 3.10 depicts this conflict that takes place when a cluster grows with the Novotny-Evertz proposed method. There, it can be seen that the average cluster size over the whole system size is not that different for the various Δ, especially as the system size increases.

To reconcile the different times of the hybrid and heat-bath implementations, the time for the heat-bath algorithm was contracted by a factor of two, defining a time step by two lattice sweeps, while a factor of $2N/(N + E_\Delta)$ was used for the Swendsen-Wang cluster, making for the same definition across the board. The upper panel of Fig. 3.11 shows how these changes of time scales affect the integrated autocorrelation time. To distinguish this "equivalent times" representation, the integrated autocorrelation time thus defined was denoted by τ^*_{int}. The result is that τ^*_{int} is a bit smaller than the τ_{int} measured in the upper panel of Fig. 3.8. The lower panel of Fig. 3.11 shows how this affects the exponent z. Since time units were change by a factor of $\sim (N + E_\Delta)^{-1}$, and E_Δ is affected by the size of the system, changes to z can be expected. Specifically, excluding corrections (see Appendix B.1.4):
(i) At $\Delta = -10$, $z = 1.172(10)$, with $Q = 0.47$ and $\chi^2/dof = 0.91$, for $L_{\text{min}} = 48$.
(ii) At $\Delta = -1$, $z = 1.172(6)$, with $Q = 0.36$ and $\chi^2/dof = 1.10$, for $L_{\text{min}} = 15$.
(iii) At $\Delta = 0$, $z = 1.241(13)$, with $Q = 0.34$ and $\chi^2/dof = 1.13$, for $L_{\text{min}} = 72$.
(iv) At $\Delta = 0.5$, $z = 1.431(15)$, with $Q = 0.40$ and $\chi^2/dof = 1.02$, for $L_{\text{min}} = 60$.
(v) At $\Delta = 0.8902$, $z = 1.801(29)$, with $Q = 0.46$ and $\chi^2/dof = 0.90$, for $L_{\text{min}} = 60$.

Including one correction term:
(i) At $\Delta = -10$, $z = 1.201(40)$, with $Q = 0.40$ and $\chi^2/dof = 1.00$, for $L_{\text{min}} = 48$.
(ii) At $\Delta = -1$, $z = 1.232(27)$, with $Q = 0.45$ and $\chi^2/dof = 0.94$, for $L_{\text{min}} = 36$.
(iii) At $\Delta = 0$, $z = 1.260(9)$, with $Q = 0.44$ and $\chi^2/dof = 1.00$, for $L_{\text{min}} = 18$.
(iv) At $\Delta = 0.5$, $z = 1.492(33)$, with $Q = 0.36$ and $\chi^2/dof = 1.09$, for $L_{\text{min}} = 48$.
(v) At $\Delta = 0.8902$, $z = 1.806(78)$, with $Q = 0.45$ and $\chi^2/dof = 0.93$, for $L_{\text{min}} = 54$.

Again, the similarity of the results in the presence or absence of a correction term is robust. The values of z thus calculated do not differ much from the previous estimates, and are actually equivalent with them within errors. Note the dependence of z on Δ, with a large increase appearing in the regime $\Delta > 0.5$, i.e. near the multicritical point.

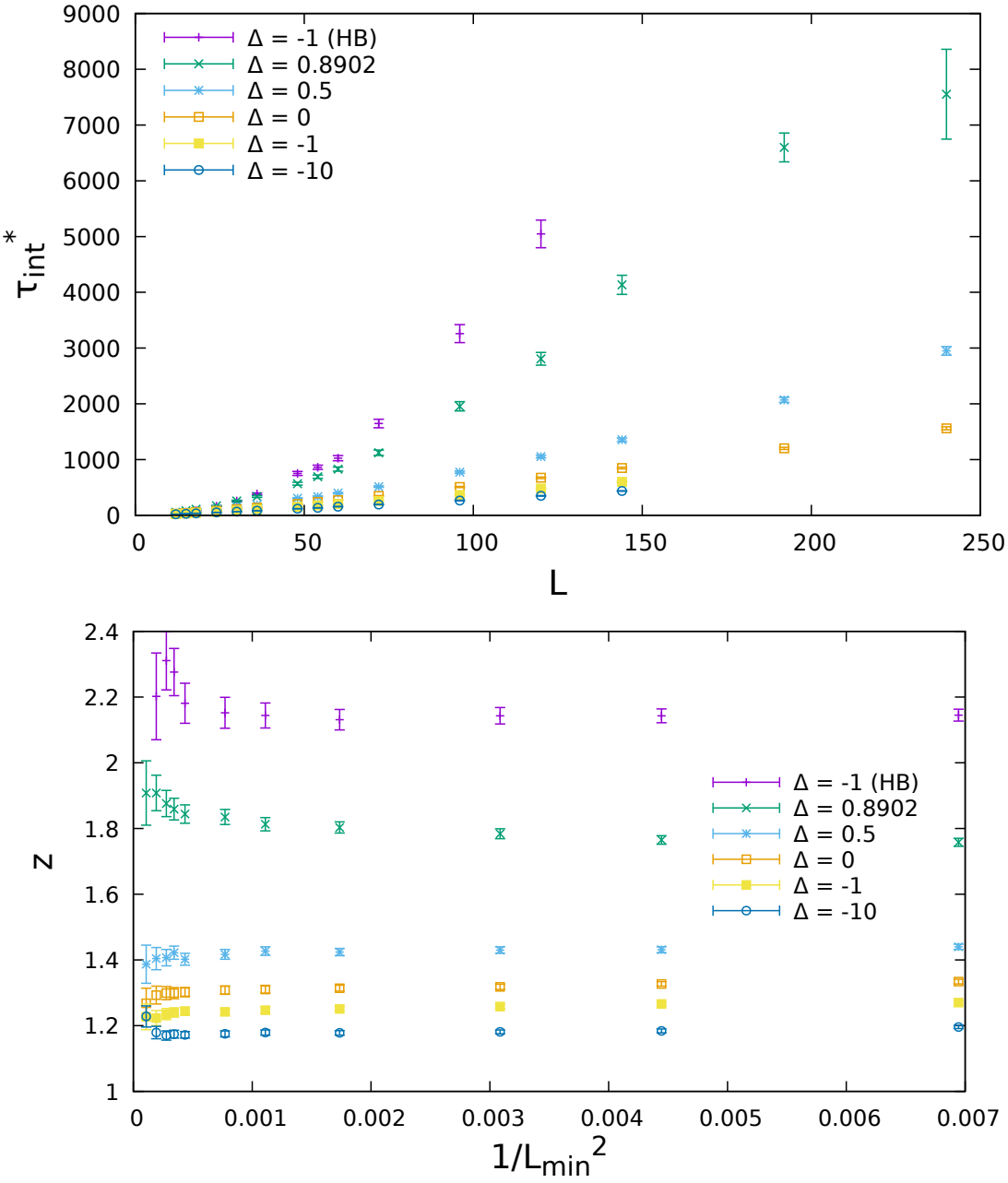

FIGURE 3.11: **Upper Panel**: Integrated autocorrelation times of the spin-1 Baxter-Wu model under different values of Δ and for various system sizes. Here equivalent times are taken into account for each simulation, equivalent to two lattice sweeps, indicated by τ^*_{int}. **Lower Panel**: Dynamical critical exponent z, obtained from fits performed on the data shown in the upper panel (with no correction terms). Each time the minimum size from where the fit starts is varied. If corrections exist, they are relatively small, or they cannot be picked up by the current results.

3.5 Discussion and Outlook

In this section, the dynamical exponent z of a Swendsen-Wang cluster algorithm for Baxter-Wu models was calculated, alongside some estimations of z for single-spin-flip algorithms. Specifically, for the spin-1/2 case, the cluster performed better than Metropolis, as was already expected from past works on the model [136, 170]. The gain in z is however relatively smaller from what one might anticipate looking at similar results for the Ising model (Section 2.6). The reason behind this relatively large value of z is ingrained in the construction of the cluster, where one third of the spins are frozen and not taken into account. On the contrary, the frozen spins create effective interactions, which might result in a zero effective-bond strength, hindering the cluster growth.

Appendix B contains an exhaustive list of all the results from fits on the integrated autocorrelation time τ_{int}, and autocorrelation time τ_x, as well as the equivalent time τ^*_{int} considered. In this Chapter only the best fits were quoted, however, all the results with an acceptable fit quality agreed with each other.

A generalisation that immediately follows is applying a hybrid scheme on the spin-1 Baxter-Wu model with a crystal field. In this model there are difficulties in characterising the universality class in the vicinity of the multicritical point (see [164] and Chapter 4), whose location is strongly disputed (see Fig. 3.2). The idea behind this Chapter was that a cluster algorithm might come a long way in resolving these issues. After showing, in Section 3.2, that such an algorithm can be used, the dynamical critical exponent z was studied along the line of continuous transitions of the model. A summary of results for the spin-1 case can be found in Appendix B, for z derived from τ_{int}, τ_x, and the more physical τ^*_{int}, which makes sure that the time units are equivalent for all simulations, across all Δ and L simulated.

The results showed that the gain experienced in the spin-1/2 counterpart of the model persists, but only for values of Δ that are non-positive. For $\Delta > 0$, the gain compared to a single-spin-flip algorithm is minimal, especially approaching the multicritical point. Certainly, further scrutiny is required to be able to express with certainty the value of the exponent z, but the current results indicate that z is an increasing function of Δ, with a large increase as Δ passes to positive values. Also, additional results are required for $\Delta \geq 0.8902 \approx \Delta_{\text{pp}}$, to see if the hybrid algorithm approaches asymptotically the scaling of the heat bath – although such an endeavour requires better knowledge of the location of the multicritical point. Certainly, a thorough study of the percolation properties of the cluster algorithm is missing, following for example the work of Picco et al. [172]. All that said, since the implementation of the cluster is a laborious task, and the current results show quite clearly that in the vicinity of the multicritical point even the hybrid algorithm struggles, it is safe to assume that this hybrid scheme will not be useful in locating and studying the multicritical point. Perhaps other cluster implementations can be thought of, where one does not need to freeze one of the sublattices each time, for example by

starting with two neighbouring seed spins and each time completing a triangle when a spin is added to the cluster.

It would be interesting to understand this behaviour of z and how the increased number of zero spins or the geometry of the interactions interfere with the dynamical scaling. The much simpler Blume-Capel model, which possesses two-spin interactions, and qualitatively has an identical phase diagram to the spin-1 Baxter-Wu model (Fig. 3.2), might be a good starting point to understand if this is something shared among models that implement dilution through the inclusion of a quadratic term, or if it is because of the more complicated three-spin interactions that appear in the Baxter-Wu case.

3.5.1 Some preliminary results for random Ising models in two dimensions

The method of calculating the dynamical critical exponent from the characteristic times τ_x could be applied to different models. Recently, a lot of interest has been garnered by the dynamical behaviour of Ising models: from the pure system in two and three dimensions studied with Glauber dynamics at equilibrium [173], to using the improved Blume-Capel model to study the exponent z of the three-dimensional Ising universality class [168], as well as the bond-diluted Ising model [174].

Here, some preliminary results are gathered, regarding the dynamical exponent of two-dimensional Ising models, simulated using the Metropolis algorithm. Specifically, the Ising model is studied in its pure, bond-diluted, and random-bond form. Firstly, the pure model is defined by

$$\mathcal{H}_{\text{pure}} = -J \sum_{\langle ij \rangle} \sigma_i \sigma_j, \tag{3.10}$$

where J is the exchange interaction strength, set to one in what follows. The bond-diluted Ising is describe by the same nearest-neighbour two-spin interactions, only some bonds can be absent. In that sense, the bond strength is generalised to

$$\mathcal{H} = -\sum_{\langle ij \rangle} J_{ij} \sigma_i \sigma_j, \tag{3.11}$$

where J_{ij} is able to take the value 1, as well as 0, drawn from a bimodal distributions, defining

$$P(J_{ij}) = p\delta(J_{ij} - 1) + (1 - p)\delta(J_{ij}). \tag{3.12}$$

Implying that a bond, J_{ij}, takes the value 1 with probability p, while a bond is broken, $J_{ij} = 0$, with probability $1 - p$. The percolation threshold of the model is $p_c = 0.5$ [175, 176].

Lastly, the random-bond model will also be considered briefly, defined by the Hamiltonian of Eq. (3.11), but this time the interaction strengths are not ones and zeros. For the current

purposes, the simple case where J_{ij} can take the values J_1 and J_2 will be considered, keeping $J_1 + J_2 = 2$, defining the distribution

$$P(J_{ij}) = \frac{1}{2}\delta(J_{ij} - J_1) + \frac{1}{2}\delta(J_{ij} - J2), \tag{3.13}$$

with $J_1, J_2 > 0$. The relative strength r is also defined as

$$r = J_1/J_2. \tag{3.14}$$

If $r = 1$ the pure model is recovered, while if $r = 0$ the bond-diluted model with $p = 0.5$ [see Eq. (3.13)].

To estimate the dynamical critical exponents of these models Metropolis simulations were performed. Here, preliminary results are shown, which however still show why these calculations have gathered so much interest in recent years. Specifically, for the pure case, results regarding the integrated autocorrelation time, τ_{int}, from one realisation were considered. For the bond-diluted system however, one thousand realisations of disorder were simulated for each system size, the average $I(t)$, Eq. (3.8), curve was estimated by averaging the individual curves from the realisations, and subsequently, τ_{int} was estimated by this one curve. For the random-bond case, the same protocol was followed, but with five hundred disorder realisation simulated for each system size. The smallest system size of 10×10 was simulated for 10^5 equilibration sweeps, followed by an additional 10^6 sweeps where data were gathered. Simulation times were increased by a factor $L^2/10^2$, depending on the system size. For the pure case systems of linear size $L \in \{10, 15, 20, 25, 30, 35, 40, 45, 50, 55, 60, 70, 80, 90, 100, 110, 120\}$ were simulated. The same goes for the random-bond case, with simulations taking place at $r = 1/4$, making $J_1 = 0.4$ and $J_2 = 1.6$. For the bond-diluted with $p = 0.8$, simulations included the sizes $L = \{140, 160, 180, 200\}$, while for $p = 0.8$ simulations were halted at $L = 100$.

Figure 3.12 shows preliminary results regarding the dynamical critical exponents from all these models. Specifically, the slopes between pairs of points $(L, \ln[\tau_{\text{int}}(L)])$, $(L', \ln[\tau_{\text{int}}(L')])$, with $L' = 2L$, were calculated each time, defining an effective exponent z_{eff} as [169]

$$z_{\text{eff}}(L) = \frac{\ln[\tau_{\text{int}}(2L)/\tau_{\text{int}}(L)]}{\ln 2}. \tag{3.15}$$

The scaling of z_{eff} follows the form [169]

$$z_{\text{eff}} = z + cL^{-\omega}, \tag{3.16}$$

z being the dynamical critical exponent, and only keeping corrections-to-scaling up to first order ($\omega = 1.75$ [177]). Fitting the results of Fig. 3.12 to Eq. (3.16) gives in the following:
(i) Pure model: $z = 2.162(12)$, with $Q = 0.44$ and $\chi^2/dof = 0.98$, and $L_{\text{min}} = 20$.
(ii) Bond diluted $p = 0.8$: $z = 2.517(4)$, with $Q = 0.54$ and $\chi^2/dof = 0.88$, and $L_{\text{min}} = 15$.

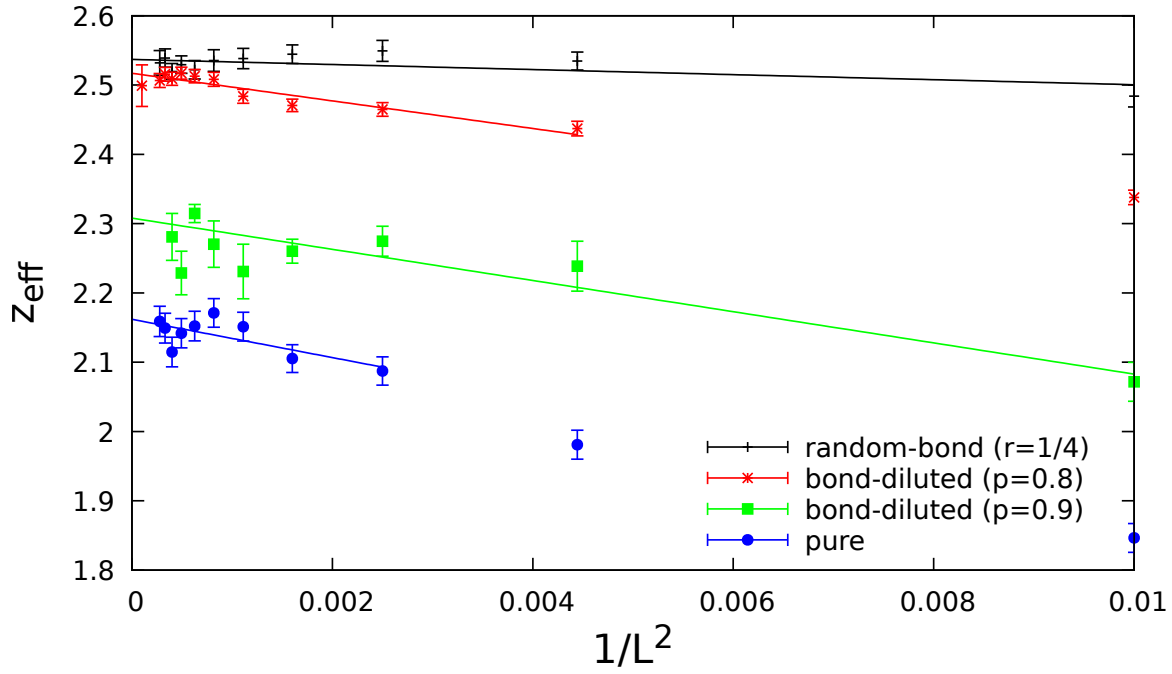

FIGURE 3.12: Effective dynamical critical exponents, calculated from the slopes of the integrated autocorrelation times computed in pairs of system sizes $(L, 2L)$.

(iii) Bond diluted $p = 0.9$: $z = 2.308(10)$, with $Q = 0.10$ and $\chi^2/dof = 1.72$, and $L_{\min} = 10$.
(iv) Random bond $r = 1/4$: $z = 2.537(5)$, with $Q = 0.48$ and $\chi^2/dof = 0.95$, and $L_{\min} = 10$.

The above preliminary results indicate that z changes as the disorder strength of the model is increased, with all the results for different types of disorder and strengths indicating a different value for the exponent z. Further simulations are required to elaborate this dependence, especially as one approaches smaller values of p or r for the bond-diluted and random-bond version of the model respectively.

Chapter 4

Universality of the Dilute Baxter-Wu Model

This chapter contains work that was published in [163–165].

This Chapter studies the question of universality in the two-dimensional spin-1 Baxter-Wu model in the presence of a crystal field Δ. Complementary results are provided by employing extensive numerical simulations of two types: (i) Wang-Landau sampling at fixed values of Δ and (ii) a parallelised variant of the multicanonical approach performed at constant temperature T. A detailed finite-size scaling analysis in the regime of second-order phase transitions in the (Δ, T) phase diagram indicates that the transition belongs to the universality class of the spin-1/2 Baxter-Wu model (and thus of the 4-state Potts model). This work resolves previous controversies in regards to the nature of the transition, attributing them to strong finite-size effects upon approaching the pentacritical point of the model.

The remainder of the Chapter is structured as follows: Section 4.1 introduces the model that will be studied and discusses the issue of its universality at length. In Section 4.2 the Wang-Landau and parallel multicanonical simulation methods that were used to study the problem are outlined, and the observables investigated are introduced. The numerical results and the relevant finite-size scaling analysis are presented in Section 4.3. In this Section, universal probability distributions are also produced. Finally, in Section 4.4 all the findings are summarised and an outlook is provided.

4.1 Introduction

As discussed in Chapter 3, the Baxter-Wu model is defined on a triangular lattice by the Hamiltonian

$$\mathcal{H}_{\mathrm{BW}} = -J \sum_{\langle xyz \rangle} \sigma_x \sigma_y \sigma_z, \tag{4.1}$$

with $J > 0$ positive, and the sum extending over all elementary triangles of the N-site lattice (Fig. 3.1). The nearest-neighbour interactions are between the three spins residing in an elementary triangle. Each of these spins belongs to one of the three different sublattices composing the whole lattice. The spin values can be $\sigma_x = \pm 1$. The analytical solution of the model provided the exponents $\alpha = 2/3$, $\nu = 2/3$, and $\gamma = 7/6$ [34, 139]. Furthermore, the central charge of the conformal field theory has been calculated to be $c = 1$ [140, 141], and the correction-to-scaling exponent $\omega = 2$ [140, 141]. Additional aspects of the spin-1/2 model have been considered recently, from short-time dynamics [178], Monte Carlo studies of critical amplitude ratios [179], longitudinal [180], and transverse [181] magnetic fields.

The spin-1 Baxter-Wu model, where $\sigma_x = \{-1, 0, 1\}$, in a crystal field Δ is a generalisation of Eq. (4.1), defined by the Hamiltonian

$$\mathcal{H} = -J \sum_{\langle xyz \rangle} \sigma_x \sigma_y \sigma_z + \Delta \sum_x \sigma_x^2 = E_J + \Delta E_\Delta. \tag{4.2}$$

Here, the spins can have the additional value of zero. The energy is broken into two part, one having to do with the spin interactions, E_J, and another with the crystal field, E_Δ. Δ can be seen as controlling the density of the zero spins, with the second term of the Hamiltonian giving rise to the fugacity in a grand canonical ensemble setting. In what follows, as usual, reduced units will be used, where $J = 1$ as well as $k_B = 1$. No exact solution exists for this case, but note that for $\Delta \to -\infty$ the pure spin-1/2 Baxter-Wu model is recovered.

As was briefly mentioned in Chapter 3, the phase diagram of the model is expected to look like the one depicted in Fig. 4.1. Reference [157] agrees with this picture, by making an analogy with dilute Potts models. However, reference [158], conjectured, using a finite-size scaling method, that a second-order transition occurs only at the limit $\Delta \to -\infty$. Contemporary works have favoured the existence of a multicritical point at a finite Δ [159, 162]. However, the location of the pentacritical point is still a bone of contention (see Fig. 4.1).

Somewhat surprisingly, the question with regards to the universality of the spin-1 Baxter-Wu model is still open. Results from reference [159], via renormalisation group, conventional finite-size scaling, and conformal invariance techniques, seem to indicate that the critical exponents vary continuously with Δ, all along the continuous transition line. This is in stark contrast to the expected behaviour of the 4-state Potts model. Qualitatively, in reference [182], using using importance sampling Monte-Carlo simulations for $\Delta = 0$, where no crystal-field energy exists, a similar conclusion was drawn, since the critical exponents were calculated to be $\nu = 0.617(3)$, $\alpha = 0.692(6)$, and $\gamma = 1.13(1)$. Additional Monte Carlo studies at $\Delta = -1$ and 1 further corroborated this picture [183]. Conversely, the work of Dias et al. [160], suggested that along the critical line, the conformal anomaly c and the exponents ν and η should coincide with those of the pure spin-1/2 Baxter-Wu and the 4-state Potts models. However, some variation was observed, possibly attributed to strong corrections-to-scaling. Finally, the

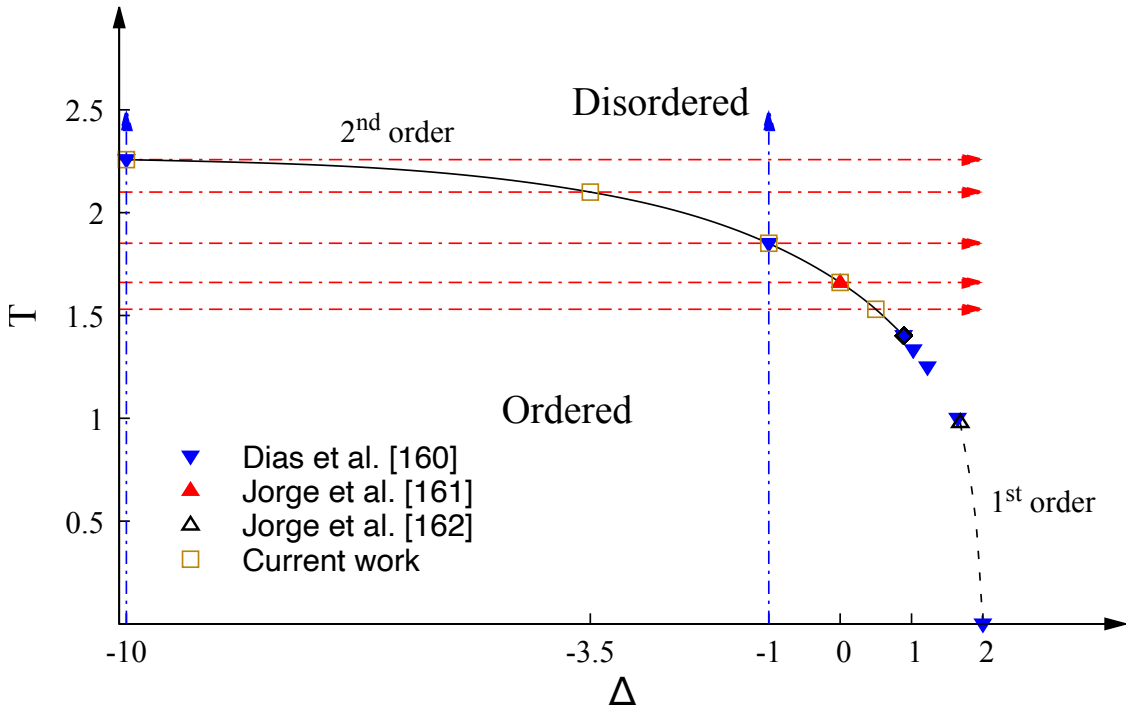

FIGURE 4.1: The phase diagram of the two-dimensional spin-1 Baxter-Wu model in a crystal field of strength Δ. The black dotted and continuous lines correspond to discontinuous and continuous transitions. The black rhombus marks an estimate of the pentacritical point $(\Delta_{pp}, T_{pp}) \approx (0.8902, 1.4)$ [160], while the black triangle indicates another, $(\Delta_{pp}, T_{pp}) \approx (0.98030, 1.68288)$ [162]. A small part of the transition line is left undrawn, due to the lack of agreement in regards to the location of the pentacritical point. Several transition points are given, including those obtained in the current thesis. Blue and red dotted arrows indicate the numerical approaches used in the present work, namely Wang-Landau and multicanonical methods at fixed values of $\Delta = \{-10, -1\}$ and $T = \{2.2578,\ 2.1,\ 1.8503,\ 1.6605,\ 1.5301\}$, respectively.

recent study of Jorge et al. [161], performing Wang-Landau sampling at $\Delta = 0$, showed that the model exhibits an indeterminacy in regards to the order of phase transition; Their analysis was consistent for both continuous and discontinuous types of transitions. For the former case, the values $\nu = 0.6438(10)$ and $\gamma = 1.1521(13)$ were computed.

In the present work, a resolution of these controversies is provided, by the use of extensive numerical simulations (see Section 4.2 below). The critical properties of the spin-1 Baxter-Wu model in a crystal-field were scrutinised, covering a large extent of the second-order transition line. Particularly, in order to identify the correct scaling behaviour, taking proper account of the role of finite-size effects, Wang-Landau simulations are performed at two fixed values of the crystal field, $\Delta = -10$, far away from the multicritical point, and $\Delta = -1$, in its vicinity. The blue vertical dashed arrows in the phase diagram of Fig. 4.1 indicate these simulations. Additional multicanonical simulations at the temperatures $T = \{2.2578, 2.1, 1.8503, 1.6603, 1.5301\}$

were performed to complement the Wang-Landau ones. Particularly, these cross the phase boundary at $\Delta \approx \{-10, -3.5, -1, 0, 0.5\}$, respectively. The multicanonical simulations are indicated by the red horizontal arrows in Fig. 4.1.

4.2 Numerical Methods and Observables

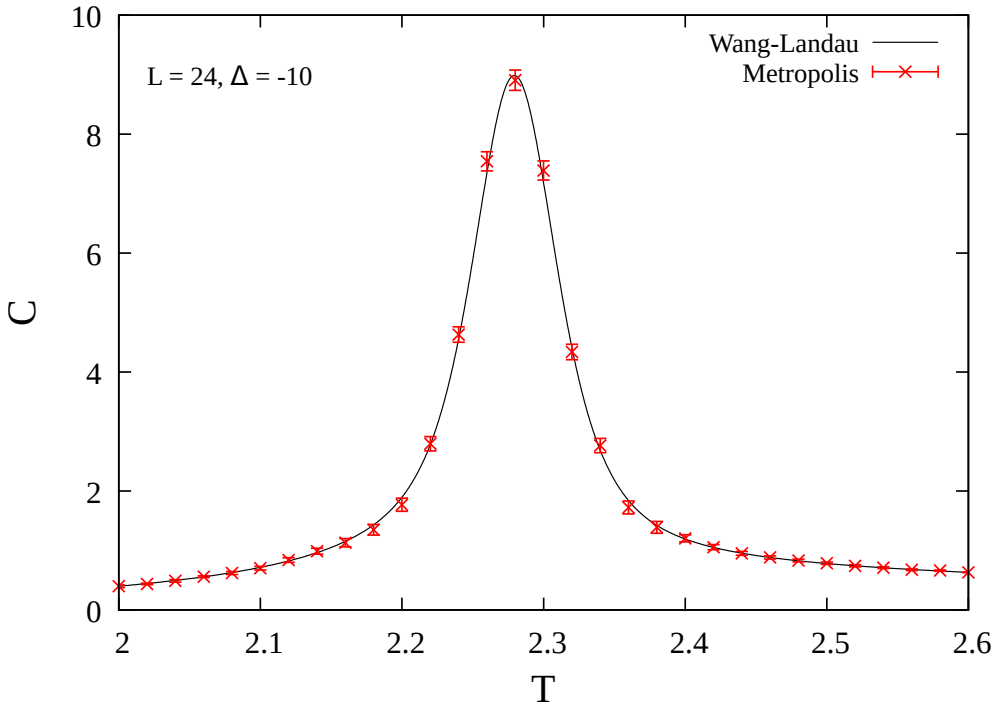

FIGURE 4.2: Comparative curves of the specific-heat of the spin-1 Baxter-Wu model, at $\Delta = -10$, for a simulations of a system with linear size $L = 24$. Results were obtained via Wang-Landau and Metropolis simulations.

Two simulations methods were used in a complementary strategy: the Wang-Landau and multicanonical algorithms. This combined scheme allowed the crossing of the phase boundary in two perpendicular directions (see Fig. 4.1) and to probe the critical properties of the model effectively. These two methods are described below, along with the observables that were measured. For a more thorough description of both the reader is referred to Chapter 2.

4.2.1 Wang-Landau simulations

The Wang-Landau simulation [92, 93] performs a random walk in the energy space, with proposed spin configurations being accepted with a probability that is proportional to the reciprocal density of states, $1/\Omega(E)$. The estimate of $\Omega(E)$, for the current energy of the system, is each time modified by the rule $\Omega(E) \to f \cdot \Omega(E)$, where f is a modification factor. Additionally,

an energy histogram is accumulated during the simulation. When it is flat enough, the factor is adjusted by $f_{j+1} = \sqrt{f_j}$, where the index indicates the iteration number. In the beginning, $f_1 = e$. For the present study, a flatness of 90% was used to indicate if the histogram has become flat, and the final iteration was chosen to be $j_{\text{final}} = 24$. Lastly, to increase statistical accuracy, averaging over several independent samples was performed, typically ~ 32.

A single-range implementation of the algorithm was utilised, instead of the more efficient multi-range approach, which splits the energy space in sub-intervals whose estimates for $\Omega(E)$ can be joined in the end. In general, the multi-range implementation is a necessity for very large lattices and can produce high accuracy results [92, 93]. However, the many subtleties in terms of boundary effects [103], especially where first-order transition characteristics appear [107], justify the current choice. The simulations were facilitated by the use of restricted energy spaces, a practice that has been quite successful in many cases, including pure and disordered models [104–108]. Care should be taken however, when estimating these ranges from a chosen pseudo-critical temperature, since one needs to account for the shift behaviour of other important pseudo-critical temperatures, extending the subspace appropriately both from low- and high-energy sides, so as to achieve an accurate estimation of all finite-size anomalies. See Section 2.5 for more details. Preliminary tests, for comparative reasons, were performed at the initial stages of this work to provide a benchmark, using the Metropolis algorithm [26, 78], see Fig. 4.2.

For the present purposes, instead of employing the final estimate of the density of states to compute thermodynamic averages, $\Omega(E)$ was used in a final production run as the weight function. Sampled observables included the energy E, and the order parameter, m, estimated from [161, 182, 183]

$$m = \sqrt{\frac{m_{\text{A}}^2 + m_{\text{B}}^2 + m_{\text{C}}^2}{3}}, \tag{4.3}$$

where $m_{\text{A}}, m_{\text{B}}$, and m_{C} are the respective sublattice magnetisations per site. Additionally, calculations included the specific heat

$$C = \left[\langle E^2 \rangle - \langle E \rangle^2\right] / (NT^2), \tag{4.4}$$

and the magnetic susceptibility

$$\chi = N \left[\langle m^2 \rangle - \langle m \rangle^2\right] / T, \tag{4.5}$$

where $N = L^2$ is the number of lattice sites. The specific-heat and magnetic-susceptibility curves, for the case $\Delta = -10$, obtained via the Wang-Landau method, can be seen in Fig. 4.3.

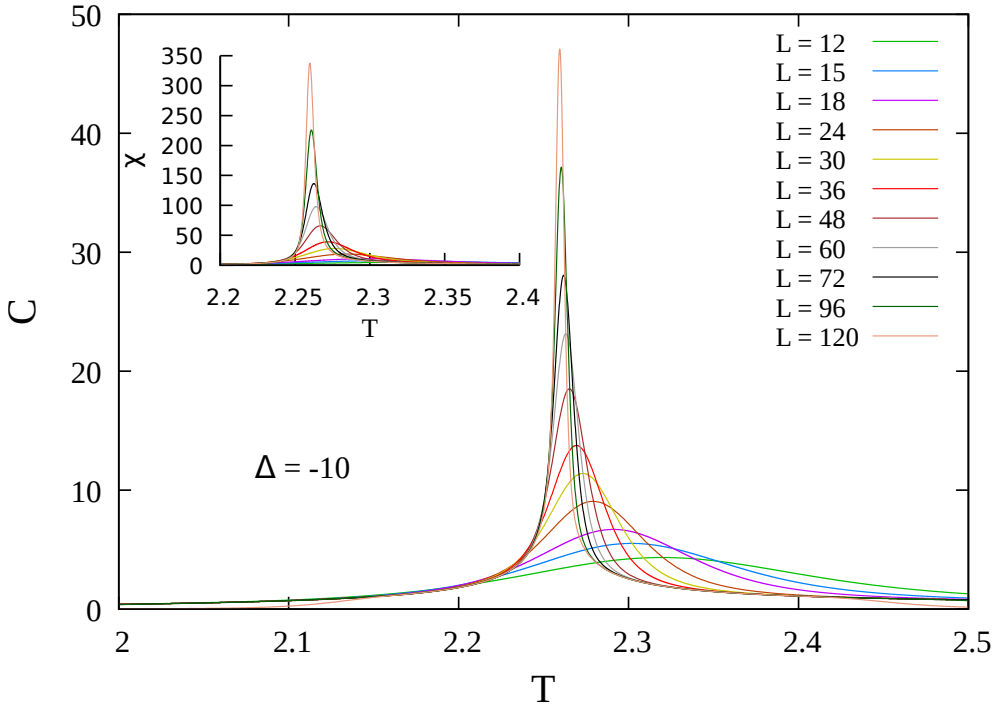

FIGURE 4.3: Specific heat (main panel) and magnetic susceptibility (inset) curves for the spin-1 Baxter-Wu model at $\Delta = -10$. Results obtain via Wang-Landau simulations.

4.2.2 Multicanonical simulations

In the multicanonical (MUCA) approach [94], a correction function is used in place of the canonical Boltzmann weight $\sim e^{-\beta E}$, with $\beta = 1/T$. The purpose behind this generalisation is to produce a flat histogram in some observed quantity. In the current study, this method was imposed to the crystal-field energy E_Δ, meaning that the temperature is fixed and results can be extrapolated to arbitrary values of Δ [154]. Specifically, the partition function

$$\mathcal{Z} = \sum_{\{E_J, E_\Delta\}} \Omega(E_J, E_\Delta) e^{-\beta(E_J + \Delta E_\Delta)}, \tag{4.6}$$

is generalised to

$$\mathcal{Z}_{\mathrm{MUCA}} = \sum_{\{E_J, E_\Delta\}} \Omega(E_J, E_\Delta) e^{-\beta E_J} W(E_\Delta), \tag{4.7}$$

with $\Omega(E_J, E_\Delta)$ being the two-parametric density of states.

Thus, the equilibrium probability distribution, in the multicanonical ensemble, is

$$P_{\mathrm{MUCA}}(E_J, E_\Delta) = \frac{\Omega(E_J, E_\Delta) e^{-\beta E_J} W(E_\Delta)}{\mathcal{Z}_{\mathrm{MUCA}}}. \tag{4.8}$$

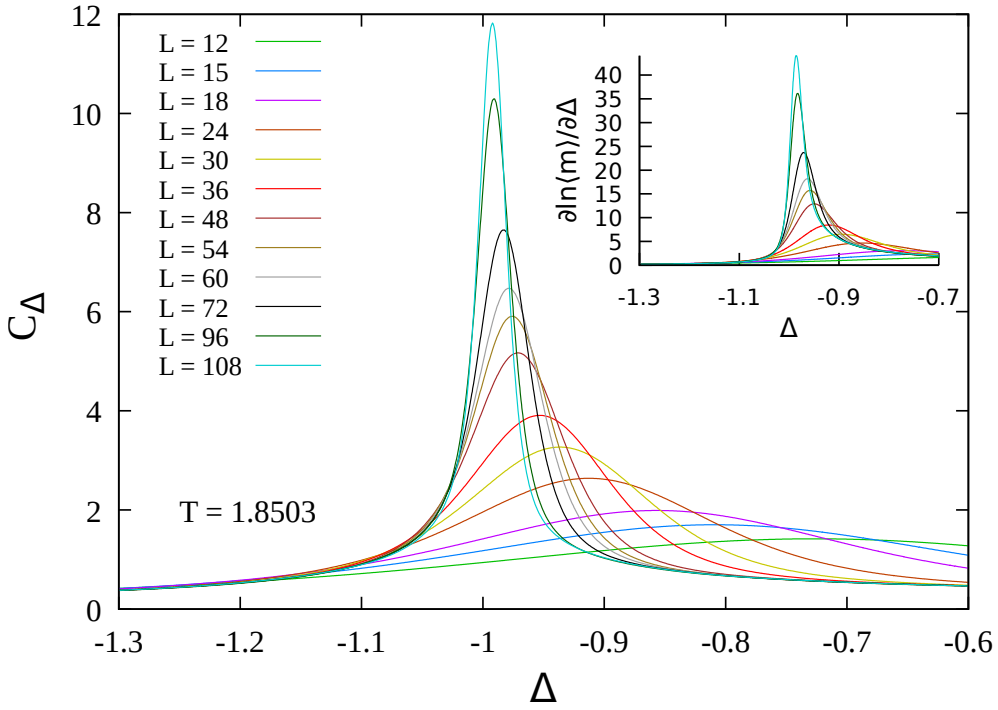

FIGURE 4.4: Specific-heat-like (main panel) and logarithmic derivative of the average magnetisation (inset) curves at $T = 1.8503$. Results obtained via multicanonical simulations.

To produce a flat histogram in the E_Δ energy space, the modified weight should be given by carrying out a summation with respect to E_J

$$W(E_\Delta) \propto \mathcal{Z}_{\text{MUCA}} \left[\sum_{E_J} g(E_J, E_\Delta) e^{-\beta E_J} \right]^{-1} . \tag{4.9}$$

The weights $W(E_\Delta)$ can then be estimated iteratively starting with some initial value, $W(E_\Delta) = 1$, for all E_Δ. Each time, the histogram of the crystal-field energy needs to be sampled as well. After n iterations, spins will be flipped following the weights $\sim e^{-\beta E_J} W^{(n)}(E_\Delta)$, and the histogram $H^{(n)}(E_\Delta)$ will be accumulated. After a pre-specified amount of spin-flip attempts, the weights are recalibrated using $W^{(n+1)}(E_\Delta) = W^{(n)}(E_\Delta) / H^{(n)}(E_\Delta)$. In general, at each iteration, the histogram $H^{(n)}(E_\Delta)$ will satisfy the equation

$$\langle H^{(n)}(E_\Delta) \rangle \propto P^{(n)}(E_\Delta) = \frac{1}{\mathcal{Z}_{\text{MUCA}}} \sum_{E_J} g(E_J, E_\Delta) e^{-\beta E_J} W^{(n)}(E_\Delta) \propto \frac{W^{(n)}(E_\Delta)}{W(E_\Delta)}, \tag{4.10}$$

justifying the update scheme [41]. When a sufficiently flat histogram has been sampled, the weight calculation process is completed and production runs can be performed.

As was discussed in Section 2.5, multicanonical simulations have a lot to gain from parallelised implementations [111, 184], as can be seen by past applications concerning the Blume-Capel model in two and three dimensions [29, 154, 156]. So, instead of sampling the histogram sequentially, parallel workers can use the same weights but different random number generators, producing an aggregated histogram which can be used to recalibrate the weights. The current simulations utilised an Nvidia K80 GPU, giving the capability to optimally run 26 624 systems at a time, 4 992 of which run in parallel. Finally, the histogram flatness was tested using the Kullback-Leibler divergence [111, 112] (also see Section 2.5 for a more thorough description of the process).

Since the multicanonical algorithm allows to continuously reweight the results to any value of the crystal-field strength Δ, canonical expectation values can be obtained by directly by reweighting. For instance, given an observable $O = O(\{\sigma\})$, its expectation value at Δ can be calculated from

$$\langle O \rangle_\Delta = \frac{\langle O(\{\sigma\}) e^{-\beta \Delta E_\Delta(\{\sigma\})} W^{-1}(E_\Delta) \rangle_{\mathrm{MUCA}}}{\langle e^{-\beta \Delta E_\Delta(\{\sigma\})} W^{-1}(E_\Delta) \rangle_{\mathrm{MUCA}}}. \tag{4.11}$$

Instead of computing T-derivatives of observables, it is then more physical to compute Δ-derivatives. For example, a Δ derivative of the energy can be calculated in place of the usual specific heat (4.4), defining a specific-heat-like quantity [154]

$$C_\Delta = \frac{1}{N} \frac{\partial E_J}{\partial \Delta} = - \left[\langle E_J E_\Delta \rangle - \langle E_J \rangle \langle E_\Delta \rangle \right] / (NT), \tag{4.12}$$

which possesses the same shift behaviour as the specific heat (see the main panel of Fig. 4.4). Furthermore, to obtain estimates of the critical exponent ν from finite-size scaling, the logarithmic derivatives of the order parameter can be calculated [185, 186], defined as

$$\frac{\partial \ln \langle m^n \rangle}{\partial \Delta} = - \left[\frac{\langle m^n E_\Delta \rangle}{\langle m^n \rangle} - \langle E_\Delta \rangle \right] / T, \tag{4.13}$$

Curves of the logarithmic derivatives for $n = 1$ can be seen the inset of Fig. 4.4.

Additionally, the magnetic susceptibility χ [Eq. (4.5)] as a function of Δ can be estimated, as well as the the fourth-order Binder cumulant of the magnetisation

$$U_m = 1 - \frac{\langle m^4 \rangle}{3 \langle m^2 \rangle^2}. \tag{4.14}$$

4.2.3 Simulation parameters

The above described simulation methods were applied on the spin-1 Baxter-Wu model on a triangular lattice with periodic boundary conditions. To accommodate for all the ground states, the linear system size L was always chosen to be a multiple of three [183], making sure that the

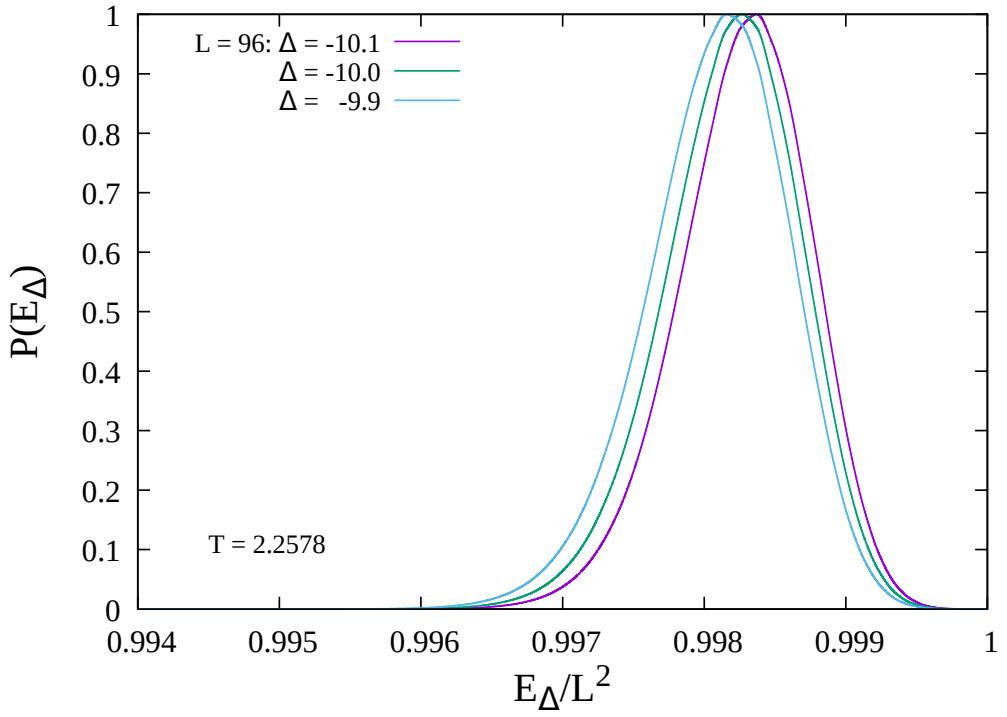

FIGURE 4.5: Normalised probability density function of the crystal-field energy for a system with linear size $L = 96$ at $T = 2.2578$. Results for three adjacent crystal field values are shown, obtained via multicanonical simulations.

one ferromagnetic and three ferrimagnetic states all have the same energy. Specifically, the considered L were within the range $12 \leq L \leq 120$. Wang-Landau simulations were performed at two values of the crystal-field strength, namely $\Delta = -10$ and -1. Additionally, multicanonical simulations were conducted at the temperatures $T = \{2.1, 1.8503, 1.6603, 1.5301\}$. Preliminary simulations were carried out at $T = 2.2578$ in order to provide an understanding for the transition order.

4.3 Results

4.3.1 Order of the transition

As discussed Section 4.1, recent studies have indicated towards discontinuous transition features along the putatively continuous part of the transition line [161]. To provide clarity regarding the order of the transition, the probability density function of the crystal-field energy, $P(E_\Delta)$, was studied, obtained via reweighting the results of the multicanonical simulations. In many cases, a double-peak structure in the density function of a finite system is a precursor of the two δ-peak structure occurring for a discontinuous phase transition [187, 188]. This however does not imply that the a double peak necessitates a first-order transition.

Figure 4.5 depicts the probability density function of the crystal-field energy, for a system of linear size $L = 96$, at the temperature $T = 2.2578$, corresponding to $\Delta = -10$ (see Fig. 4.1). Around the transition point, no sign of a double-peak structure can be observed. On the other hand, looking at the upper panel of Fig. 4.6, lowering the temperature to $T = 1.8503$ (corresponding to $\Delta = -1$), first-order-like characteristics start to appear in agreement with the results of reference [161] for the case $\Delta = 0$. It is interesting to note that for the case of $T = 2.1$ very shallow double peaks appear [163], but for the cases of $T = 1.6603$ and 1.5501 deeper double peaks appear, similarly to the upper panel of Fig. 4.6.

The existence of these structures calls for a systematic analysis of the relevant surface tension of the transition, as suggested by Lee and Kosterlitz [58, 59]. In fact, the multicanonical method is instrumental for this purpose as it allows the direct estimation of the barrier associated with the suppression of states during a first-order phase transition. Considering distributions with two peaks of equal height (eqh) [189], allows to extract the free-energy-like barrier in the E_Δ energy space,

$$\Delta F(L) = \frac{1}{2\beta} \ln \left(\frac{P_{\max}}{P_{\min}} \right)_{\text{eqh}}, \tag{4.15}$$

$P_{\max}$ and $P_{\min}$ being the maximum and local minimum of the distribution $P(E_\Delta)$, respectively. The barrier between the peaks connects a spin-0 rich phase, where E_Δ relatively small, and a spin-± 1 dominated regime, with large E_Δ. The arising surface tension – in two dimensions $\Sigma(L) = \Delta F(L)/L$ – is expected to scale as $\Sigma(L) = \Sigma_\infty + c_1 L^{-1} + \mathcal{O}\left(L^{-2}\right)$, possibly with higher-order corrections [190–192]. Similarly, the latent heat $\Delta e_\Delta(L)$, where $e_\Delta = E_\Delta / L^2$, can be defined as the distance of the two peaks in energy space.

The lower panel of Fig. 4.6 illustrates the scaling behaviour of the surface tension (main panel) and the latent heat (inset). Note the existence of a crossover for $T = 1.8503$, at a length scale of $L^* \approx 30$, where the surface tension curve changes its upward trend, indicating strong finite-size effects and possibly accounting for misleading previous conclusions concerning the order of the transition. The dashed lines in the main panel are fits, including third-order corrections terms, using a minimum system size $L \geq L^*$. The fits indicate towards a practically zero value of Σ for all the temperatures: $\Sigma(T = 1.8503, L \to \infty) = -0.00005(11)$, $\Sigma(T = 1.6603, L \to \infty) = -0.0003(9)$, $\Sigma(T = 1.5301, L \to \infty) = 0.0003(3)$. A similar, although slower downward trend can be observed for the latent heat.

4.3.2 Finite-size scaling and universality

With the second-order nature of the transition having been established, a detailed finite-size scaling analysis of the simulation data can be performed, in order to probe at the universality principles of the transition. In this Section, results obtained both complementary simulation methods are shown, in support of the expectation that the spin-1 Baxter-Wu model in a crystal

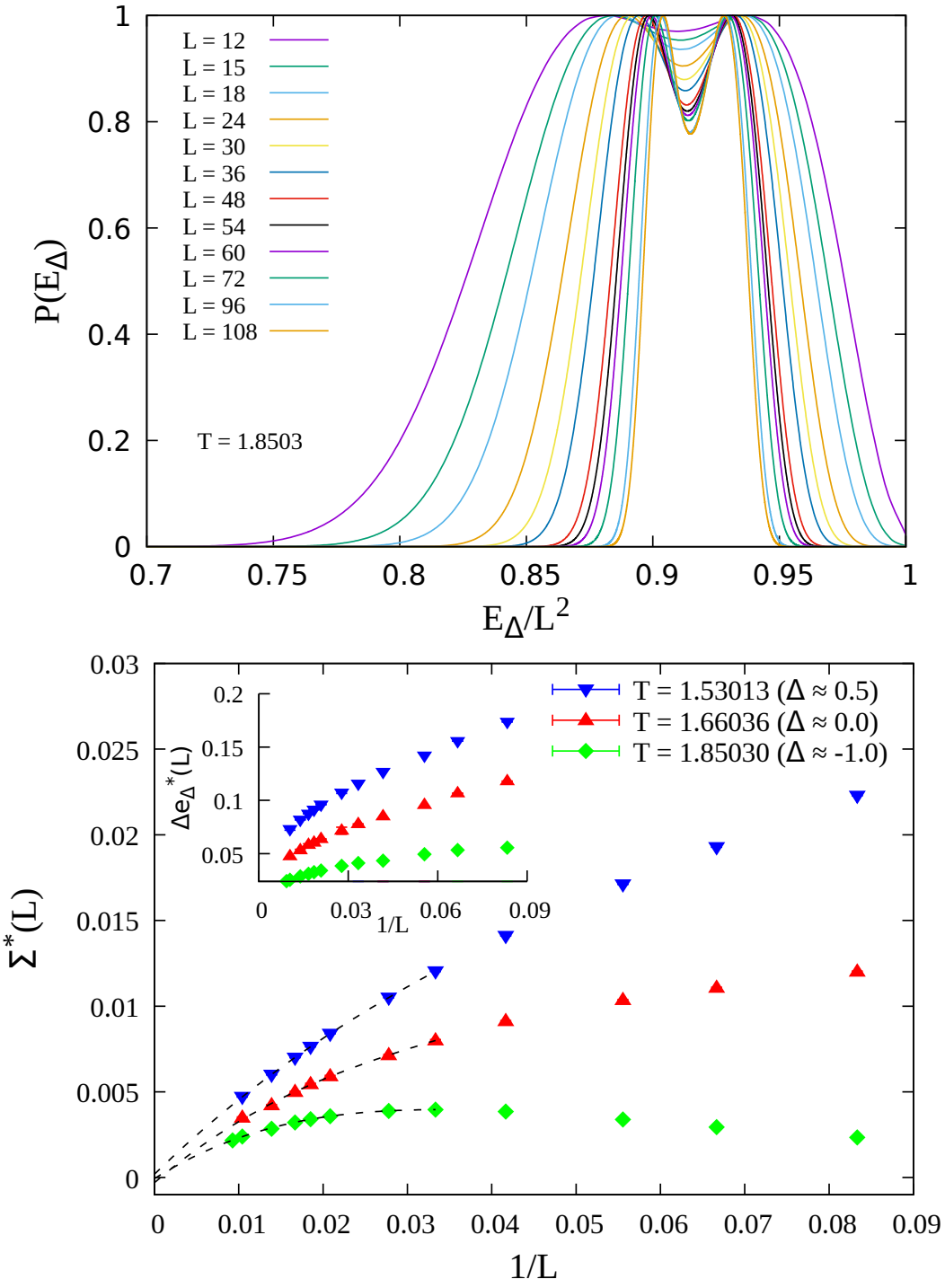

FIGURE 4.6: **Upper panel**: Probability density functions $P(E_\Delta)$ at $T = 1.8503$, for various system sizes, obtained via multicanonical simulations. The curves are reweighted to the point where two peak of equal height appear, around $\Delta \approx -1$. Similar results were observed for the smaller values of T considered. **Lower panel**: Limiting behaviour of the surface tension $\Sigma(L)$ (main panel) and latent heat $\Delta e_\Delta(L)$ (inset).

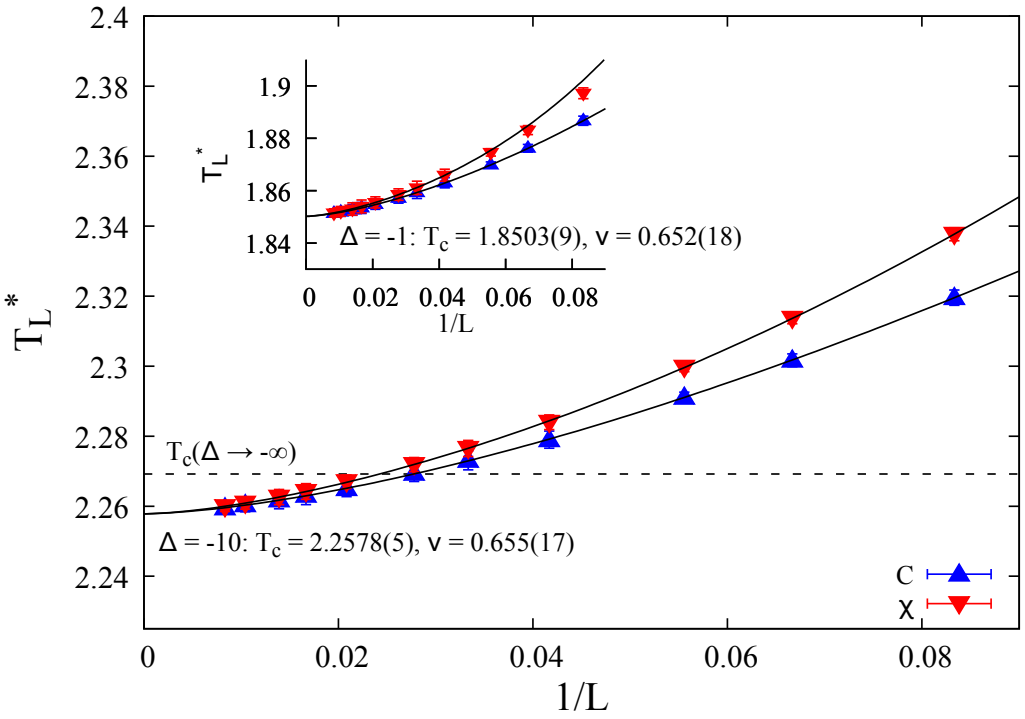

FIGURE 4.7: Shift behaviour of the peak locations of the specific heat and magnetic susceptibility as a function of the inverse linear system size at $\Delta = -10$ (main panel) and $\Delta = -1$ (inset). The black dashed line denotes the critical temperature of the model at $\Delta \to -\infty$, i.e. the critical temperature of the spin-1/2 Baxter-Wu model. In both panels the black solid lines are joint fits of the form (4.16). Data produced with the Wang-Landau algorithm.

field belongs to the same universality class as the spin-1/2 Baxter-Wu and the 4-state Potts models.

To extract the critical temperatures $T_c(\Delta)$ of the system, as well as to make a first estimate of the correlation-length critical exponent ν, the shift behaviour of suitable pseudocritical temperatures, T_L^*, is presented in Fig. 4.7. These temperatures are the peak locations of the specific-heat and magnetic susceptibility curves of Fig. 4.3. The main panel depicts results corresponding to $\Delta = -10$, while for the inset $\Delta = -1$. For each Δ, the solid lines correspond to joint fits of the expected power-law behaviour (see Section 1.4)

$$T_L^* = T_c + bL^{-1/\nu}(1 + b'L^{-\omega}). \tag{4.16}$$

The correction-to-scaling exponent takes the value $\omega = 2$ [140, 141, 160, 183] and is fixed hereafter. With $L_{\min} = 12$ the values $T_c(\Delta = -10) = 2.2578(5)$ and $T_c(\Delta = -1) = 1.8503(9)$ are produced, which agree with the values 2.2578(116) and 1.8503(94) reported in reference [160]. More importantly, the estimates $\nu = 0.655(17)$ for $\Delta = -10$ and $\nu = 0.652(18)$ for $\Delta = -1$ are in nice agreement with the 4-state Potts universality class result of $\nu = 2/3$.

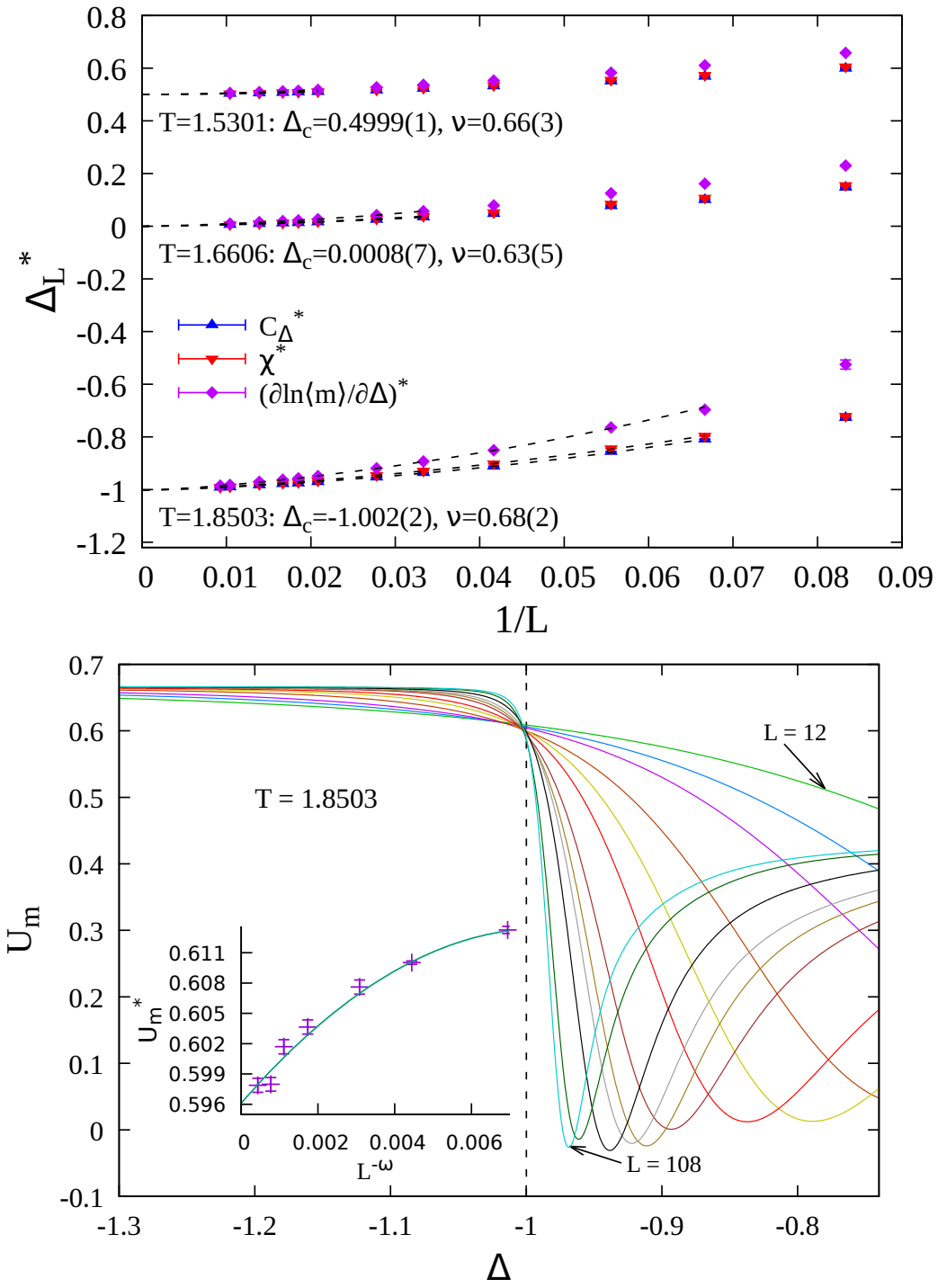

FIGURE 4.8: **Upper panel**: Shift behaviour of several pseudocritical fields, at various temperatures, as a function of the inverse linear system size. **Lower panel**: Fourth-order Binder cumulant curves of the order parameter for $T = 1.8503$. The black vertical dashed line marks the value $\Delta = -1$. The inset shows the limiting behaviour of the crossings U_m^* on pairs of lattice sizes $(L, 2L)$. Data produced at via multicanonical simulations.

Likewise, Fig. 4.8 presents the shift behaviour of several pseudocritical fields, Δ_L^*, defined as peak locations of the multicanonical observables of Section 4.2. An analogous joint fit of the form

$$\Delta_L^* = \Delta_c + bL^{-1/\nu}(1 + b'L^{-\omega}), \tag{4.17}$$

with $L_{\min} = 15$ produces the estimates $\Delta_c(T = 1.8503) = -1.002(2)$ and $\nu = 0.68(2)$, in good agreement with the Wang-Landau results presented above. Similarly, with $L_{\min} = 15$, $\Delta_c(T = 2.1) = -3.436(3)$ and $\nu = 0.67(1)$. With $L_{\min} = 24$, $\Delta_c(T = 1.6606) = 0.0008(7)$ and $\nu = 0.63(5)$. Finally, with $L_{\min} = 48$, $\Delta_c(T = 1.5301) = 0.4999(2)$ and $\nu = 0.66(3)$. Additionally, the main plot of the lower panel of Fig. 4.8 depicts typical curves of the fourth-order Binder cumulant U_m [Eq. (4.13)], where the location of the crossing point also agrees nicely with the value $\Delta = -1$. A summary of all results can be found in Table 4.2 at the end of the Chapter.

The exponent ν can also be obtained from the scaling of the logarithmic derivatives of the order parameter maxima [Eq. (4.13)]. Being dimensionless quantities, the scaling behaviour follows [185]

$$\left(\frac{\partial \ln \langle m^n \rangle}{\partial \Delta}\right)^* \sim L^{1/\nu}(1 + b'L^{-\omega}). \tag{4.18}$$

The numerical data for $n = 1$ and $n = 2$, estimated from multicanonical simulations, can be seen in Fig. 4.9. The solid lines are power-law fits of the form [Eq. (4.18)]. At $T = 2.1$, $L_{\min} = 18$ retrieves $\nu = 0.668(6)$ and $0.677(9)$, respectively for $n = 1$ and $n = 2$. At $T = 1.8503$, $L_{\min} = 18$ produces $\nu = 0.669(5)$ and $0.673(6)$. For $T = 1.6606$, with $L_{\min} = 36$, $\nu = 0.651(15)$ and $0.652(14)$. $T = 1.5301$, with $L_{\min} = 36$, returns $\nu = 0.654(28)$ and $0.653(25)$. These results also point towards the expected the spin-1/2 Baxter-Wu model universality class, where $\nu = 2/3$.

Turning to the scaling behaviour of the maxima of the specific heat [C^* and C_Δ^*, respectively for Wang-Landau and multicanonical simulations] and magnetic susceptibility (χ^*), the critical exponent-ratios α/ν and γ/ν can be estimated. Figure 4.10 depicts results from the Wang-Landau simulations (upper panel, $\Delta = -10$ and -1) and the multicanonical approach (lower panel, $T = 1.8503$, 1.6606, and 1.5301). In all cases the solid lines are fits of the form

$$C_{(\Delta)}^* \sim L^{\alpha/\nu}(1 + b'L^{-\omega}), \tag{4.19}$$

with the subscript distinguishing between C^* and C_Δ^*, and

$$\chi^* \sim L^{\gamma/\nu}(1 + b'L^{-\omega}). \tag{4.20}$$

The estimates obtained for α/ν and γ/ν are listed in the panels (see also Table 4.1 and Table 4.2 below). For most cases, the results are clearly compatible with the exact values of

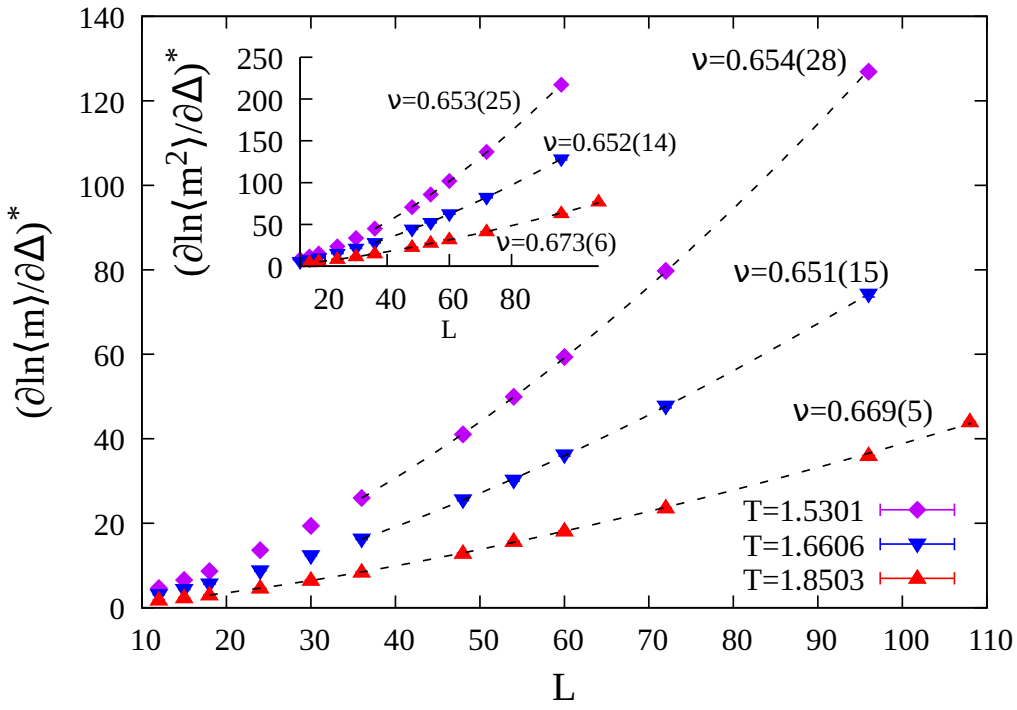

FIGURE 4.9: Finite-size scaling of the logarithmic derivatives of powers $n = 1$ (main panel) and 2 (inset) of the order parameter at various values of T. The solid lines are fits of the form (4.18). Results obtained via multicanonical simulations.

$\alpha/\nu = 1$ and $\gamma/\nu = 7/4$ of the spin-1/2 Baxter-Wu universality class [139]. However, for the multicanonical simulations at $T = 1.6606$ and $T = 1.5301$, small deviations start to appear, especially in the specific heat critical exponent.

At this point, a remark should be made about the additional correction term $b'L^{-\omega}$ appearing in the fits of Figs. 4.7 – 4.10. Although in the work of Jorge et al. for the spin-1/2 model critical exponents were obtained with very good accuracy and without the need for corrections to scaling [144], the situation here is rather different. In particular the values of scaling amplitudes b and b' in Eqs. (4.16) – (4.20) are comparable and in particular the values of b' fluctuate about the range $1 - 100$ for the various observables and cannot be neglected. Additionally, from the overall comparative tests, it is safely concluded that the fitting quality measured in terms of the probability Q is indeed improved when the correction term is included.

A universality class is characterised by a range of universal quantities which, apart from critical exponents, also include certain universal amplitude ratios g [29, 179, 194–199]. These amplitudes, in stark contrast to the exponents, also depend on system properties, lake the lattice geometry or boundary conditions. In this study, two of these universal ratios were studied: the Binder cumulant $g = U_m$ value at the crossing of the curves, and the ratio of the correlation length over the linear system size, $g = \xi/L$. Characteristic curves of ξ/L at $\Delta = -10$ can be seen in Fig. 4.11 (main panel). To estimate ξ, the second-moment definition was used [29, 200,

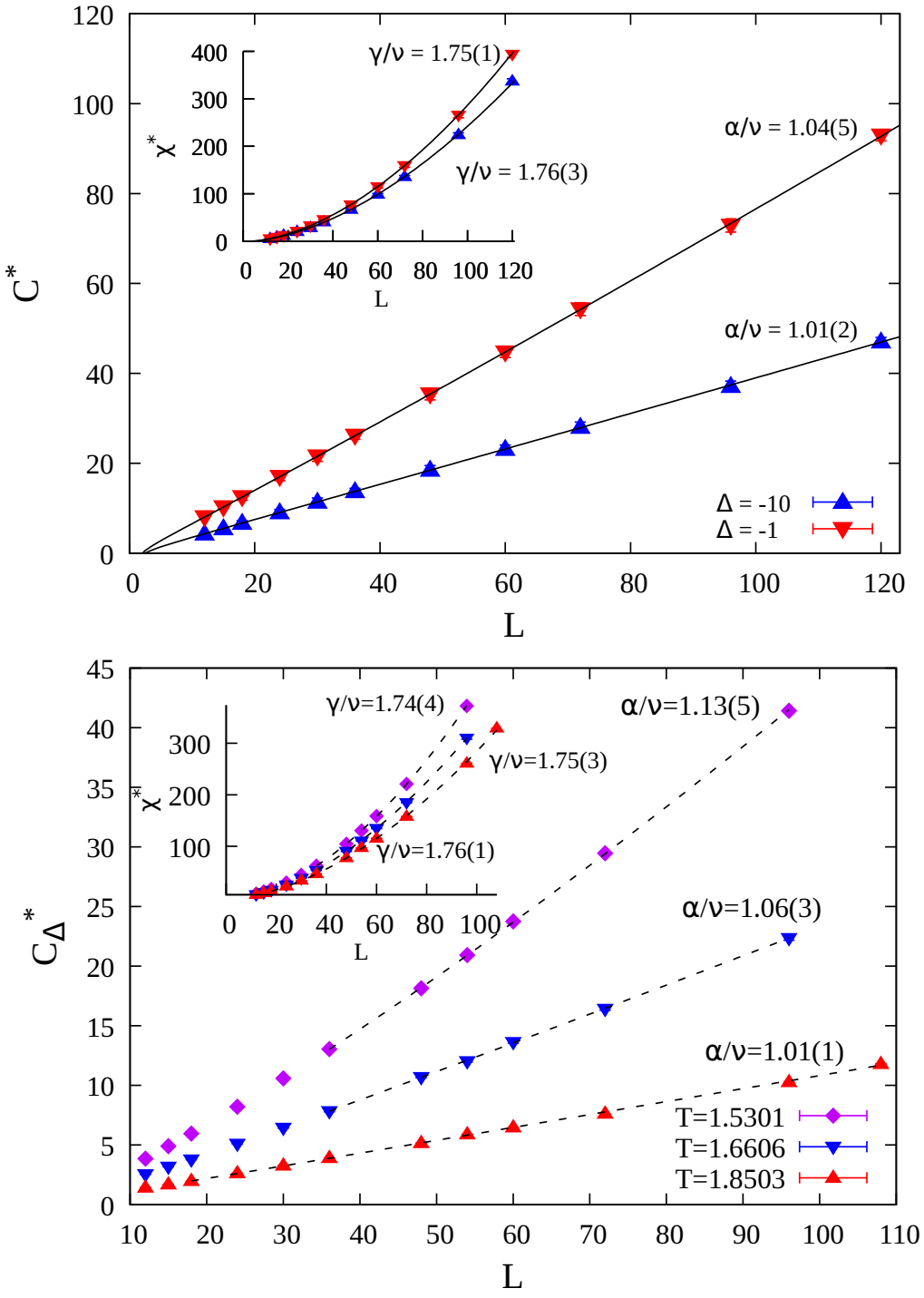

FIGURE 4.10: **Upper panel**: Finite-size scaling behaviour of C^* (main panel) and χ^* (inset) at $\Delta = -10$ and $\Delta = -1$. Data produced with the Wang-Landau algorithm. **Lower panel**: Similar analysis of data produced at $T = 1.8503$, 1.6606, and 1.5301 via multicanonical simulations.

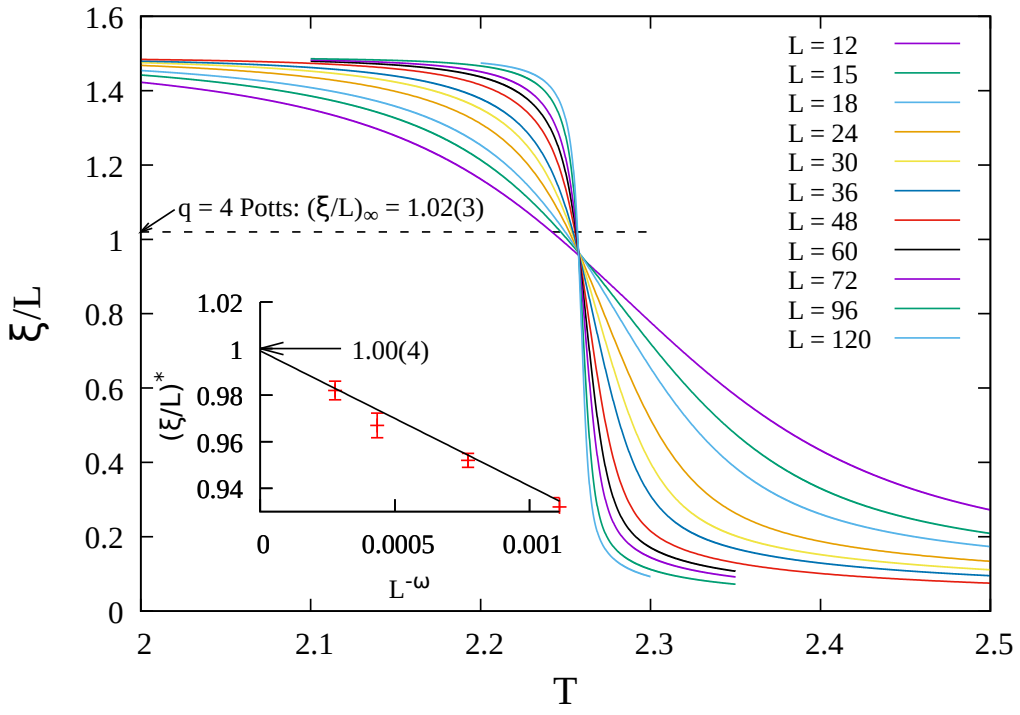

FIGURE 4.11: **Main panel**: Typical ξ/L curves as a function of the temperature obtained from Wang-Landau simulations for all pairs of system sizes studied and for $\Delta = -10$. The temperature area of the crossings conforms to the value $T_c = 2.2578$ of Fig. 4.7. **Inset**: Finite-size scaling of the correlation-length ratios at their crossing points, $(\xi/L)^*$. Results are shown for the largest pairs $(L, 2L)$ of system sizes: $(30, 60)$, $(36, 72)$, $(48, 96)$, and $(60, 120)$. The solid line shows a linear in $L^{-\omega}$ extrapolation to $L \to \infty$. The black dashed line marks the value of $(\xi/L)_\infty$ of the 4-state Potts model, as taken from Ref. [193].

201]. From the Fourier transform of the spin field, $\hat{\sigma}(\mathbf{k}) = \sum_{\mathbf{x}} \sigma_{\mathbf{x}} \exp(i\mathbf{k}\mathbf{x})$,

$$F = \left\langle |\hat{\sigma}(2\pi/L, 0)|^2 + |\hat{\sigma}(0, 2\pi/L)|^2 + |\hat{\sigma}(2\pi/L, 2\pi/L)|^2 \right\rangle /3 \tag{4.21}$$

can be determined. The correlation length can then be calculated from [201]

$$\xi \equiv \frac{1}{2\sin(\pi/L)} \sqrt{\frac{\langle m^2 \rangle}{F} - 1}. \tag{4.22}$$

Applying the quotients method was employed [113, 194–197, 202], the crystal field (or respectively the temperature) where the curves of U_m (respectively ξ/L) of the sizes L and $2L$ cross, defines finite-size pseudocritical points. There $g_{2L}/g_L = 2$. These estimates are depicted in the lower panel of Figs. 4.8 and 4.11. Denoting by g^* the value at these crossings, a scaling of the form

$$g^* = g_\infty + \mathcal{O}(L^{-\omega}) \tag{4.23}$$

can be expected, where g_∞ is universal.

The inset of Fig. 4.8 provides an estimate for the universal Binder cumulant $(U_m)_\infty$, as extracted from the sequence of the finite-size crossings U_m^*. A second-order polynomial fit in $L^{-\omega}$, yields $U_{m,\infty} = 0.596(6)$, in excellent agreement to the graphical estimate 0.595 of Capponi et al. [181]. In the same manner, the inset of Fig. 4.11 depicts the infinite-size extrapolation of the values $(\xi/L)^*$, using the four largest pairs of system sizes considered. A linear fit in $L^{-\omega}$ led to

$$\left(\frac{\xi}{L}\right)_{\infty,\ \text{spin}-1\ \text{BW}} = 1.00(4). \tag{4.24}$$

For the two-dimensional $q = 4$ Potts model, the respective value, calculated with periodic boundary conditions from the seminal work of Salas and Sokal [193], is

$$\left(\frac{\xi}{L}\right)_{\infty,\ q=4\ \text{Potts}} = 1.02(3). \tag{4.25}$$

These results are in good agreement with each other, and consist the final universality check performed in this work, accurate within a $\sim 2\%$ margin.

4.3.3 Universal distributions

Other than using critical exponents and universal ratios to characterise a universality class, probability distributions can also be utilised. In this Section, focus is placed on understanding the results concerning universal distributions from the multicanonical simulations at $(\Delta \approx 0.0008, T = 1.6606)$, for both the magnetisation, sublattice magnetisation, and for the energy. Extra focus is placed on the energy, where by performing field mixing in the fields conjugate to E_J and E_Δ, the phase diagram was crossed from different angles, in order to see if the universal distributions will be the same for all the cases considered. To calculate the distributions at the critical point, all results were reweighted at the critical value of the crystal field Δ.

For a system of linear size L, an observable Q will follow a probability distribution $P_L(Q)$. Then, its per-site equivalent quantity $q = Q/L^D$ will obey the distribution $P_L(q)$, D being the dimensionality of space. A rescaled version of this distribution can provide another indication of universality. Specifically, a universal distribution can be defined for large L by [203, 204]

$$P_L(q) = cL^x P^*(cL^y q). \tag{4.26}$$

Models in the same universality class will follow the same distribution P^*. Starting from $P_L(q)$, moments of q can be defined by

$$\langle q^n \rangle = \int q^n P(q) dq = c^n L^{x-y-ny} \int (q^*)^n P(q^*) dq^*, \tag{4.27}$$

where a simple change of variables, $q^* = cL^y q$, was used. This discussion assumed that the quantity q was a continuous variable, even though that is not the case for a finite system, but this can be reconciled by the use of very large system sizes. The quantity q is usually the energy or the magnetisation per lattice site. Thus, the value of the exponents x and y can be found directly from the variance of q and the scaling relation of Eqs. (1.76) or (1.77), respectively. It turns out that $x = y$. However, knowledge of the critical exponents or the value of x is not necessary in order to calculate the universal distribution.

Assuming that the random variable Q can take the values Q_i for some finite system L, and that the corresponding distribution $P_L(Q_i)$ is known, at least approximately, from some analytic calculation or a simulation, then the following normalisation condition should hold

$$1 = \sum_i P(Q_i) = \sum_i P(Q_i) \left(\frac{\Delta Q}{L^D}\right)^{-1} \left(\frac{\Delta Q}{L^D}\right). \tag{4.28}$$

Here, ΔQ is the difference between two consecutive Q_i. For a very large system, $\Delta q = \Delta Q / L^D$ can be manipulated as a continuous variable, defining the continuous distribution $P_L(q) = P_L(Q_i) / \left(\Delta Q / L^D\right)$. Combining this definition with the moments of Eq. (4.27) and the universal distribution of Eq. (4.26) means that the variance of the distribution, σ_q^2, and that of the universal distribution, $\sigma_{q^*}^2$, are connected via

$$\sigma_q^2 = \sigma_{q^*}^2 / (c^2 L^{2x}). \tag{4.29}$$

Thus, the scaling factors cL^x that appear in Eq. (4.26) can be estimated from the standard deviation of q. Also centring around the zero moment $q_0 = \langle q \rangle$ implies that

$$P^*\left(\sigma_q (q - q_0)\right) = \sigma_q P_L(q - q_0). \tag{4.30}$$

Since the distribution $P_L(q)$ was divided by σ_q^2, according to Eq. (4.29), the universal distribution P^* estimated by Eq. (4.30) is of unit variance.

Magnetisation and energy universal distributions

The universal probability distributions for the magnetisation per particle and the sublattice magnetisation per particle at the critical point $(\Delta = 0.0008, T = 1.6606)$, as predicted by the different system sizes, are shown in Fig. 4.12. The total magnetisation distributions, defined with $m = m_\mathrm{A} + m_\mathrm{B} + m_\mathrm{C}$, are depicted in the left panel, while the the sublattice magnetisation is shown on the right. The two plots indicate that as the system size increases, the universal distributions approach each other, exactly as expected, since in the limit of very large L distributions should converge to the universal behaviour. The errors are calculated using the jackknife method (see Appendix A).

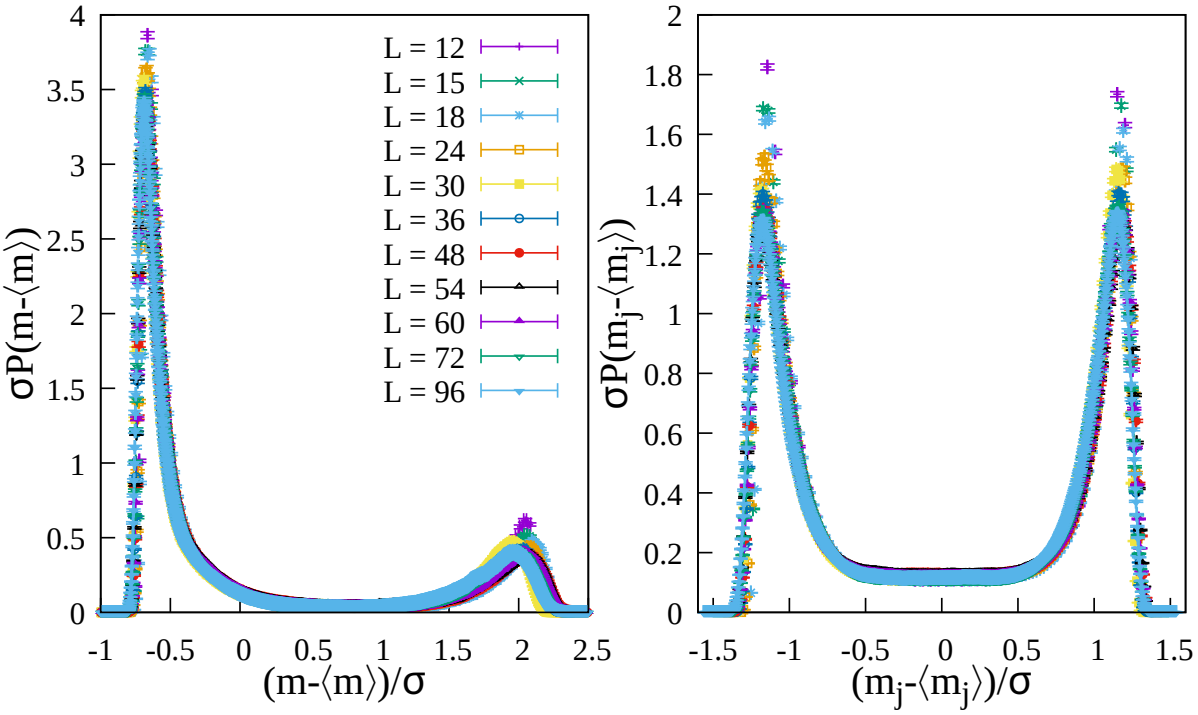

FIGURE 4.12: **Left panel**: Universal distribution of the magnetisation per particle m for the spin-1 Baxter-Wu model, at the critical point where $T = 1.6606$, for different system sizes. **Right panel**: Similar plot but for the sublattice magnetisation per particle, m_j.

The universal distribution for the energy per particle is shown in Fig. 4.13. It is evident, even just by inspection, that the energy distributions are in a sense better behaved than the magnetisation ones, showing faster convergence as the system size increases.

Field-mixed universal distributions

In cases like the spin-1 Baxter-Wu and Blume-Capel models it is perhaps more physically intuitive to study the model under a linear transformation of the fields (Δ, T). The new fields can be defined in such a way that varying them would lead to crossing the transition line in two perpendicular directions. This approach of mixing fields [205] has been applied in the past, especially for the case of locating multicritical points [155, 204, 206], by approaching them from the first-order transition line. In these cases, one of the field is chosen to be tangent to the transition line at each point. Here, the method of field-mixing is applied to the continuous line of transitions, specifically in order to see the universal distributions that arise from the energies conjugate to the new fields. In that sense, from renormalisation group arguments, the direction of the new fields does not matter for the universal behaviour. Such a transformation can be seen in Fig. 4.14.

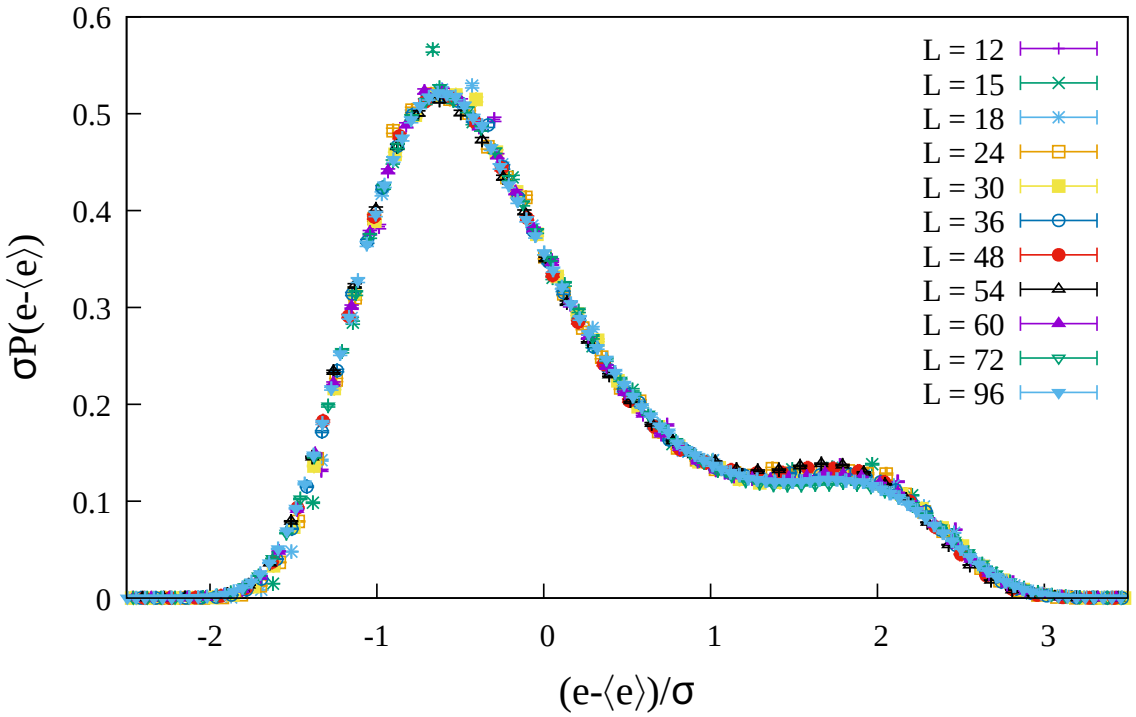

FIGURE 4.13: Universal distribution of the energy per particle e for the spin-1 Baxter-Wu model at the critical point where $T = 1.6606$ for different system sizes.

The idea of field mixing, at least in the current general case, is the following: to study a critical point move the reference frame on top of it by applying a linear transformation to the fields. For the spin-1 Baxter-Wu model, a general transformation would produce two new fields, f_q and f_g, defined as

$$f_q = (\mu - \mu_c) + r(\beta - \beta_c), \tag{4.31}$$

$$f_g = (\beta - \beta_c) - s(\mu - \mu_c). \tag{4.32}$$

In the above, instead of working directly with (Δ, T), the new fields were expressed using the equally valid variables $\beta = 1/T$ and $\mu = \beta\Delta$. The reason behind this choice is that the field-conjugate variables are easier to express. The r and s are the slopes of the newly defined reference frame in comparison to the old one. The conjugate variables then are straightforward to calculate as

$$Q = \frac{\partial \log \mathcal{Z}}{\partial f_q} = \frac{1}{1+rs}(E_\Delta + sE_J), \tag{4.33}$$

and

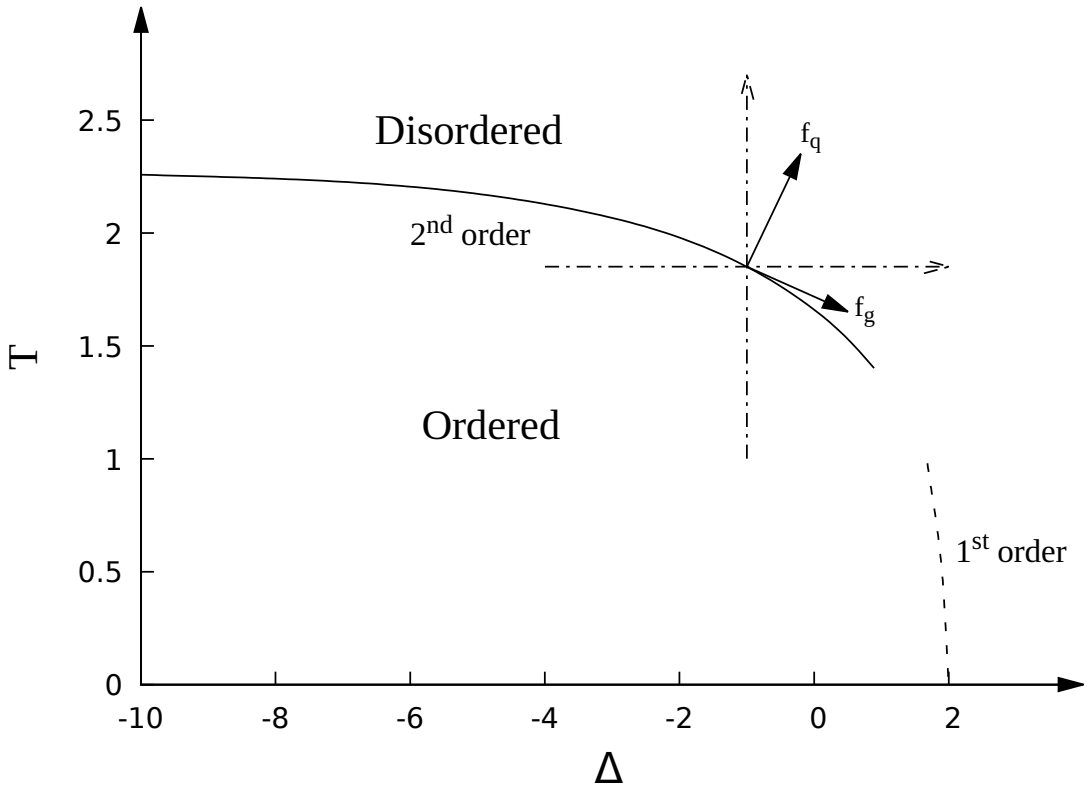

FIGURE 4.14: Phase diagram of the two-dimensional spin-1 Baxter-Wu model. A change of the coordinates is indicated by the two vectors f_q and f_g. The new coordinates are more natural when discussing crossing the critical transition line.

$$G = \frac{\partial \log \mathcal{Z}}{\partial f_g} = \frac{1}{1+rs}(E_J - rE_\Delta), \tag{4.34}$$

so in the end, mixing the two fields results in conjugate variables that simply mix the energies.

By sampling these quantities, universal distributions can be estimated in the same manner as before. Note that the constant $(1+rs)^{-1}$ in the front is unimportant since it can be absorbed by the normalisation of the distributions. Figure 4.15 compares the universal distributions of the mixed energies of Eqs. (4.33) and (4.34) with that of the total energy of the system [Eq. (4.2)], only for the largest sizes considered, and for the simulation at temperature $T = 1.6606$. The choice of the slopes s and r was such that the new fields are perpendicular to each other.[1] Different choices gave similar results, with all the distributions seemingly being on top of each other, as expected.

[1]Note that in the definitions of the new coordinates in Eqs. (4.33) and (4.34), s appears with a minus, to convenience the definitions of Q and G.

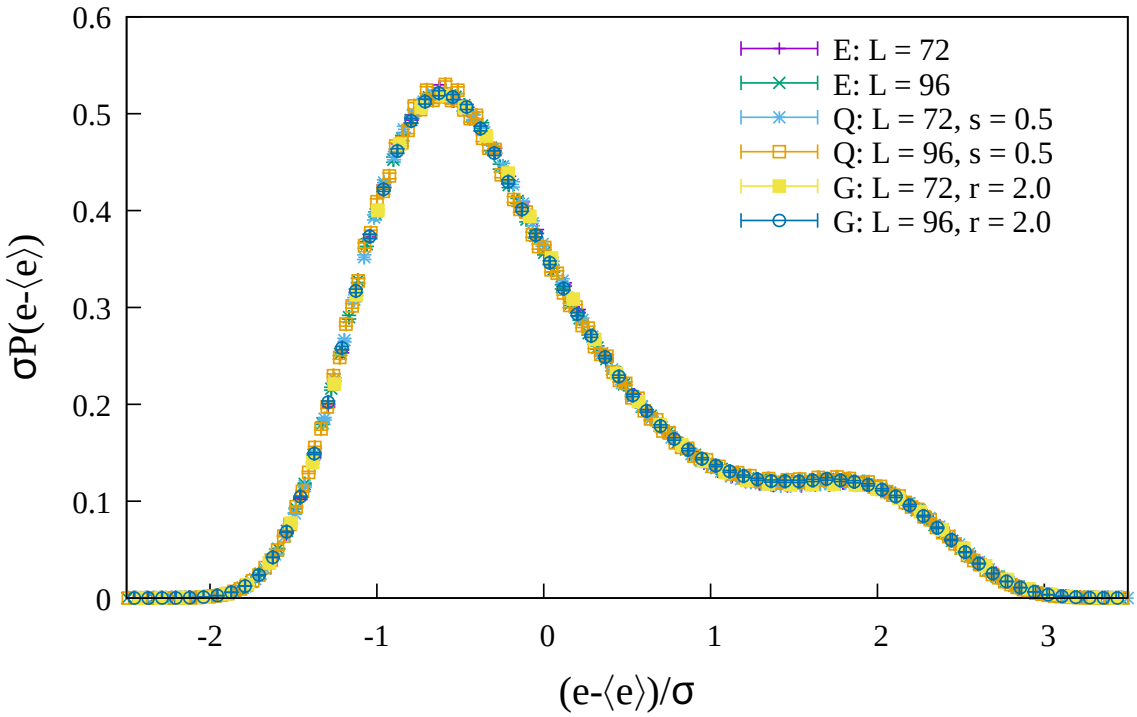

FIGURE 4.15: Universal distributions of the energy per particle, for the different types of energies defined in Eqs. (4.2), (4.33), and (4.34) for the spin-1 Baxter-Wu model at the critical point where $T = 1.6606$. Results are shown only for the two largest system sizes.

4.4 Summary and Outlook

In this Chapter, an extensive numerical study of scaling and universality in the phase diagram of the diluted Baxter-Wu model was presented. Employing a combination of Wang-Landau simulations that cross the transition at constant crystal field Δ and multicanonical simulations operating at constant temperature T, a range of the transition points was covered. Clear evidence was provided for the second-order nature of the transition in this regime. The previously reported first-order-like signature of the transition on approaching the pentacritical point are also seen here from the simulations at $\Delta \leq -1$, but a careful finite-size scaling analysis showed that they are a mere finite-size effect. Everywhere in the second-order regime the analysis clearly showed consistency with the universality class of the spin-1/2 Baxter-Wu model. From the accuracy in the determination of the critical exponents one may conclude that logarithmic corrections-to-scaling are indeed minimal. A comparative overview of the results is provided in Tables 4.1 and 4.2. While it is clear from these results that strong scaling corrections appear as the pentacritical point, where the transition changes to first-order, is approached, the exact location of this pentacritical point and its universality class were not considered here. This question is left for future work.

Additionally, the universal distributions were considered, which are yet another tool for

TABLE 4.1: A comparison of exact and numerical results for the 4-state Potts model, spin-1/2 Baxter-Wu model, and spin-1 Baxter-Wu model in a crystal field. The latter obtained via the Wang-Landau simulations at fixed values of the crystal field Δ.

	Wang-Landau				
Simulation point	T_c	ν	α/ν	γ/ν	$(\xi/L)_\infty$
spin-1/2	2.26918...	2/3	1	7/4	1.02(3) [193]
$\Delta = -10$	2.2578(5)	0.655(17)	1.01(2)	1.76(3)	1.00(4)
$\Delta = -1$	1.8503(9)	0.652(18)	1.04(5)	1.75(1)	–

TABLE 4.2: A comparison of the spin-1/2 Baxter-Wu model universality class with the results obtained via multicanonical simulations at fixed values of the temperature T. For the value of the exponent ν, the results from the logarithmic derivatives of Fig. 4.9 for $n = 1$ are reported. Averaging over all the estimations was avoided, because this would produce unreliable errors due to the statistical correlation of the estimates of ν [207, 208].

	Multicanonical				
Simulation point	Δ_c	ν	α/ν	γ/ν	$(U_m)_\infty$
spin-1/2	–	2/3	1	7/4	~ 0.595 [181]
$T = 2.1$	$-3.436(3)$	0.668(6)	1.002(9)	1.75(3)	–
$T = 1.8503$	$-1.002(2)$	0.669(5)	1.01(1)	1.76(1)	0.596(6)
$T = 1.6606$	0.0008(7)	0.651(15)	1.06(6)	1.75(3)	–
$T = 1.5301$	0.4999(2)	0.654(28)	1.13(5)	1.74(4)	–

investigating the universality principles of the model. The system sizes considered were large enough to approach the universal distributions, especially when considering the energy. Mixing fields and crossing the phase boundary at different angles was shown to be equivalent to just working with the energy of the system, as expected.

To conclude, hopefully this work settles some of the previously reported controversies over the critical behaviour of the spin-1 Baxter-Wu model and lays the foundation for intriguing extensions. One such interesting line of research would be to unveil the effect of quenched disorder in both parts of the phase diagram of the model. Additionally, a field mixing approach would be useful for locating the pentacritical point, like it has been done in the past for the tricritical point of the Blume-Capel model [155, 204, 206], as well as the tricritical point of the two-dimensional spin fluid [206].

Chapter 5

Dynamical Phase Transition in the Random Blume-Capel Model

This chapter contains work that was published in [209].

By means of Monte Carlo simulations, an investigation is carried out concerning the dynamical phase transition of the two-dimensional Blume-Capel model in the presence of a quenched random crystal-field coupling, under a periodically oscillating magnetic field. The analysis, concerning the universality features of this dynamic transition, takes place in the originally continuous transition regime of the corresponding equilibrium phase diagram, for various values of the crystal-field coupling Δ. A detailed finite-size scaling analysis indicates that the observed nonequilibrium phase transition belongs to the universality class of the equilibrium Ising ferromagnet, with additional logarithmic corrections in the scaling behaviour of the heat capacity. These results are in agreement with earlier works on dynamical phase transitions in Ising models.

5.1 Introduction

The current theory and results of critical phenomena has developed enough to allow for the comprehension of a wide variety of systems and how their universal properties arise, as well as the differences between universality classes. This understanding also extends, at least partially, to quenched disordered systems. In comparison, when it comes to nonequilibrium phase transitions, the knowledge concerning their underlying physical mechanisms is far reduced. A comprehensive classification of these transitions, undergone by many-body interacting systems far from equilibrium, is still lacking.

Following the seminal work of Tomé et al. [210], it is now understood that exposing a ferromagnetic system to an oscillating magnetic field, while below its Curie point, an interesting dynamical behaviour can arise. In general, the oscillating field creates two competing regimes, depending on the timescales of the half-period of the field, $t_{1/2}$, and the metastable lifetime τ

of the system. The later is defined as the average time it takes for the system to leave its two degenerate zero-field equilibrium states when a field of magnitude h_0 is applied, in the direction opposite to the initial magnetisation. In practice, τ can be measured as the first-passage time to zero magnetisation. When the half period is smaller than the metastable lifetime, $t_{1/2} < \tau$, it is not possible for the spins to follow the external field. Thus, the magnetisation tends to oscillate around a non-zero value, and this regime corresponds to the dynamically ordered phase. On the other hand, for $t_{1/2} > \tau$, the system has enough time to follow the magnetic field. In this case, the magnetisation oscillates around the zero value, acting in accordance to the field. This behaviour indicates a phase of dynamical disorder. In the intermediate regime, where $t_{1/2} \approx \tau$, a dynamical phase transition takes place between the dynamically ordered and disordered phases.

Many theoretical [211–231] and experimental studies [232–236] dealing with the question of dynamical phase transitions and hysteresis have been carried out through the years. From there, it is safe to say that both the amplitude and the period of the time-dependent external field play a key role in dynamic critical phenomena. Moreover, the classification of spin models with time-dependent oscillating magnetic fields in universality classes has attracted much interest in recent years [237–246]. To express the main finding in a nutshell: The critical exponents of the Ising model undergoing a dynamical phase transition agree with those of the equilibrium model, both at two and three dimensions [237–239, 241]. Also, Buendía and Rikvold [240] produced strong evidence towards the idea that dynamic phase transitions have the same universal characteristics, regardless of the choice of stochastic dynamics, by estimating the critical exponents of the two-dimensional Ising model. The authors utilised so-called soft Glauber dynamics [247], where both nucleation and interface propagation are slower and the interfaces smoother than for the standard hard Glauber and Metropolis dynamics. Additionally, Park and Pleimling [242] worked on understanding the role of surfaces in nonequilibrium phase transitions, specifically for Ising models. Their findings show that the nonequilibrium surface exponents were in disagreement to the respective equilibrium exponents. Moreover, Riego et al. [236] provided experimental evidence which, together with the numerical results of Buendía and Rikvold [244], verified that the equivalence of the dynamic and equilibrium phase transitions is limited to the area near the critical period. Lastly, Vatansever and Fytas [245, 246] showed with numerical simulations that the nonequilibrium phase transitions of the pure and random-bond Blume-Capel model belong in the universality class of the pure Ising model in equilibrium, with the presence of additional logarithmic corrections for the disordered case. Some general and useful features of the dynamical phase transition of the pure Blume-Capel model can be found in references [217, 225, 226, 228, 248, 249].

The above works in two- and three-dimensional Ising and Blume-Capel models put in place a map between the universality principles of equilibrium and dynamic phase transitions. Additionally, they provide support in favour of an earlier investigation of a Ginzburg-Landau

model with a periodically changing field [219], as well with the symmetry-based arguments of Grinstein et al. in nonequilibrium critical phenomena [250].

With the majority of studies in the field of dynamical transitions dealing with pure systems, this chapter attempts to shed some additional light to what happens when dynamic phase transitions are combined with quenched disorder (see for example [246]). Earlier mean-field and effective-field theory treatments in these problems showed that the dynamic characteristics of a typical system driven by a time-dependent magnetic field depend sensitively on the amount of disorder, giving rise to re-entrant phenomena and dynamic tricritical points [251–256].

This chapter investigates the spin-1 Blume-Capel model [145–148] on a square-lattice, with a diffusing randomness in the crystal-field coupling, under the presence of a time-dependent periodic magnetic field. This type of disorder has also been studied in the past for the equilibrium counterpart of the model [257–259], and it actually resembles the physics of random porous media in mixtures of $^3He - ^4He$ [260]. In short, extensive Monte Carlo simulations along the phase boundary advise that the dynamical phase transition of the model lies in the universality class of the equilibrium Ising model, with additional logarithmic corrections in the heat-capacity scaling, attributed to the presence of quenched disorder.

The rest of the Chapter is structured as follows: Section 5.2 the model is introduced, along side the observables studied and the numerical approach followed. Section 5.3 contains the results, and Section 5.4 gives a summary of the work.

5.2 Model and Methods

5.2.1 Model

Similar to the Baxter-Wu model in the presence of a crystal field, discussed in Chapters 3 and 4, the Blume-Capel model has a Hamiltonian containing a nearest-neighbour interactions terms, only this time interactions are between two spins, as well as a single-ion anisotropy term. With the addition of a time-dependent oscillating external magnetic field, the model is defined by the Hamiltonian

$$\mathcal{H} = -J \sum_{\langle ij \rangle} \sigma_i \sigma_j + \sum_i \Delta_i \sigma_i^2 - h(t) \sum_i \sigma_i. \tag{5.1}$$

The spin, σ_i, are allowed to take the values $\{-1, 0, +1\}$. The summation is performed over nearest neighbours, and the coupling strength $J > 0$ corresponds to ferromagnetic interactions. The crystal-field strength Δ_i controls the density of the zero spins. Choosing a site-dependent bimodal probability distribution for Δ_i

$$P(\Delta_i) = p\delta(\Delta_i + \Delta) + (1 - p)\delta(\Delta_i - \Delta), \tag{5.2}$$

implies that each site has a crystal field of strength $-\Delta$ or Δ, with probability p and $1-p$ respectively. Of course, $p \in (0,1)$, and denotes a control parameter of the disorder. The mean of the distribution is $\mu = \Delta(1-2p)$, while the standard deviation $s = 2\Delta\sqrt{p(1-p)}$. Interestingly, this form of disorder favours the appearance of zero spins in certain sites (where Δ is quenched to a positive value), while disfavouring the appearance of $\sigma = 0$ in the rest of the sites. This has interesting effects on the location of the transition points that will be discussed later. Lastly, the magnetic field term $h(t)$ defines a spatially uniform time-dependent magnetic field. This is chosen to be periodically oscillating, so that all lattice sites are exposed to a square-wave magnetic field with amplitude h_0 and half-period $t_{1/2}$, following [239–241].

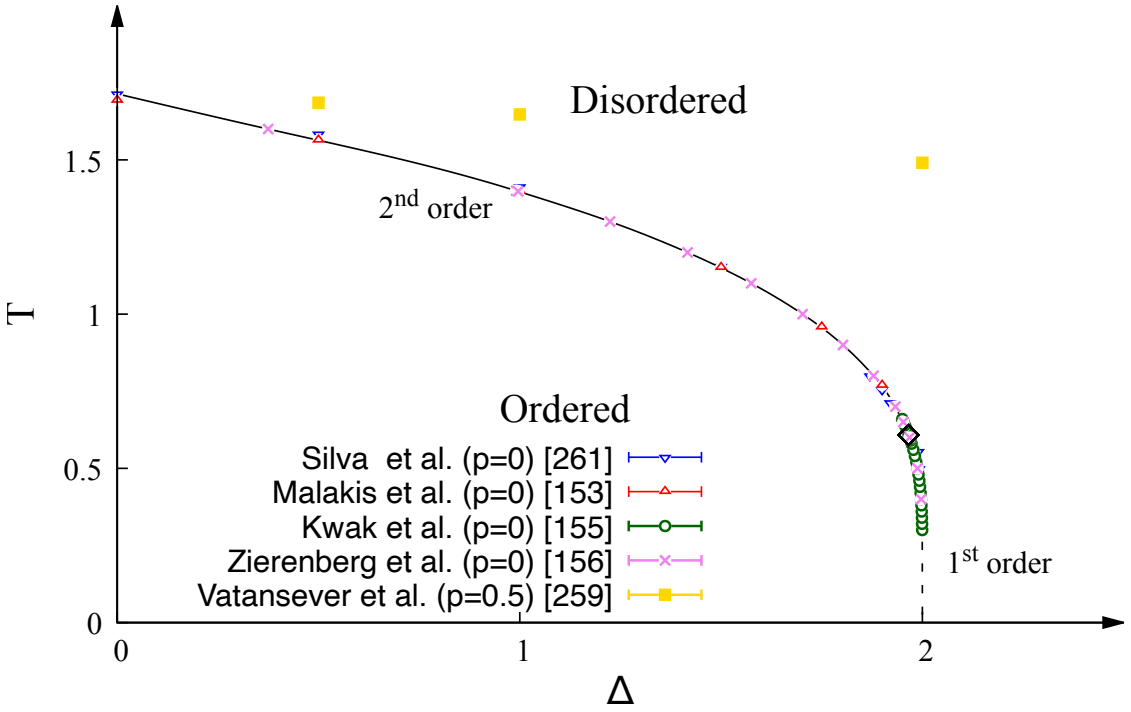

FIGURE 5.1: Phase diagram, containing results for both the pure ($p = 0$) and the random ($p = 1/2$) square-lattice Blume-Capel model. For the pure model, the ferromagnetic and paramagnetic phases are separated by a continuous transition solid line, at the small Δ regime, as well as a discontinuous dashed line, for large Δ. The two lines meet at a tricritical point (Δ_t, T_t), indicated by the black rhombus.

Even without the magnetic field term, the model of Eq. (5.1) has many interesting properties. At equilibrium, i.e. for $h(t) = 0$, and for $\Delta \to \infty$ the model maps to the random-site spin-1/2 Ising. A site will be populated with probability p or vacant with probability $1-p$ [257]. Moreover, when $p = 0$, the first term of the distribution 5.2 is absent, and the pure Blume-Capel model is recovered [153, 155, 156, 261]. In the random model ($p > 0$), a rise in the critical temperatures is observed (see Fig. 5.1) [259].

Figure 5.1 depicts the phase diagram of the model, in the (Δ, T) plane, with $h(t) = 0$, for the cases of $p = 0$, i.e. pure model, and $p = 1/2$. The pure system undergoes continuous transitions in the small-Δ regime and discontinuous transitions in the large-Δ regime. These are portrayed by the solid and dashed black lines, respectively. The second-order transitions are in the Ising universality class. The critical line crosses the temperature axis at $T_0 \approx 1.693$ [153]. The line of first-order transitions meets the x-axis at $\Delta_0 = zJ/2$. For the square lattice specifically, the coordination number is equal to $z = 4$. The tricritical point, where the two line segments join is approximately located at $\Delta_t \approx 1.966$ and $T_t \approx 0.608$ [155]. As per the rest of the thesis, the exchange-interaction strength and the Boltzmann constant were fixed to unity ($J = k_B = 1$).

5.2.2 Simulation protocol

The numerical method followed was the single-spin-flip Metropolis update, performed on a square lattice with periodic boundary conditions. [26, 78, 79]. Together with stochastic Glauber dynamics [262], these two techniques are the standard approaches to study dynamical transitions with Monte Carlo simulations [240]. The algorithm is described thoroughly in Section 2.3. Here, all transitions among the three possible spin states, i.e. $\{-1, 0, +1\}$, are considered for the proposed update.

More specifically, the above protocol was applied to the model of Eq. (5.1), with the disorder of the distribution (5.2). The external magnetic field applied was a time oscillating square-wave, uniform across the whole lattice. Simulations were performed at the values of the crystal-field strength $\Delta = 0.5, 1$, and 2, with the disorder parameter $p = 1/2$ always, and using as a guide the work of reference [259]. The linear size of the systems considered was in the range $L = 32 - 512$, with 500 independent disorder realisations used for each L to average for the results, using the jackknife method (see Appendix A). Each time 10^3 periods of the magnetic field were discarded as the thermalisation time. Data were actually collected in the subsequent 11×10^3 field periods. The time unit was set as one whole sweep of the lattice, or one Monte Carlo step per site (MCSS). The strength of the magnetic field was set to $h_0 = 0.3$, and the temperature to $T(\Delta) = 0.8 \times T_c(\Delta)$. This way ensuring that the metastable decay of the system, due to the field reversal, materialises through nucleation and growth of many droplets in the stable phase, i.e. the multi-droplet regime, a point emphasised by previous works [237, 241]. As mentioned, following the work of Vatansever et al. [259], the equilibrium critical temperatures considered were $T_c(\Delta = 0.5) = 1.6854$, $T_c(\Delta = 1) = 1.6473$, and $T_c(\Delta = 2) = 1.4907$, specific for $p = 1/2$.

5.2.3 Observables

Due to the oscillating magnetic field, it makes physical sense to study period-averaged thermodynamic observables, instead of simply averaging over the typical equilibrium observables,

such as the energy and the magnetisation. For a field with a half period $t_{1/2}$, the period-averaged magnetisation is defined by

$$Q_L = \frac{1}{2t_{1/2}} \oint M(t)dt, \tag{5.3}$$

with the integral running over a period of the field, and $M(t)$ being the time-dependent magnetisation per site

$$M(t) = \frac{1}{N} \sum_{i=1}^{N} \sigma_i(t). \tag{5.4}$$

From the discussion in Section 5.1, concerning the behaviour of the magnetisation, it is expected that in the ordered phase the probability density of Q_L becomes bimodal. To distinguish this phase from the disordered one and capture the symmetry breaking, the order parameter is defined as the average of the absolute of Q_L, i.e. $\langle |Q| \rangle_L$. A similar definition to Eq. (5.3) exists for the period-averaged energy, E.

Following the same discussion of Section 1.1.5, it is straightforward to define quantities analogous to the susceptibilities of the energy and the magnetisation at equilibrium. These susceptibilities of the period-averaged quantities play an important role in the study of the dynamical transition. The variance of the dynamic order parameter is defined as

$$\chi_L^Q = N \left[\langle Q^2 \rangle_L - \langle Q \rangle_L^2 \right], \tag{5.5}$$

behaving as a substitute for the nonequilibrium susceptibility and theoretically justified by the fluctuation-dissipation relations [227]. In the same fashion, the variance of the period-averaged energy can be designated by

$$\chi_L^E = N \left[\langle E^2 \rangle_L - \langle E \rangle_L^2 \right], \tag{5.6}$$

which can be thought of as a proxy for the heat capacity. Furthermore, with Q in place for the magnetisation, a fourth-order Binder cumulant [203, 263] can also be defined

$$U_L^Q = 1 - \frac{\langle |Q|^4 \rangle_L}{3 \langle |Q^2|^2 \rangle_L}, \tag{5.7}$$

following [237, 238].

5.3 Results

To begin with, Figs. 5.2, 5.3, and 5.4 illustrate the behaviour of the magnetisation and showcase the underlying mechanisms that lead to the dynamical phase transition. Employing a single disorder realisation for a system with linear size $L = 192$, at $\Delta = 1$, what was discussed

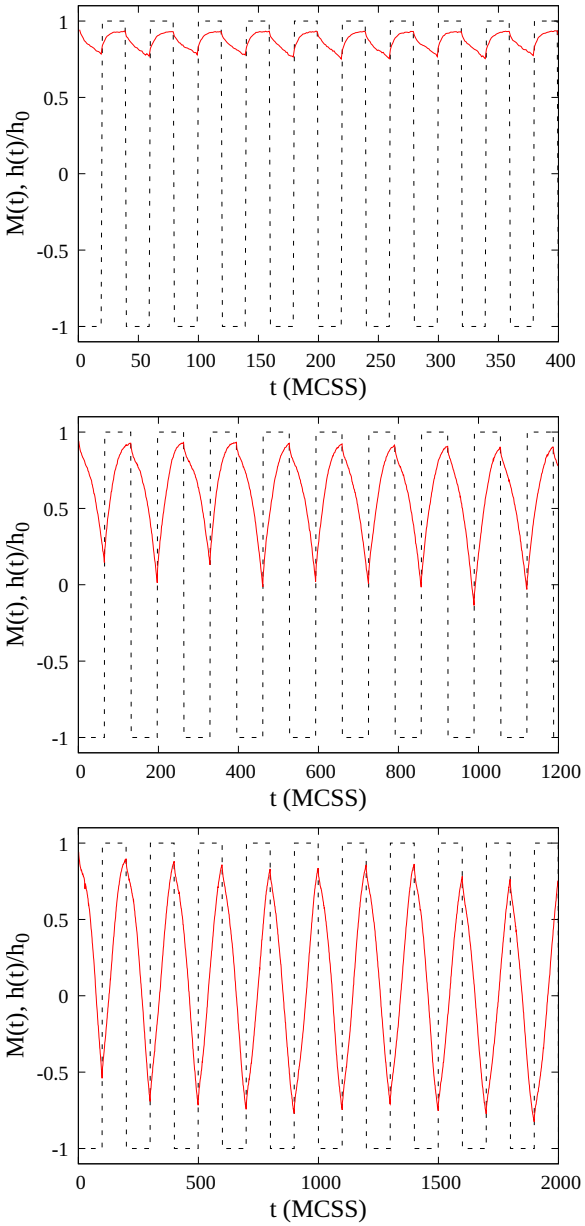

FIGURE 5.2: Time dependence of the magnetisation (red solid lines) of the random Blume-Capel model with $p = 1/2$, in a square-wave magnetic field (black dashed lines) for a system of linear size $L = 192$, at $\Delta = 1$. Three values of the half period of the external field are considered. **Upper panel**: $t_{1/2} = 20$ MCSS, corresponding to a dynamically ordered phase. **Middle panel**: $t_{1/2} = 66$ MCSS, close to the dynamic phase transition. **Lower panel**: $t_{1/2} = 100$ MCSS, corresponding to a dynamically disordered phase. For comparative reasons, the ratio $h(t)/h_0$ is displayed for the field.

in Section 5.1 can be seen in these plots. Specifically, Fig. 5.2 compares the evolution of the magnetisation with time, for different regimes of the external field's half-period. The red lines indicate the magnetisation, while the black ones the magnetic field. As expected, when the field is oscillating rapidly, as in the upper panel, the spins are not given enough time to follow. This results effectively a constant magnetisation and a dynamically ordered phase. In the lower panel, where the oscillation is slow, the spins have adequate time to switch to the orientation of the field, resulting in a zero magnetisation on average and a disordered phase. In the intermediate regime (middle panel of Fig. 5.2), the half-period $\tau_{1/2}$ and the metastable time τ are comparable. This is where the transition takes place.

Figure 5.3 tells the same tale, but from the point of view of the period-averaged magnetisation of Eq. (5.3), Q, pinpointing the role of this quantity as the order parameter. In the dynamically ordered phase, for a finite system, $Q > 0$, while in the disordered phase $Q \approx 0$. For $\tau_{1/2} \approx \tau$, an intermediary behaviour is observed, where Q is strongly fluctuating. Note that since the equality is not exact, some non-vanishing finite-size effects are expected. It is clear that the half-period is equivalent to the temperature in equilibrium systems. Since its comparative size to τ plays an important role for characterising the phase of the system, following reference [241], the parameter $\Theta = t_{1/2}/\tau$ is defined. In other words, the transition happens at the critical point $t^c_{1/2}$, or equivalently when $\Theta \approx 1$.

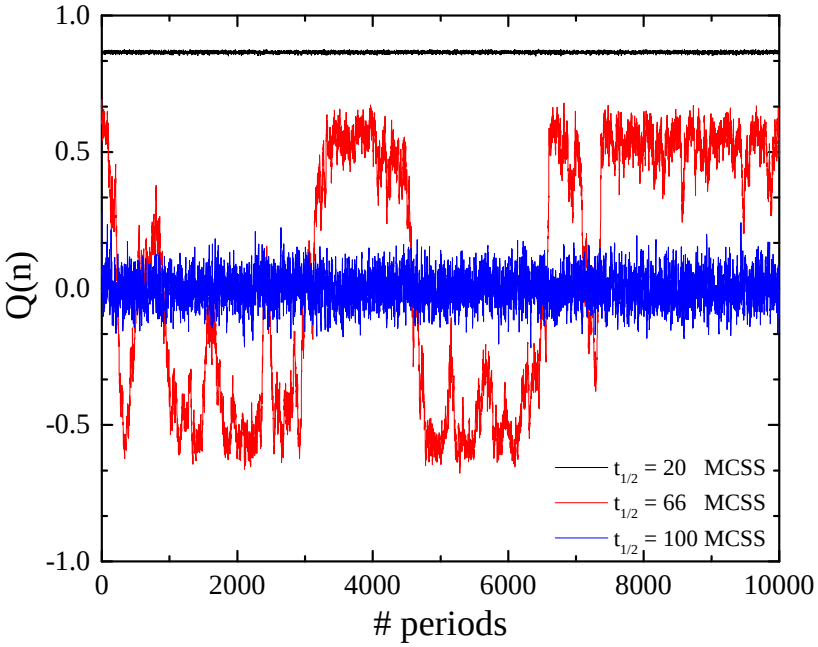

FIGURE 5.3: Period dependence of the dynamic order parameter, Q, of the random $p = 1/2$ Blume-Capel model. The plot concerns $L = 192$ and $\Delta = 1$. Three characteristic cases of the half period of the external field are shown, corresponding to Fig. 5.2.

Figure 5.4 contains some snapshots of the local order parameter Q_x, at site x, for the respective cases discussed above. When $t_{1/2} < t_{1/2}^c$ (upper panel), the majority of the time most spins are in the state $\sigma_x = +1$, i.e. in the metastable phase during the first half-period and in the stable equilibrium phase during the second half-period. Of course, thermal fluctuations are also observed. The system is then in the dynamically ordered phase, and $Q_x \approx +1$. Contrarily, on the opposite regime of a slowly varying field, the spins follow the field intently, with a small lag. In this regime, $Q_x \approx 0$ (bottom panel), and the dynamically disordered phase is observed. Around the vicinity of $t_{1/2}^c$, a dynamic phase transition is expected, and indeed large clusters of all values of Q_x are observed, ± 1 and 0 (middle panel).

As a last example for the qualitative behaviour of the system, Figs. 5.5, 5.6, and 5.7 illustrate the behaviour of the dynamic quadrupole moment O, in full analogy to Figs. 5.2, 5.3, and 5.4, respectively, using the same simulation parameters. Following the definition of Q, O is calculated from

$$O = \frac{1}{t_{1/2}} \oint \rho(t) dt, \tag{5.8}$$

with

$$\rho(t) = 1 - \frac{1}{N} \sum_{i=1}^{N} \sigma_i^2. \tag{5.9}$$

This quantity denotes the order parameter that is conjugate to the crystal-field coupling Δ. It will elucidate the role of the zero spins, $\sigma_x = 0$, something that Q_x cannot do, since it does not have the ability to distinguish between areas of zero spins and areas where the spins are distributed randomly in ± 1. Thus, in full analogy to Fig. 5.4, Fig. 5.5 illustrates configurations of the dynamic quadrupole moment O_x, over a cycle of the field. Moreover, Fig. 5.6 is analogous to Fig. 5.2, presenting how ρ of Eq. (5.9) varies with time, given the half-period of the external magnetic field. Finally, Fig. 5.7 corresponds to Fig. 5.3, presenting the time-evolution of O.

Comparing to the case of the spin-1/2 Ising model, where $\rho = 0$ due to the lack of zero spins, in the Blume-Capel case the value of O changes with Δ. At $\Delta = -\infty$, the Ising model is recovered. As it increases, vacancies start appearing, and O grows. Specifically for $p = 1/2$ and $\Delta = 1$, as was seen in the figures, the vacancies do not play a very significant role. It should be expected however that as p decreases, vacancies will become more prominent [see Eq. (5.2)]. Moreover, increasing Δ will also force more vacancies to appear, in the small-p scenario. Looking at the phase diagram of Fig. 5.1, this corresponds to studying the ex-first-order regime of the equilibrium model [259]. Looking at Figs. 5.8 and 5.9, the values $p = 0.02$ and $\Delta = 2$ for the parameters seem like a promising choice. There, configurations of the local dynamic order parameter and quadrupole moment, for different values of the half-period, are shown. The effects of the vacancies there can be seen to be of great importance for the underlying transition.

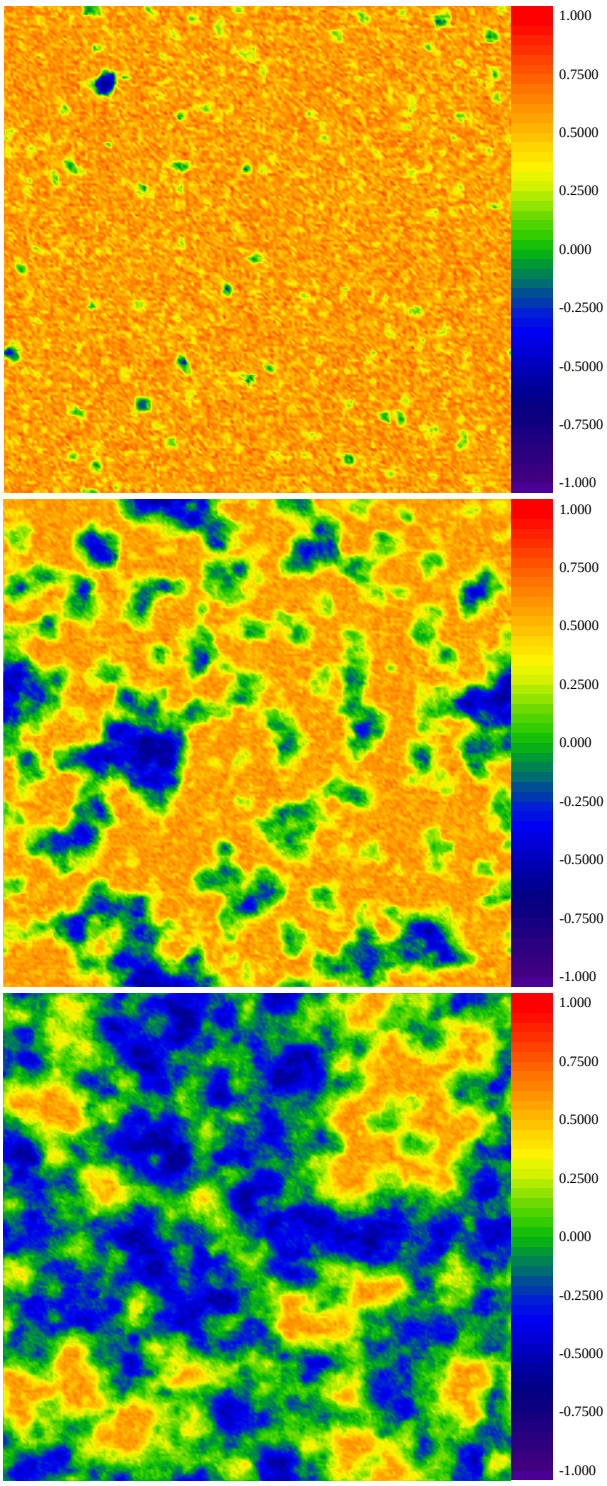

FIGURE 5.4: Configurations of the local dynamic order parameter Q_x, at site x, of the random $p = 1/2$ Blume-Capel model. Again, $L = 192$ and $\Delta = 1$. These "snapshots" concern the local period-averaged spins for three representative values of the half period. **Upper panel**: $t_{1/2} = 20$ MCSS $< t^c_{1/2}$, i.e. in the dynamically ordered phase. **Middle panel**: $t_{1/2} = 66$ MCSS $\approx t^c_{1/2}$, near the dynamic phase transition. **Lower panel**: $t_{1/2} = 100$ MCSS $> t^c_{1/2}$, i.e. in the dynamically disordered phase.

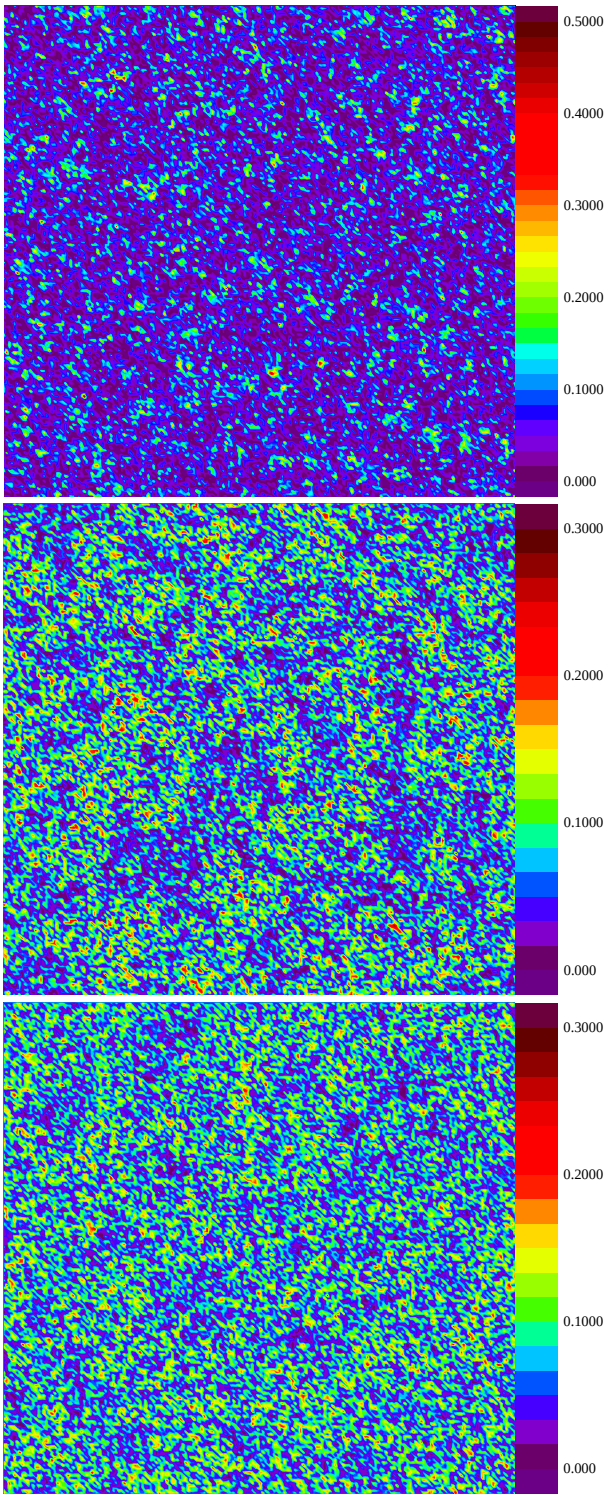

FIGURE 5.5: In full analogy with Fig. 5.4, snapshots of the period-averaged quadrupole moment, O_x, conjugate to the crystal-field coupling Δ. Simulation parameters are the same in the respective panels of Fig. 5.4.

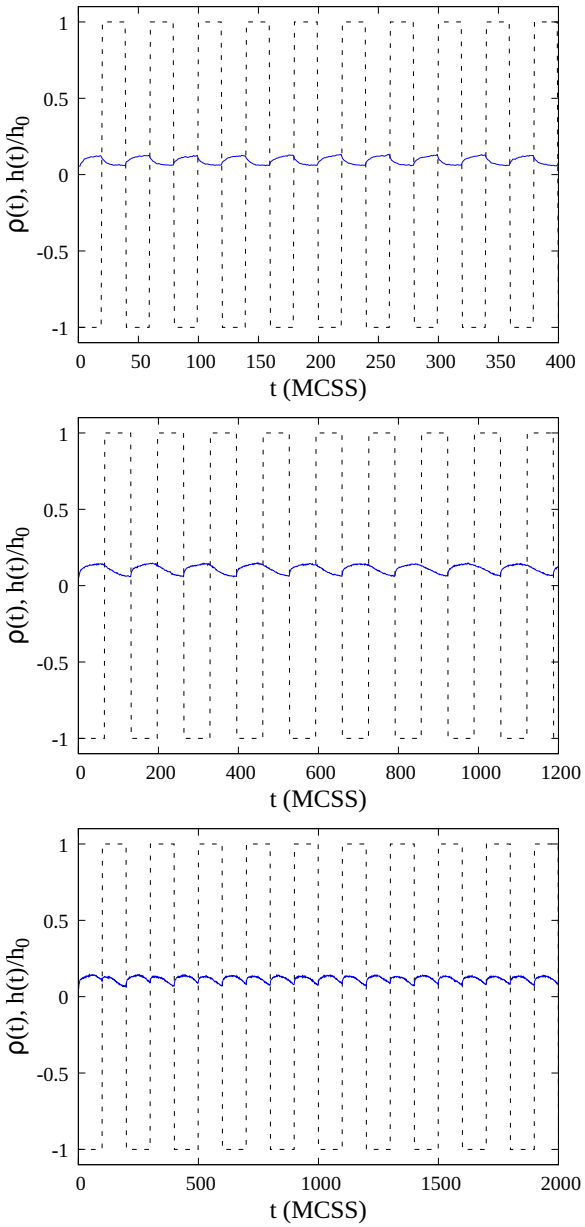

FIGURE 5.6: Time series of the order parameter conjugate to the crystal field $\rho(t)$ (solid blue curves) of the random $p = 1/2$ Blume-Capel model under the presence of a square-wave magnetic field (black dashed lines). Similar to Fig. 5.2, $L = 192$ and $\Delta = 1$. The same three values of the half period were used. **Upper panel**: $t_{1/2} = 20$ MCSS. **Middle panel**: $t_{1/2} = 66$ MCSS. **Lower panel**: $t_{1/2} = 100$ MCSS. For the sake of clarity, the ratio $h(t)/h_0$ is displayed.

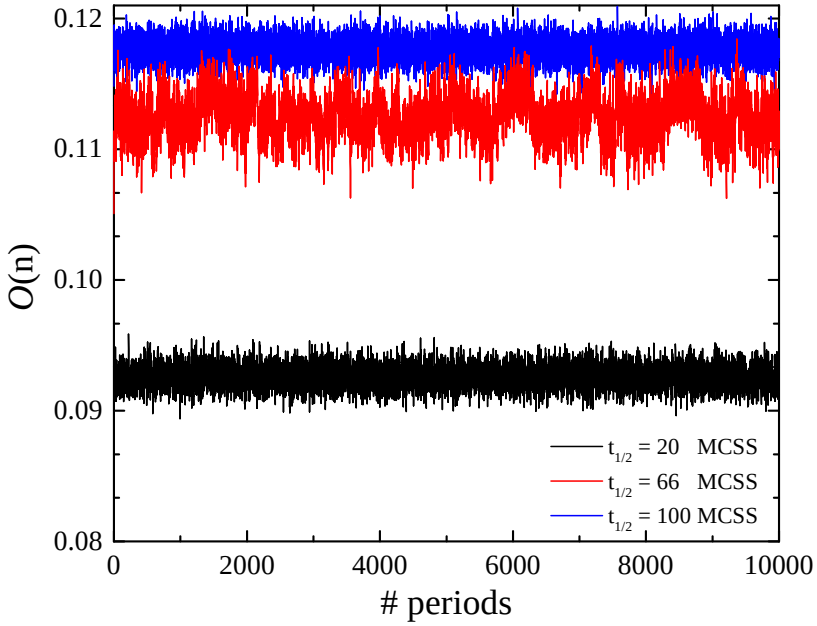

FIGURE 5.7: Period dependencies of the dynamic quadrupole moment, O, of the random $p = 1/2$ Blume-Capel model for $L = 192$ at $\Delta = 1$. The same half periods as in Fig. 5.6 were used.

To probe the properties of dynamic phase transition of the random Blume-Capel model, the finite-size scaling behaviour of the period-averaged observables and their susceptibilities was analysed. Following previous works [237–241], even though finite-size scaling is specific for equilibrium system, as discussed in Section 1.4, it can be generalised to systems that are out of equilibrium.

In Fig. 5.10 the finite-size behaviour of the dynamic order parameter Q [Eq. (5.3)] and its susceptibility χ^Q [Eq. (5.5)] are presented at $\Delta = 1$ and two characteristic system sizes. Similarly to the magnetisation in equilibrium systems, for small $t_{1/2}$, Q takes a finite value and as $t_{1/2}$ increases, Q tends to zero. A steep decline is observed around the phase transition, giving rise to a corresponding peak in the susceptibility. The location and value of the maxima of χ^Q_L, denoted as $t^\star_{1/2}$ and $(\chi^Q_L)^\star$ respectively, can be utilised for the finite-size scaling analysis. The same goes for the heat-capacity maxima, $(\chi^E_L)^\star$.

The critical half-period $t^c_{1/2}$ and the exponent ν can be determined, following the same finite-size scaling analysis performed in equilibrium systems. For $\Delta = 1$ specifically, the main panel of Fig. 5.11 shows the scaling of the locations of the maxima of the maxima of χ^Q_L and χ^E_L. A similar behaviour was seen in the two other values of Δ studied, and the findings are shown in Table 5.1. Notice that with increased Δ the value of $t^c_{1/2}$ decreases, implying that strongly favouring zero spins in half the lattice sites while strongly disfavouring them in others helps reduce the metastable time of the system. Figure 5.11 illustrates the shift behaviour of the peak locations, and an extrapolation for the critical half-period, $t^\star_{1/2}$, using a simultaneous fit of the

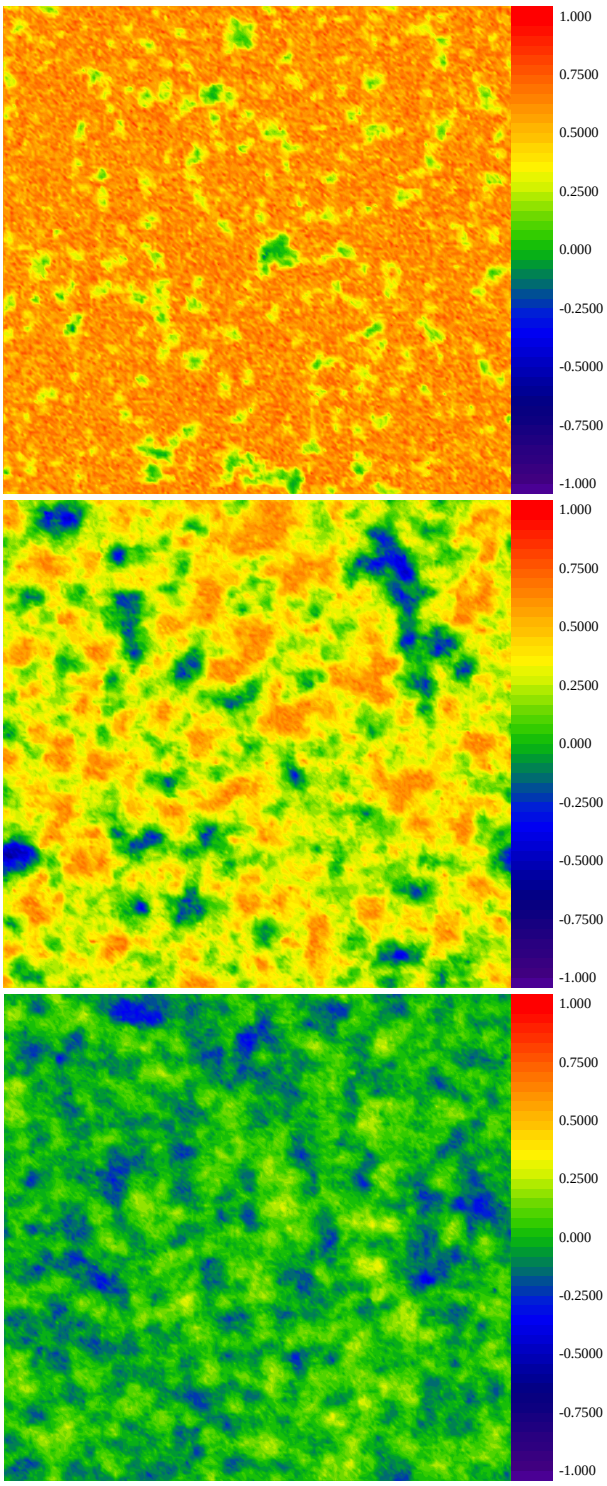

FIGURE 5.8: Configurations of the local dynamic order parameter Q_x of the random Blume-Capel model for $L = 192$, $p = 0.02$, and $\Delta = 2$. Note that for this set of (p, Δ) parameters, the critical half period of the system was approximated to be very roughly $t^c_{1/2} \approx 53$, using the peak positions of the corresponding dynamic susceptibility and heat-capacity curves. **Upper panel**: $t_{1/2} = 20$ MCSS $< t^c_{1/2}$, i.e. dynamically ordered phase. **Middle panel**: $t_{1/2} = 53$ MCSS $\approx t^c_{1/2}$, i.e. near the dynamic phase transition. **Lower panel**: $t_{1/2} = 100$ MCSS $> t^c_{1/2}$, i.e. dynamically disordered phase.

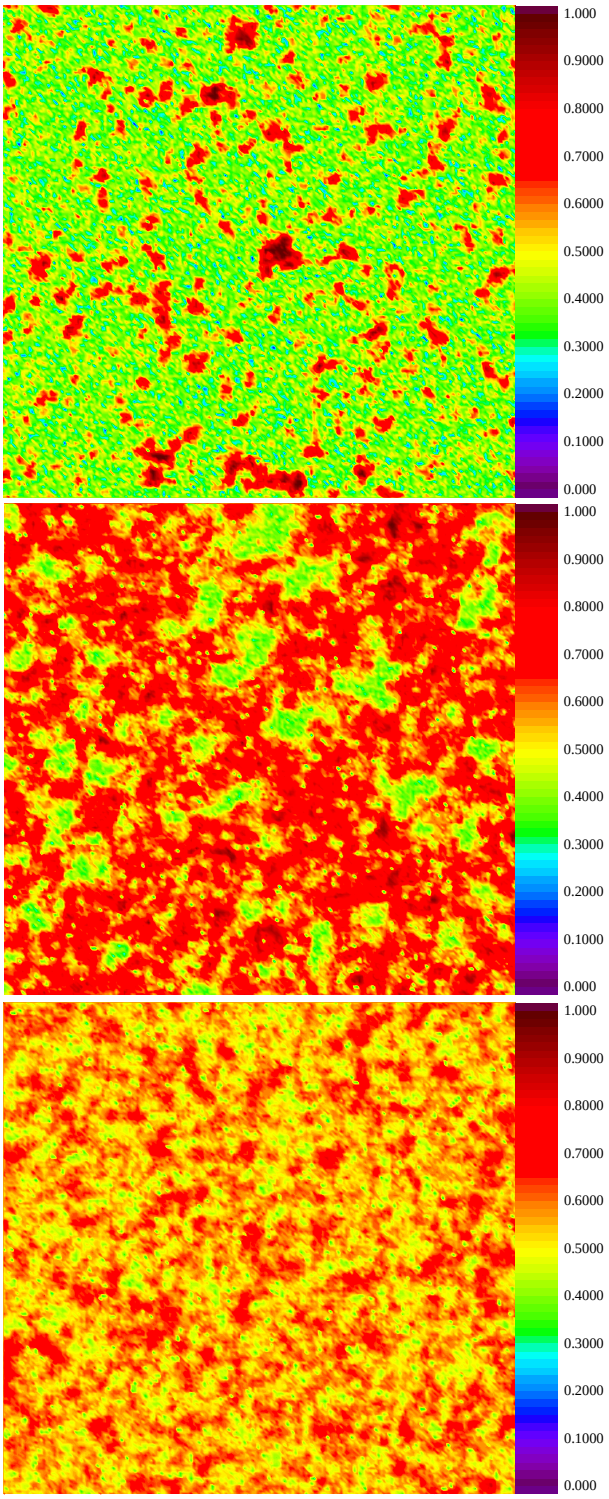

FIGURE 5.9: Snapshots of the period-averaged quadrupole moment conjugate to the crystal-field coupling Δ, in full analogy with Fig. 5.8. Simulation parameters are the same as those used in the respective panels of Fig. 5.8.

form [264–266]

$$t^{\star}_{1/2} = t^{c}_{1/2} + bL^{-1/\nu}. \tag{5.10}$$

In the end, the values $t^{c}_{1/2} = 65.96(6)$ and $\nu = 1.03(3)$ are obtained, with the latter being in agreement with the value $\nu = 1$ of the two-dimensional Ising universality class [267].

The inset of Fig. 5.11 depicts the fourth-order Binder cumulant, U^{Q}_{L} [see Eq. (5.7)] at $\Delta = 1$ and a range of sizes studied. The vertical dashed line corresponds to the critical half-period estimated from the main panel. The horizontal line marks the universal value of the Binder cumulant of the 2D equilibrium Ising model, $U^{\star} = 0.610\ 692\ 4(16)$ [268]. Even though the crossing depends on the lattice size and shape, as well as the boundary conditions and isotropic interactions [269, 270], Hasenbusch et al. [271] presented strong evidence that the two-dimensional site-diluted Ising model has the same value for the Binder cumulant as its pure counterpart, at equilibrium. The plots shown are in qualitatively agreement with this value.

Turning now to the scaling analysis of the maxima of the dynamic susceptibility and heat-capacity: Figure 5.12 exhibits the size evolution of $(\chi^{Q}_{L})^{\star}$ in a log-log plot, for the different values of the crystal-field strength considered, $\Delta = 0.5$, 1, and 2. Fits were performed using [185]

$$\left(\chi^{Q}_{L}\right)^{\star} \sim L^{\gamma/\nu}. \tag{5.11}$$

In all cases, the magnetic exponent ratio γ/ν is in very good agreement with the value of $7/4$ of the Ising universality. Results can be seen in Table 5.1. From the work of Dotsenko et al. [66] for the disordered Ising ferromagnet, it is expected that the heat-capacity maxima $(\chi^{E}_{L})^{\star}$ will follow a double logarithmic law. Although this is difficult to observe, for $L \geq 64$ (see Fig. 5.13) the data are described quite well by fits of the form

$$\left(\chi^{E}_{L}\right)^{\star} \sim \ln\left[\ln\left(L\right)\right]. \tag{5.12}$$

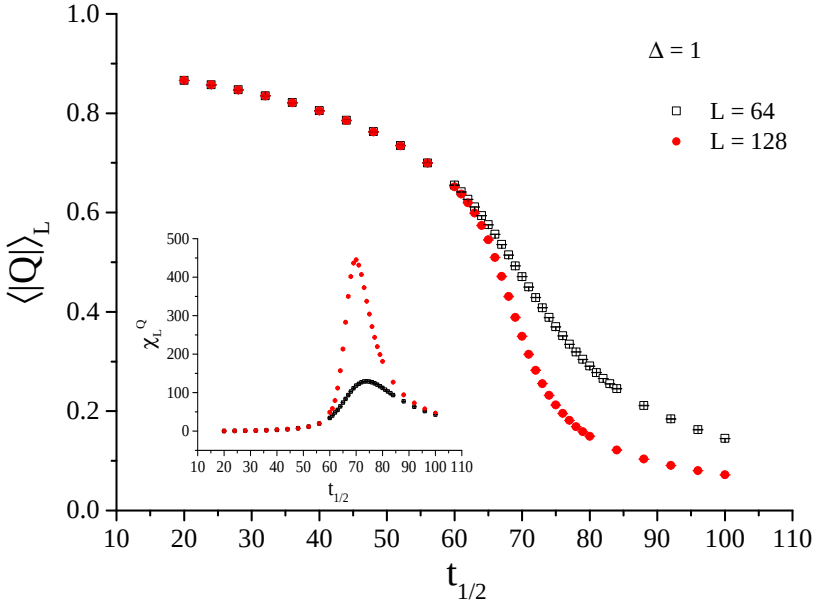

FIGURE 5.10: Characteristic dynamic order parameter curves for $\langle |Q| \rangle_L$ (main panel) and the susceptibility χ_L^Q (inset), for the random $p = 1/2$ Blume-Capel model at $\Delta = 1$, and for two system sizes.

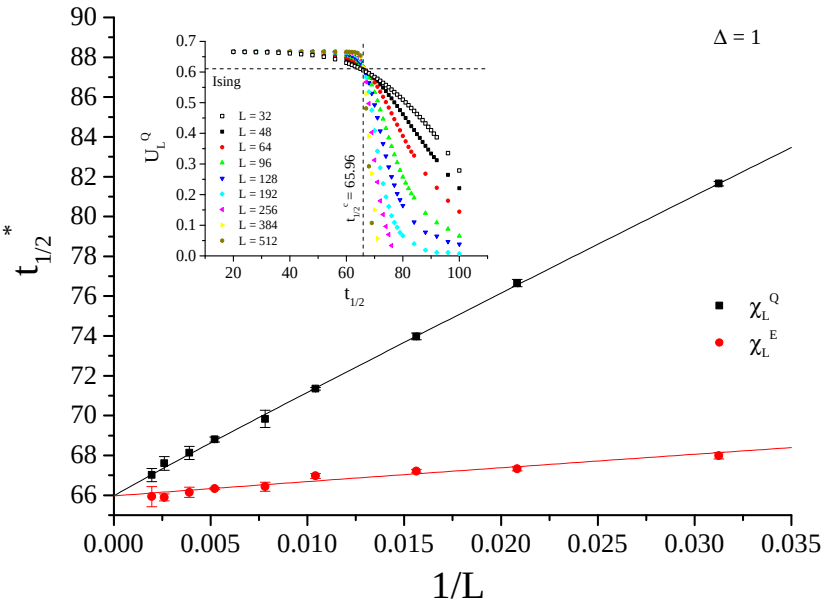

FIGURE 5.11: Shift behaviour of the two pseudocritical half periods, $t^*_{1/2}$, corresponding to the locations of the maxima of the dynamic susceptibility (filled black squares) and heat capacity (filled red circles). Results concern $p = 1/2$ and $\Delta = 1$. The inset illustrates the half-period dependency of the corresponding fourth-order Binder cumulant U_L^Q.

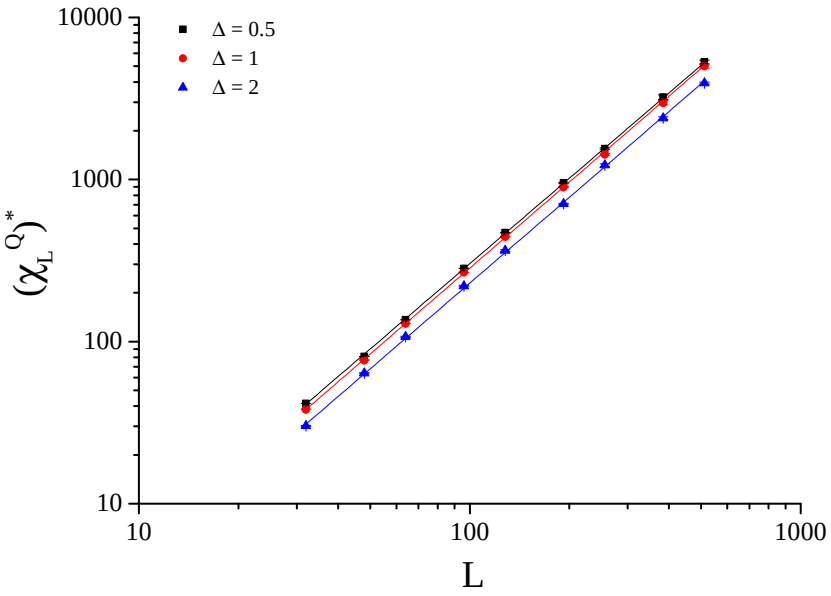

FIGURE 5.12: Finite-size scaling of the dynamic susceptibility, $(\chi_L^Q)^*$, for the random $p = 1/2$ Blume-Capel model. Results are shown for three values of Δ and a log-log scale was used.

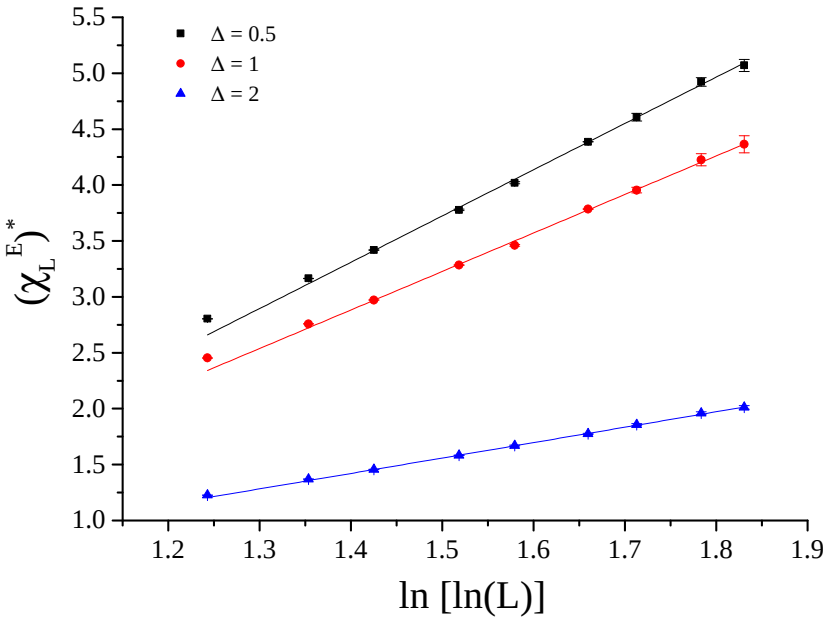

FIGURE 5.13: Double logarithmic scaling behaviour of the heat-capacity maxima $(\chi_L^E)^*$ of the random $p = 1/2$ Blume-Capel model for the three values of Δ considered.

5.4 Conclusions

This Chapter studied the two-dimensional Blume-Capel model under the effect of quenched disorder in the crystal-field coupling, by making use of extensive Monte Carlo simulations. By the application of a time-dependent oscillating external magnetic field, it was observed that the system undergoes a dynamical phase transition. To grasp the properties of this transition, initially the period averaged magnetisation and quadrupole moment were studied. The former acts like an order parameter for the system, while the latter does not play an important role for the values of Δ studied and the strength of the disorder considered. Following the application of an extensive finite-size scaling analysis, the location of the transition was estimated and critical exponents were calculated with a fairly good accuracy. All the estimates were compatible with the respective exponent of the equilibrium Ising ferromagnet. Additionally, the results revealed the anticipated double logarithmic divergence of the heat capacity. Ultimately, as discussed in Chapter 1, universality is a cornerstone in the theory of critical phenomena, it stands however on less solid foundations when it comes to off-equilibrium systems, especially when coupled with the presence of quenched disorder. Hopefully, this work will help stimulate further interest in this topic.

TABLE 5.1: A summary of critical parameters describing the dynamic phase transition of the square-lattice Blume-Capel model in a quenched random crystal field. Note that the values of Δ considered in the current work, given the randomness distribution [Eq. (5.2)] with $p = 1/2$, correspond to the second-order transition regime of the model's equilibrium phase diagram.

Δ	$t^{c}_{1/2}$	ν	γ/ν
0.5	72.41(9)	1.00(3)	1.75(1)
1	65.96(6)	1.03(3)	1.76(1)
2	47.61(7)	1.05(7)	1.75(2)

Conclusions and Outlook

In the current thesis, a number of questions were studied via Monte Carlo simulations, mostly centred around spin-1 models. In Chapter 3 the dynamical critical scaling, at equilibrium, of the three-spin nearest-neighbour interactions Baxter-Wu model was discussed. Implementing algorithms that incorporate clusters, it was shown that, in the spin-1 generalisation of the model, the dynamical exponent z depends on the value of the crystal-field strength Δ, a phenomenon that becomes more apparent as Δ crosses to positive values. Furthermore, in Chapter 4, the critical properties of the spin-1 Baxter-Wu model in a crystal field were probed. Away from the multicritical point, this model was clearly shown to undergo continuous transitions that belong to the universality class of its spin-1/2 counterpart (and thus to the respective universality class of the 4-states Potts model). However, as the multicritical point was approached along the line of continuous transitions, first-order-like characteristics started to appear in the distributions of the energy probability density function. These features were attributed to finite-size effects, via an interface tension analysis, and the model was subsequently shown to not change its scaling behaviour, at least up to $\Delta = 0.5$. Lastly, in Chapter 5, the kinetic Blume-Capel model in two-dimensions was analysed. By applying a periodically oscillating external magnetic field, as well as implementing a random disorder in the crystal-field strength, a non-equilibrium phase transition was observed, depending on the period of the oscillating magnetic field. Generalising observables to their period-averaged counterparts led to discovering that these new observables scale with critical exponents indicative of the Ising universality class.

Going one step further, Chapter 3 was based on the idea of implementing a cluster algorithm, through a hybrid scheme, to study the spin-1 Baxter-Wu model near its pentacritical point. The hybrid scheme was chosen to consist of one part Swendsen-Wang implementation of a cluster and one lattice sweep of the restricted heat bath. Judging from an implementation of a cluster in the spin-1/2 model, an increased efficiency was expected, showcased by the value of the dynamical critical exponent z. This seemed to be the case when looking at negative values of Δ. However, the three-spin interactions, in conjunction with the increased density of the zero spins, proved to be too much for such an approach. In the end, the hybrid scheme was shown to be almost as inefficient as a single-spin-flip update, at least in the vicinity of the multicritical point. It is expected then that this point of interest will probably be located and studied using the more straightforward Metropolis or heat-bath algorithms. The observed behaviour of z could be due to the specific algorithm implemented [136], paving the way for a thorough study of the percolation properties of the algorithm. It could also however be a characteristic

of models where first- and second-order transitions meet, since cluster methods work well for Potts models, but are not expected to perform the same close to these multicritical points.

In Chapter 4, using a multicanonical algorithm implemented in parallel on GPUs, was enough to study the universality of the spin-1 Baxter-Wu model for values of $\Delta \leq 0.5$. Additional Wang-Landau simulations at $\Delta = -10$ and -1 corroborated that the universality of the spin-1/2 model is retained. However, it became clear that such methods can not be implemented for the study of the pentacritical point. In the cases were $\Delta \geq 0$ the author had to implement the analysis in GMP (GNU Multiple Precision Arithmetic Library) and MPFR (GNU Multiple Precision Floating-Point Reliable Library), in order to make sure that the reweighting process was not encountering arithmetic issues. This fact, in conjunction to the conclusions for Chapter 3 make it abundantly clear to that the way to locate and study the multicritical point via Monte Carlo simulations is by using a restricted heat bath algorithm, or some of the methods discussed in Chapter 2, in conjunction with the field-mixing method [206]. To that end, some universal distributions of field-mixed conjugate energies were estimated and compared to the energy universal distribution. As expected, along the continuous transition line of the phase boundary, these distributions coincided qualitatively.

In Chapter 5, the response of critical properties to outside factors that drive the system out of equilibrium was showcased. In essence, similar to previous studies, the important conclusion that the equilibrium scaling properties are transferred to the kinetic model was drawn. It would be interesting to study what happens in the ex-first-order regime. Although this is well established for the case of the equilibrium transition [29], it is not so for the dynamic transition. Additionally, because of the shift of the phase diagram due to the incorporated disorder, and possible re-entrant phenomena, choosing the transition points that fulfil the criteria is not simple. In Chapter 5 a suggestion was given, by looking at the qualitative behaviour of the system at small values of the disorder strength and large values of the crystal-field strength.

Ultimately, spin-1 models, at their core, offer a rich foundation for exploring diverse phenomena. The ability of zero spins to mimic lattice dilution enhances the applicability of these models in describing real-world materials. Introducing elements of randomness or an oscillating external magnetic field adds further complexity, particularly when considering the regime where first-order transitions manifest on the pure model. However, navigating through such intricacies not only challenges our comprehension of critical phenomena but also provides a valuable opportunity to test and refine our methods and understanding.

As a last comment; Monte Carlo simulations will continue to benefit from the constant increase of computational power, allowing for the utilisation of better hardware as well as more elaborate methods. The addition of machine learning techniques has also been on the rise in recent years. In that sense, the field is expected to continue to grow, hoping to solve open question that still remain unanswered.

Appendix A

Data Analysis

This Appendix serves as a small discussion on data analysis, with the aim of explaining how results and errors are calculated. In that sense, it precedes the discussion on simulation methods of Chapter 2, since understanding the analysis that follows any simulation is the most important step towards designing a proper experiment. However, every method utilised is very standard and can be found in any good statistics book [57], thus including it in the main text would be somewhat redundant. Throughout this Appendix, random variables will be denoted with capital letters, for example X, while observations of these variable will be indicated by the respective small-case latter.

A.1 Mean and variance

In general, the end result of a simulation is a time series or some sampled data $\{x_i\}_{i=1}^{N}$ of an observed random variable X. In essence, X is drawn from some distribution, $P(X)$, which is unknown. Of course, if the distribution was known a priori, any information could be extracted directly from it. Firstly, the distribution should be normalised, ie

$$\int_{-\infty}^{+\infty} P(x)dx \equiv 1. \tag{A.1}$$

Then any moment of X could be calculated directly from

$$\langle X^n \rangle \equiv \int_{-\infty}^{+\infty} x^n P(x)dx. \tag{A.2}$$

Since the distribution is not known, these quantities can be approximated from the sampled data set. Of course, these estimates should be accompanied with well defined errors in order to extract any meaningful conclusions. Depending on the method the set $\{x_i\}_{i=1}^{N}$ was sampled, any moment can be estimated directly. In the most general case, the data would have been sampled from some distribution $Q(X)$, and the proper weight $P(x)$ could be assigned to each measurement

$$\overline{x^n} \equiv \frac{\sum_{i=1}^{N} x_i^n P(x_i)/Q(x_i)}{\sum_{i=1}^{N} P(x_i)/Q(x_i)} \approx \langle X^n \rangle. \tag{A.3}$$

where the denominator was used for normalisation. The quantity $\overline{x^n}$ is an unbiased estimator for $\langle X^n \rangle$, since the equation becomes exact in the limit of $N \to \infty$.[1] This is what happens for example in multicanonical and Wang-Landau simulations (see Chapter 2).

For random sampling in X that follows a flat $Q(X)$ distribution, then Eq. (A.3) simply becomes

$$\overline{x^n} \equiv \frac{\sum_{i=1}^{N} x_i^n P(x_i)}{\sum_{i=1}^{N} P(x_i)}. \tag{A.4}$$

Usually, as happens in most of the methods discussed in chapter 2, X is sampled from $P(X)$. Then $Q(X) = P(X)$ and Eq. (A.3) reduces to

$$\overline{x^n} \equiv \frac{1}{N} \sum_{i=1}^{N} x_i^n. \tag{A.5}$$

Note that with a change of variables in x_i all the above estimators can map to Eq. (A.5), just by absorbing the weight factors and the normalisation term directly into the variable x_i. For that reason, and to keep the discussion brief, focus will only be placed on the latter estimator of the mean, without any loss of generality.

It should be stressed that all the above estimators are also random variables; If the initial experiment is repeated many times, each would result in different $\overline{x^n}$. Since Eq. (A.5) is an average of random samples, it follows a Gaussian distribution.[2] This can be proven rigorously by the central limit theorem of statistics [73]. The Gaussian distribution is completely defined by its mean and variance, since all other moments are zero. The standard deviation, which is the square root of the variance, has the very handy property of indicating exactly how spread out the distribution is. Specifically, $\sim 68\%$ of the experiments would reside within one standard deviation from the mean. Additionally, $\sim 95\%$ would be within two standard deviation, etc. Thus, the standard deviation of an estimator of the mean can be used as a well defined indication of its error.

The variance of a random variable X is defined as

$$\sigma^2(X) \equiv \left\langle \left(X - \langle X \rangle\right)^2 \right\rangle = \left\langle X^2 \right\rangle - \langle X \rangle^2. \tag{A.6}$$

In order to calculate the variance of $\overline{x}$, substitute Eq. (A.5) into Eq. (A.6), and assuming translational invariance in the data set, it holds that

[1] An estimator is called biased if its mean returns the quantity of interest plus terms that decrease $\sim N$ of the data set. An example of a biased estimator will be seen in Eq. (A.11).

[2] This is true if the original distribution $P(X)$ has finite moments.

$$\sigma^2(\overline{x}) = \langle \overline{x}^2 \rangle - \langle \overline{x} \rangle^2 = \frac{\sigma^2(x_i)}{N} 2 \left[\frac{1}{2} + \sum_{k=1}^{N} \frac{\langle x_1 x_{1+k} \rangle - \langle x_1 \rangle \langle x_{1+k} \rangle}{\langle x_i^2 \rangle - \langle x_i \rangle^2} \left(1 - \frac{k}{N} \right) \right], \tag{A.7}$$

where the fact the all the individual measurements have the same variance was used, $\sigma^2(x_i) = \langle x_i^2 \rangle - \langle x_i \rangle^2$, since they come from the same distribution.

Defining the autocorrelation function as $A(k) = \langle x_1 x_{1+k} \rangle - \langle x_1 \rangle \langle x_{1+k} \rangle$, the variance can be written as

$$\sigma^2(\overline{x}) = \frac{\sigma^2(x_i)}{N} 2 \left[\frac{1}{2} + \sum_{k=1}^{N} \frac{A(k)}{A(0)} \left(1 - \frac{k}{N} \right) \right]. \tag{A.8}$$

The term in brackets measures the correlation of the data and is called the integrated autocorrelation time [41]

$$\tau_{\text{int}} \equiv \frac{1}{2} + \sum_{k=1}^{N} \frac{A(k)}{A(0)} \left(1 - \frac{k}{N} \right). \tag{A.9}$$

For uncorrelated data $\tau_{\text{int}} = \frac{1}{2}$, since $A(k) = 0$ for any $k \neq 0$. For correlated data the variance will be increased by a factor proportional to τ_{int}. The integrated autocorrelation time can then be though of also as a reduction in the number of independent measurements sampled. Specifically,

$$\sigma^2(\overline{x}) = \frac{\sigma^2(x_i)}{N} 2\tau_{\text{int}} = \frac{\sigma^2(x_i)}{N_{\text{eff}}}, \tag{A.10}$$

where the number of total measurements N has given way to the number of effective measurement N_{eff}, increasing the variance of the average. Note that for uncorrelated measurements ($\tau_{\text{int}} = 1/2$) $\sigma(\overline{x}) = \sigma(x_i)/N$.

Equation (A.10) indicates that to find $\sigma^2(\overline{x})$ it is enough to construct an estimator for the variance of the individual measurements $\sigma^2(x_i)$. To accomplish that, start from $\overline{x^2} - \overline{x}^2$ and substitute the definitions for the moments [Eq. (A.5)]

$$\left\langle \overline{x^2} - \overline{x}^2 \right\rangle = \sigma^2(x_i) - \frac{\sigma^2(x_i)}{N_{\text{eff}}}. \tag{A.11}$$

Note that this is a biased estimator for $\sigma^2(x_i)$, since it approaches it with a factor decreasing as $\sim 1/N$. Finally, using Eq. (A.10), an unbiased estimator for $\sigma^2(\overline{x})$ can be defined as

$$\sigma^2(\overline{x}) = \frac{\left\langle \overline{x^2} - \overline{x}^2 \right\rangle}{N_{\text{eff}} - 1}, \tag{A.12}$$

which implies that the error decreases as $\sim 1/\sqrt{N}$. Upon expanding, the well-known estimator for the variance of the average $\overline{x}$ is retrieved

$$\frac{\overline{x^2} - \overline{x}^2}{N_{\text{eff}} - 1} = \frac{1}{N_{\text{eff}}(N_{\text{eff}} - 1)} \sum_{i=1}^{N} (x_i - \overline{x})^2 \,. \tag{A.13}$$

This discussion is adequate when one wants to estimate the means of an observed quantity's moments and their respective error. In general functions, $f(X)$, of observables will need to be calculated. Such quantities, like the specific heat [Eq. (1.19)] and magnetic susceptibility [Eq. (1.21)], play a central role in statistical physics. A simple substitution, $f(\overline{x})$, would result in a biased estimator for $f(\langle X \rangle)$, if the function is non-linear in X.[3] A systematic way of estimating, without bias, functions of observables and their variances. The first step towards accomplishing these goals is to separate the original observables into bins.[4]

A.2 Resampling Methods

A.2.1 Binning of data

The binning of data provides a simple way of dealing with one of the issues mentioned above, namely data correlation. In general, some correlation will always exist, due to measurements being taken consecutively within small time steps, not allowing for the decorrelation of the system. After large enough time steps however, the system will have decorrelated enough to treat the measurements as uncorrelated. A general treatment in such cases can come from binning data together, transforming the original set $\{x_i\}_{i=1}^{N}$ to $\{y_k\}_{k=1}^{N_{\text{Bins}}}$, where N_{Bins} is the number of bins used. Each member of the new set is produced by averaging over $N_{\text{B}} = N/N_{\text{Bins}}$ consecutive data of the original set. By choosing $N_{\text{B}} \gg \tau_{\text{int}}$ the binned data can be considered almost uncorrelated. The new data set can be extrapolated by

$$y_k \equiv \frac{1}{N_{\text{B}}} \sum_{i=1}^{N_{\text{B}}} x_{(k-1)N_{\text{B}}+j} \tag{A.14}$$

In general, the data $\{x_i\}$ that fall on each bin can be used to calculate derived quantities. Given for example a function $f(X)$, an estimate of $f(\langle X \rangle)$ can be computed by $f_k = f(y_k)$, $k = 1, \ldots N_{\text{Bins}}$. Then the set $\{f_k\}_{k=1}^{N_{\text{Bins}}}$ can be analysed with the methods described in the previous section, solving the issue of producing both an estimator and its error.

However, binning does not deal with the biases. First of all, since $\overline{y} = \overline{x}$, $\sigma^2(\overline{x}) = \sigma^2(\overline{y})$. Additionally, starting from the definition of N_{eff} of Eq. (A.10), the integrated autocorrelation time

[3] An example of this can be seen in the estimation of the variance $\sigma^2(x_i)$ of Eq. (A.11). The estimator was biased because $\langle x_i \rangle^2$ was replaced with $\overline{x}^2$, and $\langle \overline{x}^2 \rangle \neq \langle x_i \rangle^2$.

[4] To be a bit more quantitative, for example in Eq. (A.11) the bias decreases as $1/N$. Additionally, in Eq. (A.12) the error decreases much more slowly like $1/\sqrt{N}$. In that sense, in most reasonable applications, the bias does not play a very important role.

for the binned data will be smaller. The new number of effective measurements is $N_{\text{eff}}^{(\text{Bins})} = N_{\text{Bins}} / \left(2\tau_{\text{int}}^{(\text{Bins})}\right) = N / \left(2\tau_{\text{int}}^{(\text{Bins})} N_B\right)$, and for $N_{\text{B}} > 2\tau_{\text{int}}$, the effective measurements become $N_{\text{eff}}^{(\text{Bins})} < N / \left(2\tau_{\text{int}}^{(\text{Bins})} 2\tau_{\text{int}}\right) < N / \left(2\tau_{\text{int}}\right)$, or $N_{\text{eff}}^{(\text{Bins})} < N_{\text{eff}}$.

In the end, binning produces a new set of data of smaller effective measurements. Thus, a larger bias enters in the calculations of variances in Eq. (A.11). To proceed, a process that removes the bias from these estimations is required. There are a number of ways to accomplish this, and the one used was the jackknife resampling method, which, likewise binning, manipulates the original data set and also provides a systematic way of dealing with biases.

A.2.2 Jackknife method

Similarly to the binning method, the jackknife scheme merges the data while also allowing for data overlap between the bins. Even though the new data set has similar entries, due to the overlap, there is a formal treatment that not only takes into account these additional correlations, but also removes the bias from our estimators. The discussion continues from the binning process, assuming a data set $\{x_i\}_{i=1}^{N}$ of uncorrelated measurements, produced by binning with a large enough bin size. Then, a new set $\{x_k^J\}_{k=1}^{N_{\text{Bins}}}$ is defined, where each x_k is the average of the whole data set, if the k^{th} entry is excluded. That way

$$x_k^J \equiv \frac{1}{N-1} \sum_{i \neq k, i=1}^{N} x_i. \tag{A.15}$$

This is the average of the data set if one bin of measurements is excluded. Due to the overlap the new set is trivially correlated, however these correlations can be exactly accounted for.

Mean

The jackknife method can be used to estimate $f(\langle X \rangle)$ with $f_k^J \equiv f(x_k^J), k = 1, \ldots, N$. Taking the average over all the jackknife estimates would result in

$$\overline{f^J} \equiv \frac{1}{N} \sum_{i=1}^{N} f_i^J. \tag{A.16}$$

Taylor expanding f_i^j around the mean $f(\langle X \rangle)$ and keeping only terms up to second order

$$f(x_i^J) = f(\langle X \rangle) + \left.\frac{\partial f(x)}{\partial x}\right|_{x=\langle x \rangle} \left(x_i^J - \langle x \rangle\right) + \frac{1}{2} \left.\frac{\partial^2 f(x)}{\partial x^2}\right|_{x=\langle x \rangle} \left(x_i^J - \langle x \rangle\right)^2. \tag{A.17}$$

Taking the mean

$$\langle f(x_i^J)\rangle = f(\langle X\rangle) + \frac{1}{2}\left.\frac{\partial^2 f(x)}{\partial x^2}\right|_{x=\langle x\rangle} \sigma^2(x_i^J), \tag{A.18}$$

and replacing from Eq. (A.16) results in

$$\left\langle \overline{f^J} \right\rangle = f(\langle X\rangle) + \frac{1}{2}\left.\frac{\partial^2 f(x)}{\partial x^2}\right|_{x=\langle x\rangle} \sigma^2(x_i^J). \tag{A.19}$$

The variance that appears on the right hand side is very similar in principle to the variance $\sigma^2(\overline{x})$. In fact, their only difference is that in $\sigma^2(x_i^J)$ the i^{th} data entry was excluded. Specifically, $\sigma^2(x_i^J) = \sigma^2(\overline{x})$, but when it comes to their estimator, in $\sigma^2(x_i^J)$ Eq. (A.13) needs to be applied without using x_i, resulting in $N-1$ entries. Replacing with the estimator of the jackknife data will result in

$$f(\langle X\rangle) \approx \overline{f^J} - \frac{1}{2}\left.\frac{\partial^2 f(x)}{\partial x^2}\right|_{x=\langle x\rangle} \frac{1}{N}\sum_{i=1}^{N} \frac{\left((x_i^2)^J\right) - \left(x_i^J\right)^2}{N-2}. \tag{A.20}$$

The term $(x_i^2)^J$ implies to first square the data set and then apply the jackknife resampling. Expanding the last sum and keeping terms that fall only as $\sim 1/N$ leads to[5]

$$f(\langle X\rangle) \approx \overline{f^J} - \frac{1}{2}\left.\frac{\partial^2 f(x)}{\partial x^2}\right|_{x=\langle x\rangle} \frac{\overline{x^2} - \overline{x}^2}{N-2}. \tag{A.21}$$

The same calculation for the original data set yields

$$\langle f(\overline{x})\rangle = f(\langle X\rangle) + \frac{1}{2}\left.\frac{\partial^2 f(x)}{\partial x^2}\right|_{x=\langle x\rangle} \sigma^2(\overline{x}). \tag{A.22}$$

Since the data are uncorrelated, $\sigma^2(\overline{x}) = \sigma^2(x_i)/N$, according to Eq. (A.10). Using Eq. (A.12)

$$f(\langle X\rangle) \approx f(\overline{x}) - \frac{1}{2}\left.\frac{\partial^2 f(x)}{\partial x^2}\right|_{x=\langle x\rangle} \frac{\overline{x^2} - \overline{x}^2}{N-1}. \tag{A.23}$$

Combining linearly Eqs. (A.21) and (A.23) can lead to an unbiased estimator for $\langle f(\overline{x})\rangle$. For example, excluding again terms that drop faster than $1/N$

$$f(\langle X\rangle) \approx N f(\overline{x}) - (N-1)\overline{f^J}. \tag{A.24}$$

Variance

With the same argument used in Appendix A.1, the variance of the estimators can be used as a well defined error. Specifically, the variance of $\overline{f^J}$ is

[5] Expecting the bias to decrease with $\sim 1/N$ and the error as $\sim 1/\sqrt{N}$, as discussed in Appendix A.1, there is no reason to keep the rest of the terms.

$$\sigma^2\left(\overline{f^J}\right) = \left\langle \overline{f^J}^2 \right\rangle - \left\langle \overline{f^J} \right\rangle^2. \tag{A.25}$$

Initially, the hypothesis that the original data are uncorrelated was made. Taking this into account, together with the fact that most jackknife bins consist of mostly the same data (see Eq. (A.15)) Eq. (A.10) implies that the variance of the jackknife mean can be calculated from

$$\sigma^2\left(\overline{f^J}\right) = (N-1)\sigma^2(f_i^J), \tag{A.26}$$

where $\sigma^2(f_i^J)$ is the variance of the sampled jackknife dataset.

Appendix B

Least-Square Fits

This Appendix contains a thorough reporting of various least square fits performed in the thesis. The emphasis is placed specifically in Chapter 3, where a large amount of fits were performed.

B.1 Dynamical Scaling in the Dilute Baxter-Wu Model

The following tables show the various fits performed in Chapter 3. It should be noted that the linear fits were performed using a logarithms. However, this was not an issue for the errors, since they were very small in comparison to the values of τ, making an error propagation approximation reliable. As for the non-linear fits which include corrections, one can never be too sure about being stuck in a local minimum of the parameter space. To this end, many different initial points were used, in order to make sure that the fits are reliable. Notice the cases where the correction-term errors were very large or the fit qualities unacceptable, indicating that the linear fit might be a better choice.

B.1.1 Spin-1/2 τ_{int} and τ_x fits

The fits for τ_{int} at T_c for the Swendsen-Wang algorithm follow:

	Fits without corrections: $\tau_{\text{int}} \sim L^z$					
L_{min}	z	z_{error}	a	a_{error}	Q	χ^2/dof
12	1.164	0.007	0.769	0.030	0.60	0.84
15	1.159	0.008	0.790	0.033	0.74	0.68
18	1.153	0.009	0.818	0.037	0.91	0.44
24	1.150	0.010	0.831	0.042	0.90	0.44
30	1.149	0.011	0.837	0.047	0.84	0.49
36	1.154	0.013	0.812	0.055	0.85	0.44
48	1.159	0.015	0.789	0.065	0.83	0.43
54	1.171	0.017	0.735	0.077	0.98	0.09
60	1.171	0.021	0.732	0.094	0.95	0.12
72	1.175	0.028	0.716	0.130	0.85	0.17
96	1.179	0.049	0.696	0.231	0.57	0.33

TABLE B.1: Linear fits for the integrated autocorrelation time τ_{int} of the spin-1/2 Baxter-Wu model using the Swendsen-Wang algorithm. Fits were performed using Eq. (3.6).

	Fits with corrections: $\tau_{\text{int}} = aL^z(1 + c/L^2)$							
L_{min}	z	z_{error}	a	a_{error}	c	c_{error}	Q	χ^2/dof
12	1.143	0.012	2.369	0.125	-11.988	5.393	0.91	0.47
15	1.143	0.014	2.378	0.147	-12.824	8.470	0.86	0.52
18	1.150	0.016	2.298	0.167	-3.305	13.660	0.87	0.48
24	1.161	0.021	2.176	0.209	15.835	26.228	0.88	0.44
30	1.182	0.026	1.969	0.249	62.172	46.932	0.96	0.25
36	1.188	0.034	1.903	0.314	81.740	77.375	0.93	0.28
48	1.222	0.059	1.610	0.477	195.999	189.320	0.93	0.22
54	1.187	0.072	1.919	0.698	57.195	245.683	0.96	0.11
60	1.197	0.093	1.828	0.857	100.172	361.594	0.86	0.15
72	1.208	0.144	1.721	1.272	162.017	695.368	0.60	0.28

TABLE B.2: Fits for the integrated autocorrelation time τ_{int} of the spin-1/2 Baxter-Wu model using the Swendsen-Wang algorithm, including corrections. Fits were performed using Eq. (3.7).

The fits for τ_x at T_c for $x = 1.5$ for the Swendsen-Wang algorithm follow:

	Fits with corrections: $\tau_{\text{int}} = aL^z(1 + c/L^2)$					
L_{min}	z	z_{error}	a	a_{error}	Q	χ^2/dof
12	1.143	0.003	-0.034	0.012	0.59	0.85
15	1.142	0.003	-0.030	0.013	0.57	0.86
18	1.141	0.003	-0.024	0.015	0.55	0.87
24	1.141	0.004	-0.024	0.017	0.45	0.98
30	1.141	0.004	-0.024	0.019	0.36	1.11
36	1.141	0.005	-0.024	0.022	0.26	1.29
48	1.141	0.006	-0.024	0.025	0.17	1.54
54	1.149	0.007	-0.062	0.030	0.56	0.75
60	1.149	0.008	-0.062	0.037	0.39	1.00
72	1.149	0.011	-0.062	0.052	0.22	1.50
96	1.180	0.021	-0.212	0.098	0.97	0.00

TABLE B.3: Linear fits for the autocorrelation time τ_x, for $x = 1.5$ of the spin-1/2 Baxter-Wu model using the Swendsen-Wang algorithm. Fits were performed using Eq. (3.6).

	Fits with corrections: $\tau_{\text{int}} = aL^z(1 + c/L^2)$							
L_{min}	z	z_{error}	a	a_{error}	c	c_{error}	Q	χ^2/dof
12	1.139	0.005	0.984	0.021	-2.241	2.287	0.59	0.84
15	1.140	0.006	0.981	0.024	-1.675	3.350	0.50	0.93
18	1.142	0.006	0.970	0.028	1.506	5.325	0.46	0.97
24	1.145	0.008	0.956	0.036	6.596	9.995	0.39	1.05
30	1.147	0.010	0.946	0.044	11.456	16.363	0.30	1.20
36	1.154	0.014	0.917	0.061	28.901	31.503	0.24	1.36
48	1.187	0.023	0.777	0.088	136.490	69.221	0.51	0.83
54	1.169	0.029	0.848	0.124	69.033	98.211	0.47	0.84
60	1.186	0.038	0.778	0.151	144.319	150.201	0.36	1.02
72	1.251	0.064	0.556	0.184	499.942	334.736	0.64	0.21

TABLE B.4: Fits for the autocorrelation time τ_x, for $x = 1.5$, of the spin-1/2 Baxter-Wu model using the Swendsen-Wang algorithm, including corrections. Fits were performed using Eq. (3.7).

The fits for τ_{int} at T_c for the Metropolis algorithm follow:

	Fits without corrections: $\tau_{\text{int}} \sim L^z$					
L_{min}	z	z_{error}	a	a_{error}	Q	χ^2/dof
12	2.134	0.018	-0.873	0.067	0.31	1.16
15	2.124	0.020	-0.832	0.079	0.29	1.19
18	2.140	0.024	-0.899	0.094	0.34	1.12
24	2.158	0.028	-0.977	0.114	0.37	1.08
30	2.169	0.033	-1.025	0.138	0.31	1.18
36	2.139	0.040	-0.889	0.172	0.37	1.08
48	2.136	0.050	-0.875	0.218	0.26	1.30
54	2.139	0.058	-0.891	0.260	0.17	1.62
60	2.139	0.071	-0.891	0.323	0.09	2.16
72	2.068	0.100	-0.555	0.466	0.07	2.71
96	1.860	0.188	0.453	0.899	0.05	3.71

TABLE B.5: Linear fits for the integrated autocorrelation time τ_{int} of the spin-1/2 Baxter-Wu model using the Metropolis algorithm. Fits were performed using Eq. (3.6).

	Fits with corrections: $\tau_{\text{int}} = aL^z(1 + c/L^2)$							
L_{min}	z	z_{error}	a	a_{error}	c	c_{error}	Q	χ^2/dof
12	2.137	0.033	0.410	0.058	1.710	12.034	0.26	1.25
15	2.179	0.042	0.339	0.062	36.069	25.040	0.43	1.01
18	2.174	0.048	0.346	0.075	30.716	37.173	0.34	1.13
24	2.142	0.062	0.405	0.115	-15.860	64.530	0.30	1.20
30	2.076	0.074	0.555	0.191	-130.298	90.997	0.38	1.07
36	2.111	0.100	0.467	0.224	-46.424	189.848	0.29	1.23
48	2.070	0.178	0.575	0.507	-171.024	472.083	0.19	1.51
54	1.974	0.221	0.934	1.030	-489.954	598.436	0.13	1.89
60	1.798	0.254	2.265	2.865	-1063.307	636.573	0.09	2.39
72	1.686	0.425	4.021	8.655	-1457.609	1296.909	0.03	4.71

TABLE B.6: Fits for the integrated autocorrelation time τ_{int} of the spin-1/2 Baxter-Wu model using the Metropolis algorithm, including corrections. Fits were performed using Eq. (3.7).

B.1.2 Spin-1 τ_{int} fits for the hybrid algorithm

The fits for τ_{int} at $\Delta = -10$ follow:

	No corrections linear fit: $\log \tau_{\text{int}} = a + z * L$					
L_{min}	z	z_{error}	a	a_{error}	Q	χ^2/dof
12	1.194	0.005	0.151	0.022	0.00	2.59
15	1.184	0.006	0.196	0.024	0.56	0.87
18	1.180	0.006	0.213	0.027	0.69	0.72
24	1.178	0.007	0.224	0.030	0.66	0.73
30	1.179	0.008	0.220	0.034	0.57	0.83
36	1.175	0.009	0.239	0.040	0.56	0.81
48	1.172	0.010	0.252	0.047	0.47	0.91
54	1.174	0.012	0.241	0.055	0.35	1.10
60	1.170	0.014	0.263	0.067	0.25	1.36
72	1.179	0.019	0.220	0.092	0.17	1.80
96	1.227	0.032	-0.017	0.156	0.83	0.05

TABLE B.7: Linear fits for the integrated autocorrelation time τ_{int} of the spin-1 Baxter-Wu model at $\Delta = -10$. Fits were performed using Eq. (3.6).

	Fits with corrections: $\tau_{\text{int}} = aL^z(1 + c/L^2)$							
L_{min}	z	z_{error}	a	a_{error}	c	c_{error}	Q	χ^2/dof
12	1.163	0.008	1.341	0.050	-18.572	3.741	0.62	0.81
15	1.171	0.010	1.295	0.058	-11.041	6.458	0.75	0.66
18	1.173	0.011	1.284	0.066	-8.433	10.105	0.67	0.73
24	1.174	0.014	1.274	0.086	-5.650	18.892	0.56	0.83
30	1.165	0.018	1.333	0.113	-26.457	30.130	0.54	0.84
36	1.171	0.023	1.291	0.145	-8.496	51.412	0.43	0.97
48	1.202	0.040	1.109	0.223	94.951	127.228	0.40	1.00
54	1.208	0.051	1.073	0.276	122.006	184.518	0.26	1.32
60	1.270	0.069	0.778	0.274	432.830	310.143	0.43	0.85
72	1.359	0.115	0.488	0.294	993.694	700.566	0.49	0.48

TABLE B.8: Fits for the integrated autocorrelation time τ_{int} of the spin-1 Baxter-Wu model at $\Delta = -10$, including corrections. Fits were performed using Eq. (3.7).

The fits for τ_{int} at $\Delta = -1$ follow:

	No corrections linear fit: $\log \tau_{\text{int}} = a + z * L$					
L_{min}	z	z_{error}	a	a_{error}	Q	χ^2/dof
12	1.264	0.006	0.170	0.025	0.24	1.26
15	1.260	0.006	0.188	0.028	0.33	1.14
18	1.253	0.007	0.221	0.031	0.77	0.63
24	1.247	0.008	0.248	0.035	0.94	0.37
30	1.242	0.009	0.268	0.040	0.97	0.27
36	1.238	0.010	0.287	0.046	0.98	0.20
48	1.240	0.012	0.280	0.055	0.95	0.23
54	1.236	0.014	0.297	0.064	0.93	0.22
60	1.231	0.017	0.323	0.079	0.91	0.19
72	1.219	0.023	0.377	0.108	0.98	0.02
96	1.224	0.039	0.356	0.186	0.91	0.01

TABLE B.9: Linear fits for the integrated autocorrelation time τ_{int} of the spin-1 Baxter-Wu model at $\Delta = -1$. Fits were performed using Eq. (3.6).

	Fits with corrections: $\tau_{\text{int}} = aL^z(1 + c/L^2)$							
L_{min}	z	z_{error}	a	a_{error}	c	c_{error}	Q	χ^2/dof
12	1.239	0.010	1.333	0.058	-15.126	4.464	0.18	1.38
15	1.231	0.011	1.384	0.070	-22.899	6.806	0.80	0.60
18	1.230	0.013	1.387	0.081	-23.425	10.752	0.72	0.67
24	1.228	0.016	1.400	0.108	-26.827	20.405	0.64	0.74
30	1.228	0.021	1.400	0.139	-26.827	34.796	0.52	0.87
36	1.234	0.027	1.361	0.178	-10.414	60.056	0.45	0.95
48	1.200	0.044	1.612	0.353	-120.570	126.093	0.87	0.32
54	1.192	0.056	1.678	0.474	-150.720	183.132	0.78	0.36
60	1.192	0.071	1.678	0.606	-150.720	266.929	0.58	0.54
72	1.238	0.116	1.328	0.793	90.252	573.495	0.88	0.02

TABLE B.10: Fits for the integrated autocorrelation time τ_{int} of the spin-1 Baxter-Wu model at $\Delta = -1$, including corrections. Fits were performed using Eq. (3.7).

The fits for τ_{int} at $\Delta = 0$ follow:

	No corrections linear fit: $\log \tau_{\text{int}} = a + z * L$					
L_{min}	z	z_{error}	a	a_{error}	Q	χ^2/dof
12	1.300	0.005	0.328	0.023	0.00	3.33
15	1.294	0.005	0.358	0.025	0.00	2.76
18	1.286	0.006	0.396	0.027	0.04	1.88
24	1.281	0.006	0.417	0.030	0.06	1.77
30	1.276	0.007	0.443	0.033	0.12	1.56
36	1.272	0.008	0.464	0.037	0.13	1.57
48	1.265	0.009	0.500	0.041	0.25	1.30
54	1.259	0.010	0.526	0.047	0.26	1.27
60	1.254	0.011	0.553	0.054	0.24	1.34
72	1.243	0.013	0.609	0.067	0.33	1.14
96	1.223	0.017	0.713	0.087	0.75	0.40
120	1.211	0.023	0.778	0.118	0.77	0.27
144	1.195	0.033	0.861	0.172	0.75	0.10

TABLE B.11: Linear fits for the integrated autocorrelation time τ_{int} of the spin-1 Baxter-Wu model at $\Delta = 0$. Fits were performed using Eq. (3.6).

	Fits with corrections: $\tau_{\text{int}} = aL^z(1 + c/L^2)$							
L_{min}	z	z_{error}	a	a_{error}	c	c_{error}	Q	χ^2/dof
12	1.269	0.007	1.615	0.056	-24.283	4.057	0.36	1.09
15	1.263	0.008	1.665	0.065	-32.604	6.279	0.51	0.93
18	1.262	0.009	1.673	0.074	-34.330	10.067	0.42	1.02
24	1.252	0.011	1.767	0.096	-59.752	17.542	0.61	0.81
30	1.244	0.013	1.839	0.121	-84.320	28.402	0.63	0.76
36	1.231	0.015	1.970	0.156	-136.130	43.535	0.79	0.55
48	1.212	0.021	2.186	0.246	-227.948	81.574	0.90	0.37
54	1.202	0.025	2.297	0.299	-282.800	108.380	0.89	0.34
60	1.190	0.028	2.465	0.368	-375.265	142.798	0.93	0.21
72	1.171	0.035	2.728	0.523	-530.442	230.786	0.98	0.06
96	1.158	0.062	2.930	1.006	-667.339	591.296	0.95	0.06
120	1.126	0.113	3.524	2.255	-1102.484	1379.633	1.00	0.00

TABLE B.12: Fits for the integrated autocorrelation time τ_{int} of the spin-1 Baxter-Wu model at $\Delta = 0$, including corrections. Fits were performed using Eq. (3.7).

The fits for τ_{int} at $\Delta = 0.5$ follow:

	No corrections linear fit: $\log \tau_{\text{int}} = a + z * L$					
L_{min}	z	z_{error}	a	a_{error}	Q	χ^2/dof
12	1.433	0.006	0.182	0.028	0.14	1.42
15	1.428	0.007	0.205	0.030	0.24	1.25
18	1.429	0.007	0.201	0.033	0.18	1.36
24	1.426	0.008	0.212	0.037	0.15	1.45
30	1.430	0.009	0.197	0.041	0.13	1.54
36	1.426	0.010	0.213	0.047	0.10	1.66
48	1.422	0.011	0.233	0.053	0.08	1.81
54	1.437	0.013	0.157	0.060	0.52	0.86
60	1.435	0.015	0.170	0.071	0.41	1.01
72	1.443	0.018	0.129	0.088	0.35	1.11
96	1.457	0.023	0.056	0.117	0.31	1.19
120	1.485	0.031	-0.091	0.161	0.42	0.87
144	1.521	0.045	-0.280	0.236	0.46	0.56

TABLE B.13: Linear fits for the integrated autocorrelation time τ_{int} of the spin-1 Baxter-Wu model at $\Delta = 0.5$. Fits were performed using Eq. (3.6).

	Fits with corrections: $\tau_{\text{int}} = aL^z(1 + c/L^2)$							
L_{min}	z	z_{error}	a	a_{error}	c	c_{error}	Q	χ^2/dof
12	1.422	0.010	1.262	0.057	-7.894	5.356	0.19	1.34
15	1.429	0.011	1.223	0.064	0.556	8.980	0.20	1.33
18	1.427	0.012	1.235	0.073	-3.158	13.272	0.15	1.45
24	1.434	0.015	1.191	0.089	13.698	25.187	0.13	1.54
30	1.427	0.018	1.235	0.110	-8.021	38.435	0.10	1.66
36	1.438	0.022	1.165	0.129	36.077	64.014	0.08	1.79
48	1.494	0.033	0.861	0.148	327.094	149.080	0.37	1.09
54	1.468	0.036	0.992	0.188	156.728	174.119	0.51	0.86
60	1.497	0.043	0.847	0.193	380.667	256.251	0.64	0.63
72	1.524	0.056	0.730	0.222	638.482	442.165	0.59	0.64
96	1.629	0.108	0.405	0.245	1990.350	1369.413	0.82	0.19
120	1.734	0.220	0.221	0.280	3849.717	3936.453	0.88	0.02

TABLE B.14: Fits for the integrated autocorrelation time τ_{int} of the spin-1 Baxter-Wu model at $\Delta = 0.5$, including corrections. Fits were performed using Eq. (3.7).

The fits for τ_{int} at $\Delta = 0.8902$ (which was suggested as the crystal-field value at the multi-critical point [160]) follow:

	No corrections linear fit: $\log \tau_{\text{int}} = a + z * L$					
L_{min}	z	z_{error}	a	a_{error}	Q	χ^2/dof
12	1.737	0.010	-0.277	0.041	0.84	0.62
15	1.742	0.011	-0.300	0.046	0.80	0.65
18	1.756	0.012	-0.364	0.052	0.88	0.54
24	1.769	0.014	-0.425	0.059	0.90	0.48
30	1.773	0.015	-0.444	0.068	0.86	0.53
36	1.785	0.018	-0.501	0.079	0.84	0.53
48	1.786	0.020	-0.501	0.093	0.75	0.60
54	1.789	0.023	-0.516	0.108	0.65	0.70
60	1.789	0.027	-0.516	0.129	0.52	0.84
72	1.786	0.035	-0.505	0.166	0.38	1.05
96	1.732	0.049	-0.233	0.243	0.31	1.20
120	1.705	0.071	-0.094	0.356	0.17	1.76
144	1.472	0.111	1.124	0.572	0.20	1.67

TABLE B.15: Linear fits for the integrated autocorrelation time τ_{int} of the spin-1 Baxter-Wu model at $\Delta = 0.8902$. Fits were performed using Eq. (3.6).

	Fits with corrections: $\tau_{\text{int}} = aL^z(1 + c/L^2)$							
L_{min}	z	z_{error}	a	a_{error}	c	c_{error}	Q	χ^2/dof
12	1.774	0.017	0.634	0.049	25.306	9.306	0.02	2.07
15	1.791	0.020	0.583	0.053	46.862	15.720	0.03	1.94
18	1.789	0.022	0.591	0.060	42.543	22.353	0.02	2.13
24	1.782	0.026	0.613	0.077	27.497	37.629	0.01	2.34
30	1.786	0.032	0.599	0.095	39.844	64.074	0.01	2.63
36	1.760	0.038	0.685	0.129	-50.186	91.631	0.01	2.78
48	1.737	0.056	0.775	0.222	-146.652	187.661	0.00	3.18
54	1.703	0.065	0.924	0.310	-315.505	239.520	0.00	3.63
60	1.663	0.074	1.145	0.439	-544.101	300.152	0.00	4.23
72	1.563	0.090	1.961	0.932	-1182.913	416.117	0.00	4.66
96	1.415	0.154	4.422	3.684	-2373.145	985.341	0.00	6.31
120	0.736	0.224	186.707	225.862	-7437.642	1053.091	0.08	2.98

TABLE B.16: Fits for the integrated autocorrelation time τ_{int} of the spin-1 Baxter-Wu model at $\Delta = 0.8902$, including corrections. Fits were performed using Eq. (3.7).

Owing to the bad quality of fit for the $\Delta = 0.8902$, a further fit is attempted, excluding the final point, which has large errors and seems to deviate from the general trend. This exclusion makes a large difference, since it renders the correction terms unimportant and the results more in line with the linear fit above.

	Fits with corrections: $\tau_{\text{int}} = aL^z(1 + c/L^2)$							
L_{min}	z	z_{error}	a	a_{error}	c	c_{error}	Q	χ^2/dof
12	1.796	0.018	0.578	0.047	33.264	9.974	0.49	0.95
15	1.819	0.021	0.517	0.050	62.004	17.107	0.89	0.51
18	1.821	0.023	0.513	0.056	64.694	24.528	0.83	0.56
24	1.823	0.029	0.508	0.070	68.529	42.121	0.75	0.63
30	1.841	0.036	0.464	0.082	117.901	74.088	0.75	0.61
36	1.825	0.043	0.503	0.107	64.640	108.327	0.69	0.65
48	1.848	0.067	0.446	0.153	161.512	247.442	0.60	0.73
54	1.837	0.079	0.474	0.194	99.930	327.917	0.46	0.90
60	1.817	0.092	0.525	0.252	-14.970	425.550	0.33	1.15
72	1.754	0.116	0.738	0.453	-443.406	618.298	0.24	1.41
96	1.790	0.246	0.607	0.812	-119.428	2091.419	0.10	2.78

TABLE B.17: Fits for the integrated autocorrelation time τ_{int} of the spin-1 Baxter-Wu model at $\Delta = 0.8902$, including corrections, but excluding the point $L = 240$. Fits were performed using Eq. (3.7).

B.1.3 τ_x fits for the hybrid algorithm

Since many values were tried for x, specifically $x = 1, 1.5, 2, 3, 5, 6, 8, 10$, here only the smallest value of x with acceptable qualities of fit is quoted. This value is always stated in the caption of each table.

The fits for τ_x at $\Delta = -10$ follow:

	Fits with no corrections					
$L_{\min}$	z	z_{error}	a	a_{error}	Q	χ^2/dof
12	1.162	0.002	-0.547	0.009	0.00	2.84
15	1.158	0.002	-0.528	0.010	0.17	1.42
18	1.156	0.003	-0.521	0.011	0.21	1.33
24	1.155	0.003	-0.514	0.012	0.24	1.29
30	1.155	0.003	-0.517	0.014	0.18	1.45
36	1.151	0.004	-0.495	0.017	0.78	0.53
48	1.153	0.004	-0.505	0.020	0.80	0.47
54	1.155	0.005	-0.515	0.023	0.80	0.42
60	1.155	0.006	-0.517	0.028	0.65	0.55
72	1.161	0.009	-0.543	0.040	0.66	0.42
96	1.170	0.014	-0.588	0.069	0.65	0.21

TABLE B.18: Linear fits for the integrated autocorrelation time τ_{int} of the spin-1 Baxter-Wu model at $\Delta = -10$ and $x = 1.5$. Fits were performed using Eq. (3.6).

	Fits with corrections: $\tau_{\text{int}} = aL^z(1 + c/L^2)$							
$L_{\min}$	z	z_{error}	a	a_{error}	c	c_{error}	Q	χ^2/dof
12	1.149	0.004	0.614	0.010	-7.333	1.588	0.34	1.12
15	1.151	0.004	0.608	0.011	-5.340	2.729	0.32	1.16
18	1.151	0.005	0.608	0.013	-5.340	4.186	0.24	1.30
24	1.153	0.006	0.604	0.017	-2.846	7.529	0.17	1.47
30	1.147	0.008	0.622	0.023	-16.391	12.525	0.20	1.42
36	1.163	0.010	0.574	0.027	28.573	21.724	0.92	0.28
48	1.173	0.017	0.546	0.047	63.241	54.005	0.92	0.23
54	1.174	0.022	0.544	0.061	66.366	77.573	0.82	0.30
60	1.185	0.028	0.512	0.072	119.861	111.378	0.81	0.21
72	1.188	0.043	0.504	0.112	138.167	214.937	0.52	0.41

TABLE B.19: Fits for the integrated autocorrelation time τ_x of the spin-1 Baxter-Wu model at $\Delta = -10$ and $x = 1.5$, including corrections. Fits were performed using Eq. (3.7).

The fits for τ_x at $\Delta = -1$ follow:

	Fits with no corrections					
L_{min}	z	z_{error}	a	a_{error}	Q	χ^2/dof
12	1.203	0.002	-0.408	0.010	0.00	2.73
15	1.200	0.003	-0.393	0.011	0.04	1.90
18	1.197	0.003	-0.380	0.012	0.18	1.39
24	1.195	0.003	-0.368	0.013	0.57	0.84
30	1.191	0.004	-0.354	0.016	0.75	0.61
36	1.193	0.004	-0.362	0.019	0.76	0.56
48	1.195	0.005	-0.372	0.022	0.73	0.56
54	1.198	0.006	-0.385	0.026	0.82	0.39
60	1.198	0.007	-0.385	0.030	0.67	0.51
72	1.195	0.009	-0.371	0.043	0.51	0.67
96	1.203	0.015	-0.410	0.074	0.33	0.94

TABLE B.20: Linear fits for the integrated autocorrelation time τ_{int} of the spin-1 Baxter-Wu model at $\Delta = -1$ and $x = 1.5$. Fits were performed using Eq. (3.6).

	Fits with corrections: $\tau_{\text{int}} = aL^z(1 + c/L^2)$							
L_{min}	z	z_{error}	a	a_{error}	c	c_{error}	Q	χ^2/dof
12	1.189	0.004	0.712	0.013	-9.464	1.947	0.63	0.80
15	1.187	0.005	0.716	0.015	-10.816	3.126	0.57	0.85
18	1.187	0.005	0.718	0.018	-11.583	5.078	0.47	0.95
24	1.191	0.006	0.704	0.022	-4.880	7.807	0.50	0.90
30	1.202	0.009	0.666	0.028	21.180	15.610	0.88	0.39
36	1.203	0.011	0.662	0.035	25.194	24.975	0.80	0.46
48	1.210	0.019	0.640	0.061	47.975	60.815	0.71	0.53
54	1.199	0.024	0.679	0.081	1.522	83.571	0.67	0.52
60	1.198	0.029	0.679	0.101	1.524	115.009	0.46	0.77
72	1.234	0.047	0.563	0.138	200.119	242.777	0.43	0.61

TABLE B.21: Fits for the integrated autocorrelation time τ_x of the spin-1 Baxter-Wu model at $\Delta = -1$ and $x = 1.5$, including corrections. Fits were performed using Eq. (3.7).

The fits for τ_x at $\Delta = 0$ follow:

	Fits with no corrections					
$L_{\min}$	z	z_{error}	a	a_{error}	Q	χ^2/dof
12	1.266	0.002	-0.359	0.010	0.00	3.36
15	1.264	0.002	-0.349	0.011	0.00	3.06
18	1.262	0.003	-0.340	0.012	0.00	2.98
24	1.260	0.003	-0.331	0.013	0.00	2.96
30	1.259	0.003	-0.326	0.014	0.00	3.19
36	1.258	0.003	-0.320	0.016	0.00	3.50
48	1.254	0.004	-0.298	0.017	0.00	2.92
54	1.250	0.004	-0.279	0.020	0.02	2.61
60	1.246	0.005	-0.258	0.022	0.04	2.36
72	1.240	0.005	-0.229	0.026	0.10	1.93
96	1.229	0.008	-0.169	0.039	0.36	1.08
120	1.217	0.010	-0.106	0.053	0.91	0.09
144	1.213	0.014	-0.084	0.076	0.88	0.02

TABLE B.22: Linear fits for the integrated autocorrelation time τ_{int} of the spin-1 Baxter-Wu model at $\Delta = 0$ and $x = 1.5$. Fits were performed using Eq. (3.6).

	Fits with corrections: $\tau_{\text{int}} = aL^z(1 + c/L^2)$							
$L_{\min}$	z	z_{error}	a	a_{error}	c	c_{error}	Q	χ^2/dof
12	1.256	0.003	0.736	0.011	-9.411	2.101	0.02	2.06
15	1.254	0.004	0.741	0.013	-11.392	3.129	0.01	2.18
18	1.253	0.004	0.747	0.014	-14.775	4.671	0.01	2.31
24	1.249	0.005	0.762	0.018	-24.413	8.223	0.01	2.34
30	1.243	0.006	0.788	0.022	-46.058	12.845	0.04	2.06
36	1.231	0.007	0.836	0.029	-93.352	19.766	0.38	1.06
48	1.217	0.009	0.902	0.044	-162.435	36.920	0.83	0.48
54	1.212	0.011	0.930	0.054	-196.743	50.568	0.86	0.38
60	1.207	0.013	0.953	0.064	-229.322	67.920	0.84	0.36
72	1.201	0.016	0.987	0.085	-281.531	103.708	0.80	0.33
96	1.181	0.028	1.103	0.172	-502.475	276.783	0.86	0.15
120	1.202	0.054	0.981	0.299	-209.232	720.932	0.75	0.10

TABLE B.23: Fits for the integrated autocorrelation time τ_x of the spin-1 Baxter-Wu model at $\Delta = 0$ and $x = 1.5$, including corrections. Fits were performed using Eq. (3.7).

The fits for τ_x at $\Delta = 0.5$ follow:

	Fits with no corrections					
$L_{\min}$	z	z_{error}	a	a_{error}	Q	χ^2/dof
12	1.411	0.002	-0.557	0.011	0.03	1.90
15	1.410	0.003	-0.555	0.012	0.02	2.04
18	1.412	0.003	-0.563	0.013	0.03	1.96
24	1.411	0.003	-0.560	0.014	0.02	2.13
30	1.413	0.004	-0.569	0.016	0.02	2.24
36	1.416	0.004	-0.585	0.019	0.03	2.11
48	1.415	0.004	-0.580	0.021	0.02	2.36
54	1.418	0.005	-0.592	0.022	0.02	2.42
60	1.423	0.005	-0.621	0.027	0.06	2.14
72	1.429	0.007	-0.648	0.035	0.06	2.30
96	1.442	0.009	-0.717	0.045	0.36	1.06
120	1.449	0.012	-0.757	0.061	0.32	1.14
144	1.456	0.017	-0.792	0.088	0.16	1.97

TABLE B.24: Linear fits for the integrated autocorrelation time τ_{int} of the spin-1 Baxter-Wu model at $\Delta = 0.5$ and $x = 1.5$. Fits were performed using Eq. (3.6).

	Fits with corrections: $\tau_{\text{int}} = aL^z(1 + c/L^2)$							
$L_{\min}$	z	z_{error}	a	a_{error}	c	c_{error}	Q	χ^2/dof
12	1.413	0.004	0.566	0.010	1.886	2.317	0.02	1.99
15	1.416	0.004	0.556	0.012	6.767	3.749	0.03	1.91
18	1.415	0.005	0.560	0.013	4.528	5.244	0.02	2.07
24	1.421	0.006	0.543	0.015	18.847	8.961	0.05	1.85
30	1.426	0.007	0.528	0.018	36.540	16.346	0.06	1.86
36	1.426	0.008	0.528	0.023	36.540	27.184	0.04	2.13
48	1.454	0.012	0.455	0.029	179.006	54.227	0.61	0.75
54	1.458	0.014	0.445	0.032	206.054	66.910	0.55	0.80
60	1.460	0.015	0.440	0.036	222.612	89.674	0.41	0.99
72	1.482	0.021	0.391	0.044	429.503	165.723	0.69	0.49
96	1.486	0.035	0.381	0.075	487.368	386.152	0.49	0.72
120	1.524	0.069	0.307	0.121	1064.511	1022.909	0.31	1.03

TABLE B.25: Fits for the integrated autocorrelation time τ_x of the spin-1 Baxter-Wu model at $\Delta = 0.5$ and $x = 1.5$, including corrections. Fits were performed using Eq. (3.7).

The fits for τ_x at $\Delta = 0.8902$ follow:

	Fits with no corrections					
$L_{\min}$	z	z_{error}	a	a_{error}	Q	χ^2/dof
12	1.752	0.005	-0.822	0.022	0.00	6.94
15	1.757	0.006	-0.844	0.024	0.00	7.14
18	1.773	0.006	-0.916	0.027	0.00	4.38
24	1.781	0.007	-0.950	0.029	0.00	3.86
30	1.796	0.008	-1.021	0.036	0.00	2.90
36	1.818	0.010	-1.125	0.045	0.26	1.27
48	1.826	0.011	-1.167	0.052	0.40	1.03
54	1.831	0.013	-1.190	0.059	0.36	1.10
60	1.834	0.015	-1.202	0.069	0.25	1.35
72	1.837	0.018	-1.221	0.089	0.15	1.76
96	1.821	0.026	-1.140	0.129	0.10	2.26
120	1.784	0.040	-0.950	0.199	0.09	2.94
144	1.456	0.017	-0.792	0.088	0.16	1.97

TABLE B.26: Linear fits for the integrated autocorrelation time τ_{int} of the spin-1 Baxter-Wu model at $\Delta = 0.8902$ and $x = 3$. Fits were performed using Eq. (3.6).

	Fits with corrections: $\tau_{\text{int}} = aL^z(1 + c/L^2)$							
$L_{\min}$	z	z_{error}	a	a_{error}	c	c_{error}	Q	χ^2/dof
12	1.810	0.008	0.315	0.011	38.989	4.796	0.00	4.68
15	1.834	0.009	0.280	0.012	71.678	8.095	0.04	1.93
18	1.841	0.011	0.270	0.014	84.355	12.872	0.04	1.95
24	1.856	0.013	0.251	0.015	115.951	19.493	0.15	1.51
30	1.858	0.015	0.249	0.018	120.675	30.231	0.10	1.72
36	1.848	0.019	0.262	0.025	82.450	53.143	0.08	1.88
48	1.824	0.027	0.297	0.041	-21.347	96.026	0.08	1.95
54	1.805	0.031	0.328	0.053	-117.984	124.657	0.08	2.12
60	1.792	0.037	0.352	0.067	-194.825	166.998	0.05	2.68
72	1.740	0.047	0.464	0.115	-539.322	248.682	0.07	2.68
96	1.577	0.083	1.129	0.504	-1821.432	541.617	0.36	0.85

TABLE B.27: Fits for the integrated autocorrelation time τ_x of the spin-1 Baxter-Wu model at $\Delta = 0.5$ and $x = 3$, including corrections. Fits were performed using Eq. (3.7). This fit excludes the largest size of $L = 240$.

B.1.4 τ^*_{int} fits for the hybrid algorithm

The fits for τ^*_x at $\Delta = -10$ follow:

	Fits without corrections					
L_{min}	z	z_{error}	a	a_{error}	Q	χ^2/dof
12	1.194	0.005	0.151	0.022	0.00	2.59
15	1.184	0.006	0.196	0.024	0.56	0.87
18	1.180	0.006	0.213	0.027	0.69	0.72
24	1.178	0.007	0.223	0.030	0.66	0.73
30	1.179	0.008	0.219	0.034	0.57	0.83
36	1.175	0.009	0.238	0.040	0.56	0.81
48	1.172	0.010	0.252	0.047	0.47	0.91
54	1.174	0.012	0.240	0.055	0.35	1.10
60	1.170	0.014	0.262	0.067	0.25	1.36
72	1.178	0.019	0.220	0.092	0.17	1.80
96	1.227	0.032	-0.018	0.156	0.83	0.05

TABLE B.28: Linear fits for the integrated autocorrelation time τ^*_{int} of the spin-1 Baxter-Wu model at $\Delta = -10$. Fits were performed using Eq. (3.6). The time was contracted so that at each time step $2N$ spins are updated.

	Fits with corrections: $\tau_{\text{int}} = aL^z(1 + c/L^2)$							
L_{min}	z	z_{error}	a	a_{error}	c	c_{error}	Q	χ^2/dof
12	1.163	0.008	1.340	0.050	-18.565	3.741	0.62	0.81
15	1.171	0.010	1.294	0.057	-11.031	6.459	0.75	0.66
18	1.173	0.011	1.283	0.066	-8.422	10.105	0.67	0.73
24	1.174	0.014	1.273	0.086	-5.637	18.893	0.56	0.83
30	1.165	0.018	1.332	0.113	-26.440	30.131	0.54	0.84
36	1.171	0.023	1.290	0.145	-8.480	51.413	0.43	0.97
48	1.201	0.040	1.108	0.223	94.983	127.231	0.40	1.00
54	1.208	0.051	1.072	0.276	122.050	184.524	0.26	1.32
60	1.270	0.069	0.777	0.274	432.882	310.151	0.43	0.85
72	1.359	0.115	0.488	0.294	993.767	700.586	0.49	0.48

TABLE B.29: Fits with correction term for the integrated autocorrelation time τ^*_{int} of the spin-1 Baxter-Wu model at $\Delta = -10$. Fits were performed using Eq. (3.7). The time was contracted so that at each time step $2N$ spins are updated.

The fits for τ_x^* at $\Delta = -1$ follow:

	Fits without corrections					
$L_{\min}$	z	z_{error}	a	a_{error}	Q	χ^2/dof
12	1.262	0.006	0.144	0.025	0.27	1.21
15	1.258	0.006	0.161	0.028	0.36	1.10
18	1.251	0.007	0.193	0.031	0.79	0.61
24	1.245	0.008	0.220	0.035	0.94	0.36
30	1.240	0.009	0.240	0.040	0.97	0.26
36	1.236	0.010	0.258	0.046	0.98	0.20
48	1.238	0.012	0.251	0.055	0.95	0.23
54	1.234	0.014	0.268	0.064	0.93	0.22
60	1.229	0.017	0.294	0.079	0.91	0.18
72	1.218	0.023	0.347	0.108	0.98	0.02
96	1.222	0.039	0.326	0.186	0.91	0.01

TABLE B.30: Linear fits for the integrated autocorrelation time τ_{int}^* of the spin-1 Baxter-Wu model at $\Delta = -1$. Fits were performed using Eq. (3.6). The time was contracted so that at each time step $2N$ spins are updated.

	Fits with corrections: $\tau_{\text{int}} = aL^z(1 + c/L^2)$							
$L_{\min}$	z	z_{error}	a	a_{error}	c	c_{error}	Q	χ^2/dof
12	1.237	0.010	1.295	0.057	-14.819	4.475	0.19	1.36
15	1.229	0.011	1.344	0.068	-22.508	6.821	0.80	0.60
18	1.228	0.013	1.347	0.079	-22.953	10.772	0.72	0.67
24	1.226	0.016	1.360	0.105	-26.290	20.431	0.64	0.74
30	1.226	0.021	1.360	0.135	-26.290	34.828	0.52	0.87
36	1.232	0.027	1.320	0.173	-9.583	60.119	0.45	0.94
48	1.199	0.044	1.564	0.342	-119.633	126.189	0.87	0.32
54	1.191	0.056	1.628	0.460	-149.646	183.265	0.78	0.36
60	1.191	0.071	1.628	0.588	-149.646	267.097	0.58	0.54
72	1.236	0.116	1.287	0.769	91.596	573.830	0.88	0.02

TABLE B.31: Fits with correction term for the integrated autocorrelation time τ_{int}^* of the spin-1 Baxter-Wu model at $\Delta = -1$. Fits were performed using Eq. (3.7). The time was contracted so that at each time step $2N$ spins are updated.

The fits for τ_x^* at $\Delta = 0$ follow:

	Fits without corrections					
L_{min}	z	z_{error}	a	a_{error}	Q	χ^2/dof
12	1.296	0.005	0.288	0.023	0.00	3.19
15	1.290	0.005	0.317	0.025	0.00	2.65
18	1.283	0.006	0.354	0.027	0.05	1.81
24	1.278	0.006	0.375	0.030	0.07	1.71
30	1.273	0.007	0.401	0.033	0.14	1.51
36	1.269	0.008	0.420	0.037	0.14	1.52
48	1.262	0.009	0.455	0.041	0.26	1.27
54	1.257	0.010	0.481	0.047	0.28	1.25
60	1.252	0.011	0.507	0.054	0.25	1.32
72	1.241	0.013	0.563	0.067	0.34	1.13
96	1.221	0.017	0.666	0.087	0.75	0.40
120	1.209	0.023	0.731	0.118	0.77	0.27
144	1.194	0.033	0.813	0.172	0.75	0.10

TABLE B.32: Linear fits for the integrated autocorrelation time τ_{int}^* of the spin-1 Baxter-Wu model at $\Delta = 0$. Fits were performed using Eq. (3.6). The time was contracted so that at each time step $2N$ spins are updated.

	Fits with corrections: $\tau_{\text{int}} = aL^z(1 + c/L^2)$							
L_{min}	z	z_{error}	a	a_{error}	c	c_{error}	Q	χ^2/dof
12	1.266	0.007	1.546	0.054	-23.762	4.074	0.39	1.06
15	1.260	0.008	1.593	0.062	-31.891	6.303	0.53	0.91
18	1.260	0.009	1.600	0.071	-33.406	10.101	0.44	1.00
24	1.249	0.011	1.688	0.092	-58.522	17.589	0.63	0.79
30	1.242	0.013	1.756	0.116	-82.593	28.475	0.65	0.75
36	1.229	0.015	1.879	0.149	-133.856	43.647	0.80	0.55
48	1.210	0.021	2.083	0.235	-224.919	81.738	0.90	0.37
54	1.201	0.025	2.187	0.285	-279.029	108.608	0.89	0.34
60	1.188	0.028	2.347	0.350	-371.745	143.034	0.94	0.21
72	1.170	0.035	2.597	0.498	-526.244	231.136	0.98	0.06
96	1.157	0.062	2.787	0.958	-662.390	591.973	0.95	0.06
120	1.124	0.113	3.356	2.148	-1099.714	1380.273	1.00	0.00

TABLE B.33: Fits with correction term for the integrated autocorrelation time τ_{int}^* of the spin-1 Baxter-Wu model at $\Delta = 0$. Fits were performed using Eq. (3.7). The time was contracted so that at each time step $2N$ spins are updated.

The fits for τ_x^* at $\Delta = 0.5$ follow:

	Fits without corrections					
$L_{\min}$	z	z_{error}	a	a_{error}	Q	χ^2/dof
12	1.428	0.006	0.136	0.028	0.15	1.41
15	1.423	0.007	0.158	0.030	0.24	1.26
18	1.424	0.007	0.153	0.033	0.18	1.36
24	1.422	0.008	0.163	0.037	0.15	1.46
30	1.426	0.009	0.147	0.041	0.13	1.54
36	1.423	0.010	0.162	0.047	0.10	1.67
48	1.419	0.011	0.181	0.053	0.08	1.83
54	1.434	0.013	0.104	0.060	0.51	0.87
60	1.431	0.015	0.117	0.071	0.40	1.02
72	1.439	0.018	0.076	0.088	0.35	1.12
96	1.454	0.023	0.002	0.117	0.31	1.19
120	1.482	0.031	-0.146	0.161	0.42	0.88
144	1.518	0.045	-0.336	0.236	0.46	0.55

TABLE B.34: Linear fits for the integrated autocorrelation time τ_{int}^* of the spin-1 Baxter-Wu model at $\Delta = 0.5$. Fits were performed using Eq. (3.6). The time was contracted so that at each time step $2N$ spins are updated.

	Fits with corrections: $\tau_{\text{int}} = aL^z(1 + c/L^2)$							
$L_{\min}$	z	z_{error}	a	a_{error}	c	c_{error}	Q	χ^2/dof
12	1.419	0.010	1.199	0.055	-7.188	5.384	0.18	1.35
15	1.425	0.011	1.161	0.061	1.574	9.024	0.20	1.33
18	1.423	0.012	1.172	0.069	-1.920	13.329	0.15	1.45
24	1.431	0.015	1.128	0.084	15.536	25.280	0.13	1.54
30	1.424	0.018	1.169	0.104	-5.588	38.570	0.10	1.67
36	1.435	0.022	1.102	0.122	39.310	64.234	0.08	1.79
48	1.492	0.033	0.814	0.141	330.441	149.368	0.36	1.09
54	1.465	0.036	0.938	0.178	159.716	174.383	0.50	0.86
60	1.494	0.043	0.801	0.183	384.743	256.687	0.64	0.63
72	1.521	0.056	0.690	0.210	643.299	442.842	0.59	0.64
96	1.626	0.108	0.382	0.232	1998.150	1371.539	0.82	0.19
120	1.731	0.220	0.209	0.265	3852.700	3938.498	0.88	0.02

TABLE B.35: Fits with correction term for the integrated autocorrelation time τ_{int}^* of the spin-1 Baxter-Wu model at $\Delta = 0.5$. Fits were performed using Eq. (3.7). The time was contracted so that at each time step $2N$ spins are updated.

The fits for τ_x^* at $\Delta = 0.8902$ follow:

	Fits without corrections					
$L_{\min}$	z	z_{error}	a	a_{error}	Q	χ^2/dof
12	1.730	0.010	-0.328	0.042	0.04	1.85
15	1.736	0.011	-0.354	0.047	0.04	1.87
18	1.751	0.012	-0.423	0.053	0.25	1.25
24	1.765	0.014	-0.490	0.060	0.59	0.83
30	1.771	0.016	-0.516	0.070	0.55	0.86
36	1.785	0.018	-0.584	0.081	0.76	0.60
48	1.788	0.021	-0.595	0.097	0.66	0.69
54	1.795	0.024	-0.629	0.112	0.58	0.76
60	1.801	0.029	-0.660	0.134	0.46	0.90
72	1.809	0.037	-0.697	0.176	0.32	1.16
96	1.778	0.053	-0.542	0.263	0.24	1.43
120	1.799	0.079	-0.651	0.399	0.10	2.72

TABLE B.36: Linear fits for the integrated autocorrelation time τ_{int}^* of the spin-1 Baxter-Wu model at $\Delta = 0.8902$. Fits were performed using Eq. (3.6). The time was contracted so that at each time step $2N$ spins are updated.

	Fits with corrections: $\tau_{\text{int}} = aL^z(1 + c/L^2)$							
$L_{\min}$	z	z_{error}	a	a_{error}	c	c_{error}	Q	χ^2/dof
12	1.780	0.018	0.569	0.046	31.261	9.848	0.54	0.89
15	1.802	0.021	0.513	0.049	58.073	16.829	0.89	0.51
18	1.802	0.023	0.511	0.056	59.235	24.106	0.83	0.56
24	1.802	0.028	0.511	0.070	59.235	41.318	0.75	0.63
30	1.819	0.036	0.471	0.082	103.394	72.573	0.73	0.63
36	1.802	0.042	0.513	0.108	45.776	106.044	0.68	0.66
48	1.820	0.066	0.467	0.159	121.740	240.906	0.58	0.76
54	1.806	0.078	0.501	0.203	51.846	319.115	0.45	0.93
60	1.786	0.091	0.560	0.265	-72.014	413.791	0.32	1.18
72	1.720	0.115	0.797	0.484	-510.216	602.157	0.24	1.42
96	1.747	0.241	0.687	0.903	-264.798	2015.167	0.09	2.82

TABLE B.37: Fits with correction term for the integrated autocorrelation time τ_{int}^* of the spin-1 Baxter-Wu model at $\Delta = 0.8902$. Fits were performed using Eq. (3.7). The time was contracted so that at each time step $2N$ spins are updated. Removing the largest system size improved the quality of fit in all cases for the current Δ.

B.1.5 τ_{int} fits for the heat bath algorithm

Even thought the emphasis of Chapter 3 was placed on the cluster algorithm for the Baxter-Wu model and its application, through a hybrid scheme, in the spin-1 case, results were also extracted for single spin flip updates. The results of the fits of the heat bath simulations at $\Delta = -1$ are presented in this section.

The fits for τ_x^* at $\Delta = 0.8902$ follow:

	Fits without corrections: $\tau_{\text{int}} = aL^z(1 + c/L^2)$					
L_{min}	z	z_{error}	a	a_{error}	Q	χ^2/dof
12	2.145	0.018	-1.059	0.067	0.42	1.03
15	2.143	0.021	-1.054	0.080	0.33	1.14
18	2.143	0.025	-1.054	0.097	0.25	1.28
24	2.131	0.031	-1.003	0.124	0.20	1.40
30	2.144	0.038	-1.057	0.155	0.15	1.58
36	2.152	0.047	-1.090	0.196	0.09	1.88
48	2.181	0.061	-1.217	0.260	0.07	2.20
54	2.276	0.072	-1.646	0.310	0.49	0.81
60	2.311	0.089	-1.808	0.392	0.37	0.99
72	2.202	0.132	-1.303	0.601	0.39	0.74

TABLE B.38: Linear fits for the integrated autocorrelation time τ_{int} of the spin-1 Baxter-Wu model at $\Delta = -1$, using the heat-vath algorithm. Fits were performed using Eq. (3.6).

	Fits with corrections: $\tau_{\text{int}} = aL^z(1 + c/L^2)$							
L_{min}	z	z_{error}	a	a_{error}	c	c_{error}	Q	χ^2/dof
12	2.140	0.038	0.353	0.056	-0.905	12.433	0.31	1.17
15	2.140	0.047	0.353	0.070	-0.905	21.244	0.23	1.31
18	2.141	0.056	0.352	0.084	-0.940	33.302	0.16	1.50
24	2.219	0.083	0.245	0.091	97.609	90.315	0.20	1.44
30	2.262	0.111	0.200	0.102	177.059	170.871	0.14	1.65
36	2.351	0.158	0.129	0.098	413.494	365.892	0.12	1.85
48	2.608	0.448	0.036	0.081	1469.034	2058.300	0.10	2.09
54	2.556	0.491	0.048	0.118	960.565	2046.070	0.17	1.77
60	1.802	0.327	2.000	3.179	-1303.454	622.983	0.67	0.18

TABLE B.39: Fits with corrections for the integrated autocorrelation time τ_{int} of the spin-1 Baxter-Wu model at $\Delta = -1$, using the heat-vath algorithm. Fits were performed using Eq. (3.7).

B.2 Universality of the Dilute Baxter-Wu Model

The fits for the universal exponents of the spin-1 Baxter-Wu model in a crystal field using the multicanonical algorithm are presented. For the specific heat, magnetic susceptibility, and logarithmic derivatives of the magnetisation maxima, the fits follow the form $aL^x(1+c/L^2)$, where a, x, c are parameters to be set by the fitting process. Specifically, x is a critical exponent ration, either α/ν or γ/ν or $1/\nu$, for the specific heat, magnetic susceptibility, and logarithmic derivatives, respectively. For the location of the critical point, fits followed the form $\Delta_c + aL^{-1/\nu}(1+c/L^2)$. For the crossing value of the binder cumulant, the scaling law $U_c + c/L^2$ was utilised. The tables that follow show how the fit parameters and the fit quality behave by varying the minimum system size used in the fits.

$L_{\min}$	α/ν	$(\alpha/\nu)_{\text{error}}$	a	a_{error}	c	c_{error}	Q	χ^2/dof
12	0.989	0.003	0.034	0.000	58.389	1.141	0.01	2.55
15	0.988	0.005	0.034	0.001	57.633	2.153	0.01	2.95
18	1.002	0.009	0.032	0.001	67.019	3.864	0.14	1.25
24	0.981	0.013	0.035	0.002	49.489	9.262	0.38	1.04
30	0.952	0.019	0.040	0.003	17.046	18.335	0.94	0.14
36	0.951	0.029	0.040	0.005	15.750	39.157	0.82	0.20
48	0.985	0.084	0.034	0.013	78.830	152.813	0.65	0.21

TABLE B.40: Fits for the specific-heat-like quantity maxima, C^*_Δ, at $T = 2.1$.

$L_{\min}$	γ/ν	$(\gamma/\nu)_{\text{error}}$	a	a_{error}	c	c_{error}	Q	χ^2/dof
12	1.803	0.005	0.065	0.001	-7.189	1.145	0.37	1.09
15	1.796	0.008	0.067	0.002	-10.094	2.511	0.42	1.00
18	1.797	0.010	0.066	0.003	-9.518	4.861	0.31	1.19
24	1.787	0.019	0.069	0.006	-16.817	12.874	0.23	1.40
30	1.747	0.031	0.083	0.011	-57.390	27.316	0.37	1.06
36	1.776	0.049	0.073	0.016	-18.627	59.773	0.27	1.29
48	1.949	0.183	0.032	0.028	321.900	389.627	0.25	1.30

TABLE B.41: Fits for the magnetic susceptibility maxima, χ^*, at $T = 2.1$.

$L_{\min}$	ν	$(\nu)_{\text{error}}$	a	a_{error}	c	c_{error}	Q	χ^2/dof
12	0.686	0.004	0.026	0.001	67.393	3.058	0.29	1.21
15	0.683	0.006	0.025	0.001	70.078	5.261	0.23	1.35
18	0.668	0.006	0.024	0.002	78.395	9.375	0.24	1.36
24	0.673	0.014	0.027	0.003	50.642	20.271	0.32	1.17
30	0.688	0.022	0.031	0.006	18.292	39.295	0.28	1.29
36	0.699	0.031	0.029	0.008	45.494	80.325	0.16	1.86
48	0.566	0.080	0.006	0.007	766.104	628.545	0.60	0.27

TABLE B.42: Fits for the logarithmic derivative maxima, $(d \ln \langle m \rangle / d\Delta)^*$, at $T = 2.1$.

$L_{\min}$	α/ν	$(\alpha/\nu)_{\text{error}}$	a	a_{error}	c	c_{error}	Q	χ^2/dof
12	1.017	0.010	0.100	0.004	18.172	3.516	0.54	0.88
15	1.013	0.011	0.102	0.005	15.101	5.731	0.48	0.94
18	1.011	0.013	0.103	0.006	12.227	9.848	0.39	1.06
24	1.021	0.020	0.098	0.009	28.731	24.526	0.34	1.14
30	1.029	0.024	0.094	0.010	42.541	34.945	0.26	1.30
36	1.039	0.032	0.090	0.014	65.115	59.460	0.18	1.57
48	1.104	0.071	0.065	0.023	243.943	194.792	0.16	1.73
54	1.317	0.147	0.023	0.017	1054.795	605.944	0.86	0.16

TABLE B.43: Fits for the specific-heat-like quantity maxima, C_Δ^*, at $T = 1.8503$.

$L_{\min}$	γ/ν	$(\gamma/\nu)_{\text{error}}$	a	a_{error}	c	c_{error}	Q	χ^2/dof
12	1.772	0.008	0.081	0.003	-11.388	2.375	0.31	1.17
15	1.763	0.010	0.085	0.004	-17.792	4.644	0.42	1.02
18	1.759	0.012	0.086	0.005	-22.445	8.404	0.36	1.10
24	1.767	0.018	0.083	0.007	-11.405	20.656	0.29	1.23
30	1.772	0.021	0.081	0.008	-3.420	26.428	0.21	1.43
36	1.772	0.028	0.081	0.011	-3.420	48.896	0.13	1.78
48	1.820	0.058	0.064	0.018	123.668	147.313	0.10	2.06
54	1.979	0.104	0.029	0.015	677.323	374.263	0.60	0.52

TABLE B.44: Fits for the magnetic susceptibility maxima, χ^*, at $T = 1.8503$.

$L_{\min}$	ν	$(\nu)_{\text{error}}$	a	a_{error}	c	c_{error}	Q	χ^2/dof
12	0.667	0.005	0.039	0.002	9.228	5.238	0.41	1.03
15	0.667	0.005	0.039	0.002	9.228	5.238	0.41	1.03
18	0.669	0.006	0.040	0.002	4.998	9.683	0.33	1.14
24	0.666	0.009	0.039	0.003	13.803	21.590	0.26	1.29
30	0.664	0.010	0.038	0.004	20.106	26.238	0.18	1.52
36	0.668	0.013	0.039	0.005	2.481	47.545	0.12	1.85
48	0.660	0.024	0.036	0.009	50.968	130.449	0.07	2.41
54	0.602	0.034	0.017	0.008	546.436	309.729	0.54	0.62

TABLE B.45: Fits for the logarithmic derivative maxima, $(d \ln \langle m \rangle / d\Delta)^*$, at $T = 1.8503$.

$L_{\min}$	α/ν	$(\alpha/\nu)_{\text{error}}$	a	a_{error}	c	c_{error}	Q	χ^2/dof
12	1.081	0.007	0.162	0.004	10.920	2.007	0.75	0.64
15	1.085	0.009	0.159	0.006	13.199	3.465	0.73	0.63
18	1.078	0.010	0.164	0.007	8.286	5.127	0.83	0.47
24	1.074	0.016	0.166	0.011	4.918	12.331	0.74	0.55
30	1.062	0.022	0.175	0.017	-9.519	22.608	0.70	0.55
36	1.059	0.030	0.178	0.024	-14.284	38.981	0.54	0.73
48	1.067	0.065	0.171	0.053	2.931	135.749	0.34	1.08
54	1.001	0.097	0.235	0.109	-163.574	218.640	0.22	1.47

TABLE B.46: Fits for the specific-heat-like quantity maxima, C_{Δ}^{*}, at $T = 1.6606$.

$L_{\min}$	γ/ν	$(\gamma/\nu)_{\text{error}}$	a	a_{error}	c	c_{error}	Q	χ^2/dof
12	1.789	0.006	0.089	0.002	-9.061	1.561	0.66	0.73
15	1.789	0.008	0.089	0.003	-9.061	3.029	0.56	0.84
18	1.780	0.010	0.092	0.004	-15.032	4.680	0.78	0.53
24	1.774	0.016	0.095	0.006	-20.740	11.635	0.71	0.58
30	1.764	0.023	0.099	0.010	-32.417	22.392	0.64	0.64
36	1.754	0.031	0.104	0.014	-46.906	39.217	0.50	0.89
48	1.792	0.068	0.087	0.028	37.239	144.233	0.38	0.98
54	1.729	0.101	0.118	0.057	-126.709	233.884	0.24	1.37

TABLE B.47: Fits for the magnetic susceptibility maxima, χ^{*}, at $T = 1.6606$.

$L_{\min}$	ν	$(\nu)_{\text{error}}$	a	a_{error}	c	c_{error}	Q	χ^2/dof
12	0.643	0.003	0.062	0.002	8.978	2.173	0.81	0.56
15	0.642	0.004	0.061	0.002	10.795	3.886	0.76	0.59
18	0.644	0.005	0.062	0.003	6.681	5.944	0.77	0.56
24	0.645	0.007	0.063	0.005	4.708	13.957	0.65	0.66
30	0.644	0.011	0.062	0.007	7.297	27.120	0.51	0.82
36	0.651	0.015	0.067	0.010	-17.699	45.357	0.41	0.95
48	0.648	0.032	0.065	0.023	-2.680	155.965	0.24	1.42
54	0.703	0.053	0.116	0.059	-302.366	225.766	0.32	1.00

TABLE B.48: Fits for the logarithmic derivative maxima, $(d \ln \langle m \rangle / d\Delta)^{*}$, at $T = 1.6606$.

$L_{\min}$	α/ν	$(\alpha/\nu)_{\text{error}}$	a	a_{error}	c	c_{error}	Q	χ^2/dof
12	1.178	0.008	0.190	0.001	12.918	0.227	0.00	44.09
15	1.188	0.010	0.182	0.001	17.891	0.388	0.00	12.51
18	1.189	0.013	0.181	0.001	18.571	0.656	0.00	14.32
24	1.198	0.020	0.175	0.002	25.900	1.544	0.00	11.54
30	1.207	0.030	0.167	0.002	38.001	3.220	0.00	9.65
36	1.208	0.041	0.167	0.003	39.672	5.589	0.00	12.82
48	1.132	0.053	0.207	0.008	-58.986	16.259	0.43	0.85
54	1.142	0.135	0.198	0.013	-34.202	32.239	0.35	0.88

TABLE B.49: Fits for the specific-heat-like quantity maxima, C_{Δ}^{*}, at $T = 1.5301$.

$L_{\min}$	γ/ν	$(\gamma/\nu)_{\text{error}}$	a	a_{error}	c	c_{error}	Q	χ^2/dof
12	1.820	0.0024	0.092	0.001	-5.458	0.591	0.34	1.13
15	1.824	0.0032	0.090	0.001	-3.729	1.084	0.62	0.76
18	1.823	0.0041	0.091	0.002	-4.729	1.936	0.55	0.83
24	1.824	0.0065	0.090	0.003	-3.129	4.680	0.44	0.97
30	1.826	0.0097	0.090	0.004	-1.642	10.011	0.31	1.20
36	1.829	0.0133	0.088	0.005	3.521	17.808	0.20	1.56
48	1.744	0.0373	0.114	0.015	-107.750	52.083	0.90	0.80
54	1.791	0.0443	0.106	0.022	-68.946	103.904	0.94	0.48

TABLE B.50: Fits for the magnetic susceptibility maxima, χ^*, at $T = 1.5301$.

$L_{\min}$	$(U_m)_\infty$	$((U_m)_\infty)_{\text{error}}$	c	c_{error}	Q	χ^2/dof
12	0.597	0.005	2.651	0.298	0.06	1.98
15	0.596	0.006	3.295	0.391	0.37	1.08
18	0.594	0.007	4.831	1.210	0.46	0.90
24	0.592	0.008	7.143	2.469	0.48	0.82

TABLE B.51: Fits for the value at the crossing of the binder cumulant, U_m, at $T = 1.8503$.

The fits concerning the Wang-Landau simulations follow. The scaling laws for the specific heat and magnetic susceptibility are identical to those discussed above for the case of multicanonical simulations.

$L_{\min}$	α/ν	$(\alpha/\nu)_{\text{error}}$	a	a_{error}	c	c_{error}	Q	χ^2/dof
12	1.013	0.018	0.362	0.005	-6.010	1.080	0.35	1.11
15	1.016	0.024	0.362	0.006	-6.242	1.905	0.26	1.27
18	1.016	0.030	0.362	0.008	-6.242	4.323	0.18	1.48
24	1.017	0.035	0.361	0.011	-5.031	8.130	0.12	1.77
30	1.018	0.049	0.359	0.014	-2.544	14.175	0.07	2.20
36	1.020	0.053	0.356	0.017	1.428	19.812	0.03	2.91
48	1.037	0.107	0.327	0.030	56.879	55.008	0.02	3.75
60	1.056	0.185	0.297	0.049	131.473	120.922	0.01	6.99

TABLE B.52: Fits for the specific-heat maxima, C^*, at $\Delta = -10$.

$L_{\min}$	α/ν	$(\alpha/\nu)_{\text{error}}$	a	a_{error}	c	c_{error}	Q	χ^2/dof
12	1.04	0.05	0.609	0.008	-3.962	1.057	0.54	0.87
15	1.05	0.05	0.607	0.010	-3.524	1.854	0.44	0.98
18	1.05	0.06	0.604	0.013	-1.895	4.219	0.35	1.12
24	1.05	0.06	0.598	0.017	1.692	7.875	0.27	1.28
30	1.06	0.08	0.586	0.022	10.649	13.718	0.22	1.44
36	1.06	0.09	0.576	0.026	19.424	19.175	0.15	1.77
48	1.07	0.17	0.550	0.047	49.429	51.462	0.09	2.46
60	1.10	0.31	0.473	0.074	166.359	115.322	0.06	3.51

TABLE B.53: Fits for the specific-heat maxima, C^*, at $\Delta = -1$.

Bibliography

[1] J. S. Kennedy, "Phase transformation in locust biology", Biological Reviews **31**, 349–370 (1956) (cited on page 1).

[2] X. Wang and L. Kang, "Molecular mechanisms of phase change in locusts", Annual Review of Entomology **59**, 225–244 (2014) (cited on page 1).

[3] A. Carballo-Castro and L. F. Seoane, "Phase transitions in a simple model of focal stroke imitate recovery and suggest neurorehabilitation strategies", bioRxiv, 10.1101/2022.12.14.520421 (2023) (cited on page 1).

[4] M. Levy, "Stock market crashes as social phase transitions", Journal of Economic Dynamics and Control **32**, Applications of statistical physics in economics and finance, 137–155 (2008) (cited on page 1).

[5] R. Solé, J. Sardanyés, and S. F. Elena, "Phase transitions in virology", Reports on Progress in Physics **84**, 115901 (2021) (cited on page 1).

[6] L. Li, Y. Fan, A. Zeng, and Z. Di, "Binary opinion dynamics on signed networks based on Ising model", Physica A: Statistical Mechanics and its Applications (2019) (cited on page 1).

[7] I. Ferri, C. J. P. Vicente, M. Palassini, and A. Díaz-Guilera, "Three-State Opinion Model on Complex Topologies", Entropy **24** (2022) (cited on page 1).

[8] E. Fermi, *Thermodynamics* (Courier Corporation, 2012) (cited on page 2).

[9] B. He, V. Martin, and F. Setterwall, "Phase transition temperature ranges and storage density of paraffin wax phase change materials", Energy **29**, 1785–1804 (2004) (cited on page 2).

[10] M. E. Fisher, "The theory of equilibrium critical phenomena", Reports on progress in physics **30**, 615 (1967) (cited on pages 2, 7, 15).

[11] M. E. Fisher, "The renormalization group in the theory of critical behavior", Reviews of Modern Physics **46**, 597 (1974) (cited on pages 2, 7).

[12] N. Goldenfeld, *Lectures on phase transitions and the renormalization group* (CRC Press, 2018) (cited on pages 2, 7, 14–15, 17–18, 21–24, 26–27).

[13] M. Le Bellac, F. Mortessagne, and G. G. Batrouni, *Equilibrium and non-equilibrium statistical thermodynamics* (Cambridge University Press, 2004) (cited on pages 2–3, 7–8, 10–11, 16).

[14] J. Cardy, *Scaling and renormalization in statistical physics*, Vol. 5 (Cambridge university press, 1996) (cited on pages 2, 7, 13, 16, 18, 20, 22, 24, 26, 28).

[15] M. Kardar, *Statistical Physics of Fields* (Cambridge University Press, 2007) (cited on pages 2, 7, 17–18).

[16] R. Mould, "Pierre Curie, 1859–1906", Current Oncology **14**, 74–82 (2007) (cited on page 3).

[17] E. Ising, "Beitrag zur theorie des ferro-und paramagnetismus", PhD thesis (Grefe & Tiedemann Hamburg, Germany, 1924) (cited on page 3).

[18] T. Ising, R. Folk, R. Kenna, B. Berche, and Y. Holovatch, "The fate of Ernst Ising and the fate of his model", arXiv preprint arXiv:1706.01764 (2017) (cited on page 3).

[19] R. Peierls, "On Ising's model of ferromagnetism", Mathematical Proceedings of the Cambridge Philosophical Society **32**, 477–481 (1936) (cited on page 3).

[20] R. B. Griffiths, "Peierls Proof of Spontaneous Magnetization in a Two-Dimensional Ising Ferromagnet", Phys. Rev. **136**, A437–A439 (1964) (cited on page 3).

[21] L. Onsager, "Crystal Statistics. I. A Two-Dimensional Model with an Order-Disorder Transition", Phys. Rev. **65**, 117–149 (1944) (cited on page 3).

[22] K. G. Wilson, "Renormalization Group and Critical Phenomena. I. Renormalization Group and the Kadanoff Scaling Picture", Phys. Rev. B **4**, 3174–3183 (1971) (cited on pages 3, 16, 18).

[23] K. G. Wilson, "Renormalization Group and Critical Phenomena. II. Phase-Space Cell Analysis of Critical Behavior", Phys. Rev. B **4**, 3184–3205 (1971) (cited on pages 3, 16, 18).

[24] K. G. Wilson and J. Kogut, "The renormalization group and the ε expansion", Physics reports **12**, 75–199 (1974) (cited on pages 3, 16).

[25] G. Mussardo, *Statistical field theory: an introduction to exactly solved models in statistical physics*, Oxford graduate texts (Oxford University Press, Oxford ; New York, 2010) (cited on pages 3, 7, 15).

[26] N. Metropolis, A. W. Rosenbluth, M. N. Rosenbluth, A. H. Teller, and E. Teller, "Equation of State Calculations by Fast Computing Machines", The Journal of Chemical Physics **21**, 1087–1092 (1953) (cited on pages 4, 36, 83, 107).

[27] W. K. Hastings, "Monte Carlo sampling methods using Markov chains and their applications", Biometrika **57**, 97–109 (1970) (cited on page 4).

[28] A. B. Harris, "Effect of random defects on the critical behaviour of Ising models", Journal of Physics C: Solid State Physics **7**, 1671–1692 (1974) (cited on pages 5, 29–31).

[29] N. G. Fytas, J. Zierenberg, P. E. Theodorakis, M. Weigel, W. Janke, and A. Malakis, "Universality from disorder in the random-bond Blume-Capel model", Phys. Rev. E **97**, 040102 (2018) (cited on pages 5, 86, 93, 124).

[30] K. Huang, *Introduction to statistical physics* (CRC press, 2009) (cited on pages 7–8, 10).

[31] M. Kardar, *Statistical physics of particles* (Cambridge University Press, 2007) (cited on pages 7, 10, 23).

[32] L. D. Landau and E. M. Lifshitz, *Statistical Physics: Volume 5*, Vol. 5 (Elsevier, 2013) (cited on pages 7–10).

[33] H. E. Stanley, *Phase transitions and critical phenomena*, Vol. 7 (Clarendon Press, Oxford, 1971) (cited on page 7).

[34] Baxter, R. J., *Exactly Solved Models in Statistical Mechanics* (Academic, New York, 1982) (cited on pages 7, 54, 62, 80).

[35] J. M. Yeomans, *Statistical mechanics of phase transitions* (Clarendon Press, 1992) (cited on page 7).

[36] M. E. Fisher, "Renormalization group theory: Its basis and formulation in statistical physics", Reviews of Modern Physics **70**, 653 (1998) (cited on page 7).

[37] D. J. Amit and V. Martin-Mayor, *Field theory, the renormalization group, and critical phenomena: graphs to computers* (World Scientific Publishing Company, 2005) (cited on page 7).

[38] M. Le Bellac and G. Barton, *Quantum and statistical field theory* (1991) (cited on pages 7, 14, 19).

[39] H. Risken, *The Fokker-Planck equation* (Springer, 1996) (cited on pages 8, 33).

[40] K. Binder and A. P. Young, "Spin glasses: Experimental facts, theoretical concepts, and open questions", Reviews of Modern Physics **58**, 801–976 (1986) (cited on pages 8, 29).

[41] W. Janke, "Monte Carlo methods in classical statistical physics", in *Computational many-particle physics* (Springer, 2008), pages 79–140 (cited on pages 13–14, 33, 41, 48–50, 85, 127).

[42] P. Ehrenfest, *Phasenumwandlungen im ueblichen und erweiterten Sinn, classifiziert nach den entsprechenden Singularitaeten des thermodynamischen Potentiales* (NV Noord-Hollandsche Uitgevers Maatschappij, 1933) (cited on page 16).

[43] L. P. Kadanoff, "Scaling laws for ising models near T_c", Physics Physique Fizika **2**, 263–272 (1966) (cited on pages 16, 18, 23).

[44] P. Lepage, "How to Renormalize the Schrodinger Equation", arXiv:nucl-th/9706029 (1997) (cited on page 16).

[45] S. H. Strogatz, *Nonlinear dynamics and chaos with student solutions manual: With applications to physics, biology, chemistry, and engineering* (CRC press, 2018) (cited on page 18).

[46] M. Nauenberg and B. Nienhuis, "Renormalization-Group Approach to the Solution of General Ising Models", Phys. Rev. Lett. **33**, 1598–1601 (1974) (cited on page 18).

[47] K. G. Wilson, "The renormalization group and critical phenomena", Rev. Mod. Phys. **55**, 583–600 (1983) (cited on page 18).

[48] R. H. Swendsen, "Monte Carlo Renormalization Group", Physical Review Letters **42**, 859–861 (1979) (cited on pages 19, 51).

[49] J. M. J. van Leeuwen, "Singularities in the Critical Surface and Universality for Ising-Like Spin Systems", Phys. Rev. Lett. **34**, 1056–1058 (1975) (cited on page 19).

[50] R. H. Swendsen, "Monte Carlo renormalization-group studies of the $d = 2$ Ising model", Phys. Rev. B **20**, 2080–2087 (1979) (cited on pages 19, 51).

[51] T. A. Witten and J. J. Prentis, "Optimal real-space renormalisation", Journal of Physics A: Mathematical and General **14**, 447–457 (1981) (cited on page 19).

[52] P. M. Lenggenhager, D. E. Gökmen, Z. Ringel, S. D. Huber, and M. Koch-Janusz, "Optimal Renormalization Group Transformation from Information Theory", Phys. Rev. X **10**, 011037 (2020) (cited on page 19).

[53] J.-H. Chung and Y.-J. Kao, "Neural Monte Carlo renormalization group", Physical Review Research **3**, 023230 (2021) (cited on pages 19, 51).

[54] K. Levenberg, "A method for the solution of certain non-linear problems in least squares", Quarterly of applied mathematics **2**, 164–168 (1944) (cited on page 26).

[55] D. W. Marquardt, "An Algorithm for Least-Squares Estimation of Nonlinear Parameters", Journal of the Society for Industrial and Applied Mathematics **11**, 431–441 (1963) (cited on page 26).

[56] W. H. Press, S. A. Teukolsky, W. T. Vettering, and B. P. Flannery, "Numerical Recipes in C++: The Art of Scientific Computing (2nd edn)1 Numerical Recipes Example Book (C++) (2nd edn)2 Numerical Recipes Multi-Language Code CD ROM with LINUX or UNIX Single-Screen License Revised Version3", European Journal of Physics **24**, 329 (2003) (cited on page 26).

[57] P. Young, *Everything you wanted to know about Data Analysis and Fitting but were afraid to ask*, arXiv: 1210.3781, Oct. 2014 (cited on pages 26, 125).

[58] J. Lee and J. M. Kosterlitz, "New numerical method to study phase transitions", Phys. Rev. Lett. **65**, 137–140 (1990) (cited on pages 27, 88).

[59] J. Lee and J. M. Kosterlitz, "Finite-size scaling and Monte Carlo simulations of first-order phase transitions", Phys. Rev. B **43**, 3265–3277 (1991) (cited on pages 27, 88).

[60] W. Janke, "Accurate first-order transition points from finite-size data without power-law corrections", Phys. Rev. B **47**, 14757–14770 (1993) (cited on page 27).

[61] C. Borgs and J. Z. Imbrie, "A unified approach to phase diagrams in field theory and statistical mechanics", Communications in mathematical physics **123**, 305–328 (1989) (cited on page 27).

[62] D. S. Fisher, G. M. Grinstein, and A. Khurana, "Theory of random magnets", Physics Today **41**, 56–67 (1988) (cited on page 28).

[63] T. Nattermann and J. Villain, "Random-field ising systems: A survey of current theoretical views", Phase transitions **11**, 5–51 (1988) (cited on page 28).

[64] A. K. Hartmann, *Random-field systems, spin glasses and vertex covers: on the relation of statistical physics and combinatorial optimization* (Kumulative, 2004) (cited on page 29).

[65] R. Brout, "Statistical Mechanical Theory of a Random Ferromagnetic System", Physical Review **115**, 824–835 (1959) (cited on pages 29, 31).

[66] V. S. Dotsenko and V. S. Dotsenko, "Phase transition in the 2D Ising model with impurity bonds", ZhETF Pisma Redaktsiiu **33**, 40 (1981) (cited on pages 30, 118).

[67] M. Aizenman and J. Wehr, "Rounding of first-order phase transitions in systems with quenched disorder", Phys. Rev. Lett. **62**, 2503–2506 (1989) (cited on pages 30, 32).

[68] K. Hui and A. N. Berker, "Random-field mechanism in random-bond multicritical systems", Phys. Rev. Lett. **62**, 2507–2510 (1989) (cited on page 30).

[69] A. Nihat Berker, "Critical behavior induced by quenched disorder", Physica A: Statistical Mechanics and its Applications **194**, 72–76 (1993) (cited on page 30).

[70] C. Chatelain, B. Berche, W. Janke, and P.-E. Berche, "Softening of first-order transition in three-dimensions by quenched disorder", Phys. Rev. E **64**, 036120 (2001) (cited on page 30).

[71] C. Chatelain, B. Berche, W. Janke, and P.-E. Berche, "Monte Carlo study of phase transitions in the bond-diluted 3D 4-state Potts model", Nuclear Physics B **719**, 275–311 (2005) (cited on page 30).

[72] N. Ma, A. W. Sandvik, and D.-X. Yao, "Criticality and Mott glass phase in a disordered two-dimensional quantum spin system", Phys. Rev. B **90**, 104425 (2014) (cited on page 30).

[73] A. M. Mood, F. A. Graybill, and D. C. Boes, *Introduction to the Theory of Statistics 1974* (McGraw-Hill Kogakusha, 1974) (cited on pages 31, 126).

[74] S. Wiseman and E. Domany, "Lack of self-averaging in critical disordered systems", Physical Review E **52**, 3469–3484 (1995) (cited on page 31).

[75] A. Aharony and A. B. Harris, "Absence of Self-Averaging and Universal Fluctuations in Random Systems near Critical Points", Physical Review Letters **77**, 3700–3703 (1996) (cited on page 31).

[76] S. Wiseman and E. Domany, "Finite-Size Scaling and Lack of Self-Averaging in Critical Disordered Systems", Physical Review Letters **81**, 22–25 (1998) (cited on page 32).

[77] J. Cardy, "Quenched randomness at first-order transitions", Physica A: Statistical Mechanics and its Applications **263**, Proceedings of the 20th IUPAP International Conference on Statistical Physics, 215–221 (1999) (cited on page 32).

[78] D. Landau and K. Binder, *A Guide to Monte Carlo Simulations in Statistical Physics* (Cambridge university press, 2000) (cited on pages 33, 35, 39, 50, 83, 107).

[79] M. E. Newman and G. T. Barkema, *Monte Carlo methods in statistical physics* (Clarendon Press, 1999) (cited on pages 33–35, 39, 49, 107).

[80] J. Piilo, S. Maniscalco, K. Härkönen, and K.-A. Suominen, "Non-Markovian Quantum Jumps", Phys. Rev. Lett. **100**, 180402 (2008) (cited on page 33).

[81] J. Lee, "New Monte Carlo algorithm: Entropic sampling", Phys. Rev. Lett. **71**, 211–214 (1993) (cited on page 35).

[82] D. Loison, C. L. Qin, K. D. Schotte, and X. F. Jin, "Canonical local algorithms for spin systems: heat bath and Hasting's methods", The European Physical Journal B **41**, 395–412 (2004) (cited on pages 37–38, 58).

[83] U. Wolff, "Comparison between cluster Monte Carlo algorithms in the Ising model", Physics Letters B **228**, 379–382 (1989) (cited on pages 40, 50).

[84] R. H. Swendsen and J.-S. Wang, "Nonuniversal critical dynamics in Monte Carlo simulations", Phys. Rev. Lett. **58**, 86–88 (1987) (cited on pages 40, 58).

[85] R. B. Potts, "Some generalized order-disorder transformations", Mathematical Proceedings of the Cambridge Philosophical Society **48**, 106–109 (1952) (cited on page 41).

[86] C. Fortuin and P. Kasteleyn, "On the random-cluster model: I. Introduction and relation to other models", Physica **57**, 536–564 (1972) (cited on page 41).

[87] C. Fortuin, "On the random-cluster model ii. the percolation model", Physica **58**, 393–418 (1972) (cited on page 41).

[88] C. Fortuin, "On the random-cluster model: III. The simple random-cluster model", Physica **59**, 545–570 (1972) (cited on page 41).

[89] H. W. J. Blote, E Luijten, and J. R. Heringa, "Ising universality in three dimensions: a Monte Carlo study", Journal of Physics A: Mathematical and General **28**, 6289–6313 (1995) (cited on pages 41, 58).

[90] M. Hasenbusch, "Finite size scaling study of lattice models in the three-dimensional Ising universality class", Phys. Rev. B **82**, 174433 (2010) (cited on page 41).

[91] A. Malakis, A. N. Berker, N. G. Fytas, and T. Papakonstantinou, "Universality aspects of the d = 3 random-bond Blume-Capel model", Physical Review E **85**, 061106 (2012) (cited on pages 41, 58).

[92] F. Wang and D. P. Landau, "Efficient, Multiple-Range Random Walk Algorithm to Calculate the Density of States", Phys. Rev. Lett. **86**, 2050–2053 (2001) (cited on pages 42–43, 82–83).

[93] F. Wang and D. P. Landau, "Determining the density of states for classical statistical models: A random walk algorithm to produce a flat histogram", Phys. Rev. E **64**, 056101 (2001) (cited on pages 42–43, 82–83).

[94] B. A. Berg and T. Neuhaus, "Multicanonical ensemble: A new approach to simulate first-order phase transitions", Phys. Rev. Lett. **68**, 9–12 (1992) (cited on pages 42, 44, 84).

[95] J. Lidmar, "Improving the efficiency of extended ensemble simulations: The accelerated weight histogram method", Phys. Rev. E **85**, 056708 (2012) (cited on page 42).

[96] A. Cunha Netto, C. Silva, A. Caparica, and R Dickman, "Wang-Landau sampling in three-dimensional polymers", Brazilian journal of physics **36**, 619–622 (2006) (cited on page 43).

[97] D. F. Parsons and D. R. Williams, "Globule transitions of a single homopolymer: A Wang-Landau Monte Carlo study", Physical Review E **74**, 041804 (2006) (cited on page 43).

[98] D. F. Parsons and D. R. Williams, "An off-lattice Wang-Landau study of the coil-globule and melting transitions of a flexible homopolymer", The Journal of chemical physics **124** (2006) (cited on page 43).

[99] W. Paul, T. Strauch, F. Rampf, and K. Binder, "Unexpectedly normal phase behavior of single homopolymer chains", Physical Review E **75**, 060801 (2007) (cited on page 43).

[100] N. Rathore and J. J. de Pablo, "Monte Carlo simulation of proteins through a random walk in energy space", The Journal of chemical physics **116**, 7225–7230 (2002) (cited on page 43).

[101] N. Rathore, I. Knotts Thomas A., and J. J. de Pablo, "Erratum: "Density of states simulations of proteins" [J. Chem. Phys. 118, 4285 (2003)]", The Journal of Chemical Physics **118**, 9460–9461 (2003) (cited on page 43).

[102] T. Wüst and D. Landau, "The HP model of protein folding: A challenging testing ground for Wang–Landau sampling", Computer Physics Communications **179**, 124–127 (2008) (cited on page 43).

[103] A. G. Cunha-Netto, A. A. Caparica, S.-H. Tsai, R. Dickman, and D. P. Landau, "Improving Wang-Landau sampling with adaptive windows", Phys. Rev. E **78**, 055701 (2008) (cited on pages 43, 83).

[104] A. Malakis, A. Peratzakis, and N. G. Fytas, "Estimation of critical behavior from the density of states in classical statistical models", Phys. Rev. E **70**, 066128 (2004) (cited on pages 43–44, 83).

[105] A. Malakis, S. S. Martinos, I. A. Hadjiagapiou, N. G. Fytas, and P. Kalozoumis, "Entropic sampling via Wang-Landau random walks in dominant energy subspaces", Phys. Rev. E **72**, 066120 (2005) (cited on pages 43–44, 83).

[106] A. Malakis and N. G. Fytas, "Lack of self-averaging of the specific heat in the three-dimensional random-field Ising model", Phys. Rev. E **73**, 016109 (2006) (cited on pages 43, 83).

[107] N. G. Fytas, A. Malakis, and K. Eftaxias, "First-order transition features of the 3D bimodal random-field Ising model", Journal of Statistical Mechanics: Theory and Experiment **2008**, P03015 (2008) (cited on pages 43, 83).

[108] N. G. Fytas and P. E. Theodorakis, "Universality in disordered systems: The case of the three-dimensional random-bond Ising model", Phys. Rev. E **82**, 062101 (2010) (cited on pages 43, 83).

[109] J. K. Salmon, M. A. Moraes, R. O. Dror, and D. E. Shaw, "Parallel Random Numbers: As Easy as 1, 2, 3", in Proceedings of 2011 international conference for high performance computing, networking, storage and analysis, SC '11 (2011) (cited on page 46).

[110] M. Manssen, M. Weigel, and A. K. Hartmann, "Random number generators for massively parallel simulations on GPU", The European Physical Journal Special Topics **210**, 53–71 (2012) (cited on page 46).

[111] J. Gross, J. Zierenberg, M. Weigel, and W. Janke, "Massively parallel multicanonical simulations", Computer Physics Communications **224**, 387–395 (2018) (cited on pages 46–48, 86).

[112] S. Kullback and R. A. Leibler, "On information and sufficiency", The annals of mathematical statistics **22**, 79–86 (1951) (cited on pages 48, 86).

[113] M. Nightingale, "Scaling theory and finite systems", Physica A: Statistical Mechanics and its Applications **83**, 561–572 (1976) (cited on pages 50, 66, 95).

[114] N. Ito, K. Hukushima, K. Ogawa, and Y. Ozeki, "Nonequilibrium relaxation of fluctuations of physical quantities", Journal of the Physical Society of Japan **69**, 1931–1934 (2000) (cited on page 50).

[115] S.-k. Ma, "Renormalization Group by Monte Carlo Methods", Physical Review Letters **37**, 461–464 (1976) (cited on page 51).

[116] G. S. Pawley, R. H. Swendsen, D. J. Wallace, and K. G. Wilson, "Monte Carlo renormalization-group calculations of critical behavior in the simple-cubic Ising model", Physical Review B **29**, 4030–4040 (1984) (cited on page 51).

[117] R. H. Swendsen, "Monte Carlo Calculation of Renormalized Coupling Parameters", Physical Review Letters **52**, 1165–1168 (1984) (cited on page 51).

[118] M. A. Novotny and D. P. Landau, "Monte Carlo renormalization group for quantum systems", Physical Review B **31**, 1449–1456 (1985) (cited on page 51).

[119] C. F. Baillie, R. Gupta, K. A. Hawick, and G. S. Pawley, "Monte Carlo renormalization-group study of the three-dimensional Ising model", Physical Review B **45**, 10438–10453 (1992) (cited on page 51).

[120] H. W. J. Blöte, J. R. Heringa, A. Hoogland, E. W. Meyer, and T. S. Smit, "Monte Carlo Renormalization of the 3D Ising Model: Analyticity and Convergence", Physical Review Letters **76**, 2613–2616 (1996) (cited on page 51).

[121] D. Ron, A. Brandt, and R. H. Swendsen, "The surprising convergence of the Monte Carlo renormalization group for the d=3 Ising Model", Physical Review E **95**, arXiv:1703.02430 [cond-mat], 053305 (2017) (cited on page 51).

[122] D. Bachtis, G. Aarts, and B. Lucini, "Adding machine learning within Hamiltonians: Renormalization group transformations, symmetry breaking and restoration", Phys. Rev. Res. **3**, 013134 (2021) (cited on page 51).

[123] E. Marinari and G. Parisi, "Simulated Tempering: A New Monte Carlo Scheme", Europhysics Letters **19**, 451 (1992) (cited on page 51).

[124] K. Hukushima and K. Nemoto, "Exchange Monte Carlo Method and Application to Spin Glass Simulations", Journal of the Physical Society of Japan **65**, 1604–1608 (1996) (cited on page 51).

[125] Y. Iba, "Population Monte Carlo algorithms", Transactions of the Japanese Society for Artificial Intelligence **16**, 279–286 (2001) (cited on page 51).

[126] J. Machta, "Population annealing with weighted averages: A Monte Carlo method for rough free-energy landscapes", Phys. Rev. E **82**, 026704 (2010) (cited on page 51).

[127] M. Weigel, L. Barash, L. Shchur, and W. Janke, "Understanding population annealing Monte Carlo simulations", Phys. Rev. E **103**, 053301 (2021) (cited on page 51).

[128] S. R. White, "Density matrix formulation for quantum renormalization groups", Phys. Rev. Lett. **69**, 2863–2866 (1992) (cited on page 51).

[129] S. R. White, "Density-matrix algorithms for quantum renormalization groups", Phys. Rev. B **48**, 10345–10356 (1993) (cited on page 51).

[130] U. Schollwöck, "The density-matrix renormalization group", Rev. Mod. Phys. **77** (2005) (cited on page 51).

[131] M. Levin and C. P. Nave, "Tensor Renormalization Group Approach to Two-Dimensional Classical Lattice Models", Physical Review Letters **99**, 120601 (2007) (cited on page 51).

[132] Z. Y. Xie, H. C. Jiang, Q. N. Chen, Z. Y. Weng, and T. Xiang, "Second Renormalization of Tensor-Network States", Physical Review Letters **103**, 160601 (2009) (cited on page 51).

[133] H. H. Zhao, Z. Y. Xie, Q. N. Chen, Z. C. Wei, J. W. Cai, and T. Xiang, "Renormalization of tensor-network states", Physical Review B **81**, 174411 (2010) (cited on page 51).

[134] T. Nishino and K. Okunishi, "Corner transfer matrix renormalization group method", Journal of the Physical Society of Japan **65**, 891–894 (1996) (cited on page 51).

[135] C. Chatelain and A. Gendiar, "Absence of logarithmic divergence of the entanglement entropies at the phase transitions of a 2D classical hard rod model", The European Physical Journal B **93**, 1–15 (2020) (cited on page 51).

[136] M. A. Novotny and H. G. Evertz, "Computer studies of the baxter-wu model: algorithms, corrections to scaling, and regular impurities", in Computer simulation studies in condensed-matter physics vi, edited by D. P. Landau, K. K. Mon, and H.-B. Schüttler (1993), pages 188–192 (cited on pages 53, 56, 62, 66, 74, 123).

[137] D. W. Wood and H. P. Griffiths, "A self dual relation for an Ising model with triplet interactions", Journal of Physics C: Solid State Physics **5**, L253 (1972) (cited on pages 53–54).

[138] D. Merlini and C. Gruber, "Spin-½ Lattice System: Group Structure and Duality Relation", J. Math. Phys. **13**, 1814–1823 (1972) (cited on page 54).

[139] R. J. Baxter and F. Y. Wu, "Exact Solution of an Ising Model with Three-Spin Interactions on a Triangular Lattice", Phys. Rev. Lett. **31**, 1294–1297 (1973) (cited on pages 54, 62, 80, 93).

[140] F. C. Alcaraz and J. C. Xavier, "Conformal invariance studies of the Baxter - Wu model and a related site-colouring problem", Journal of Physics A: Mathematical and General **30**, L203 (1997) (cited on pages 54, 64, 80, 90).

[141] F. C. Alcaraz and J. C. Xavier, "Critical and off-critical studies of the Baxter-Wu model with general toroidal boundary conditions", Journal of Physics A: Mathematical and General **32**, 2041 (1999) (cited on pages 54, 64, 80, 90).

[142] E. Domany and E. K. Riedel, "Phase transitions in two-dimensional systems", Journal of Applied Physics **49**, 1315–1320 (1978) (cited on page 54).

[143] F. Y. Wu, "The Potts model", Rev. Mod. Phys. **54**, 235–268 (1982) (cited on page 54).

[144] S. L. A. C. LN Jorge LS Ferreira, "Critical Behavior of the Spin-1/2 Baxter-Wu Model: Entropic Sampling Simulations", Braz J Phys **46**, 556–564 (2016) (cited on pages 54, 93).

[145] M. Blume, "Theory of the First-Order Magnetic Phase Change in Uo_2", Phys. Rev. **141**, 517–524 (1966) (cited on pages 55, 105).

[146] H. Capel, "Physica (Utr.) 32, 966 (1966); HW Capel", Physica (Utr.) **32**, 966 (1966) (cited on pages 55, 105).

[147] H. Capel, "Physica (Utr.) 33, 295 (1967); HW Capel", Physica (Utr.) **33**, 295 (1967) (cited on pages 55, 105).

[148] H. Capel, "Physica (Utrecht) 37 (1967) 423", Physica (Utrecht) **37**, 423 (1967) (cited on pages 55, 105).

[149] S. Moss de Oliveira, P. de Oliveira, and F. de Sá Barreto, "The spin-S Blume-Capel RG flow diagram", Journal of Statistical Physics **78**, 1619–1627 (1995) (cited on page 55).

[150] J. C. Xavier, F. C. Alcaraz, D. P. a. Lara, and J. A. Plascak, "Critical behavior of the spin-$\frac{3}{2}$ Blume-Capel model in two dimensions", Phys. Rev. B **57**, 11575–11581 (1998) (cited on page 55).

[151] J. A. Plascak and D. P. Landau, "Universality and double critical end points", Phys. Rev. E **67**, 015103 (2003) (cited on page 55).

[152] A. Malakis, A. N. Berker, I. A. Hadjiagapiou, and N. G. Fytas, "Strong violation of critical phenomena universality: Wang-Landau study of the two-dimensional Blume-Capel model under bond randomness", Phys. Rev. E **79**, 011125 (2009) (cited on page 55).

[153] A. Malakis, A. N. Berker, I. A. Hadjiagapiou, N. G. Fytas, and T. Papakonstantinou, "Multicritical points and crossover mediating the strong violation of universality: Wang-Landau determinations in the random-bond $d = 2$ Blume-Capel model", Phys. Rev. E **81**, 041113 (2010) (cited on pages 55, 106–107).

[154] J. Zierenberg, N. G. Fytas, and W. Janke, "Parallel multicanonical study of the three-dimensional Blume-Capel model", Phys. Rev. E **91**, 032126 (2015) (cited on pages 55, 84, 86).

[155] W. Kwak, J. Jeong, J. Lee, and D.-H. Kim, "First-order phase transition and tricritical scaling behavior of the Blume-Capel model: A Wang-Landau sampling approach", Phys. Rev. E **92**, 022134 (2015) (cited on pages 55, 98, 102, 106–107).

[156] J. Zierenberg, N. Fytas, M. Weigel, W. Janke, and A. Malakis, "Scaling and universality in the phase diagram of the 2D Blume-Capel model", The European Physical Journal Special Topics **226**, 022134 (2017) (cited on pages 55, 58, 86, 106).

[157] B. Nienhuis, A. N. Berker, E. K. Riedel, and M. Schick, "First- and Second-Order Phase Transitions in Potts Models: Renormalization-Group Solution", Phys. Rev. Lett. **43**, 737–740 (1979) (cited on pages 55, 80).

[158] W. Kinzel, E. Domany, and A. Aharony, "Finite size scaling analysis of the dilute Baxter-Wu model", Journal of Physics A: Mathematical and General **14**, L417 (1981) (cited on pages 55, 80).

[159] M. L. M. Costa, J. C. Xavier, and J. A. Plascak, "Phase diagram and critical behavior of the spin-1 Baxter-Wu model with a crystal field", Phys. Rev. B **69**, 104103 (2004) (cited on pages 55, 80).

[160] D. A. Dias, J. C. Xavier, and J. A. Plascak, "Critical behavior of the spin-1 and spin-3/2 Baxter-Wu model in a crystal field", Phys. Rev. E **95**, 012103 (2017) (cited on pages 55–56, 66, 80–81, 90, 141).

[161] L. Jorge, L. Ferreira, and A. Caparica, "On the order of the phase transition in the spin-1 Baxter–Wu model", Physica A: Statistical Mechanics and its Applications **542**, 123417 (2020) (cited on pages 55, 81, 83, 87–88).

[162] L. Jorge, P. Martins, C. J. DaSilva, L. Ferreira, and A. Caparica, "An entropic simulational study of the spin-1 Baxter–Wu model in a crystal field", Physica A: Statistical Mechanics and its Applications **576**, 126071 (2021) (cited on pages 55–56, 80–81).

[163] N. G. Fytas, A. Vasilopoulos, E. Vatansever, A. Malakis, and M. Weigel, "Multicanonical simulations of the 2D spin-1 Baxter-Wu model in a crystal field", Journal of Physics: Conference Series **2207**, 012008 (2022) (cited on pages 55–56, 79, 88).

[164] A. Vasilopoulos, N. G. Fytas, E. Vatansever, A. Malakis, and M. Weigel, "Universality in the two-dimensional dilute Baxter-Wu model", Physical Review E **105**, 054143 (2022) (cited on pages 56, 59–60, 66, 74, 79).

[165] A. R. S. Macêdo, A. Vasilopoulos, M. Akritidis, J. A. Plascak, N. G. Fytas, and M. Weigel, "Two-dimensional dilute Baxter-Wu model: Transition order and universality", Phys. Rev. E **108**, 024140 (2023) (cited on pages 56, 66, 79).

[166] Y. Miyatake, M. Yamamoto, J. J. Kim, M. Toyonaga, and O. Nagai, "On the implementation of the 'heat bath' algorithms for Monte Carlo simulations of classical Heisenberg spin systems", Journal of Physics C: Solid State Physics **19**, 2539 (1986) (cited on page 58).

[167] N. Madras and A. D. Sokal, "The pivot algorithm: A highly efficient Monte Carlo method for the self-avoiding walk", Journal of Statistical Physics **50**, 109–186 (1988) (cited on page 61).

[168] M. Hasenbusch, "Dynamic critical exponent z of the three-dimensional Ising universality class: Monte Carlo simulations of the improved Blume-Capel model", Physical Review E **101**, 022126 (2020) (cited on pages 61, 75).

[169] M. Hasenbusch, A. Pelissetto, and E. Vicari, "Relaxational dynamics in 3D randomly diluted Ising models", Journal of Statistical Mechanics: Theory and Experiment **2007**, P11009–P11009 (2007) (cited on pages 61, 64, 76).

[170] I. Velonakis and S. Martinos, "A new cluster algorithm for the Baxter–Wu model", Physica A: Statistical Mechanics and its Applications **390**, 24–30 (2011) (cited on pages 62, 66, 74).

[171] W. V. W.H. Press S.A. Teukolsky and B. Flannery, *Numerical Recipes in C 2nd ed.* (Cambridge University Press, 1992) (cited on page 64).

[172] M. Picco, R. Santachiara, and A. Sicilia, "Geometrical properties of parafermionic spin models", Journal of Statistical Mechanics: Theory and Experiment **2009**, P04013 (2009) (cited on page 74).

[173] Z. Liu, E. Vatansever, G. T. Barkema, and N. G. Fytas, "Critical dynamical behavior of the Ising model", Phys. Rev. E **108**, 034118 (2023) (cited on page 75).

[174] W. Zhong, G. T. Barkema, and D. Panja, "Super slowing down in the bond-diluted Ising model", Physical Review E **102**, 022132 (2020) (cited on page 75).

[175] C. K. Harris and R. B. Stinchcombe, "Critical Dynamics at the Percolation Threshold by Fractal and Scaling Approaches", Phys. Rev. Lett. **50**, 1399–1402 (1983) (cited on page 75).

[176] S. Jain, "Non-universality in the dynamics at the percolation threshold", Journal of Physics A: Mathematical and General **19**, L667 (1986) (cited on page 75).

[177] N. G. Fytas, V. Martín-Mayor, G. Parisi, M. Picco, and N. Sourlas, "Evidence for Supersymmetry in the Random-Field Ising Model at $D = 5$", Phys. Rev. Lett. **122**, 240603 (2019) (cited on page 76).

[178] I. Hadjiagapiou, A. Malakis, and S. Martinos, "Short-time scaling via Monte Carlo single spin-flip algorithms for the Baxter–Wu model", Physica A: Statistical Mechanics and its Applications **356**, 563–574 (2005) (cited on page 80).

[179] L. N. Shchur and W. Janke, "Critical amplitude ratios of the Baxter–Wu model", Nuclear Physics B **840**, 491–512 (2010) (cited on pages 80, 93).

[180] I. Velonakis and S. Martinos, "Baxter–Wu model in the presence of an external magnetic field", Physica A: Statistical Mechanics and its Applications **392**, 2016–2024 (2013) (cited on page 80).

[181] S. Capponi, S. S. Jahromi, F. Alet, and K. P. Schmidt, "Baxter-Wu model in a transverse magnetic field", Phys. Rev. E **89**, 062136 (2014) (cited on pages 80, 96, 102).

[182] M. L. M. Costa and J. A. Plascak, "Monte Carlo study of the spin-1 Baxter-Wu model", Brazilian Journal of Physics **34**, 419–421 (2004) (cited on pages 80, 83).

[183] M. L. M. Costa and J. A. Plascak, "Monte Carlo study of the Spin-1 Baxter-Wu model in a crystal field", Journal of Physics: Conference Series **686**, 012011 (2016) (cited on pages 80, 83, 86, 90).

[184] J. Zierenberg, M. Marenz, and W. Janke, "Scaling properties of a parallel implementation of the multicanonical algorithm", Computer Physics Communications **184**, 1155–1160 (2013) (cited on page 86).

[185] A. M. Ferrenberg and D. P. Landau, "Critical behavior of the three-dimensional Ising model: A high-resolution Monte Carlo study", Phys. Rev. B **44**, 5081–5091 (1991) (cited on pages 86, 92, 118).

[186] A. A. Caparica, A. Bunker, and D. P. Landau, "Classical ferromagnet with double-exchange interaction: High-resolution Monte Carlo simulations", Phys. Rev. B **62**, 9458–9462 (2000) (cited on page 86).

[187] K. Binder and D. P. Landau, "Finite-size scaling at first-order phase transitions", Phys. Rev. B **30**, 1477–1485 (1984) (cited on page 87).

[188] K. Binder, "Theory of first-order phase transitions", Reports on Progress in Physics **50**, 783 (1987) (cited on page 87).

[189] C. Borgs and S. Kappler, "Equal weight versus equal height: a numerical study of an asymmetric first-order transition", Physics Letters A **171**, 37–42 (1992) (cited on page 88).

[190] A. Nußbaumer, E. Bittner, T. Neuhaus, and W. Janke, "Monte Carlo study of the evaporation/condensation transition of Ising droplets", Europhysics Letters **75**, 716 (2006) (cited on page 88).

[191] A. Nußbaumer, E. Bittner, and W. Janke, "Monte Carlo study of the droplet formation-dissolution transition on different two-dimensional lattices", Phys. Rev. E **77**, 041109 (2008) (cited on page 88).

[192] E. Bittner, A. Nußbaumer, and W. Janke, "Anisotropy of the interface tension of the three-dimensional Ising model", Nuclear Physics B **820**, 694–706 (2009) (cited on page 88).

[193] J. Salas and A. Sokal, "Logarithmic Corrections and Finite-Size Scaling in the Two-Dimensional 4-State Potts Model", Journal of Statistical Physics **88**, 567–615 (1997) (cited on pages 95–96, 102).

[194] N. G. Fytas and V. Martín-Mayor, "Universality in the Three-Dimensional Random-Field Ising Model", Phys. Rev. Lett. **110**, 227201 (2013) (cited on pages 93, 95).

[195] N. G. Fytas and V. Martín-Mayor, "Efficient numerical methods for the random-field Ising model: Finite-size scaling, reweighting extrapolation, and computation of response functions", Phys. Rev. E **93**, 063308 (2016) (cited on pages 93, 95).

[196] N. G. Fytas, V. Martín-Mayor, M. Picco, and N. Sourlas, "Phase Transitions in Disordered Systems: The Example of the Random-Field Ising Model in Four Dimensions", Phys. Rev. Lett. **116**, 227201 (2016) (cited on pages 93, 95).

[197] N. G. Fytas, V. Martín-Mayor, M. Picco, and N. Sourlas, "Restoration of dimensional reduction in the random-field Ising model at five dimensions", Phys. Rev. E **95**, 042117 (2017) (cited on pages 93, 95).

[198] M. Hasenbusch, "Universal amplitude ratios in the three-dimensional Ising universality class", Phys. Rev. B **82**, 174434 (2010) (cited on page 93).

[199] M. Hasenbusch, "The three-dimensional XY universality class: a high precision Monte Carlo estimate of the universal amplitude ratio A+/A-", Journal of Statistical Mechanics: Theory and Experiment **2006**, P08019 (2006) (cited on page 93).

[200] F. Cooper, B. Freedman, and D. Preston, "Solving φ 1,24 field theory with Monte Carlo", Nuclear Physics B **210**, 210–228 (1982) (cited on page 93).

[201] H. G. Ballesteros, L. A. Fernández, V Martín-Mayor, A. M. Sudupe, G Parisi, and J. J. Ruiz-Lorenzo, "Scaling corrections: site percolation and Ising model in three dimensions", Journal of Physics A: Mathematical and General **32**, 1 (1999) (cited on pages 93, 95).

[202] H. Ballesteros, L. Fernández, V. Martín-Mayor, and A. Muñoz Sudupe, "New universality class in three dimensions?: the antiferromagnetic RP2 model", Physics Letters B **378**, 207–212 (1996) (cited on page 95).

[203] K. Binder, "Finite size scaling analysis of Ising model block distribution functions", Zeitschrift für Physik B Condensed Matter **43**, 119–140 (1981) (cited on pages 96, 108).

[204] J. Plascak and P. Martins, "Probability distribution function of the order parameter: Mixing fields and universality", Computer Physics Communications **184**, 259–269 (2013) (cited on pages 96, 98, 102).

[205] A. D. Bruce and N. B. Wilding, "Scaling fields and universality of the liquid-gas critical point", Phys. Rev. Lett. **68**, 193–196 (1992) (cited on page 98).

[206] N. B. Wilding and P. Nielaba, "Tricritical universality in a two-dimensional spin fluid", Phys. Rev. E **53**, 926–934 (1996) (cited on pages 98, 102, 124).

[207] M. Weigel and W. Janke, "Cross Correlations in Scaling Analyses of Phase Transitions", Phys. Rev. Lett. **102**, 100601 (2009) (cited on page 102).

[208] M. Weigel and W. Janke, "Error estimation and reduction with cross correlations", Phys. Rev. E **81**, 066701 (2010) (cited on page 102).

[209] A. Vasilopoulos, Z. D. Vatansever, E. Vatansever, and N. G. Fytas, "Monte Carlo study of the two-dimensional kinetic Blume-Capel model in a quenched random crystal field", Phys. Rev. E **104**, 024108 (2021) (cited on page 103).

[210] T. Tomé and M. J. de Oliveira, "Dynamic phase transition in the kinetic Ising model under a time-dependent oscillating field", Phys. Rev. A **41**, 4251–4254 (1990) (cited on page 103).

[211] W. S. Lo and R. A. Pelcovits, "Ising model in a time-dependent magnetic field", Phys. Rev. A **42**, 7471–7474 (1990) (cited on page 104).

[212] M. F. Zimmer, "Ising model in an oscillating magnetic field: Mean-field theory", Phys. Rev. E **47**, 3950–3955 (1993) (cited on page 104).

[213] M. Acharyya and B. K. Chakrabarti, "Response of Ising systems to oscillating and pulsed fields: Hysteresis, ac, and pulse susceptibility", Phys. Rev. B **52**, 6550–6568 (1995) (cited on page 104).

[214] B. K. Chakrabarti and M. Acharyya, "Dynamic transitions and hysteresis", Rev. Mod. Phys. **71**, 847–859 (1999) (cited on page 104).

[215] M. Acharyya, "Nonequilibrium phase transition in the kinetic Ising model: Divergences of fluctuations and responses near the transition point", Phys. Rev. E **56**, 1234–1237 (1997) (cited on page 104).

[216] M. Acharyya, "Multiple dynamic transitions in an anisotropic Heisenberg ferromagnet driven by polarized magnetic field", Phys. Rev. E **69**, 027105 (2004) (cited on page 104).

[217] G. M. Buendía and E. Machado, "Kinetics of a mixed Ising ferrimagnetic system", Phys. Rev. E **58**, 1260–1265 (1998) (cited on page 104).

[218] G. M. Buendía and E. Machado, "Magnetic behavior of a mixed Ising ferrimagnetic model in an oscillating magnetic field", Phys. Rev. B **61**, 14686–14690 (2000) (cited on page 104).

[219] H. Fujisaka, H. Tutu, and P. A. Rikvold, "Dynamic phase transition in a time-dependent Ginzburg-Landau model in an oscillating field", Phys. Rev. E **63**, 036109 (2001) (cited on pages 104–105).

[220] H. Jang, M. J. Grimson, and C. K. Hall, "Exchange anisotropy and the dynamic phase transition in thin ferromagnetic Heisenberg films", Phys. Rev. E **68**, 046115 (2003) (cited on page 104).

[221] H. Jang, M. J. Grimson, and C. K. Hall, "Dynamic phase transitions in thin ferromagnetic films", Phys. Rev. B **67**, 094411 (2003) (cited on page 104).

[222] X. Shi, G. Wei, and L. Li, "Effective-field theory on the kinetic Ising model", Physics Letters A **372**, 5922–5927 (2008) (cited on page 104).

[223] A. Punya, R. Yimnirun, P. Laoratanakul, and Y. Laosiritaworn, "Frequency dependence of the Ising–hysteresis phase–diagram: Mean field analysis", Physica B: Condensed Matter **405**, 3482–3488 (2010) (cited on page 104).

[224] P. Riego and A. Berger, "Nonuniversal surface behavior of dynamic phase transitions", Phys. Rev. E **91**, 062141 (2015) (cited on page 104).

[225] M. Keskin, O. Canko, and U. Temizer, "Dynamic phase transition in the kinetic spin-1 Blume-Capel model under a time-dependent oscillating external field", Phys. Rev. E **72**, 036125 (2005) (cited on page 104).

[226] M. Keskin, O. Canko, and U. Temizer, "Dynamic phase transition in the kinetic spin-1 Blume-Capel model: Phase diagrams in the temperature and crystal-field interaction plane", Journal of Experimental and Theoretical Physics **104**, 936–942 (2007) (cited on page 104).

[227] D. T. Robb, P. A. Rikvold, A. Berger, and M. A. Novotny, "Conjugate field and fluctuation-dissipation relation for the dynamic phase transition in the two-dimensional kinetic Ising model", Phys. Rev. E **76**, 021124 (2007) (cited on pages 104, 108).

[228] B. Deviren and M. Keskin, "Dynamic magnetic hysteresis behavior and dynamic phase transition in the spin-1 Blume–Capel model", Journal of Magnetism and Magnetic Materials **324**, 1051–1058 (2012) (cited on page 104).

[229] Y. Yüksel, E. Vatansever, and H. Polat, "Dynamic phase transition properties and hysteretic behavior of a ferrimagnetic core–shell nanoparticle in the presence of a time dependent magnetic field", Journal of Physics: Condensed Matter **24**, 436004 (2012) (cited on page 104).

[230] Y. Yüksel, E. Vatansever, and H. Polat, "Nonequilibrium phase transitions and stationary-state solutions of a three-dimensional random-field Ising model under a time-dependent periodic external field", Phys. Rev. E **85**, 051123 (2012) (cited on page 104).

[231] E. Vatansever, "Monte Carlo simulation of dynamic phase transitions and frequency dispersions of hysteresis curves in core/shell ferrimagnetic cubic nanoparticle," Physics Letters A **381**, 1535–1542 (2017) (cited on page 104).

[232] Y.-L. He and G.-C. Wang, "Observation of dynamic scaling of magnetic hysteresis in ultrathin ferromagnetic Fe/Au(001) films", Phys. Rev. Lett. **70**, 2336–2339 (1993) (cited on page 104).

[233] D. T. Robb, Y. H. Xu, O. Hellwig, J. McCord, A. Berger, M. A. Novotny, and P. A. Rikvold, "Evidence for a dynamic phase transition in $[Co/Pt]_3$ magnetic multilayers", Phys. Rev. B **78**, 134422 (2008) (cited on page 104).

[234] J.-S. Suen and J. L. Erskine, "Magnetic Hysteresis Dynamics: Thin $p(1 \times 1)$ Fe Films on Flat and Stepped W(110)", Phys. Rev. Lett. **78**, 3567–3570 (1997) (cited on page 104).

[235] A. Berger, O. Idigoras, and P. Vavassori, "Transient Behavior of the Dynamically Ordered Phase in Uniaxial Cobalt Films", Phys. Rev. Lett. **111**, 190602 (2013) (cited on page 104).

[236] P. Riego, P. Vavassori, and A. Berger, "Metamagnetic Anomalies near Dynamic Phase Transitions", Phys. Rev. Lett. **118**, 117202 (2017) (cited on page 104).

[237] S. W. Sides, P. A. Rikvold, and M. A. Novotny, "Kinetic Ising Model in an Oscillating Field: Finite-Size Scaling at the Dynamic Phase Transition", Phys. Rev. Lett. **81**, 834–837 (1998) (cited on pages 104, 107–108, 115).

[238] S. W. Sides, P. A. Rikvold, and M. A. Novotny, "Kinetic Ising model in an oscillating field: Avrami theory for the hysteretic response and finite-size scaling for the dynamic phase transition", Phys. Rev. E **59**, 2710–2729 (1999) (cited on pages 104, 108, 115).

[239] G. Korniss, C. J. White, P. A. Rikvold, and M. A. Novotny, "Dynamic phase transition, universality, and finite-size scaling in the two-dimensional kinetic Ising model in an oscillating field", Phys. Rev. E **63**, 016120 (2000) (cited on pages 104, 106, 115).

[240] G. M. Buendía and P. A. Rikvold, "Dynamic phase transition in the two-dimensional kinetic Ising model in an oscillating field: Universality with respect to the stochastic dynamics", Phys. Rev. E **78**, 051108 (2008) (cited on pages 104, 106–107, 115).

[241] H. Park and M. Pleimling, "Dynamic phase transition in the three-dimensional kinetic Ising model in an oscillating field", Phys. Rev. E **87**, 032145 (2013) (cited on pages 104, 106–107, 110, 115).

[242] H. Park and M. Pleimling, "Surface Criticality at a Dynamic Phase Transition", Phys. Rev. Lett. **109**, 175703 (2012) (cited on page 104).

[243] K. Tauscher and M. Pleimling, "Surface phase diagram of the three-dimensional kinetic Ising model in an oscillating magnetic field", Phys. Rev. E **89**, 022121 (2014) (cited on page 104).

[244] G. M. Buendía and P. A. Rikvold, "Fluctuations in a model ferromagnetic film driven by a slowly oscillating field with a constant bias", Phys. Rev. B **96**, 134306 (2017) (cited on page 104).

[245] E. Vatansever and N. G. Fytas, "Dynamic phase transition of the Blume-Capel model in an oscillating magnetic field", Phys. Rev. E **97**, 012122 (2018) (cited on page 104).

[246] E. Vatansever and N. G. Fytas, "Dynamic phase transitions in the presence of quenched randomness", Phys. Rev. E **97**, 062146 (2018) (cited on pages 104–105).

[247] P. A. Rikvold and M Kolesik, "Soft versus hard dynamics for field-driven solid-on-solid interfaces", Journal of Physics A: Mathematical and General **35**, L117 (2002) (cited on page 104).

[248] X. Shi and G. Wei, "Effective-field and Monte Carlo studies of a kinetic Blume–Capel model", Physica Scripta **89**, 075805 (2014) (cited on page 104).

[249] M. Acharyya and A. Halder, "Blume-Capel ferromagnet driven by propagating and standing magnetic field wave: Dynamical modes and nonequilibrium phase transition", Journal of Magnetism and Magnetic Materials **426**, 53–59 (2017) (cited on page 104).

[250] G. Grinstein, C. Jayaprakash, and Y. He, "Statistical Mechanics of Probabilistic Cellular Automata", Phys. Rev. Lett. **55**, 2527–2530 (1985) (cited on page 105).

[251] G. Gulpinar and E. Vatansever, "Effects of the Quenched Random Crystal Field on the Dynamic Spin-1 Blume-Capel Model", Journal of Statistical Physics **146**, 787–799 (2012) (cited on page 105).

[252] G. Gulpinar, E. Vatansever, and M. Agartioglu, "Effective-field theory with the differential operator technique for a kinetic Blume–Capel model with random diluted single-ion anisotropy", Physica A: Statistical Mechanics and its Applications **391**, 3574–3584 (2012) (cited on page 105).

[253] Ü. Akıncı, Y. Yüksel, E. Vatansever, and H. Polat, "Effective field investigation of dynamic phase transitions for site diluted Ising ferromagnets driven by a periodically oscillating magnetic field", Physica A: Statistical Mechanics and its Applications **391**, 5810–5817 (2012) (cited on page 105).

[254] E. Vatansever, U. Akinci, and H. Polat, "Time dependent magnetic field effects on the±J Ising model", Journal of magnetism and magnetic materials **344**, 89–95 (2013) (cited on page 105).

[255] E. Vatansever, Ü. Akıncı, Y. Yüksel, and H. Polat, "Investigation of oscillation frequency and disorder induced dynamic phase transitions in a quenched-bond diluted Ising ferromagnet", Journal of magnetism and magnetic materials **329**, 14–23 (2013) (cited on page 105).

[256] E. Vatansever and H. Polat, "Magnetic response of a disordered binary ferromagnetic alloy to an oscillating magnetic field", Physics Letters A **379**, 1568–1575 (2015) (cited on page 105).

[257] N. S. Branco and B. M. Boechat, "Real-space renormalization-group study of the two-dimensional Blume-Capel model with a random crystal field", Phys. Rev. B **56**, 11673–11677 (1997) (cited on pages 105–106).

[258] Sumedha and S. Mukherjee, "Emergence of a bicritical end point in the random-crystal-field Blume-Capel model", Phys. Rev. E **101**, 042125 (2020) (cited on page 105).

[259] E. Vatansever, Z. D. Vatansever, P. E. Theodorakis, and N. G. Fytas, "Ising universality in the two-dimensional Blume-Capel model with quenched random crystal field", Phys. Rev. E **102**, 062138 (2020) (cited on pages 105–107, 111).

[260] C. Buzano, A. Maritan, and A. Pelizzola, "A cluster variation approach to the random-anisotropy Blume-Emery-Griffiths model", Journal of Physics: Condensed Matter **6**, 327 (1994) (cited on page 105).

[261] C. J. Silva, A. A. Caparica, and J. A. Plascak, "Wang-Landau Monte Carlo simulation of the Blume-Capel model", Phys. Rev. E **73**, 036702 (2006) (cited on page 106).

[262] R. J. Glauber, "Time-Dependent Statistics of the Ising Model", Journal of Mathematical Physics **4**, 294–307 (1963) (cited on page 107).

[263] K. Binder, "Critical Properties from Monte Carlo Coarse Graining and Renormalization", Phys. Rev. Lett. **47**, 693–696 (1981) (cited on page 108).

[264] M. E. Fisher, *Scaling, universality and renormalization group theory*, Vol. 85 (Springer, May 1983), page 051123 (cited on page 118).

[265] V. Privman, *Finite size scaling and numerical simulation of statistical systems*, Vol. 85 (World Scientific, May 1990), page 051123 (cited on page 118).

[266] K. Binder, H. Gausterer, and C. Lang, "Computational methods in field theory", Schladming Lecture Notes **85**, 59 (1992) (cited on page 118).

[267] A. E. Ferdinand and M. E. Fisher, "Bounded and Inhomogeneous Ising Models. I. Specific-Heat Anomaly of a Finite Lattice", Phys. Rev. **185**, 832–846 (1969) (cited on page 118).

[268] J. Salas and A. D. Sokal, "Universal amplitude ratios in the critical two-dimensional Ising model on a torus", Journal of Statistical Physics **98**, 551–588 (2000) (cited on page 118).

[269] W. Selke, "The critical Binder cumulant for isotropic Ising models on square and triangular lattices", Journal of Statistical Mechanics: Theory and Experiment **2007**, P04008 (2007) (cited on page 118).

[270] W. Selke and L. N. Shchur, "Critical Binder cumulant in a two-dimensional anisotropic Ising model with competing interactions", Phys. Rev. E **80**, 042104 (2009) (cited on page 118).

[271] M. Hasenbusch, F. P. Toldin, A. Pelissetto, and E. Vicari, "Universal dependence on disorder of two-dimensional randomly diluted and random-bond $\pm J$ Ising models", Phys. Rev. E **78**, 011110 (2008) (cited on page 118).